

https://dspace.org/

Impact of microwave irradiation on the properties of the manganese oxide based electrode materials for lithium-ion and sodium-ion batteries

Nkosi, Funeka Phumzile

2018

https://hdl.handle.net/10539/26725

Downloaded from a DSpace repository. https://dspace.org/

Impact of microwave irradiation on the properties of the manganese oxide based electrode materials for lithium-ion and sodium-ion batteries



Funeka Phumzile Nkosi

A Thesis submitted for the faculty of Science at the University of Witwatersrand Johannesburg, in the fulfilment for the degree of

Doctor of Philosophy in Chemistry

Supervisor: Prof. Kenneth I. Ozoemena

Co-Supervisor: Dr. Caren Billing

Johannesburg, March 2018

DECLARATION

I declare that this thesis is my own, unaided work. It is being submitted for the degree of Doctor of Philosophy in the University of the Witwatersrand, Johannesburg. It has not been submitted before for any degree or examination in any other university.

SIGNATURE: ..... Date: .....

DEDICATION

This work is dedicated to my family. Without them I am nothing.

"The LORD is my strength and my song.
HE has given me victory." (Exodus 15:2)

ACKNOWLEDGEMENTS

Firstly, I would like to thank the Council for Scientific and Industrial Research (CSIR) for providing me with the opportunity to achieve my dreams. I am deeply indebted to the CSIR Energy Materials group for giving me the Ph.D. studentship that funded this Ph.D. work. I am grateful to the whole Energy Materials team for everything they have done for me during my Ph.D. studies.

I would like to render my warmest thanks to my supervisor, Professor Kenneth Ozoemena for his continuous support, advice, and encouragement. I am grateful for his expert advice that has been invaluable throughout all the stages of this Ph.D. I cannot imagine a better supervisor and mentor.

I would like to thank my co-supervisor Dr. Caren Billing for her contribution and support during my Ph.D. studies.

My very sincere thanks to Dr. Nithya Palaniyandy and Dr. Kumar Raju for their friendship, mentorship, selfless support and generous care. I have learnt a lot from them and I enjoyed working with them. In them, I have found a brother and a sister.

I would like to thank my colleagues and friends at the CSIR and University of Witwatersrand for their help and encouragement. I would like to thank Mr. Josiah Jideani for helping me format this Ph.D. thesis.

I would like to express my profound gratitude to my beloved mother, brothers, sisters, nephews, and nieces for their continuous support and unconditional love. I appreciate so much my sisters Nomfundo Gcabashe and Gugulethu Mncube for their assistance and encouragement. I thank them for always being there for me. I am nothing without my family.

Lastly, I would like to thank God for His mercy and grace towards me. His love never failed me. I thank Him for providing me with this opportunity and I praise Him for giving me the strength and capability to complete this degree.

RESEARCH OUTPUTS

❖ Publications

1. **Funeka P. Nkosi**, Kumar Raju, Nithyadharseni Palaniyandy, M. V. Reddy, Caren Billing, and Kenneth I. Ozoemena. *Insights into the Synergistic Roles of Microwave and Fluorination Treatments Towards Enhancing the Cycling Stability of P2-Type* $Na_{0.67}[Mg_{0.28}Mn_{0.72}]O_2$ *Cathode Material for Sodium-Ion Batteries.J.* ECS, 164 (13) (2017) A1-A9.
2. **Funeka P. Nkosi**, Nithyadharseni Palaniyandy, Kumar Raju, Noshin Omar, Caren Billing, and Kenneth I. Ozoemena. *Effects of Synthesis Combustion Fuels on Suppressing Voltage Decay in High-Energy-Dense* $Li_{1.2}Mn_{0.52}Co_{0.13}Ni_{0.13}Al_{0.02}O_2$ *Cathode Material for Lithium-ion Batteries* (submitted-2018).
3. **Funeka P. Nkosi**, Nithyadharseni Palaniyandy, Kumar Raju, Noshin Omar, Caren Billing, and Kenneth I. Ozoemena. *Microwave-Assisted Retardation of the Li2MnO3 Activation for Enhanced Interfacial Properties of the High-Energy Density Layered Li1.2Mn0.52Co0.13Ni0.13Al0.02O2 Cathode Materials* (submitted-2018).
4. Nithyadharseni Palaniyandy, **Funeka P. Nkosi**, Kumar Raju, and Kenneth I. Ozoemena. *Facile conversion of electrolytic* MnO_2 *to the* Mn_xO_y *nano- and micro-structures as anode materials for rechargeable lithium-ion batteries.* J. Electro Analytical Chem. (To be submitted-2018)
5. Nithyadharseni Palaniyandy, **Funeka P. Nkosi**, Kumar Raju, and Kenneth I. Ozoemena. *Fluorinated* Mn_3O_4 *nanospheres for lithium-ion batteries: Low-cost synthesis with enhanced capacity, cyclability and charge-transport. J.* Mater. Chem. Phys (in press-2018: DOI10.1016/j.matchemphys.2018.01.003).
6. Kumar Raju, **Funeka P. Nkosi**, Elumalai Viswanathan, Mkhulu K. Mathe, Krishnan Damodaranc and Kenneth I. Ozoemena. *Microwave-enhanced electrochemical cycling performance of the* $LiNi_{0.2}Mn_{1.8}O_4$ *spinel cathode material at elevated temperature,* Phys. Chem. Chem. Phys**.**, 18, (2016), 13074-13083.

❖ Patent/invention disclosure

1. K.I. Ozoemena and **F.P. Nkosi**, "Production of a spinel material" (PCT Patent Application No. PCT/ZA2015/050019 – filed 30 October 2015; WO App/Pub. No.: WO2016070205A3, Pub. Date: Sept 9, 2016).

❖ **Conferences**

1. **Funeka P. Nkosi**, Nithyadharseni Palaniyandy, Kumar Raju, Caren Billing and Kenneth I Ozoemena. *The Effects of Combustion Fuels (Urea and Ethylene Glycol) on the Physico-Chemical and Electrochemical Performance of LMNCA.* 233rd ECS Meeting, Seattle, Washington, USA, May 2018.
2. **Funeka P. Nkosi**, Nithyadharseni Palaniyandy, Kumar Raju, Mesfin Kebede, Caren Billing and Kenneth I Ozoemena. *Enhancing the Electrochemical Performance of P2-type $Na_{0.67}[Mg_{0.28}Mn_{0.72}]O_2$ Cathode for Sodium-ion Batteries using Microwave Irradiation.* The 4th International Symposium on Electrochemistry, Johannesburg, South Africa, April 2018.
3. Kenneth I. Ozoemena and **Funeka P. Nkosi** *Unravelling the effects of microwave irradiation on the performance of cathode materials for advanced batteries*. The 4th International Symposium on Electrochemistry, Johannesburg, South Africa, April 2018.
4. **Funeka P. Nkosi**, Nithyadharseni Palaniyandy, Kumar Raju, Mesfin Kebede, Caren Billing and Kenneth I Ozoemena. *The Role of Combustion Fuels (urea and ethylene glycol) Towards Improving the Electrochemical Performance of LMNCA Cathode Material.* The 7th International Conference on Nanoscience and Nanotechnology in Africa, Durban, South Africa, April 2018.
5. **Funeka P. Nkosi,** Kumar Raju, Nithyadharseni Palaniyandy, Caren Billing, and Kenneth I. Ozoemena. *Improving cycle performance of P2-type $Na_{0.67}Mg_{0.28}Mn_{0.72}O_2$ cathode for sodium-ion batteries***.** 7th SANi-NYRS symposium, Pretoria, South Africa, October 2017.
6. **Funeka P. Nkosi**, Nithyadharseni Palaniyandy, Kumar Raju and Kenneth I. Ozoemena. *Microwave irradiation on manganese oxide based cathode materials for lithium-ion batteries*. European School of Materials Science Symposium, Saarland University, Germany, November 2016.
7. **Funeka P. Nkosi** and Kenneth I. Ozoemena. *Enhancing Electrochemical Performance of Spinel $LiMn_2O_4$ based Cathode Materials for Lithium-ion Battery using Microwave Irradiation,* DST/NRF Nanotechnology Symposium, Pretoria, South Africa, June 2016.
8. **Funeka P. Nkosi,** *African youth skills acquisition, development and innovation,* Post UN/UNESCO Youth forum for Africa, South Africa, May 2016.
9. **Funeka P. Nkosi** and Kenneth I. Ozoemena. *The effect of microwave irradiation on the electrochemistry of spinel lithium manganese oxide cathode materials for lithium- ion,*

University of Witwatersrand School of chemistry 2nd colloquium, Johannesburg, South Africa, April 2016.

10. **Funeka P. Nkosi** and Kenneth I. Ozoemena *Microwave irradiation as an essential step in the synthesis of spinel $LiMn_2O_4$ cathode materials for lithium-ion batteries.* 5th CSIR Emerging Researcher Symposium, Pretoria, South Africa, October 2015.

❖ **Workshops**

1. *Scientific Writing for Scientists and Engineers*. Presented by Prof Noel Buckley and organized by the electrochemical society, ECS 277th Meeting, Chicago, USA, May 2015.
2. Solar Fuel and Energy Storage: Swiss Southern African Joint Research Programme. (Workshop conference), Pretoria, South Africa, October 2016
3. DST/UL: SA international energy storage workshop, Nelspruit, South Africa, October 2017.

❖ **Overseas research visits and collaboration**

1. European School of Materials Science, *Saarland University*, Germany, 03 November 2016- 30 November 2016.
2. Vrije Universiteit Brussel Battery Innovation Center, *Vrije Universiteit Brussel*, Belgium, 01 April – 09 April 2017 (manuscript in progress-to be submitted in 2018)

❖ **CSIR internal collaboration**

1. CSIR Energy Materials (EM) and Mechatronics and Micro-Manufacturing (MMM) printed sensor and batteries collaboration.

❖ **Junior student supervision**

1. Supervised one BSc honors student during vacation work at the CSIR (November-December 2015)

SOCIETIES/CLUBS/ORGANIZATIONS

1. South African Chemical Institute (since 2017)
2. Electrochemical Society (since 2017)
3. Full member of Organisation of Women in Science for the Developing World (OWSD), (since 2016)
4. International Society of Electrochemistry (since 2015)

AWARDS, HONOURS AND PRIZES

1. 2017 South Africa's women in science awards 2017 and TATA Africa Scholarship for Women in Science, Engineering and Technology (Ph.D. category) (September 2017)
2. 2017 Mail & Guardian Top 200 young South African (Science and Technology category) (June 2017)
3. Lindau Nobel Laureate Alumni (Young scientist status), 67th Lindau Nobel Laurette Meeting (Chemistry), (June 2017)
4. Science Today Alumni, South Africa's best postgrad science writing (November 2016)
5. Best Master's degree studentship excellence award, CSIR excellence awards 2016 (November 2016)
6. Best poster presentation, 3rd place, DST/NRF Nanotechnology Symposium, (June 2016)
7. Semi-finalist, Famelab South Africa, (March 2016)
8. Best Master's degree studentship, CSIR Materials Science and Manufacturing excellence awards, (November 2015)
9. Best oral presentation (Ph.D. category), 5th CSIR emerging researchers' symposium, (October 2015)

ABSTRACT

This work involved the study of manganese oxide based materials as cathode materials in lithium-ion batteries (LIBs) and sodium-ion batteries (SIBs). A lithium manganese rich-transition metal oxide, $Li_{1.2}Mn_{0.52}Co_{0.13}Ni_{0.13}Al_{0.02}O_2$ (LMNCA) cathode material was successfully prepared using the combustion method. Urea and ethylene glycol (EG) were used as fuels during the combustion synthesis and their effect on the physical and electrochemical properties of the samples were evaluated. This study revealed that the combustion synthesis of electrode materials depends greatly on the type of fuel to produce materials with enhanced electrochemical properties. LMNCA prepared by urea (LMNCA-urea) delivered the higher specific capacity of 295 mAh/g with a capacity retention of 84 % after 50 cycles, while the LMNCA prepared by EG (LMNCA-EG) gave a capacity of 240 mAh/g and a capacity retention of 78 % after 50 cycles. Even though LMNCA-urea has enhanced cycle performance, it has higher voltage fade and decomposition of electrolyte occurs upon cycling as compared to LMNCA-EG. The effect of microwave irradiation on the combustion synthesis of LMNCA using either the urea or EG was also studied. The microwave irradiation improved the capacity and the rate capability of LMNCA-EG by decreasing the particle size and tuning the oxidation state of the manganese ion content. The capacity retention after 50 cycles at 0.1 C is 88 % and 82 % for LMNCA-EG and LMNCA-urea, respectively. A novel method using α-MnO_2 nanowires as manganese precursor to prepare LMNCA cathode material is also reported. The XRD analysis revealed pure, crystalline LMNCA powders with good hexagonal ordering. The SEM images showed that LMNCA powders exhibited plate-like particles with smooth surfaces, an unusual morphology for LMNCA materials. The LMNCA material exhibited excellent cycle performance and good rate capability. The capacity retention was 95 % and 96 % after the 50^{th} and 100^{th} cycles, respectively. The preparation of P2-type $Na_{0.67}Mg_{0.28}Mn_{0.72}O_2$ (NaMgMnO) cathode materials for sodium-ion batteries using a urea combustion method is also reported for the first time. The effect of microwave irradiation and fluorination was investigated with the aim to improve the capacity retention and the rate capability of NaMgMnO cathode material. The powder XRD analyses showed that pure single phase P2-type powders were successfully prepared. SEM analyses revealed an impact of microwave irradiation and fluorination on the morphology of the materials. The galvanostatic charge-discharge and the electrochemical impedance spectroscopy studies showed that both microwave irradiation and fluorination improved the capacity, coulombic efficiency, cycle performance and impedance of NaMgMnO cathode materials.

TABLE OF CONTENTS

DECLARATION ..... **i**

DEDICATION ..... **ii**

ACKNOWLEDGEMENTS ..... **iii**

RESEARCH OUTPUTS ..... **iv**

SOCIETIES/CLUBS/ORGANIZATIONS ..... **vii**

AWARDS, HONOURS AND PRIZES ..... **vii**

ABSTRACT ..... **viii**

LIST OF FIGURES ..... **xiv**

LIST OF TABLES ..... **xix**

LIST OF SCHEMES ..... **xxi**

LIST OF SYMBOLS ..... **xxii**

LIST OF ABBREVIATIONS ..... **xxiv**

CHAPTER 1 Introduction **1**

1.1 Introduction 1

1.2 Motivation and Rationale 1

1.3 Objectives of the study 4

1.4 Outline of the thesis 4

1.5 References 5

CHAPTER 2 Literature Review **6**

2.1 Introduction 6

2.2 Lithium-Ion Batteries 6

2.2.1 Background of lithium-ion batteries 6

2.2.2 Working principle of lithium-ion batteries 7

2.2.3 Application of lithium-ion batteries 9

2.2.4 Manganese oxide based cathode materials 11

2.2.5 Lithium and manganese rich nickel manganese cobalt oxide (LMR-NMC) 12

2.3 Sodium-Ion Batteries 31
2.3.1 Background of sodium-ion batteries 31
2.3.2 Working principle of sodium-ion batteries 34
2.3.3 Applications of sodium-ion batteries 34
2.3.4 Cathode materials for sodium-ion batteries 35
2.3.5 P2-type $Na_{0.67}Mg_{0.28}Mn_{0.72}O_2$ cathode material 42
2.4 Electrochemical characterization of cathode materials 45
2.4.1 Cyclic voltammetry 45
2.4.2 Galvanostatic charge-discharge 46
2.4.3 Electrochemical impedance spectroscopy 47
2.4.4 Diffusion coefficient of lithium-ions 49
2.5 References 51
CHAPTER 3 Experimental Method 63
3.1 Introduction 63
3.2 Chemicals and Materials 63
3.3 Synthesis Procedures 63
3.3.1 Combustion synthesis of LMNCA powders using urea and ethylene glycol fuels 63
3.3.2 Microwave irradiation of LMNCA prepared using urea and ethylene glycol combustion synthesis. 66
3.3.3 Preparation of LMNCA from α-MnO_2 nanowires 67
3.3.4 Preparation of NaMgMnO cathode materials 68
3.4 Materials Characterization 69
3.4.1 Powder x-ray diffraction 69
3.4.2 Scanning electron microscopy and Energy dispersive x-ray spectroscopy 69
3.4.3 Transmission electron microscopy 69
3.4.4 X-ray photoelectron spectroscopy 70
3.4.5 Raman spectroscopy 70

3.4.6 Brunauer- Emmett-Teller (BET) surface area 70
3.5 Coin cells 70
3.5.1 Electrode fabrication for lithium-ion and sodium-ion batteries 70
3.5.2 Fabrication of coin cells 71
3.5.1 Characterization of coin cells 72
CHAPTER 4 Investigating the effect of combustion fuel on the synthesis of lithium manganese rich – transition metal oxides: Comparative studies of structure and electrochemistry 74
4.1 Introduction 74
4.2 Results and Discussions 75
4.2.1 Powder X-ray Diffraction Characterization 75
4.2.2 X-ray Photoelectron Spectroscopy Characterization (XPS) 77
4.2.3 Raman Spectroscopy Characterization 79
4.2.4 Scanning Electron Microscopy Characterization (SEM) 80
4.2.5 Transmission Electron Microscopy Characterization (TEM) 81
4.2.6 Brunuar Emmett Teller (BET) Surface Area 81
4.2.7 Electrochemical Characterization 82
4.3 Conclusions 98
4.4 References 99
CHAPTER 5 Effect of microwave irradiation on the LMNCA cathode materials prepared using urea and ethylene glycol combustion synthesis 102
5.1 Introduction 102
5.2 Results and Discussions 103
5.2.1 Powder X-ray Diffraction Characterization 103
5.2.2 X-ray Photoelectron Spectroscopy Characterization (XPS) 104
5.2.3 Scanning Electron Microscopy Characterization (SEM) 107
5.2.4 Electrochemical Characterization 108
5.3 Conclusions 120
5.4 References 121

CHAPTER 6 Preparation of LMNCA cathode materials from α-MnO_2 nanowires.... 123

6.1 Introduction....123

6.2 Results and Discussions....124

6.2.1 Powder X-ray Diffraction Characterization....124

6.2.2 X-ray Photoelectron Spectroscopy Characterization (XPS)....125

6.2.3 Scanning Electron Microscopy Characterization (SEM)....126

6.2.4 Transmission Electron Microscopy Characterization (TEM)....129

6.2.5 Electrochemical Characterization....131

6.3 Conclusions....136

6.4 References....137

CHAPTER 7 The effect of microwave irradiation on the preparation of P2-type $Na_{0.67}Mg_{0.28}Mn_{0.72}O_2$ cathode materials for sodium-ion batteries....139

7.1 Introduction....139

7.2 Results and discussion....140

7.2.1 Powder X-ray Diffraction Characterization....140

7.2.2 X-ray Photoelectron Spectroscopy Characterization (XPS)....141

7.2.3 Scanning Electron Microscopy Characterization (SEM)....143

7.2.4 Energy–Dispersive X-ray Spectroscopy (EDX)....144

7.2.5 Electrochemical Characterization....147

7.3 Conclusion....156

7.4 References....157

CHAPTER 8 Fluorination of P2-type $Na_{0.67}Mg_{0.28}Mn_{0.72}O_2$ cathode materials for sodium-ion batteries....158

8.1 Introduction....158

8.2 Results and Discussion....159

8.2.1 Powder X-ray Diffraction Characterization....159

8.2.2 X-ray Photoelectron Spectroscopy Characterization (XPS)....161

8.2.3 Scanning Electron Microscopy Characterization (SEM) 163
8.2.4 Electron Dispersive X-ray spectroscopy 165
8.2.5 Transmission Electron Microscopy Characterization (TEM) 166
8.2.6 Electrochemical Characterization 167
8.3 Conclusions 176
8.4 References 177
CHAPTER 9 General conclusions and Future work 178
9.1 Introduction 178
9.2 Conclusion 178
9.2.1 Preparation of LMNCA cathode materials using urea and ethylene glycol combustion synthesis. 178
9.2.2 The effect of microwave irradiation on LMNCA cathode materials prepared using urea and ethylene glycol combustion synthesis. 178
9.2.3 Preparation of LMNCA cathode materials from α-MnO_2 nanowires 179
9.2.4 The effect of microwave irradiation on the preparation of P2-type $Na_{0.67}Mg_{0.28}Mn_{0.72}O_2$ cathode materials for sodium-ion batteries 179
9.2.5 Fluorination on the electrochemistry of P2-type $Na_{0.67}Mg_{0.28}Mn_{0.72}O_2$ cathode materials for sodium-ion batteries 179
9.3 Future work 180

LIST OF FIGURES

Figure 1.1: The pie chart shows world manganese ore production and the bar chart shows the world reserves of manganese ore in terms of metal content 2

Figure 2.1: Comparison of various secondary batteries 7

Figure 2.2: The basic structure and working principle of lithium-ion batteries; (a) shows the charge cycle and (b) shows the discharge cycle of a typical lithium-ion 8

Figure 2.3: Applications of lithium-ion batteries 9

Figure 2.4: Different structures of cathode materials (a) layered structure, (b) spinel structure, and (c) olivine structure 11

Figure 2.5: Comparison of lithium-ion cathode materials 12

Figure 2.6: (a) The $LiMO_2$ structure (M = Mn, Co, Ni), (b) Li_2MnO_3 structure and (c) 'layered-layered' LMR-NMC structure 14

Figure 2.7: Typical charge-discharge of LMR-NMC cathode materials between 2.0 V – 4.8 V vs. Li 16

Figure 2.8: Effects of charging on the structure of LMR-NMC materials 17

Figure 2.9: (a) LMR-NMC cathode after 60 cycles with small domains of spinel nucleated, (b and c) nucleated spinel crystal domains in different crystal orientations, blue circled region show amorphized lattices, (d) FFT of the TEM image in (c) showing lattice distortions. (e) Schematic drawing showing the different mechanisms of spinel formation from the $LiMO_2$ ($R3m$) and Li_2MnO_3 (C_2/m). 19

Figure 2.10: Surface reactions occurring during 1st cycle charging (before voltage plateau and at voltage plateau) and discharging (after voltage plateau) for a typical LMR-NMC cathode material [51]. 20

Figure 2.11: Results for LMR-NMC show (a,b) voltage fade charge-discharge profiles, (c) voltage fade and hysteresis in differential capacity vs. voltage plots and (d-f) voltage fade in LMR-NMC materials synthesized utilising different methods. 22

Figure 2.12: (a) LMNCO cathode material coated with graphene and (b) cycle performance for the graphene coated LMNCO 24

Figure 2.13: Scheme for the glucose combustion synthesis of LMNC cathode material 28

Figure 2.14: Microwave irradiation vs. convectional heating. 30

Figure 2.15: Sodium-ion batteries research publications history 32

Figure 2.16: Elemental abundance in the Earth's crust 33

Figure 2.17: Working principle of sodium-ion batteries 34

Figure 2.18: Applications of sodium-ion batteries 35
Figure 2.19: (a) Frame work of Prussian blue analogues and (b) electrochemical performance of Prussian blue analogues as cathode materials in sodium-ion batteries 37
Figure 2.20: Organic cathode materials used in sodium-ion batteries 38
Figure 2.21: Crystal structure of polyanionic cathode material (a) NASICON $Na_3V_2(PO_4)_3$, (b) olivine $NaFePO_4$, (c) Na_2FePO_4F, (d) Na_2FeSO_4F 39
Figure 2.22: Structural classification of layered sodium transition metal oxide cathodes and phase transition processes induced by sodium extraction 41
Figure 2.23: Average discharge potential and volumetric energy density (Wh/L) vs. volumetric capacity (Ah/L) for cathode materials for SIBs and LIBs 42
Figure 2.24: The structure of $Na_{2/3}[Mg_{0.28}Mn_{0.72}]O_2$, (a) shows the stacking of MO_2 in the structure and (b) shows the Mg-Mn ordering in the TM layers 43
Figure 2.25: Jahn-Teller distortion of high spin Mn^{3+} ions 44
Figure 2.26: Typical cyclic voltammogram of LMR-NMC ($Li[Li_{0.2}Mn_{0.54}Ni_{0.13}Co_{0.13}Al_{0.02}]O_2$) cathode material cycled between 2.5 V and 4.8 V at 0.1 mV s^{-1} 46
Figure 2.27: Nyquist plot and equivalent circuit (inset) of LMR-NMC cathode material 48
Figure 2.28: EIS behaviour of cathode material at different frequency ranges 49
Figure 3.1: Components of a coin cells and coin cells fabricated from the prepared cathode materials. 72
Figure 4.1: PXRD pattern of LMNCA-urea and LMNCA-EG samples. 76
Figure 4.2: XPS of LMNCA powders prepared from urea and EG combustion methods. 78
Figure 4.3: Raman analysis of LMNCA-urea and LMNCA-EG samples 79
Figure 4.4: SEM images and particle size distribution histogram of urea-combustion and EG-combustion samples 80
Figure 4.5: TEM images of LMNCA-urea sample. 81
Figure 4.6: BET surface area analysis of LMNCA-urea and LMNCA-EG samples. 82
Figure 4.7: Cyclic voltammograms between 2.0 V - 4.8 V at 0.1 mV s^{-1} at room temperature. 83
Figure 4.8: (a-b) Charge-discharge at 0.1 C between 2.0 - 4.8 V, and (c-d) corresponding differential capacity curves (dQ/dV vs. V) plots for the LMNCA-urea and -EG samples. 84
Figure 4.9: (a) Mid-point voltage curves at 0.1 C, (b-c) cycle performance and coulombic efficiency at 0.1 C between 2.0 - 4.8 V for LMNCA-urea and LMNCA-EG samples. 87
Figure 4.10: Rate capability at different current densities for LMNCA-urea and LMNCA-EG samples. 88

Figure 4.11: XRD patterns of LMNCA-urea and LMNCA-EG electrodes after 100 cycles. . 89
Figure 4.12: SEM analysis of the LMNCA-urea and LMNCA-EG electrodes after 100 cycles at 0.1 C. 90
Figure 4.13: EDX mapping and elemental analysis of LMNCA-EG electrode after 100 cycles. 91
Figure 4.14: O 1s, F 1s, P 2p, Li 1s and C 1s XPS spectra for LMNCA-EG electrode after 100 cycles. 93
Figure 4.15: Post-morterm studies- (a-g) EDX analysis of LMNCA-urea, (h) XPS analysis of LMNCA-urea and (i,j) XPS of F 1s and P 2p peaks for LMNCA-urea and LMNCA-EG. 95
Figure 4.16: (a) Nyquist plots (-Z'' vs. Z') and (b) Z' vs. $\omega^{-1/2}$ curves of LMNCA-urea and LMNCA-EG samples. 97
Figure 5.1: PXRD patterns of LMNCA-urea mic and LMNCA-EG mic samples. 103
Figure 5.2: XPS data of Mn 3s and Mn $2p_{3/2}$ for (a,c) LMNCA-EG mic, and (b,d) LMNCA-urea mic samples. 105
Figure 5.3: XPS data of Co 2p and Ni 2p for (a,c) LMNCA-EG mic, and (b,d) LMNCA- urea mic samples. Symbol "S" denotes the satellite signals for the corresponding metal ions. 107
Figure 5.4: SEM images of (a-b) LMNCA-urea mic and (c-d) LMNCA-EG mic sample. .. 108
Figure 5.5: Cyclic voltammetry at 0.1 mV s^{-1} between 2.0 - 4.8 V (a) LMNCA-urea mic and (b) LMNCA-EG mic. 109
Figure 5.6: Galvanostatic charge-discharge at 0.1 C for (a) LMNCA-EG mic and (b) LMNCA-urea mic after 50 cycles. 111
Figure 5.7: Differential capacity vs. voltage curves for (a-c) LMNCA-EG mic and (d-f) LMNCA-urea mic after 90 cycles. 112
Figure 5.8: Cycle performance and the coulombic efficiency of the materials (a) LMNCA-urea mic and (b) LMNCA-EG mic, and (c) Cycle performance of both samples at 2 C. 114
Figure 5.9: Rate capability of LMNCA-urea mic and LMNCA-EG mic materials. 116
Figure 5.10: EIS and diffusion co-efficient analysis of LMNCA-urea mic and LMNCA-EG mic samples. 118
Figure 6.1: PXRD patterns of α-MnO_2 nanowires and LMNCA cathode materials. 125
Figure 6.2: XPS data of Mn $2p_{3/2}$ for LMNCA sample prepared from α-MnO_2 nanowires.. 126

Figure 6.3: (a) Low magnification SEM images, (b) High magnification, (c) Low magnification TEM, (d) High magnification TEM, (e) High resolution TEM and (f) SAED image of α-MnO_2 nanowires.....127
Figure 6.4: SEM images of LMNCA powders (a-b) and (c) EDX elemental analysis and composition. 128
Figure 6.5: EDX elemental mapping of prepared LMNCA sample.....129
Figure 6.6: High resolution TEM and SAED pattern of the prepared LMNCA sample.....130
Figure 6.7: Cyclic voltammograms (current density vs. voltage) of the prepared LMNCA cathode. Scan rate: 0.1 mV s^{-1}; voltage range: 1.5 – 4.4 V vs. Li/Li^+. 131
Figure 6.8: Cycle performance and coulombic efficiency at (a) 0.1 C and (b) 5 C rate. 132
Figure 6.9: Rate capacity at different current rates. 133
Figure 6.10: Electrochemical Impedance Spectroscopy of LMNCA sample. 135
Figure 7.1: XRD patterns of the prepared NaMgMnO samples.....140
Figure 7.2: XPS spectra for the (a) NaMgMnO-a and (b) NaMgMnO-ma samples. 142
Figure 7.3: SEM images of (a) NaMgMnO-a and (b) NaMgMnO-ma samples. 144
Figure 7.4: EDX analysis of NaMgMnO-a. 145
Figure 7.5: EDX analysis of NaMgMnO-ma. 146
Figure 7.6: Cyclic voltammograms (current density vs. voltage) of the cells of (a) NaMgMnO-a and (b) NaMgMnO-ma. Scan rate: 0.1 mV s^{-1}. Voltage range: 1.5 – 4.4 V vs. Na/Na^+. 148
Figure 7.7: Galvanostatic charge-discharge graphs (voltage vs. specific capacity) of the cells containing the following cathode materials (a) NaMgMnO-a and (b) NaMgMnO-ma. 149
Figure 7.8: Discharge capacity and coulombic efficiency vs. cycle number graphs of NaMgMnO-a and NaMgMnO-ma containing cells. 150
Figure 7.9: Rate performance at different current densities of the NaMgMnO samples. 152
Figure 7.10: Nyquist plots (Z″ vs. Z') measured (a) before (OCV) and (b) after cycling (100 cycles). The dots and the straight line represent the experimental and fitted data, respectively. 154
Figure 7.11: Plots of Z' vs. $\omega^{-1/2}$ of NaMgMnO-a and NaMgMnO-ma.....155
Figure 8.1: PXRD pattern of the prepared (a) NaMgMnO-af and (b) NaMgMnO-maf samples. 160
Figure 8.2: XPS spectra for the (a) NaMgMnO-af and (b) NaMgMnO-maf samples. 162
Figure 8.3: SEM analysis NaMgMnO-af (a,b,c) and NaMgMnO-maf (d, e, f) samples. 164
Figure 8.4: EDX mapping of the NaMgMnO-af samples. 165
Figure 8.5: EDX mapping of the NaMgMnO-maf samples. 166

Figure 8.6: Typical TEM analysis of the fluorine-doped NaMgMnO (a,b) TEM images, (c) HR-TEM image and FFT image mapping of the NaMgMnO-af sample. 167

Figure 8.7: Cyclic voltammograms (current density vs. voltage) of (a) NaMgMnO-af, NaMgMnO-a (inset) and (b) NaMgMnO-maf. Scan rate: 0.1 mV s^{-1}. Voltage range: 1.5 – 4.4 V vs. Na/Na^{+}. 168

Figure 8.8: Galvanostatic charge-discharge graphs (voltage vs. specific capacity) of (a) NaMgMnO-af and (b) NaMgMnO-maf. 170

Figure 8.9: Discharge capacity vs. cycle number and coulombic efficiency graphs of NaMgMnO-af and NaMgMnO-maf compared to the pristine NaMgMnO-a sample. ... 171

Figure 8.10: Rate capability curves of NaMgMnO-af and NaMgMnO-maf compared to the pristine NaMgMnO-a sample. 173

Figure 8.11: Nyquist plots ($-Z''$ vs. Z') of NaMgMnO-af and NaMgMnO-maf compared to the pristine NaMgMnO-a sample measured before (at OCV) and after cycling (100 cycles). The dots and the straight lines represent the experimental and fitted data, respectively. 174

Figure 8.12: Z' vs. $\omega^{-1/2}$ curves for NaMgMnO-af and NaMgMnO-maf for fresh and aged cells. 175

LIST OF TABLES

Table 2.1: Example of electric vehicles based on lithium-ion batteries 10
Table 2.2: Comparison of synthesis methods for $Li_{1.2}Mn_{0.54}Ni_{0.13}Co_{0.13}O_2$ cathode. 27
Table 2.3: Characteristics of sodium-ion batteries and lithium-ion batteries 33
Table 2.4: Electrochemical performance of polyanions and pyrophosphates based cathode materials 39
Table 3.1: List of materials and reagents used in this thesis. 65
Table 4.1: Summary of crystallographic parameters 77
Table 4.2: XPS analysis of LMNCA-urea and LMNCA-EG samples 78
Table 4.3: Raman analysis of LMNCA materials synthesis by urea and EG combustion 79
Table 4.4: Summary of particle surface area, pore volume and average particle size 82
Table 4.5: EDX elemental composition of the LMNCA sample 91
Table 4.6: Elemental identification and quantification of LMNCA-EG and LMNCA-urea. . 94
Table 4.7: Electrochemical impedance spectroscopy fitted parameters 98
Table 5.1: Summary of crystallographic results LMNCA-urea mic and LMNCA-EG mic samples 104
Table 5.2: Summary of Mn $2p_{3/2}$ peak positions and cation distribution of the LMNCA-EG mic and LMNCA-urea mic samples 106
Table 5.3: Capacity retention and coulombic efficiency at 0.1 C and 2 C of LMNCA-urea mic and LMNCA-EG mic samples. 115
Table 5.4: Comparison of R_{ct} and Z_w of LMNCA-urea mic and LMNCA-EG mic with non-microwave irradiated LMNCA-urea and LMNCA-EG samples 117
Table 5.5: Electrochemical impedance spectroscopy fitted parameters and diffusion coefficient. 119
Table 6.1: Summary of crystallographic results of α-MnO_2 nanowires and LMNCA cathode materials. 125
Table 6.2: Summary of Mn $2p_{3/2}$ peak positions and cation distribution of the LMNCA sample prepared from α-MnO_2 nanowires 126
Table 6.3: Comparison of the prepared LMNCA sample with literature. 134
Table 6.4: Impedimetric data of prepared LMNCA sample. 135
Table 7.1: Summary of refined crystallographic parameters for the prepared NaMgMnO samples 141
Table 7.2: XPS (Mn $2p_{3/2}$ spectra) data of the NaMgMnO-a and NaMgMnO-ma samples . 143

Table 7.3: Elemental composition obtained from EDX 147
Table 7.4: Summary of discharge capacity and capacity retention of NaMgMnO samples . 151
Table 7.5: Impedimetric data of NaMgMnO-a and NaMgMnO-ma. 155
Table 7.6: The calculated diffusion coefficients. 156
Table 8.1: Summary of crystallographic data of NaMgMnO-af and NaMgMnO-maf compared to NaMgMnO-a sample. 161
Table 8.2: XPS (Mn $2p_{3/2}$ spectra) data of the NaMgMnO-af and NaMgMnO-maf samples compared to the pristine NaMgMnO-a sample. 163
Table 8.3: Summary of discharge capacity and capacity retention of fluorine doped NaMgMnO samples compared to the pristine NaMgMnO-a sample. 172
Table 8.4: Impedimetric data of NaMgMnO-af and NaMgMnO-maf compared to the pristine NaMgMnO-a sample. 175
Table 8.5: The calculated Na-ion diffusion coefficients 176

LIST OF SCHEMES

Scheme 3.1: Combustion synthesis of LMNCA using EG and urea as a fuels. 64
Scheme 3.2: Hybrid microwave irradiation-combustion synthesis of LMNCA powders. 67
Scheme 3.3: Schematic representation of NaMgMnO samples including fluorination and microwave irradiation treatments. 68

LIST OF SYMBOLS

α:	Alpha
Al:	Aluminium
Å:	Angstrom
ca:	Approximately
cm:	Centimetres
CO_2:	Carbon dioxide
^oC:	Degrees Celsius
C_{Li}:	Concentration of the Lithium
D_{Li}:	Diffusion Coefficient of the Lithium
E:	Energy density
$E_{1/2}$:	Half- wave potential
eV:	Electron volt
F:	Faraday constant
f:	Frequency
g:	Grams
GHz:	Giga Hertz
Hz:	Hertz
h:	Hour
m:	Mass
M:	Molar Mass
mL:	Millilitre(s)
mol:	Moles
No:	Number
n:	Number of electrons
nm:	Nanometre(s)
P:	Power density
OCV:	Open circuit voltage
Q_{in}:	Charge capacity
Q_{out}:	Discharge capacity
R:	Universal gas constant
r:	Radius of electrode
R_{ct}:	Charge transfer resistance

R_f:	Film resistance
R_{SEI}:	Solution resistance
ω:	Radial Frequency
T:	Temperature
V:	Volts
Z_w:	Warburg impedance
Z':	Imaginary impedance
Z":	Real impedance
λ:	Wavelength
σ:	Diffusion coefficient
Ω:	Ohm

LIST OF ABBREVIATIONS

a.u:	Arbitrary Units
BET:	Brunauer Emmett Teller
CCD:	Charge Couple Device
CE:	Coloumbic Efficiency
CFSE:	Crystal Field Stabilisation Energy
C-rate:	Charge –Discharge Rate
CPE:	Constant Phase Element
CSIR:	Council for Scientific and Industrial Research
CV:	Cyclic Voltammetry
DEC:	Diethyl Carbonate
DMC:	Dimethyl Carbonate
EC:	Ethylene Carbonate
EDX:	Energy-Dispersive X-Ray Spectroscopy
EEC:	Equivalent Electric Circuit
EG:	Ethylene Glycol
EIS:	Electrochemical Impedance Spectroscopy
EMD:	Electrolytic Manganese Dioxide
ESS:	Energy Storage System
EV:	Electric Vehicle
FESEM:	Field Emission Scanning Electron Microscopy
FFT:	Fast Fourier Transformation
FTIR:	Fourier-Transform Infrared Spectroscopy
FWHM:	Full Width Half Maximum
GHG:	Greenhouse Gases
HEV:	Hybrid Electrical Vehicle
HF:	Hydrogen Fluoride
HS:	High Spin
HRTEM:	High-Resolution Transmission Electron Microscopy
IC:	Internal Combustion
ICL:	Irreversible Capacity Loss
LIB:	Lithium-Ion Battery
LMO:	Lithium Manganese Oxide ($LiMn_2O_4$)

LMNC: Lithium Manganese Nickel Cobalt Oxide ($Li_{1.2}Mn_{0.54}Ni_{0.13}Co_{0.13}O_2$)

LMNCA: Lithium Manganese Nickel Cobalt Aluminum Oxide ($Li_{1.2}Mn_{0.52}Ni_{0.13}Co_{0.13}Al_{0.02}O_2$)

LMNCA-mic: Microwave treated $Li_{1.2}Mn_{0.52}Ni_{0.13}Co_{0.13}Al_{0.02}O_2$

LMR-NMC: Lithium Manganese Rich Nickel Manganese Cobalt Oxide

LMNO: Lithium Manganese Nickel Oxide ($LiMn_{1.5}Ni_{0.5}O_4$)

LTMO: Lithium Transition Metal Oxide

LCO: Lithium Cobalt Oxide ($LiCoO_2$)

NCA: Lithium Nickel Cobalt Aluminium Oxide ($LiNi_{0.80}Co_{0.15}Al_{0.05}O_2$)

NMP: N-methyl-2-pyrrolidone

NMC: Lithium Nickel Manganese Cobalt Oxide ($LiMn_xNi_yCo_zO_2$)

NaMgMnO: Sodium Magnesium Manganese Oxide ($Na_{0.67}Mg_{0.28}Mn_{0.72}O_2$)

NaMgMn-a: $Na_{0.67}Mg_{0.28}Mn_{0.72}O_2$ annealed

NaMgMn-ma: $Na_{0.67}Mg_{0.28}Mn_{0.72}O_2$ microwave irradiated and then annealed

NaMgMn-af: $Na_{0.67}Mg_{0.28}Mn_{0.72}O_{1.98}F_{0.02}$ annealed

NaMgMn-maf: $Na_{0.67}Mg_{0.28}Mn_{0.72}O_{1.98}F_{0.02}$ microwave irradiated and then annealed

PC: Polycarbonate

PHEV: Plug-in Hybrid Electrical Vehicle

PV(s): Photovoltaic(s)

PP: Polypropylene

PVDF: Polyvinylidene Fluoride

REDOX: Reduction-Oxidation

SA: South Africa

SAED: Selected Area Electron Diffraction

SEM: Scanning Electron Microscope

SEI: Solid Electrolyte Interface

SIB: Sodium-Ion Batteries

TEM: Transmission Electron Microscope

TM: Transition Metal

TGA: Thermal Gravimetric Analysis

XPS: X-ray Photoelectron (or Photoemission) Spectroscopy

XRD: X-ray Diffraction

CHAPTER 1

Introduction

1.1 Introduction

This chapter gives a brief overview of the motivation and rationale for the research project. It also presents aims and objectives of the study, and finally the layout of the thesis.

1.2 Motivation and Rationale

Lithium-ion batteries (LIBs) are of great significance as power sources for portable electronic devices. Lithium-ion batteries are also important in realizing cleaner and energy-efficient automobiles such as electric vehicles. Electric vehicles are attractive alternative cars to petrol cars as they also contribute to the reduction of green-house gas (GHG) emissions which impact on climate change, health and environmental pollution. Literature estimate that electric vehicles such as plug-in hybrid vehicle (PHEV) could halve the use of petroleum in cars and reduce transport GHG emissions by 65 % [1, 2].

Sodium-ion batteries (SIBs) are also rechargeable batteries widely studied as promising energy storage systems for renewable energy sources. This is because these batteries are cheaper and have high energy density which is important for grid scale application. Renewable energy (wind, and solar) sources are cheap, environmentally friendly and provide universal access. Therefore they are alternative energy sources important to supplement the main streams of energy supply and their use will reduce the increasing energy demand especially in the African continent and also contribute in decreasing the GHG emissions repercussions.

Cost is an important factor in the commercialization of the lithium-ion and sodium-ion batteries. The cost of the preparation of the electrode materials has the potential to limit the full utilisation of the LIBs and SIBs. Expensive batteries are unusable because they also make the devices in which they are used expensive and unaffordable. One of the ways to reduce the cost of lithium-ion batteries is to use cheaper electrode materials (cathode and anode). At least 40 % of the cost of these batteries comes from the cathode materials.

Manganese based cathode materials are the cheaper cathode materials because of the abundance of the mananganese source especially in South Africa. South Africa is one of the major exporters of manganese ore in the world and currently has the largest Mn ore reserve in the whole world, as can be seen in Figure 1.1.

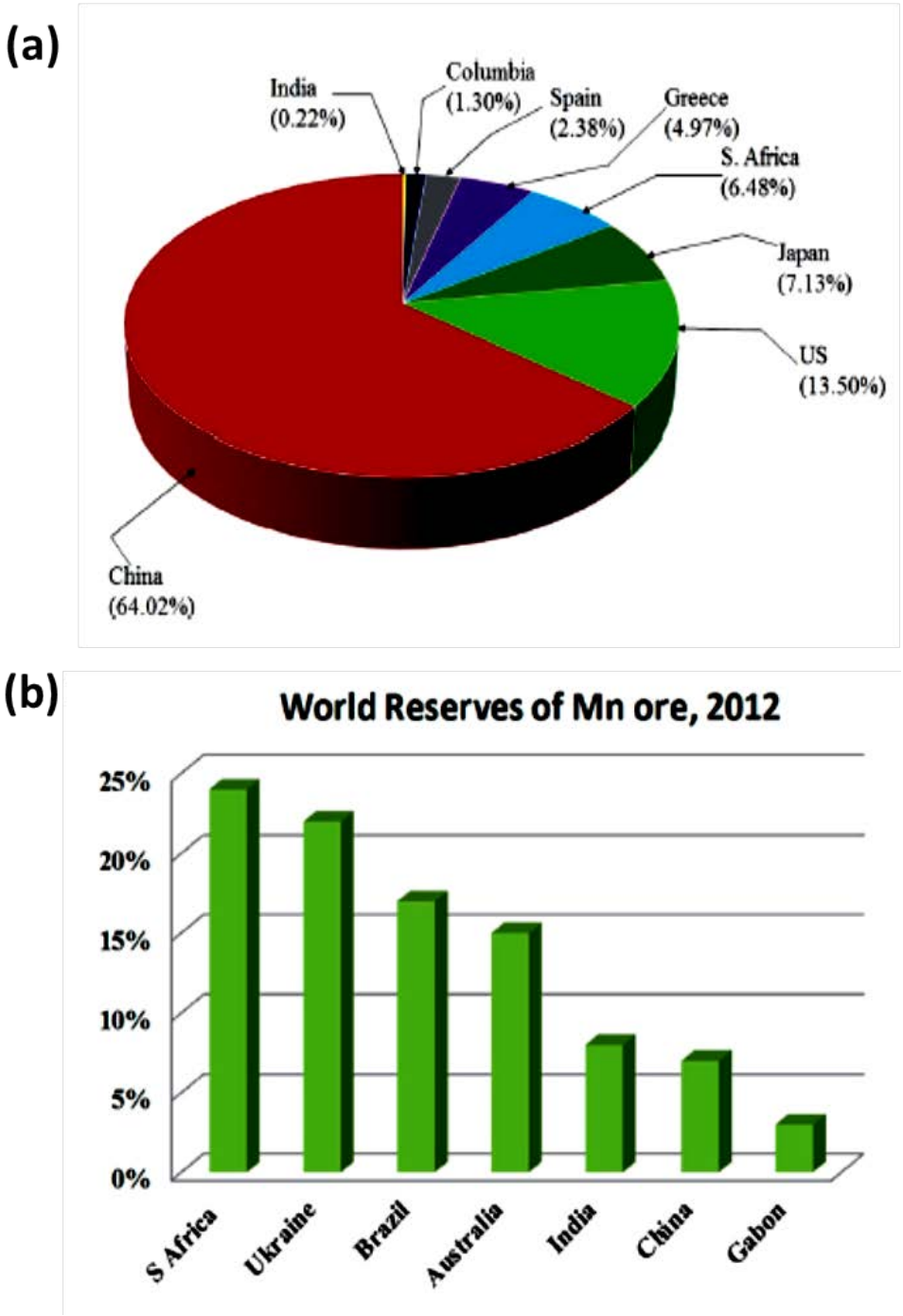


Figure 1.1: The pie chart shows world manganese ore production and the bar chart shows the world reserves of manganese ore in terms of metal content [3].

Manganese based cathode materials are not only low cost but also have a good voltage characteristics, they are easy to prepare and environmentally friendly. This is evident from cathode materials as the lithium manganese oxide (LMO) is currently being used in most electric cars such as Nissan Leaf, Chevrolet Volt and Renault Fluence. Other examples of best performing manganese based cathode materials are the lithium nickel manganese cobalt oxide (NMC), lithium–manganese rich manganese cobalt oxide (LMR-NMC), lithium manganese nickel oxide (LMNO).

However, manganese based cathode materials suffer from capacity fade upon cycling. This is mainly due to the presence of the high spin Mn^{3+} ions in the structure because the manganese ions in the structure exists in the Mn^{3+} and Mn^{4+} oxidation states. The Mn^{4+} oxidation state is redox inactive and the Mn^{3+} (d^4) oxidation state is redox active but causes Jahn-Teller distortion of the structure. Jahn-Teller distortion results in change of the structure and thus results in a change in the electrochemical properties, especially capacity retention. The Mn^{3+} oxidation state also undergoes disproportionation reaction that causes the dissolution of the electrode materials in the electrolyte.

Therefore, this thesis studies the manganese oxide based cathode materials such as the LMR-NMC and NaMgMnO cathode materials for lithium-ion and sodium-ion batteries, respectively. The investigation of the electrochemical performance of LMR-NMC materials is technologically significant as these cathode materials have the potential to improve energy densities and reduce costs for electric vehicles and hybrid electric vehicles [4]. Sodium cathode materials such as P2-type sodium magnesium manganese oxide $Na_{0.67}Mg_{0.28}Mn_{0.72}O_2$ (NaMgMnO) can offer high capacity and good voltage characteristics [5,6]. Both of these types of cathode materials also suffer from capacity fade amongst other problems.

In this work we investigate the effect of fuel for the combustion synthesis of LMR-NMC cathode materials to improve capacity fade. This is because it is widely reported that the synthesis methods and experimental conditions influence the stoichiometry, crystal structure, morphology, and electrochemistry of the electrode materials. We demonstrate that fuels with different chemical properties have an impact on the electrochemical properties of LMNCA cathode materials. The effect of microwave irradiation on the combustion synthesis of manganese oxide based materials (LMNCA and NaMgMnO) is also investigated with the aim to use microwave irradiation to reduce capacity fade and improve the cycle performance. This work demonstrates that the application of microwave irradiation at the pre-annealing steps of the synthesis can be used to enhance the structure, morphological and tune the Mn^{3+}:Mn^{4+} ratio to improve the capacity and capacity retention. Microwave irradiation also offers rapid heating

rates and energy savings. Surface fluorine doping is also used to dope fluorine at the oxygen sites to stabilize the structure to improve capacity fade. The strong ionicity of fluorine over oxygen (or oxyanion) in electrode materials also results in the increase in operating voltage and energy density [7]. We show that modifying the surface of NaMgMnO cathode with minute amounts of fluoride atoms results in increased capacity and improved capacity retention. Lastly, we studied the preparation of LMNCA cathode using manganese oxide nanowires as manganese precursor to improve the morphology of the LMNCA cathode which resulted in improved capacity retention.

1.3 Objectives of the study

The objectives of the research project were as follows:

- To synthesise LMNCA cathode material using urea and ethylene glycol as fuel in combustion synthesis.
- To investigate the effect of microwave irradiation in the combustion synthesis of LMNCA cathode material.
- To synthesize LMNCA cathode material using manganese oxide nanowires as manganese precursor.
- To synthesize NaMgMnO cathode material using the combustion menthod.
- To investigate the effect of microwave irradiation in the combustion synthesis of NaMgMnO cathode material.
- To investigate the effect of fluorination and dual microwave irradiation and fluorination treatment in the synthesis of NaMgMnO cathode material.
- To investigate the electrochemical performance of the prepared cathode materials in lithium-ion and sodium-ion batteries.

1.4 Outline of the thesis

Chapter 1 (Introduction): This is an introductory chapter giving the motivation and objectives of the study. The chapter also presents the outline of the thesis.

Chapter 2 (Literature review): This chapter presents a literature review on LMR-NMC and NaMgMnO cathode materials.

Chapter 3 (Experimental methodology): This chapter presents and describes all the experimental procedures and all the characterization techniques used in this study.

Chapter 4 (Results and discussions): This chapter presents and discuss the results obtained in using urea and ethylene glycol in the combustion synthesis of LMNCA. This chapter reports the impact of these different fuels in the structure, morphology and electrochemical performance of LMNCA cathode materials.

Chapter 5 (Results and discussions): This chapter reports the effect of microwave irradiation in the combustion synthesis using urea and ethylene glycol for the preparation of LMNCA cathode material.

Chapter 6 (Results and discussions): This chapter presents and discuss the results obtained in this study of the preparation of LMNCA cathode from manganese dioxide nanowires. The impact of manganese dioxide nanowires on the physical and electrochemical properties of LMNCA cathode is reported.

Chapter 7 (Results and discussions): This chapter reports the preparation of P2-type NaMgMnO cathode using the combustion method. The impact of microwave irradiation on the electrochemical performance of P2-type NaMgMnO cathode is also reported.

Chapter 8 (Results and discussions): This chapter presents and discuss the results obtained in the study of surface fluorination of NaMgMnO cathode. The effect of fluorination of pristine and microwave irradiated NaMgMnO cathode is reported.

Chapter 9 (Conclusions and future works): This chapter presents the conclusions made from the results obtained in the study and gives recommendations for future work.

1.5 References

[1] J. Axsen, K.S. Kurani, A. Burke, Transport Policy, 17 (2010) 173-182.

[2] J. Gonder, A. Simpson, Measuring and reporting fuel economy of plug-in hybrid electric vehicles, National Renewable Energy Laboratory 2006.

[3] A. Biswal, B.C. Tripathy, K. Sanjay, T. Subbaiah, M. Minakshi, RSC Advances, 5 (2015) 58255-58283.

[4] F. Lin, I.M. Markus, D. Nordlund, T. Weng, M.D. Asta, H.L. Xin, M.M Doeff, Nature Communications, 5 (2014) 3529.

[5] H. Pan, Y. Hu, L. Chen, Energy & Environmental Science, 6 (2013) 2338-2360.

[6] X. Xu, S. Ji, R. Gao, J. Liu, RSC Advances, 5 (2015) 51454-51460.

[7] K. Amine, Z. Chen, S. Kang, Journal of Fluorine Chemistry, 128 (2007) 263-268.

CHAPTER 2

Literature Review

2.1 Introduction

This chapter reviews the history, working principle and applications of lithium-ion and sodium-ion batteries. The challenges and available solutions in the performance of LMR-NMC and P2-Type cathode materials are reported. The chapter concludes with a review on the characterization techniques important for studying cathode materials for lithium-ion and sodium-ion batteries.

2.2 Lithium-Ion Batteries

2.2.1 Background of lithium-ion batteries

A battery is an energy storage device that converts chemical energy into electrical energy. The name battery was coined by Benjamin Franklin in 1748 [1] and the first true battery was invented by Alessandro Volta in 1800 [2]. Since their invention, batteries have become very essential for our daily living especially due to the rapidly improving technology that has made our lives dependent on it. Lithium-ion and sodium-ion batteries are amongst the newest types of secondary batteries.

Batteries are classified into two major types, namely primary and secondary batteries. Primary batteries are non-rechargeable batteries as their chemical reaction cannot be reversed. Examples of these batteries include; Lithium/sulfur dioxide (Li/SO_2), Lithium/manganese oxide (Li/MnO_2) and Lithium/carbon monofluoride (Li/CF_x) batteries, amongst others [3]. Secondary batteries are rechargeable batteries for example lithium-ion, sodium-ion, lead-acid, lithium-sulfur, sodium-sulfur, nickel-zinc molten salt and nickel-cadmium, amongst others [3-8].

Lithium-ion batteries are rechargeable batteries based on the movement of lithium ions between the anode and the cathode during charge and discharge, hence they were named lithium-ion

batteries. LIBs were firstly commercialized in 1991 by Sony Company [9], but research into these batteries started in the early 1970's [10]. The first commercial LIBs use the layered lithium cobalt oxide (LCO) as the cathode and graphite (C) as the anode material, and a non-aqueous Li-ion electrolyte [11]. LIBs have high specific power, high specific energy and are lighter compared to other secondary batteries such lead acid, nickel-cadmium and nickel metal hydride batteries [12]. It is for these reasons that LIBs have been used in most portable electronics and currently in electric transportation. Figure 2.1 shows a comparison of some properties of LIBs with other secondary batteries. The figure shows that LIB competes well with other secondary batteries.

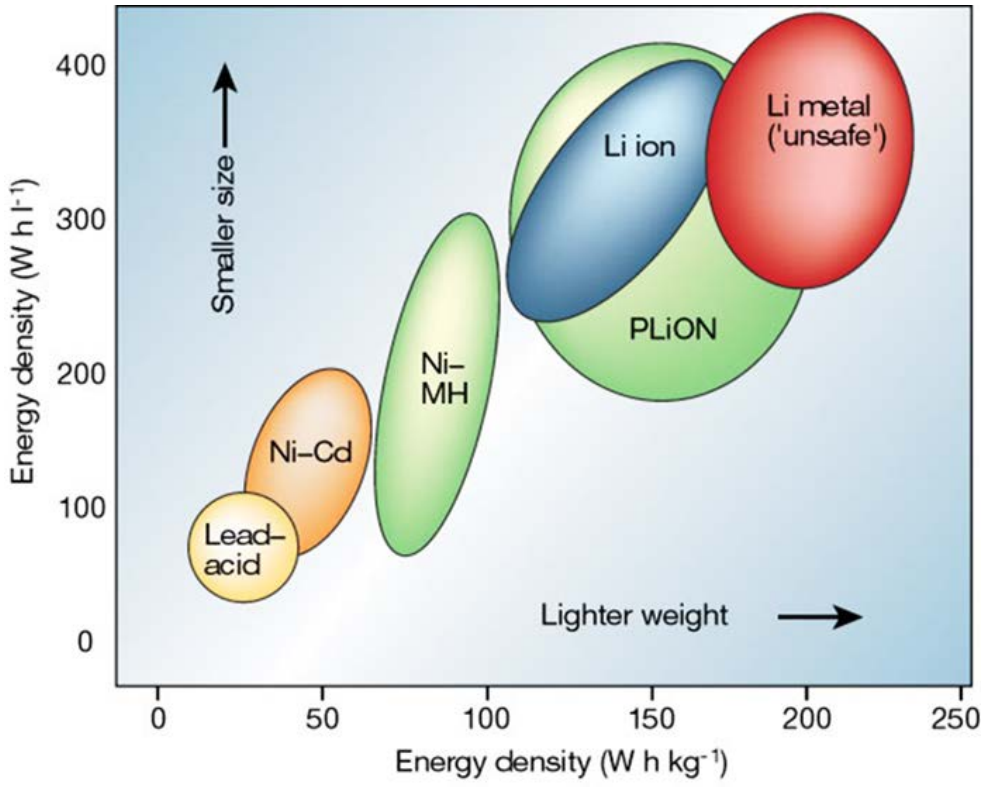


Figure 2.1: Comparison of various secondary batteries [12]

2.2.2 Working principle of lithium-ion batteries

LIBs contain a positive electrode (cathode), negative electrode (anode), electrolyte and separator. The anode is made from materials such as graphite. The cathode is normally made from Lithium Transition Metal Oxides (LTMOs). The separator is made from a micro-porous polymer membrane and prevents short circuiting by separating the cathode and anode. The electrolyte is the medium that facilitates the movement of lithium-ions during charging and discharging. Figure 2.2 shows the basic structure and working principles of LIBs.

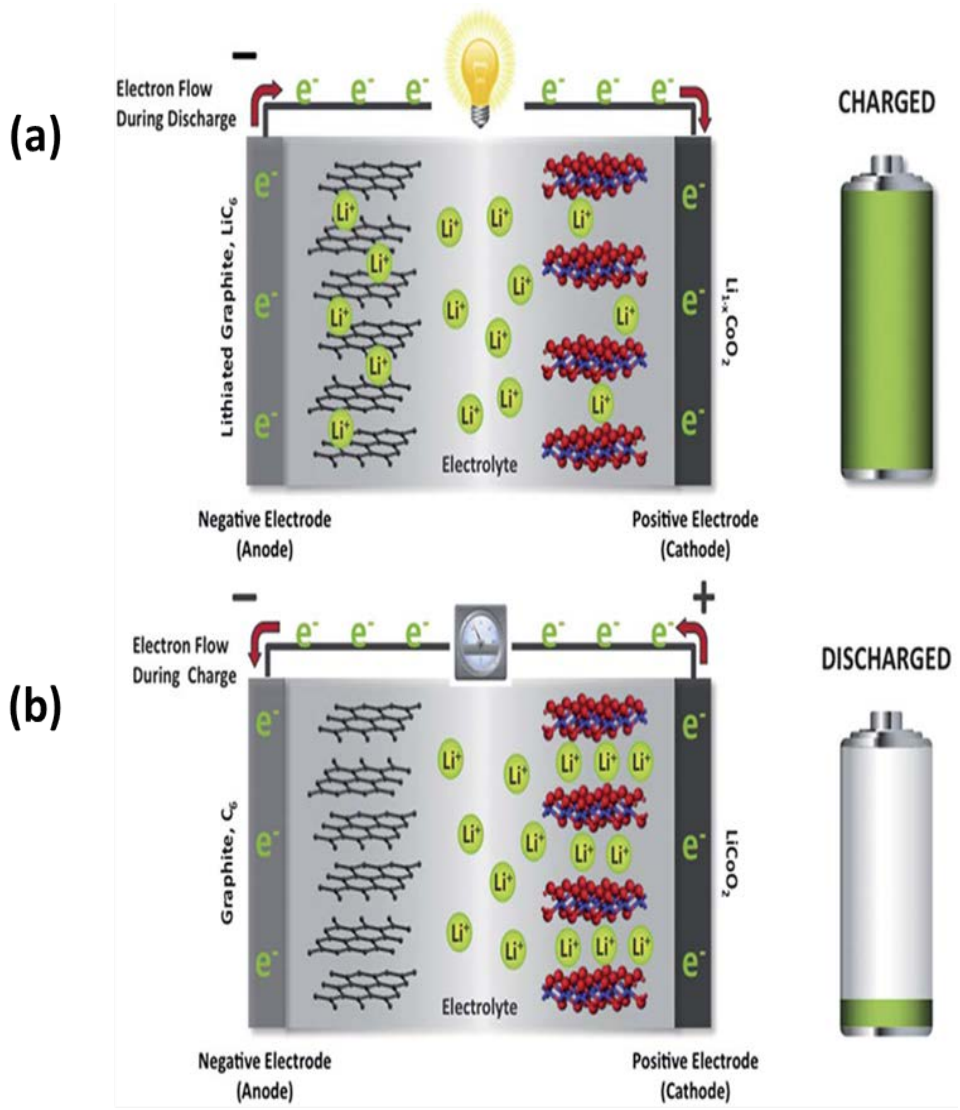


Figure 2.2: The basic structure and working principle of lithium-ion batteries; (a) shows the charge cycle and (b) shows the discharge cycle of a typical lithium-ion [13].

During charging, Li-ions move from the cathode to the anode. During discharging, the Li-ions move back to the cathode from the anode. During both charging and discharging, the electrons flow in the opposite direction to the Li-ions through the external circuit for charge compensation. The charging and discharging of the Li-ion battery involves simple oxidation-reduction (REDOX) chemical reactions such are following:

Cathode:	$LiMO_2 \rightleftarrows Li_{1-x}MO_2 + xLi^+ + xe-$	(2.1)
Anode:	$C + xLi^+ + xe^- \rightleftarrows Li_xC$	(2.2)
Overall:	$LiMO_2 + C \rightleftarrows Li_xC + Li_{1-x}MO_2$	(2.3)

2.2.3 Application of lithium-ion batteries

2.2.3.1 Electronic devices

LIBs are used in portable electronic devices such as mobile phones, calculators, laptops, camcorders and power tools [14]. Lithium-ion batteries are also used in industrial applications such as uninterruptible power supply (UPS) systems, fork lifts, medical electronic machinery and others. They have currently also found application in electric cars. The use of electric vehicles could reduce the green-house gasses emissions that result in global warming. Global warming causes droughts, floods and reduces agricultural yields and these result in food scarcity, human deaths and potential extinction of animal and plant species. The wide application of LIBs as shown in Figure 2.3 is due to their remarkable properties which include compact size, flexibility, light weight, high power, and high capacity characteristics.

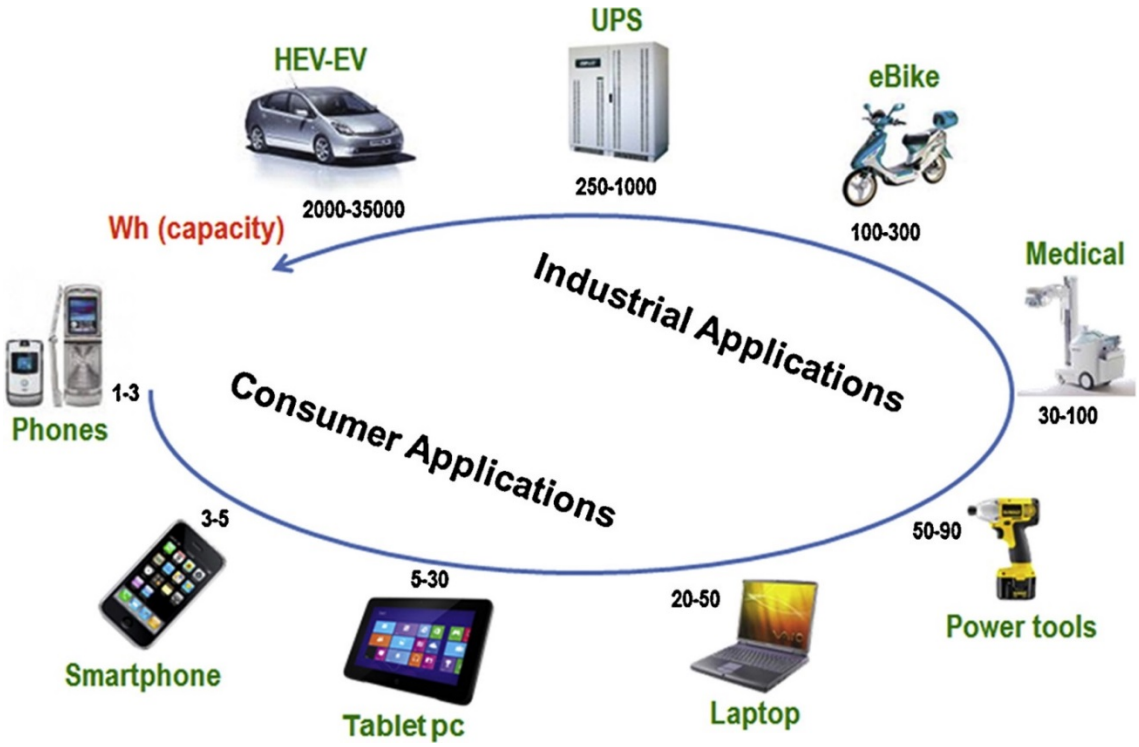


Figure 2.3: Applications of lithium-ion batteries [15].

2.2.3.2 Electric transportation

Batteries have revolutionised, for the second time, the automobile industry. Lithium-ion batteries are currently found in electric cars such as the Nissan Leaf and Tesla Model S. The high energy density and power density of LIBs in comparison to the other secondary batteries, allows them to be used in different electric vehicles. There are three types of

electric cars, viz. the pure electric vehicle (EV), hybrid electric vehicle (HEV), and plug-in hybrid electric (PHEV) vehicle. Pure electric vehicles operate on batteries instead of internal combustion (IC) engines, which use petrol, for vehicular propulsion. The HEV combines an internal combustion engine and electric motor in a parallel configuration [16]. The electric motor is used for starting the vehicle and low-speed propulsion and the IC engine is used for higher speed and long distance propulsion [16]. The PHEV combines the electric motor and IC engine in the serial configuration. In PHEV the electric motor is used for propulsion and the IC engine is activated only after the battery power is used up, i.e. to run the generator and produce electricity for running the electric motor [16]. LIBs are also used in other electric transportation such as electric buses, hybrid trains and railcars [17]. Table 2.1 shows different electric vehicles and their lithium-ion battery chemistries.

Electric vehicles are environmentally friendly as they have zero or reduced green-house gas emissions such as carbon dioxide (CO_2) emissions [18]. Electric vehicles and PHEVs are estimated to halve the use of petroleum in cars and reduce transport GHG emissions by 65% [19,20].

Table 2.1: Example of electric vehicles based on lithium-ion batteries [21].

Vehicle	Positive electrode	Negative electrode
Nissan Leaf	Lithium manganese oxide: LMO	Graphite: C
Chevrolet Volt	Lithium manganese oxide: LMO	Graphite: C
Renault Fluence	Lithium manganese oxide: LMO	Graphite: C
BYP E6	Lithium iron phosphate: LFP	Graphite: C
Subaru G4e	Lithium vanadium phosphate: LVP	Graphite: C
Honda Fit	Lithium nickel cobalt manganese oxide: NCM	Lithium titanate: LTO
Tesla Model S	Lithium nickel cobalt aluminium oxide: NCA	Graphite: C

2.2.4 Manganese oxide based cathode materials

The electrochemical performance of LIBs and SIBs is determined by the intrinsic properties of the cathode and anode materials [22]. However, the cathode contributes at least 30% of the performance and the total cost of the batteries [23]. It is for that reason that the work in this thesis focuses on the improvement of the cathode materials. The research for this thesis work is directed at manganese based cathode materials because of the low cost of manganese due to its abundance especially in South Africa. Research in manganese based cathode materials is one of the means in reducing the cost of LIBs and SIBs. Such studies are important since cost is one of the most important factors for commercialisation.

Cathode materials can be categorized in terms of structure. The conventional cathode materials include layer structured cathodes $LiMO_2$ (M = Co, Ni, Mn, etc.), spinel structured cathodes LiM_2O_4 (M = Mn, etc.), and olivine structured cathodes $LiMPO_4$ (M = Fe, Mn, Ni, Co, etc.) [24]. The different structures of the conventional cathode materials are shown in Figure 2.4.

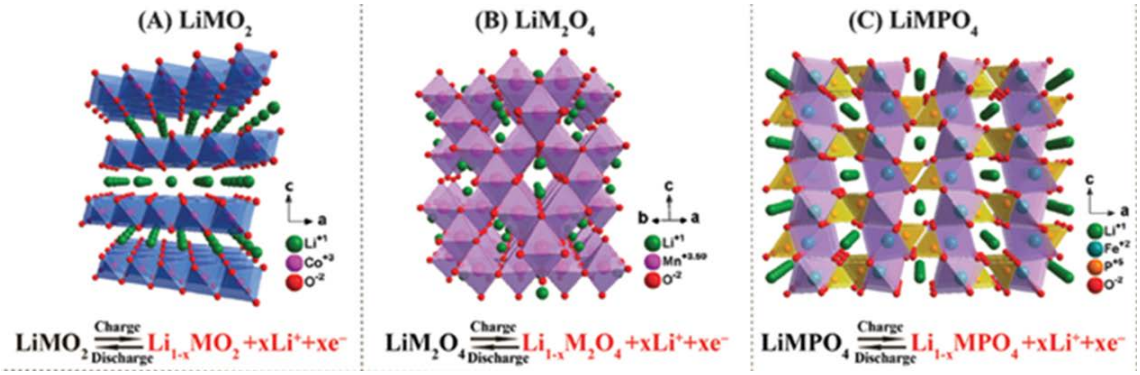


Figure 2.4: Different structures of cathode materials (a) layered structure, (b) spinel structure, and (c) olivine structure [25].

The structure is important because it determines the properties and the performance of the cathode materials. The commercially available layered $LiCoO_2$ is a 3 V cathode material for LIBs and has a theoretical capacity of 267 mAh/g vs. Li [25]. The spinel $LiMn_2O_4$ (LMO) and the olivine $LiFePO_4$ (LFP) are 4 V cathode materials LIBs and also recently became commercially available. The theoretical capacity of LMO is 148 mAh/g vs. Li [25,26] and LFP is 170 mAh/g vs. Li [27]. Cathodes materials for sodium-ion batteries are nearing the commercialization stage.

2.2.5 Lithium and manganese rich nickel manganese cobalt oxide (LMR-NMC)

Lithium and manganese-rich nickel, manganese, cobalt oxide is a 5 V cathode for future generation lithium-ion batteries. LMR-NMC cathode materials were first proposed by Thackeray *et al*. in 2007 and is amongst the family of Li_2MnO_3-stabilized $LiMO_2$ cathode materials [28,29]. These cathode materials are attractive and promising candidates for the near term integration into the market place [29,30].

The development of LMR-NMC cathode materials was motivated by the shortage of high voltage materials (> 3 V vs. Li) which possess high capacity, good structural stability, cycle performance and rate capability [31]. This is because the commercially available LCO has low practical capacity at 140 mAh/g, structural and chemical instabilities at deep charge [32,33], is toxic and expensive [32]. These disadvantages limit the application of LCO in high power applications such as the electric cars. The spinel LMO and the olivine LFP also deliver a low practical capacity between 100-140 mAh/g above 3 V vs. Li, which is not suitable for the high power applications [31]. Figure 2.5 compares the LMR-NMC cathode material with other cathode materials for lithium-ion batteries.

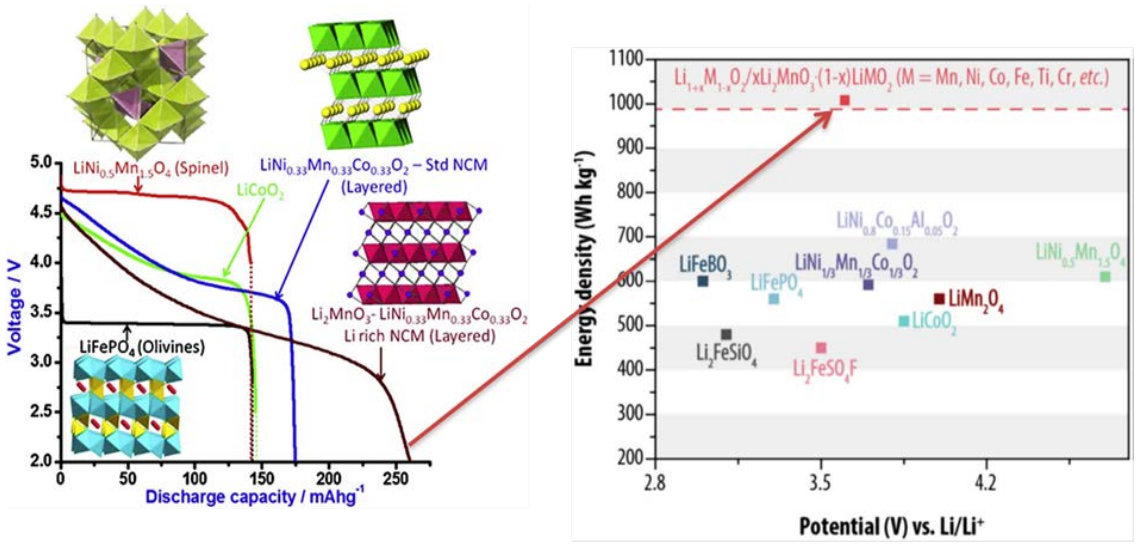


Figure 2.5: Comparison of lithium-ion cathode materials [15].

However, the history of LMR-NMC cathode materials dates back to 1990's. In the late 1990's Thackeray's group reported work on stabilizing MnO_2 compounds with Li_2O structural unit [31]. This strategy involved stabilizing the layered $LiMO_2$ or spinel LiM_2O_4 by integrating it with a structurally compatible component which is electrochemically inactive (i.e. does not contribute to the capacity) between 4 and 3 V [31]. In addition, Thackeray also reported the

successful preparation of Li_2MnO_3-stabilized layered MnO_2 electrode. These reports by Thackeray led to the preparation of structurally integrated 'layered–layered' $xLi_2MnO_3 \cdot (1-x)LiMO_2$ and 'layered–spinel' $xLi_2MO_3 \cdot (1-x)\ LiM_2O_4$ materials which are stable between 2.0 V – 4.8 V [31]. 'Layered–layered' electrodes, particularly $xLi_2MnO_3 \cdot (1-x)LiMO_2$ (M = Mn, Ni, Co) electrodes appear as promising high voltage and capacity electrode materials [31].

2.2.5.1 Application of LMR-NMC

LMR-NMC cathode materials have been extensively studied [34] and their development addresses the following:

(1) Need for suitable cathode materials for electric vehicles

LMR-NMC is suitable to be used in electric vehicles and hybrid vehicles because of its high capacity, high energy density and low cost as shown in Figure 2.7, compared to the conventional cathodes such as the LCO, LMO and LFP cathode materials [35-38]. The practical capacity of LMR-NMC is above 250 mAh/g while the practical capacity of LMO is 110 mAh/g, LCO is 120 mAh/g and LFP is 150 mAh/g.

(2) Need to increase the range of electric cars

The need to increase the range of electric vehicles has led to enhancing currently available cathode materials and identifying new cathode materials for the lithium-ion batteries. For example, the short range of 160 km or 100 miles for the Nissan Leaf electric car [39] could be increased using LMR-NMC cathode materials because of their high capacity and highest energy density of ca. 900 Wh/kg compared to all the other cathodes [40].

(3) Increasing energy consumption

Modern societies rely greatly on the use of electronic devices, such cell-phones and electronic kitchen appliances, to lead their lives. This resulted in the rapid increase in the demand for rechargeable batteries over the past few years. Additionally, the intermittent nature of renewable energy sources and electric mobility has also increased the demand for high energy density storage devices. LMR-NMC cathode materials can be used in lithium-ion batteries for such applications.

2.2.5.2 Structure of LMR-NMC cathode materials

LMR-NMC cathode materials are based on the composite 'layered-layered' $xLi_2MnO_3 \cdot (1\text{-}x)$ $LiMO_2$ (M = Mn, Co, Ni) structure. Therefore LMR-NMC is a mixture of Li_2MnO_3 and $LiMO_2$ layered materials which have the same layered rock salt structure but different space groups. The difference in space groups is due to the different atomic and electronic configurations in the structures of these materials [31]. Li_2MnO_3 (also written $Li[Li_{1/3}Mn_{2/3}]O_2$) is shown in Figure 2.6 (a) and belongs to a monoclinic crystal system with C_2/m space group symmetry. The transition metal (TM) layers in Li_2MnO_3 are occupied by the Li^+ and Mn^{+4} ions. $LiMO_2$ shown in Figure 2.6 (b) belongs to a trigonal crystal system with $R\bar{3}m$ space group symmetry. The TM layers are occupied by only TM ions and the average oxidation state of the M cations is three.

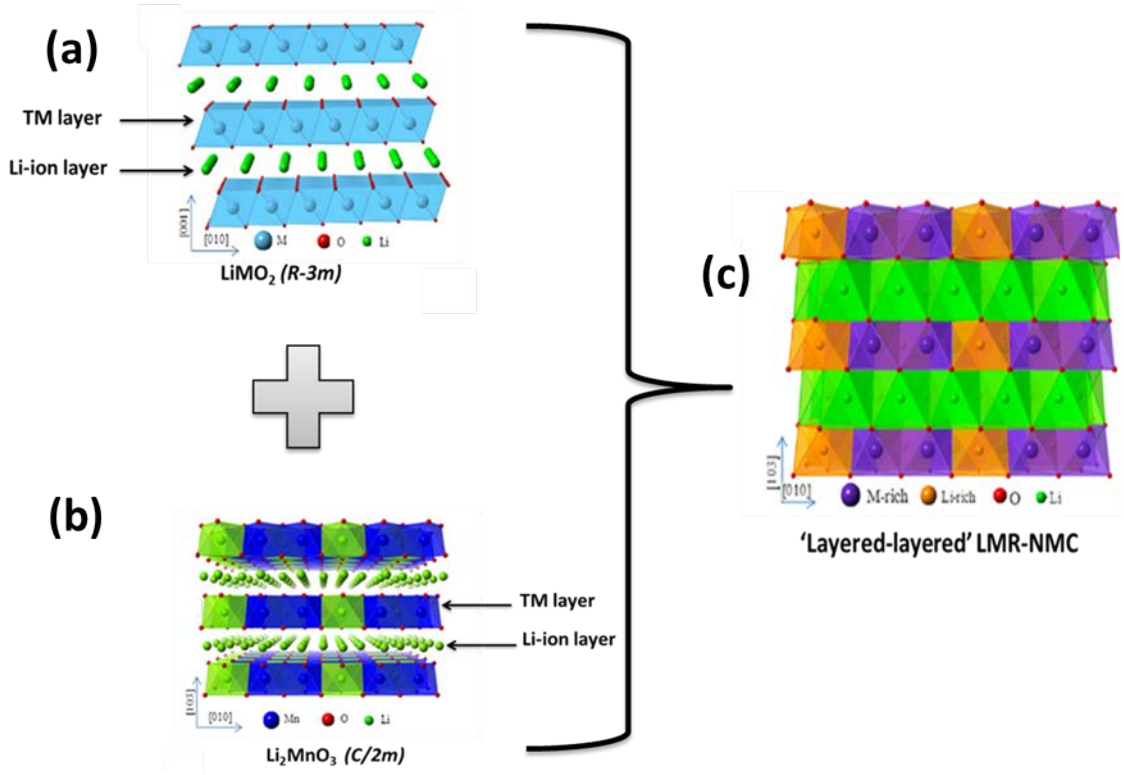


Figure 2.6: (a) The $LiMO_2$ structure (M = Mn, Co, Ni), (b) Li_2MnO_3 structure and (c) 'layered-layered' LMR-NMC structure [41].

These two structures are compatible as they have similar cubic close-packed layers having interlayer spacing of ~4.7 Å [(001) for monoclinic and (003) for trigonal]. This compatibility allows their integration at an atomic level to form $Li_{1+y}M_{1-y}O_2$ (M = Co, Mn, Ni) [31]. Therefore after integration it is very difficult to distinguish the Li_2MnO_3 from $LiMO_2$ in the

composite material [31]. The high resolution transmission electron microscopy (HRTEM) of a $0.3Li_2MnO_3{\cdot}0.7LiMn_{0.5}Ni_{0.5}O_2$ composite structure revealed the coincidence of (001) and (003) lattice fringes of the Li_2MnO_3 and $LiMn_{0.5}Ni_{0.5}O_2$ components [30,31].

The Li_2MnO_3 phase is important for the structural stability and electrochemical properties of the LMR-NMC cathode material upon cycling [31]. This phase increases the stability of layered LMO_2 electrode over a wider compositional range without compromising the electrochemical performance. This is because all the manganese ions are in the tetravalent state in the Li_2MnO_3 phase; it is then electrochemically inactive between 2.0 V and 4.4 V. Also, the reduction of the manganese ions as a consequence of lithium insertion into Li_2MnO_3 is inhibited [31]. During this reaction, depletion of lithium ions from the lithium layer is compensated by the diffusion of lithium from octahedral sites in the manganese layer of the Li_2MnO_3 component to tetrahedral sites in the lithium-depleted layer thereby providing the additional binding energy necessary to maintain structural stability.

However, it is still a scientific debate occurring in literature as to whether the structure of LMR-NMC cathode materials is a true homogeneous solid solution or invariantly contains nanoscale inhomogeneity [28]. In the latter, the two components are viewed as a complex nanocomposite structure containing nanosized Li_2MnO_3 regions, typically less than 5 nm, embedded in a $LiMO_2$ matrix with some allowed disorder [28,30,42-46]. However, both phases coexist in a single nanoparticle despite how the structure of LMR-NMC is viewed [47].

2.2.5.3 Charging and discharging of LMR-NMC materials

During charging and discharging, lithium extraction and insertion occurs with the concomitant oxidation and reduction of the M ions. LMR-NMC materials are suitable for charge and discharging between 2.0 V to 4.8 V. During the initial charge of LMR-NMC materials to 4.8 V vs. Li, the lithium extraction occurs in two steps and the corresponding ideal reactions are shown in equation 2.4 and equation 2.5 [48]:

$$LiMO_2 \rightarrow MO_2 + Li^+ + e^- \quad (2.4)$$

$$Li_2MnO_3 \rightarrow MnO_2 + 2Li^+ + \frac{1}{2}O_2 + 2e^- \quad (2.5)$$

(a) *Charging: 2 V to 4.4 V*

In this voltage range only the $LiMO_2$ component is electrochemically active and operates as a true insertion electrode [31]. Lithium ions are extracted from the LMO_2 phase with a concomitant oxidation of Ni^{2+} to Ni^{4+} and Co^{3+} to Co^{4+}. The manganese ions are spectator ions and are not oxidised in this voltage range. Figure 2.7 displays the typical charge-discharge curve for LMR-NMC material.

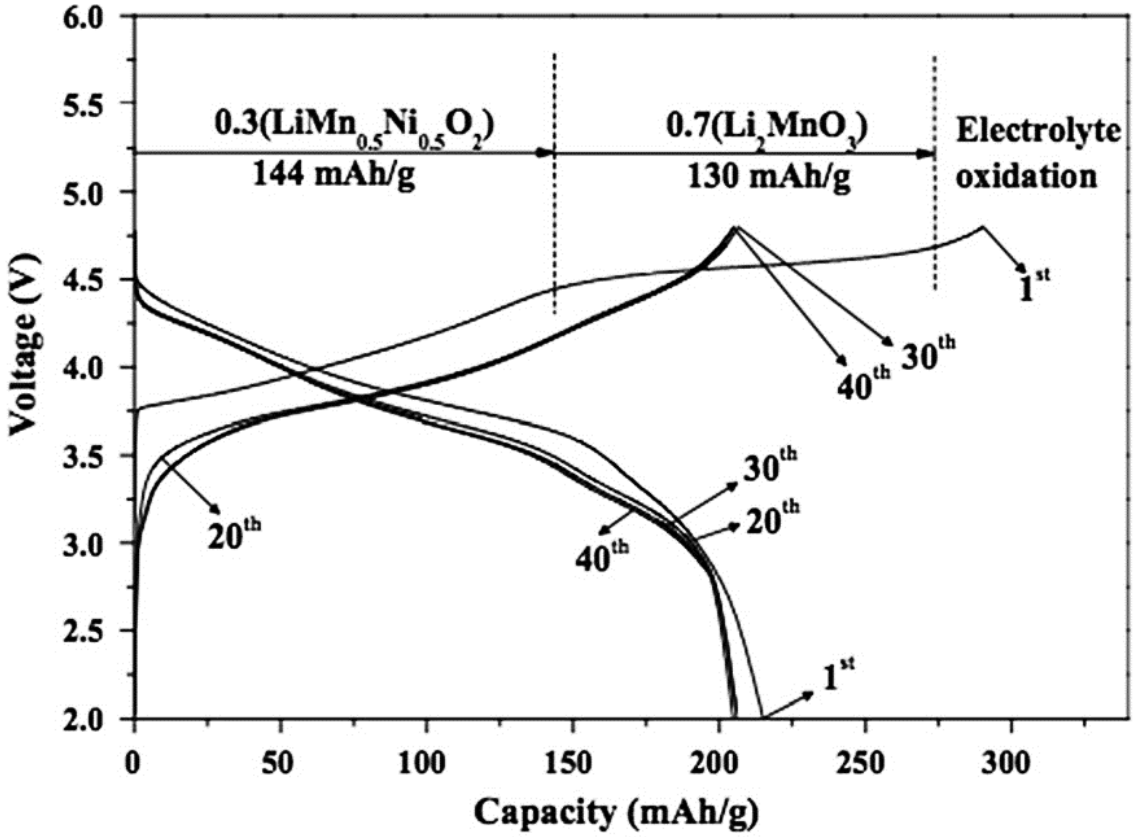


Figure 2.7: Typical charge-discharge of LMR-NMC cathode materials between 2.0 V – 4.8 V vs. Li [49].

(b) *Charging: 4.4- 4.8 V*

In this voltage range the Li_2MnO_3 component is activated. When charging above 4.4 V more lithium ions are extracted from the electrode. The lithium and oxygen are simultaneously extracted from the Li_2MnO_3 component in a combined electrochemical process (lithium removal) and chemical process (oxygen loss) due to the activation of the Li_2MnO_3 component (electrochemical process) [34,50]. In this voltage range the lithium is extracted as Li_2O and this results in a long plateau between 4.4 V and 4.8 V.

The loss of oxygen gas is irreversible and its quantification has been difficult, but it is not more than 50 % of the required stoichiometric requirement [42,51-54]. However, not all oxygen is lost as gas as some may react with the electrolyte [54-56]. Interestingly, the overall layered configuration of the LMR-NMC structure is not destroyed despite the release of oxygen from the electrode surface during the Li_2MnO_3 activation [55,57]. Figure 2.8 shows the effect of charging on the structure of the LMR-NMC materials. Charging above 4.4 V results in a layered MO_2 electrode structure in which the M octahedral sites are occupied almost exclusively by manganese and nickel [50]. This material becomes the host structure for reversible lithium ion insertion/extraction from the second cycle onwards and gives rise to reversible capacities in excess of 200 mAh/g. [50]. The complete extraction of Li_2O from the Li_2MnO_3 results in an electrochemically active spinel MnO_2 [31].

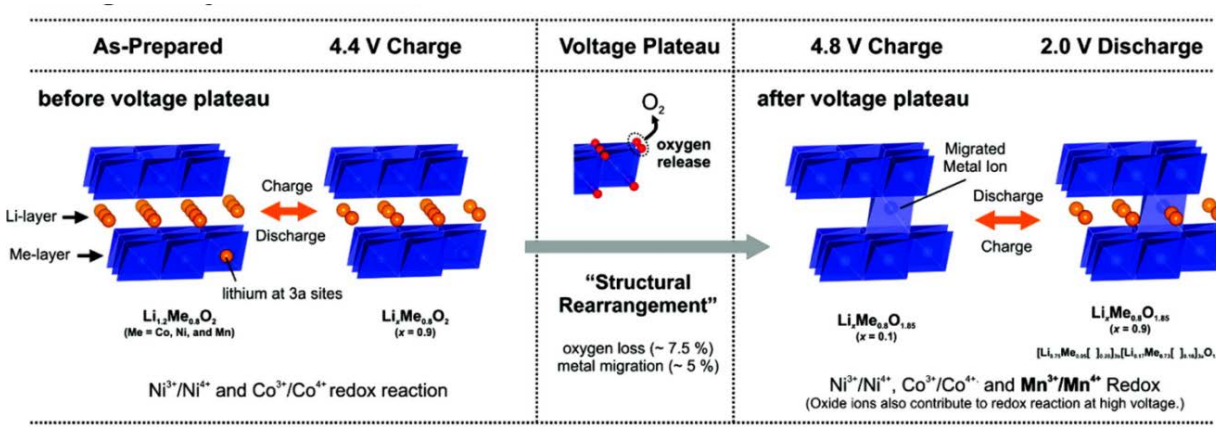


Figure 2.8: Effects of charging on the structure of LMR-NMC materials [51].

2.2.5.4 Advantages of LMR-NMC cathode materials

1. *High capacity*

   LMR-NMC has significantly higher capacities compared to other layered cathode materials such as LCO and NCA since Mn^{4+} ions are more stable in their fully charged state compared to Ni^{4+} and Co^{4+} ions [54]. LMR-NMC cathodes are known to deliver high capacity of > 200 mAh/g when charged at high potentials > 4.4 V vs. Li [58-60]. The layered LMR-NMC electrodes exhibit exceptionally high electrochemical capacities due to the activation of the Li_2MnO_3 component. However, the capacity and cycling stability is dependent on the value of x ($xLi_2MnO_3 \cdot (1-x)\ LiMO_2$ (M = Mn, Co, Ni)) and the relative amounts of manganese, nickel and cobalt in the $LiMO_2$ component

[31]. The reported capacities of LMR-NMC cathode materials are higher than their theoretical capacity of approximately 260 mAh/g [31]. This theoretical capacity is calculated from the mass of the $xLi_2MnO_3 \cdot (1\text{-}x)\ LiMO_2$ parent component before cycling [31]. The high capacity in LMR-NMC material is also due to the 'excess' lithium-ions from the Li_2MnO_3 phase which becomes available during the activation at > 4.4 V [28,42] and/or the surface reaction through electrode-electrolyte reduction [61,62] and/or hydrogen exchange [63]. The latter is generated from decomposition of the electrolyte especially at higher temperatures > 55°C. Higher capacity is obtained for LMR-NMC at high temperatures also because about 25% excess lithium are removed at the higher temperature [63]. Generally, the oxygen loss is the dominant mechanism of Li overcapacity during electrochemical charging [34,63-66].

2. *Cost*

   LMR-NMC cathode materials are cheaper because they contain reduced amount of cobalt compared to LCO. These materials are cheap because they are also rich in manganese [67-69]. Manganese is cheaper than both Co and Ni as it is one of the most abundant elements on the earth's crust.

3. *Safety*

   LMR-NMC materials meet the safety requirements of advanced Li-ion batteries [29]. Since the LMR-NMC materials are manganese rich; they also possess superior safety qualities compared to cobalt- and nickel-rich cathode materials [29].

2.2.5.5 Disadvantages of LMR-NMC cathode materials

Since nothing is perfect in life, LMR-NMC cathode materials suffer from some short comings that hinder their further commercialisation.

1. **Poor cycling performance**

   The poor cycle performance in LMR-NMC cathode materials is due to several factors occurring during the cycling of these materials. These factors are discussed below:

   (a) Spinel formation: Electron microscopy studies reported in literature indicate that the poor cycle performance in LMR-NMC cathode materials is partially due to structural reconstruction inducing a structural transition from the 'layered-layered' to 'layered-spinel' at the surface and/or in the bulk [43,47,61,70,71]. Spinel formation occurs upon cycling of LMR-NMC and is one of the primary factors

contributing to poor rate capability and capacity fade due to the blockage of the Li-ion diffusion channels [47,72]. Gu and co-workers reported that a spinel phase gradually forms upon cycling from both the $LiMO_2$ and Li_2MnO_3 components in LMR-NMC materials and the mechanism of formation is different for both components [47], as shown in Figure 2.9 (e). The formation of a spinel from the $LiMO_2$ component occurs through the migration of transition metal ions to the Li-ion sites (Li-ion layer), then the Li-ions move into the tetrahedral sites, and this causes the distortion of oxygen lattices [47,73]. As a result, mosaic structured spinel grains form within the parent particle. In this formation a $LiMn_2O_4$-type cubic spinel is formed from the surface of the particle and is extended to the inner part of the particle [47,61]. This happens without breaking the $LiMO_2$ lattice. While the formation of the spinel from Li_2MnO_3 is caused by the removal of Li^+ and O^{2-} during the Li_2MnO_3 activation upon high voltage cycling. This results in the breakdown of the crystal lattices (amorphization), crack formation, and porosity formation [45]. In this case, the spinel formation follows a nucleation and growth mechanism, which results in spinel clusters with different orientations in the distorted/amorphized lattices [47] as shown in Figure 2.9 (a-d).

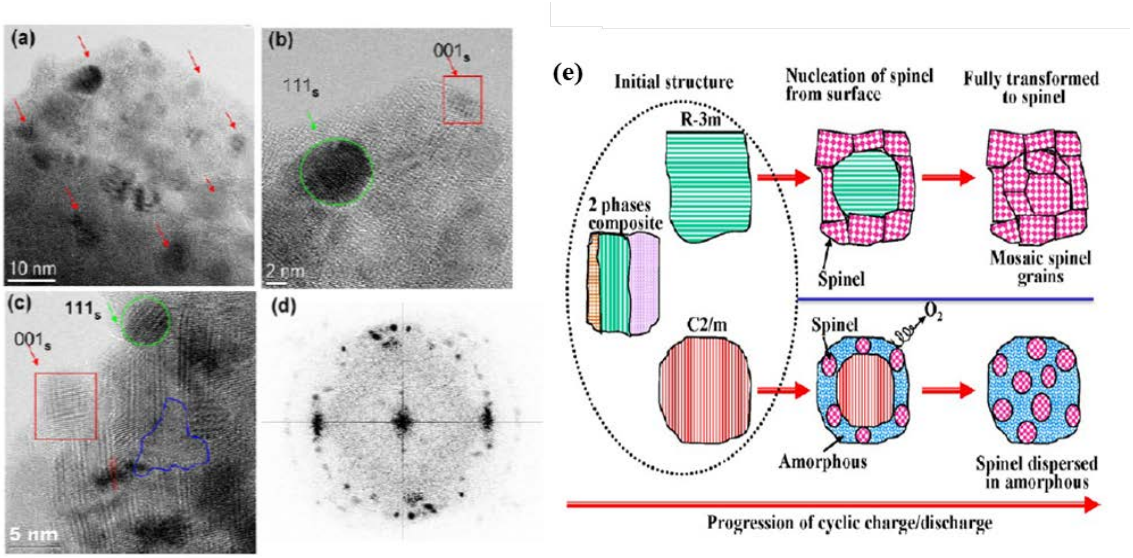


Figure 2.9: (a) LMR-NMC cathode after 60 cycles with small domains of spinel nucleated, (b and c) nucleated spinel crystal domains in different crystal orientations, blue circled region show amorphized lattices, (d) FFT of the TEM image in (c) showing lattice distortions. (e) Schematic drawing showing the different mechanisms of spinel formation from the $LiMO_2$ ($R\bar{3}m$) and Li_2MnO_3 (C_2/m).

(b) SEI formation: The poor cycle performance is due to the chemical evolutions at the surfaces of the LMR-NMC materials. The cycling to high electrode voltages results in the build-up of a complex solid electrolyte interphase (SEI) rich in LiF and organic components due to the decomposition of the electrolyte (chemical evolution) [70]. These then impact the capacity retention upon cycling. Figure 2.10 shows the surface reactions occurring during charging and discharging of LMR-NMC materials. The poor cycle performance is also due to the decomposition of electrolyte at high cell potentials as the $LiPF_6$ based electrolyte is only stable up to 4.5 V [68,74]. The products of electrolyte decomposition also contribute to the SEI formation.

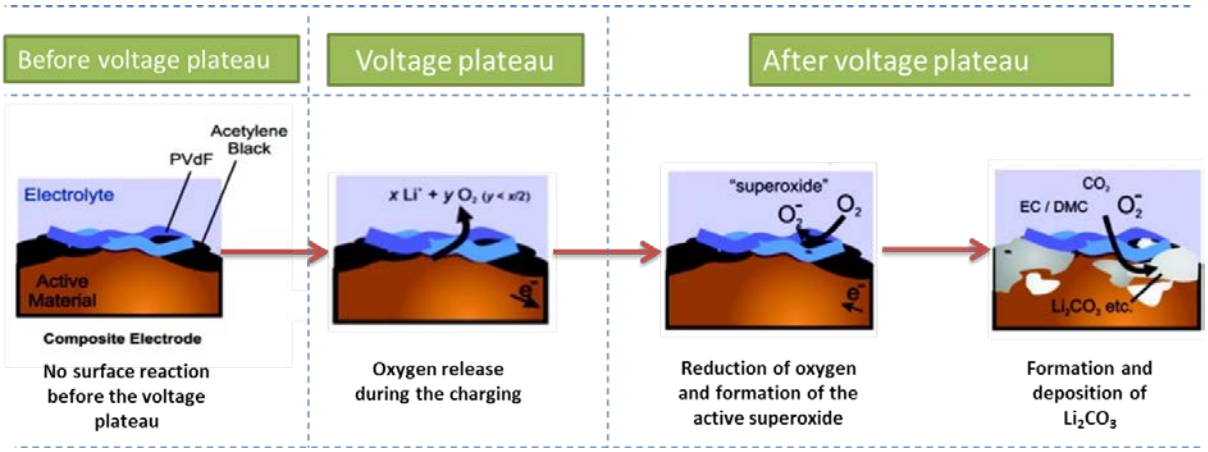


Figure 2.10: Surface reactions occurring during 1st cycle charging (before voltage plateau and at voltage plateau) and discharging (after voltage plateau) for a typical LMR-NMC cathode material [51].

(c) Manganese dissolution: The spectroscopic studies of LMR-NMC cathode materials revealed that not all the manganese ions are in the Mn^{4+} state, but there exist some Mn^{3+} ions [43]. Also, discharging to lower potentials, i.e. at 2.0 V, results in the reduction of Mn^{4+} to Mn^{3+} ions [75]. The dissolution of transition metals, particularly manganese, during cycling results in poor cycling performance. Manganese ions in the three oxidation state undergoes Jahn-Teller distortion and disproportionation reaction as shown in equation 2.6:

$$\text{Disproportionation reaction: } Mn^{3+} \rightarrow Mn^{4+} + Mn^{2+} \qquad (2.6)$$

The disproportionation reaction of Mn^{3+} ions results in the formation of Mn^{2+} ions which are soluble in the electrolyte. The Jahn-Teller distortion results in the distortion of the structure and this impacts specifically the cycle performance.

(d) Destruction of the electrode surface: The cycling performance of LMR-NMC cathode materials is also impacted by the destruction of the electrode surface which also accelerates the dissolutions of the transition metals [75].

2. Voltage fade

Voltage fade is one of the most critical problems in LMR-NMC materials because it limits the management of state-of-charge, energy output (total available energy of the battery after cycling) and efficiency in the battery systems [29]. Voltage fade is defined as the continuous decrease in energy output of the cells despite capacity retention of the electrode [29].

The activation of the Li_2MnO_3 phase at high voltages (> 4.4 V) also causes the hysteresis and voltage fade regardless of the composition of LMR-NMC and the synthetic method used [29,42,76]. The effects of activation results in the decrease in the average voltage which decreases the energy output of the cells. Looking carefully at the charge-discharge curves in Figure 2.11, it is clear that the voltage fade is observed during the discharge curve between 3 and 4 V [43]. Figure 2.11 (a,b) depict the difference between the voltage fade and absent of voltage fade in charge-discharge profiles for LMR-NMC, (c) shows the differential capacity vs. voltage plot showing the voltage fade and hysteresis in LMR-NMC materials and (d-f) indicates the existence of voltage fade in LMR-NMC materials synthesized using different methods.

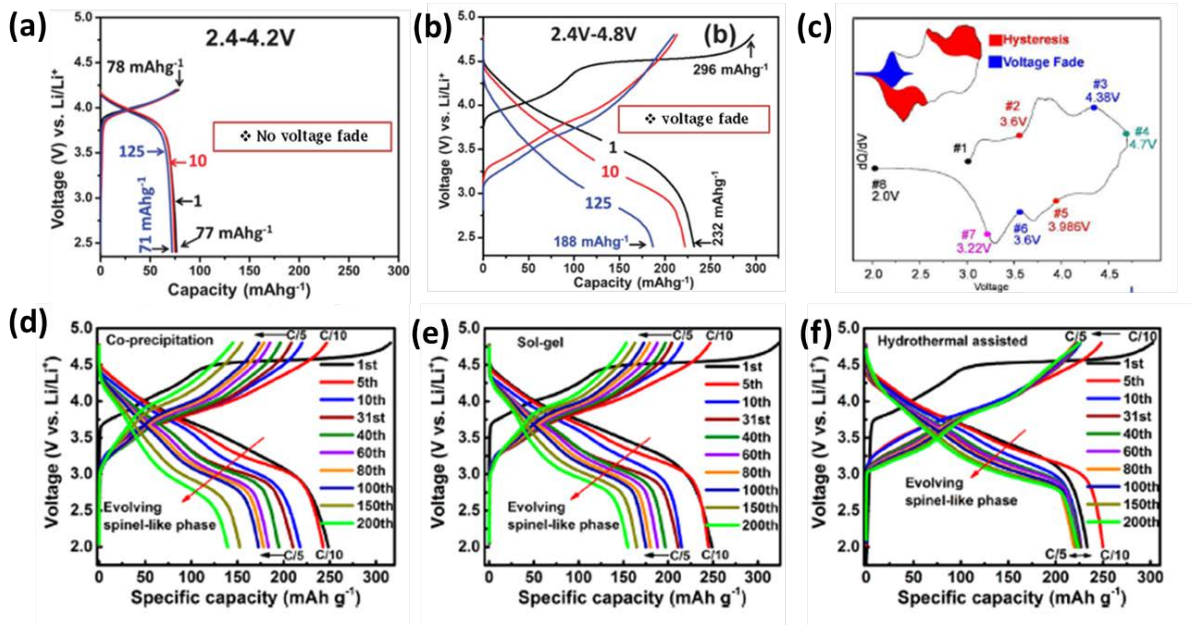


Figure 2.11: Results for LMR-NMC show (a,b) voltage fade charge-discharge profiles, (c) voltage fade and hysteresis in differential capacity vs. voltage plots and (d-f) voltage fade in LMR-NMC materials synthesized utilising different methods.

3. 1st cycle irreversible capacity loss

LMR-NMCs suffer from irreversible 1st cycle capacity [32,33,77]. The reactions of the electrode with the electrolyte, the loss of Li_2O and the inability to insert all the Li-ions back into the lattice during discharge lead to the huge irreversible capacity loss in the initial cycle [32,33,67]. However, when LMR-NMC materials are initially charged > 4.5 V the Li_2MnO_3 activation occurs before electrolyte oxidation [10]. The first cycle irreversible capacity loss (ICL) in LMR-NMC materials is between 40–100 mAh/g on charging to 4.8 V depending on the composition [33,69] or discharge capacity can be 20–30% less than it is on charge [7, 12]. The ICL in the first cycle also results in poor initial coulombic efficiency.

4. Poor rate capability

LMR-NMCs also suffer from poor rate capability which is due to the low lithium-ion diffusion coefficient inside the Li_2MnO_3 phase and the large charge transfer resistance between the electrolyte and Li_2MnO_3 phase [67]. The poor rate capability of these materials could also be attributed to the low electronic conductivity associated with the Mn^{4+} ions [77] as the LMR-NMC materials are rich in Mn^{4+} ions. The formation of a thick amorphous solid SEI layer on the surface of the materials during charging also

results in poor rate capability [61]. Additionally, the removal of Li_2O reduces the rate capability because of structural damage on the surface of the electrode particles [62].

5. **Impedance rise**

   The extensive removal of Li_2O damages the electrode surface and results in the increase in cell impedance [31,75,78]. The formation of the SEI layer, decomposition of the electrolyte, surface reconstruction and chemical evolution also contribute to the increase in the impedance upon cycling [70].

2.2.5.6 Solutions to the disadvantages of LMR-NMC cathode materials

More research efforts have been reported in literature to solve the challenges discussed above inhibiting the application of LMR-NMC cathode materials in electric vehicles. The efforts include the following:

(a) Coating

LMR-NMC materials have been coated with metal oxides such as Al_2O_3 [32], V_2O_5 [33] , RuO_2, TiO_2 [79], $AlPO_4$ [69], ZrO_2[80], MnO_2 [67], La_2O_3 [81], MgO [82], $Na_2S_2O_8$ [83], ZnO [84,85] and Li_2SiO_3[86]. Coating of the LMR-NMC cathode materials with these inert oxide materials minimizes the cathode-electrolyte interfacial reactions. This improves the first cycle irreversible capacity loss and reduces the side reactions between the LMR-NMC cathode material and the electrolyte [67]. But these coating strategies still exhibit poor rate capabilities because the materials used have poor conductivity and thus surface modification with these materials increases the surface electronic resistance and this then results in poor rate capability. Carbon based coating strategies have been reported to improve the rate capability. LMR-NMC has been coated with graphene, carbon nanotubes, and porous carbon materials. These carbon materials have excellent electronic conductivity and thus coating with them improves the capacity, cycling performance and the rate capability [68]. Figure 2.12 shows the improvement of rate capability of LMNCO material by carbon coating strategy.

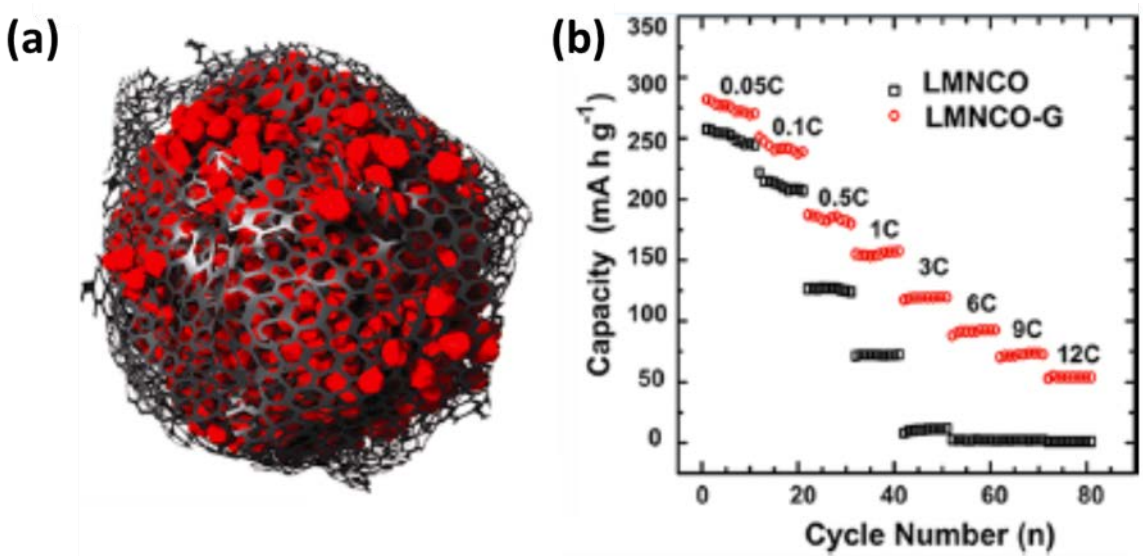


Figure 2.12: (a) LMNCO cathode material coated with graphene and (b) cycle performance for the graphene coated LMNCO [68].

LMR-NMC materials have also been coated with fluorides such as AlF_3 [79,87], Mg_2F [88], FeF_3 [89], ZrF_4 [90], CaF_2 [91] to improve the cycle performance. The coating with fluorides improves initial coulombic efficiency, capacity retention and rate capability due to the suppression of electrolyte decomposition, stable electrolyte/electrode interfacial structure and spinel formation [91].

Equation 2.7 relates the reaction rate constant (k) of electrode side reactions to the electrode over-potential.

$$k = k^0 \cdot \exp\left[\frac{\beta n F \Delta\varphi}{RT}\right] \tag{2.7}$$

where k represents the reaction rate constant, k^0 is the standard rate constant, β is the barrier symmetry factor, n is the number of electrons involved in the electrode reaction, F is the Faraday constant, $\Delta\varphi$ is the over-potential, R is the universal gas constant, and T is the absolute temperature [68]. According to the electrode kinetics from equation 2.7, decreasing the over-potential decreases the rate of the electrode side reactions. The electrode over-potential mainly originates from the electrochemical and concentration polarizations [68]. Therefore decreasing the polarization and improving the electrode conductivity is beneficial in depressing the side reactions [68].

The LMR-NMC materials have also been surface coated with $LiNiPO_4$ to improve their rate capability. Kang and Thackeray reported that such coatings also lead to good

reversible capacity. The $LiNiPO_4$ acts as an excellent Li-ion conductor as well as an efficient protective layer. This helps in stabilizing the surface of the electrode and thus improves the rate capability [48].

(b) Mild-acid treatment

The 1st cycle irreversible capacity can be reduced by chemically leaching some Li_2O from the Li_2MnO_3 by acid treatment [92,93]. In this strategy certain amounts of lithium is extracted from the material prior to the cell assembly using the acid treatment employing acids such as nitric acid (HNO_3). This method can reduce the 1st cycle irreversible capacity and increase the coulombic efficiency to almost 100% [92-94]. However, this treatment results in the poor cycling performance, due to the H^+/Li^+ exchange process and the removal of oxygen (as H_2O) during the dehydrating process [92-94].

(c) Doping

Partial substitution of transition metal (TM) ions is one of the efforts made to improve the electrochemical performance of LMR-NMC cathode materials. LMR-NMC materials have been doped with elements such as Al [95,96], Mg [97-99], Cr [100], Ru [101,102], Mo [103], Y [104], Sn [105], V [106], Zr [107], Zn [108] and others.

Doping with Mg, Al, Mo or Y impacts the structural stability and thus improves the cycle performance of the LMR-NMC materials [97,103]. Doping with Cr or V improves the rate capability [100,106]. Ru-doping improves the initial coulombic efficiency [101] and Y-doping improves also the capacity.

LMR-NMC cathode materials have been doped with anions like the fluoride (F^-) ions [94,109]. Anion doping is relatively easy to control compared to cation doping as there is only one kind of anion in the cathode. Fluoride doping was used to stabilize the structure and improve the electrochemical performance of LMR-NMC [110,111]. The fluoride anions are used to partially substitute the oxygen, as the F^- ions form strong bonds with TMs and this improves the structural stability [111]. A minute amount is often used, e.g. for $Li_{1.2}Mn_{0.54}Ni_{0.13}Co_{0.13}O_{2-x}F_x$ ($x \leq 0.05$) gives enhanced electrochemical properties [110]. Fluoride doping suppresses the spinel formation, enhances the stability of the electrode surface against HF attack, reduces the formation of LiF in the SEI layer, and maintains a stable charge transfer resistance [110,111]. These then result in improved cycle performance and coulombic efficiency. Surface

doping results in higher capacities and improved coloumbic efficiency compared to bulk doping [110].

(d) Synthesis methods

LMR-NMC cathode materials are generally prepared by co-precipitation [29,60,69,112-114]. Co-precipitation method is slow, needs precise control of feeding speed and pH. Due to these disadvantages of co-precipitation other synthesis methods were investigated such as the freeze drying [75], combustion[115,116], sol-gel [117-120], hydrothermal [121,122], Pechini [95], molten salt and microwave irradiation methods [123,124] amongst others.

The electrochemical performance of LMR-NMC depends on the synthesis methods [94,96,116,124]. Literature confirms that most the problems associated with LMR-NMC materials are closely related to the structure, stoichiometry, and morphology which are greatly influenced by the synthesis methods and conditions [116,125,126]. Therefore, there is a need for continued investigation of synthesis methods to be able to overcome the hurdles associated with this material. Table 2.2 compares different synthesis methods used for the preparation of $Li_{1.2}Mn_{0.54}Ni_{0.13}Co_{0.13}O_2$ cathode material and shows that different synthesis methods results in different particle size and electrochemical performances.

Table 2.2: Comparison of synthesis methods for $Li_{1.2}Mn_{0.54}Ni_{0.13}Co_{0.13}O_2$ cathode.

Method	Particle size	Initial discharge capacity (mAh/g)	1st cycle Irreversible capacity	Capacity retention	Ref
Hydrothermal	20-200 nm	251.9 mAh/g , 1 C	87 mAh/g or 74 %	75 %@ 140 cycles	[121]
Sucrose combustion	100-200 nm	275 mAh/g, 0.1 C (18 mA/g)	50 mAh/g or 84 %	80 % @ 50 cycles	[120]
Sol-gel	200-400 nm	265 mAh/g, 0.1 C (18 mA/g)	60 mAh/g or 82 %	83 % @50 cycles	[120]
Sol-gel	100-250 nm	277.3 mAh/g, 0.1 C (18 mA/g)	86 mAh/g or 76 %	98 % @ 50 cycles	[127]
Polymer-pyrolysis	100-150 nm	290 mAh/g, 0.1 C (20 mA/g)	61 mAh/g or 83 %	75 % @ 70 cycles	[128]
Co-precipitation	200-500 nm	249 mAh/g, 0.1 C (18 mA/g)	76 mAh/g or 76 %	82 % @ 30 cycles	[116]
Molten salts	200-300 nm	277.2 mAh/g, 0.1 C (20 mA/g)	71 mAh/g or 79 %	94 % @ 80 cycles	[129]
Pechini	~90 nm	258 mAh/g, 0.1 C (22.5 mA/g)	82 mAh/g or 76 %	62 % @ 50 cycles	[130]
Ultrasonic spray-pyrolysis	~ 0.5-5 μm	291 mAh/g, 0.1 C (25 mA/g)	45 mAh/g or 87 %	92 % @ 50 cycles	[131]

(e) Combustion method

The combustion method is an effective technique for the synthesis of cathode materials for lithium-ion batteries [132-134]. This method involves the combustion reaction of some oxidizers and fuels such as glycine, citric acid, glucose and urea [135,136]. The exothermic reaction gives off heat that allows a chemical reaction to occur forming the oxide powders. Figure 2.13 shows an example of the combustion synthesis of LMNC cathode material.

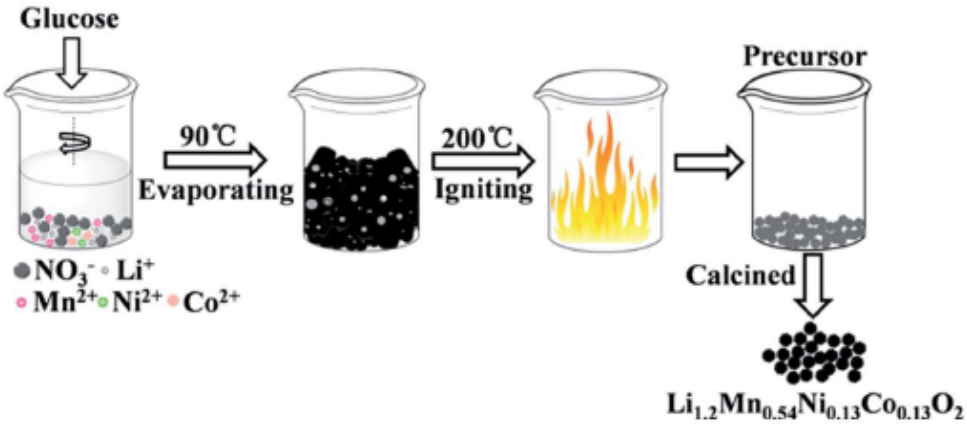


Figure 2.13: Scheme for the glucose combustion synthesis of LMNC cathode material [135].

This synthesis method is low cost, simple and gives powders with perfect structures and uniform particle size distribution. The powders also show excellent electrochemical performance. Due to these advantages, the combustion method was used in this work to prepare the LMNCA cathode material.

The combustion fuel is a very important component in the combustion synthesis of oxide materials. It has an effect on the flame properties and the evolution of gases during the combustion synthesis. These then have an impact on the powder properties of the oxide materials. Powder properties such as particle size, crystallinity, surface area and morphology are very important for the electrochemical performance of the oxide electrode materials.

Urea is a popular and attractive fuel for the combustion synthesis of oxide materials. When urea is used as a fuel in the combustion synthesis it uses its ability to react rapidly with the nitrate reagents to aid combustion. During combustion synthesis when urea is used as a fuel the following takes place: as the solution mixture of the reagent nitrates

and urea is heated to 500℃, it firstly undergoes dehydration and then gel formation. The gel foams as the solution is heated due to the formation of gases such as nitrogen oxides (NO_x), NH_3 and HNCO. The foam then erupts with a flame because of the accumulation of the hypergolic mixture of these gases, burns to incandescence and decomposes to give an oxide powder. This mechanism is proposed based on the literature reported for the preparation of ceramic materials [137].

Ethylene glycol (EG) has been used as fuel in the combustion synthesis of ceramic materials. When EG is used in the combustion synthesis of oxide materials it acts as a fuel and a complexing agent. During combustion synthesis when EG is used as a fuel the following takes place: as EG is mixed in water with the reagent nitrates, it complexes the metal cations (Ni, Mn, Co, Al) and increases their solubility. When the mixture is heated at 500 ℃ , the EG complexes the metal ions and prevents them from precipitating as the water evaporates. A high viscosity honey-like consistency results and forms viscous foam as the water is completely evaporated. The foam then ignites and burns to incandescence and decomposes to the oxide powder with evolution of gases (CO_2, N_2 and H_2O). This mechanism is proposed based on the literature reported for the preparation of ceramic materials [137].

(f) Microwave irradiation

Microwaves are electromagnetic waves with wavelengths ranging from 1 mm to 1 nm and corresponding frequencies between 300 MHz and 300 GHz [138]. During microwave irradiation the energy is delivered directly to the materials through molecular interaction with the electromagnetic field [139]. Figure 2.14 compares microwave irradiation with convectional heating.

Microwave irradiation heats the materials through dipolar polarization or ionic conduction. When a material is irradiated the dipoles or ions in the material align with the applied electric field. When the applied electric field oscillates, the ion or dipole field in the material will realign itself with the applied field. This then results in the loss of energy in the form of heat through the molecular friction and dielectric loss. Therefore the microwaves penetrate the materials during heating to deposit energy and results in volumetric heating throughout the material. Microwave heating transfers the electromagnetic energy into thermal energy.

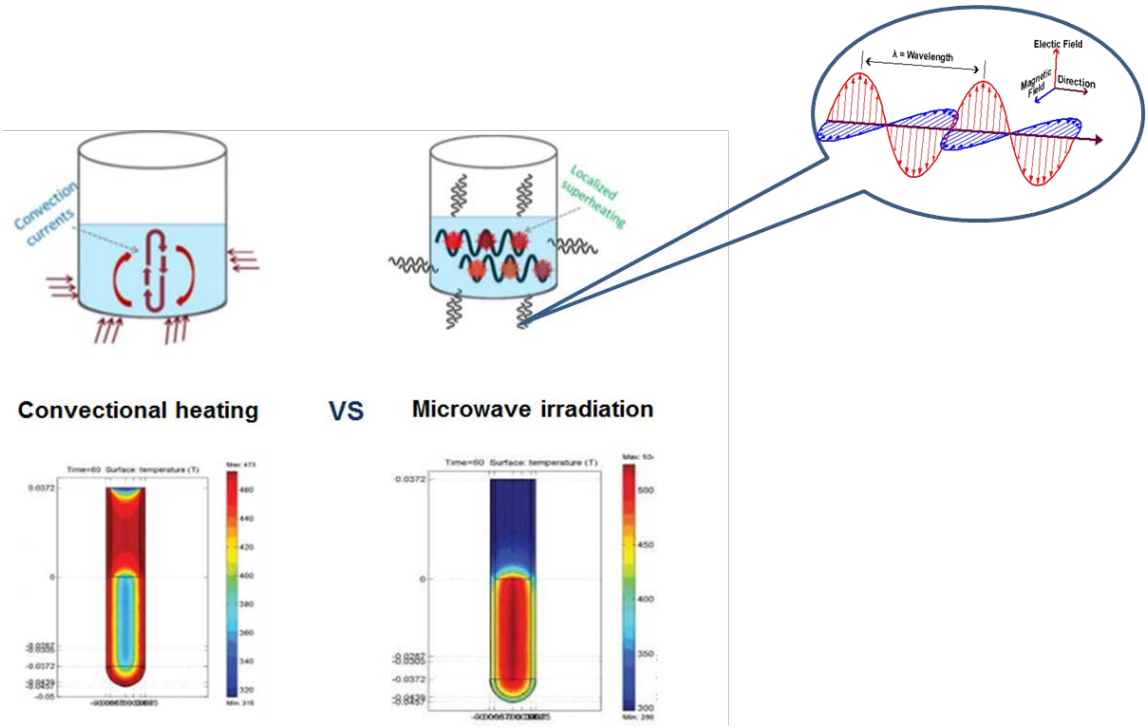


Figure 2.14: Microwave irradiation vs. convectional heating.

So microwave irradiation involves energy conversion rather than heat transfer. In conventional heating processes, the energy is delivered to the surface of the material by radiation or convection and then transferred to the bulk of the material by conduction [138]. The reaction mixture in contact with the hot vessel walls is heated first in conventional heating, while the microwave irradiation raises the temperature from the inside, as seen Figure 2.14. Microwave irradiation has the following advantages:

Properties of microwave irradiation

- Volumetric heating
- Low energy consumption
- Clean, reproducible
- Easily automated
- High temperatures
- Fast heating rates, short reaction times
- High quality products

Microwave irradiation has been used in the synthesis of the electrode materials for lithium-ion batteries [140]. The resultant powders have fine microstructures, small particles and improved electrochemical properties. In this work we strategically applied

microwave irradiation as a tool to curb capacity fading and improve the electrochemical properties of the studied cathode materials.

.

2.2.5.7 $Li[Li_{0.2}Mn_{0.54}Ni_{0.13}Co_{0.13}]O_2$ cathode material

$Li[Li_{0.2}Mn_{0.54}Ni_{0.13}Co_{0.13}]O_2$ is from a class of $xLi_2MnO_3\cdot(1-x)LiNi_{1/3}Co_{1/3}Mn_{1/3}O_2$ LMR-NMC materials. This class of LMR-NMC materials have been reported to show good electrochemical performance [115]. $Li[Li_{0.2}Mn_{0.54}Ni_{0.13}Co_{0.13}]O_2$ cathode material can be rewritten in two-component notation as $0.5\ Li_2MnO_3\cdot 0.5\ LiNi_{1/3}Co_{1/3}Mn_{1/3}O_2$ (x = 0.5). This material is a type of a LMR-NMC material employed for the efforts of this thesis in the study of manganese rich cathodes for lithium-ion batteries.

Lithium Nickel Manganese Cobalt Oxide $Li[Li_{0.2}Mn_{0.54}Ni_{0.13}Co_{0.13}]O_2$ will be referred to as LMNC in this thesis. The theoretical capacity of LMNC, based on complete extraction of lithium is 377 mAh/g [110]. The theoretical discharge capacity for the initial cycle was determined as 251 mAh/g. At room temperature this material could deliver an initial discharge capacity of 250 mAh/g when discharged from 4.8 to 2.0 V at 18 mA/g [112]. At elevated temperatures (50℃) this material could deliver a discharge capacity of 286 mAh/g when discharged from 4.6 to 2.5 V at 0.05 mA/cm [60].

Like all other LMR-NMC cathode materials LMNC suffers from capacity fade, poor rate capability, initial irreversible capacity loss and voltage fade, as discussed above. Some of the strategies discussed in solving these challenges with LMR-NMC cathode materials were also tried here, particularly doping with minute amounts of Al–ions in the structure of LMNC to stabilize the structure and thus improves capacity retention and rate capability [130,141,142].

2.3 Sodium-Ion Batteries

2.3.1 Background of sodium-ion batteries

SIBs have been studied alongside LIBs, but lost attention after the first commercialization of LIBs in 1991 [143]. SIBs have similar chemistry and properties to LIBs and thus have recently drawn wide attention as the most attractive alternative to LIBs for smart grid applications [144-146]. Figure 2.15 shows the publications in SIBs research between 1980-2015. The increase in publications signifies the renewed interest in the sodium ion batteries.

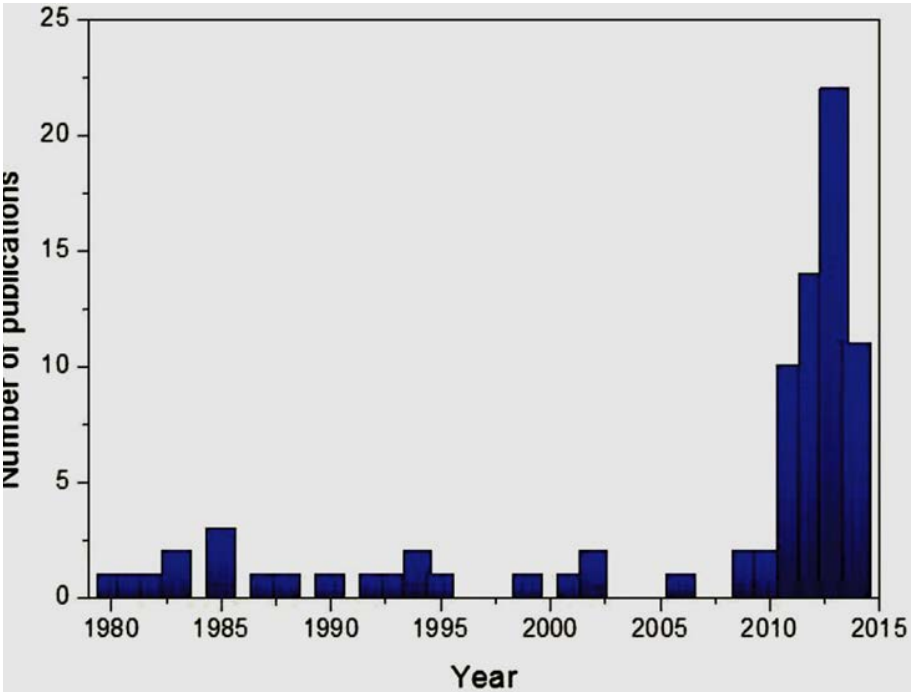


Figure 2.15: Sodium-ion batteries research publications history [147].

The research in SIBs is renewed because of the abundance of sodium which has a potential to decrease the price of batteries, which is another problem for lithium-ion batteries. Table 2.3 shows the characteristics of sodium-ion batteries and lithium-ion batteries. Lithium resources are unevenly distributed (mainly in South America), and therefore, the production of LIBs depends on the import of lithium from South America. In contrast, sodium resources are unlimited everywhere, as sodium is one of the most abundant elements in the Earth's crust, as seen in Figure 2.16. However, SIBs have low energy density compared to LIBs, but this is not an issue for large scale stationery applications.

Table 2.3: Characteristics of sodium-ion batteries and lithium-ion batteries [148].

Category	Lithium	Sodium
Cation radius (Å)	0.76	1.06
Atomic weight (g/mol)	6.9	23
Cost, carbonates ($/ton)	5000	150
Capacity, metal	3829	1165
Coordination preference	Octahedral and tetrahedral	Octahedral and prismatic
Melting point (℃)	180.5	97.7
Distribution	70% in South America	Everywhere

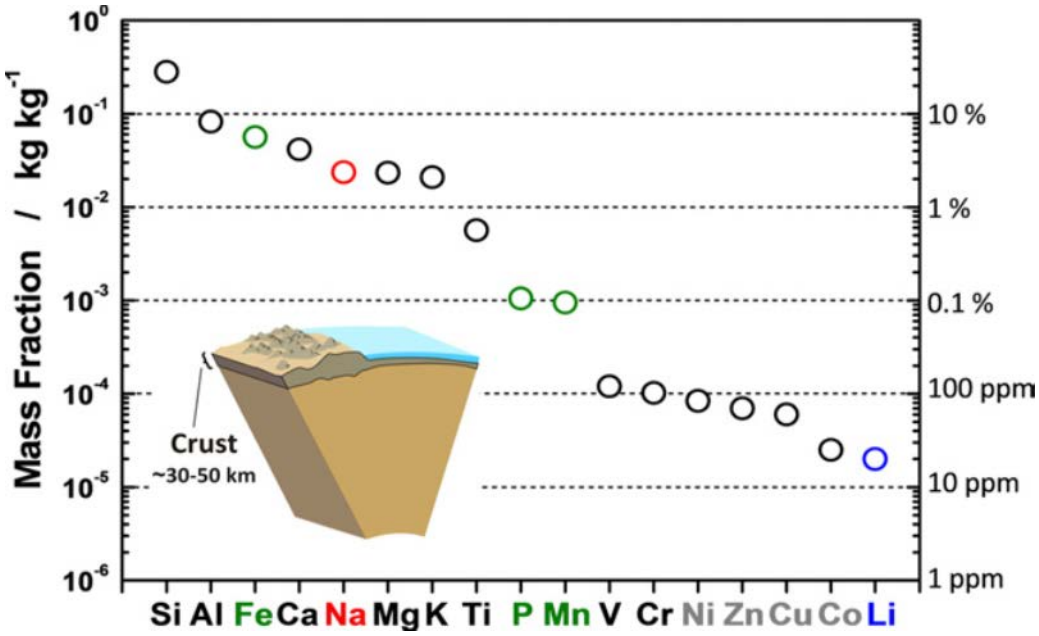


Figure 2.16: Elemental abundance in the Earth's crust [149].

Sodium-ion batteries are based on layered intercalation compounds as electrode materials they are operated at ambient temperatures, have low maintenance cost and cheaper compared to their counterparts Na-$NiCl_2$ (ZEBRA) and Na-S batteries. Na-$NiCl_2$ and Na-S batteries are operated in the molten state at high temperatures (300-350^{o}C) to maintain the sodium in the liquid state. Thus Na-$NiCl_2$ and Na-S batteries are considered as molten salt batteries. Na-S batteries were developed in the 1960's by Ford Motor Company and contain molten sodium as anode, sodium β"-alumina as electrolyte and molten Sulphur as cathode. ZEBRA (Zeolite

Battery Research Africa) batteries were developed in the 1980's by Council for Scientific and Industrial Research (CSIR)-South Africa and contain molten sodium as an anode, molten sodium tetrachloroaluminate ($NaAlCl_4$) as electrolyte and a metal chloride ($NiCl_2$) as cathode.

2.3.2 Working principle of sodium-ion batteries

The working principle and internal configuration of sodium-ion batteries is the same as the lithium-ion batteries as described in Section 2.2.2. Figure 2.17 shows the working principle of SIBs. However, the cathode in sodium-ion batteries is made of sodium-based materials and the anode is made of sodium foil or graphite. Glass-fibre filter paper is used as the separator in sodium-ion batteries while polypropylene separator is used in lithium-ion batteries. The electrolyte in sodium-ion batteries is also different from lithium-ion batteries. Typically, sodium-perchlorate ($NaClO_4$) is used as the electrolyte in sodium-ion batteries while lithium-hexafluorophosphate ($LiPF_6$) is used in lithium-ion batteries.

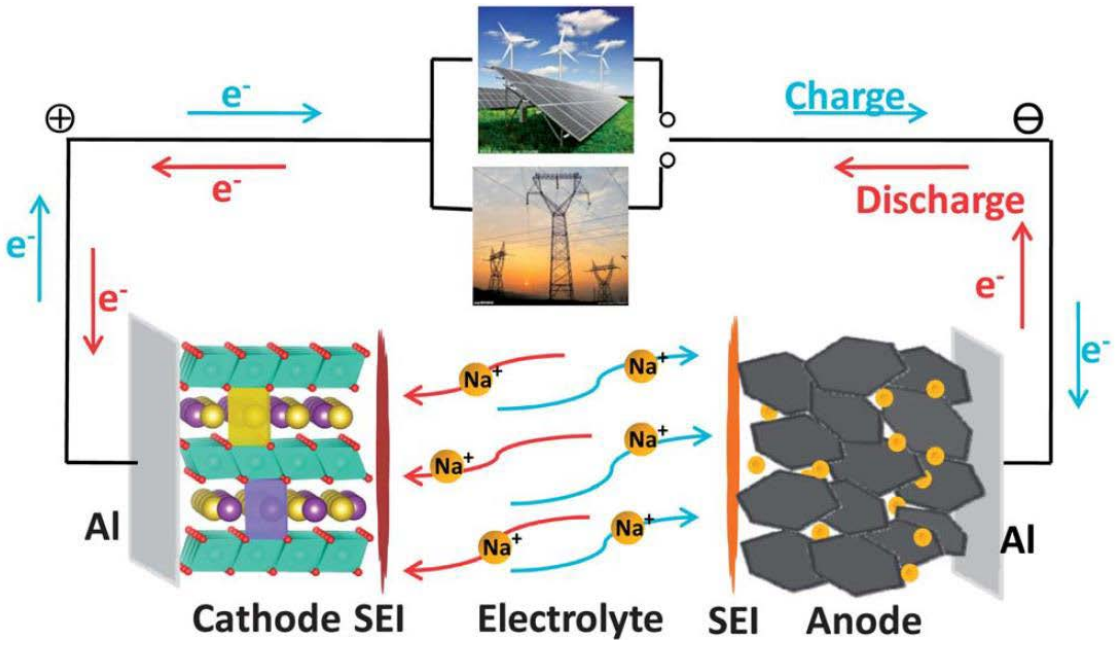


Figure 2.17: Working principle of sodium-ion batteries [148].

2.3.3 Applications of sodium-ion batteries

SIBs can be used to directly store energy from renewable energy sources such as wind, solar and wave, or be used as energy storage systems for smart grid application. Renewable energy sources are alternative means for energy generation since fossil fuels, which are primary

sources of energy, will be depleted in years to come. Renewables are cheap, environmentally friendly and provide universal access. However, the intermittent nature of renewable energy sources requires effective energy storage systems to save the energy when the demand is low and provide the energy when the demand is high. Figure 2.18 shows examples of renewable energy sources.



Figure 2.18: Applications of sodium-ion batteries [150].

SIBs are favorable for smart grid applications because they are cheap and have high voltage characteristics [143,151,152]. Sodium is cheap and it is the 4th most abundant element on the earth's crust and is uniformly distributed around the world [153]. Therefore SIBs can be used to store the energy and help to integrate the renewable energy sources with the power grid.

2.3.4 Cathode materials for sodium-ion batteries

Cathode materials also play an important role in sodium-ion batteries. The energy density and rate capability of a sodium-ion battery depends greatly on the theoretical capacity and thermodynamics of the cathode material.

The research in cathode materials for sodium-ion batteries started around the same time as the research in the cathode materials for lithium-ion batteries since 1970. The requirements for

cathode materials for sodium- ion batteries are similar to that of lithium-ion battery cathode materials. This is because of the similar chemistry of sodium-ion with lithium-ion, since they are found in the same group in the periodic table. The cathode materials for sodium-ion batteries should allow reversible intercalation and de-intercalation of Na-ions within the crystal structure during charge and discharge at redox potential greater than 2 V vs. Na^+/Na. These cathode materials should also exhibit low volume expansion during charge and discharge to allow good cycle performance [154]. There are different types of cathode materials studied for sodium-ion batteries. These include layered oxides, polyanions and pyrophosphates, organic materials and Prussian blue analogues. A type of layered oxide cathodes materials were studied in thesis.

1. Prussian blue analogues

Prussian blue analogues such as ($Na_xMFe(CN)_6$, where M = Fe, Co, Ni) have been studied as cathode materials for sodium-ion batteries [155]. The Prussian blue analogues are based on the $A_xM[D(CN)_6].nH_2O$ crystal structure (A is alkali metal ion, M is N-coordinated transition metal ion and D is C-coordinated transition metal ion). The example of Prussian blue analogues used as cathode materials include $KFe[Fe(CN)_6]$, rhombohedral $Na_{1.72}MnFe(CN)_6$ and cubic $Na_{1.4}MnFe(CN)_6$, $NaZnFe(CN)_6$, $NaFe[Fe(CN)_6]$, $Na_2Mn^{II}[Mn^{II}(CN)_6]$, and others [155-159]. However, Prussian blue compounds exhibit poor cycle efficiency and structural instability due to the distortion of the lattice during charge and discharge as a result of the existence of the vacancies and coordinating water which break down the bridging of the M-CN-D framework [157]. Figure 2.19a shows a frame work of Prussian blue analogues and Figure 2.19b shows a typical electrochemical performance of Prussian blue analogues as cathode materials in sodium-ion batteries.

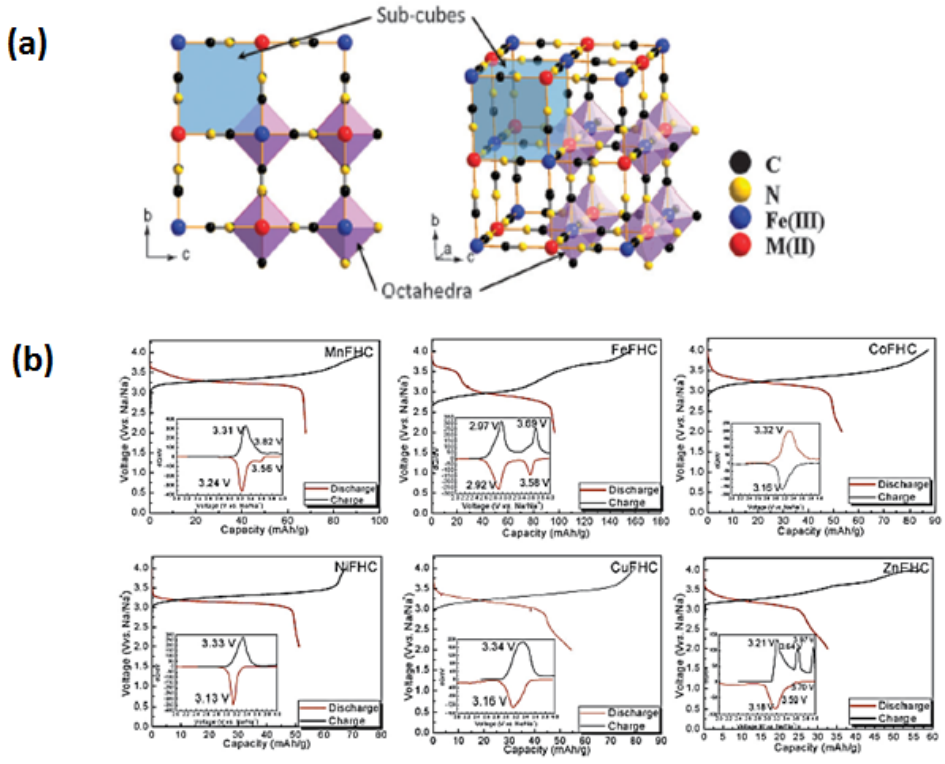


Figure 2.19: (a) Frame work of Prussian blue analogues and (b) electrochemical performance of Prussian blue analogues as cathode materials in sodium-ion batteries [156].

2. Organic materials

Multifunctional organic compounds such as bipolar porous organic electrode (BPOE) are also used as cathode materials for sodium-ion batteries. This type of cathode materials are shown to deliver an energy density of 500 W h/kg and a power density of 10 kW/kg, which is comparable to that of layered oxides and polyanion cathode materials [154]. Organic electrode materials are candidates for sodium ion batteries because they are cheap, environmental friendliness and are recyclable. However, organic electrodes are suffers from poor electronic conductivity, low thermal stability and they dissolve in organic electrolyte. Figure 2.20 shows example of organic cathode materials used in sodium-ion batteries.

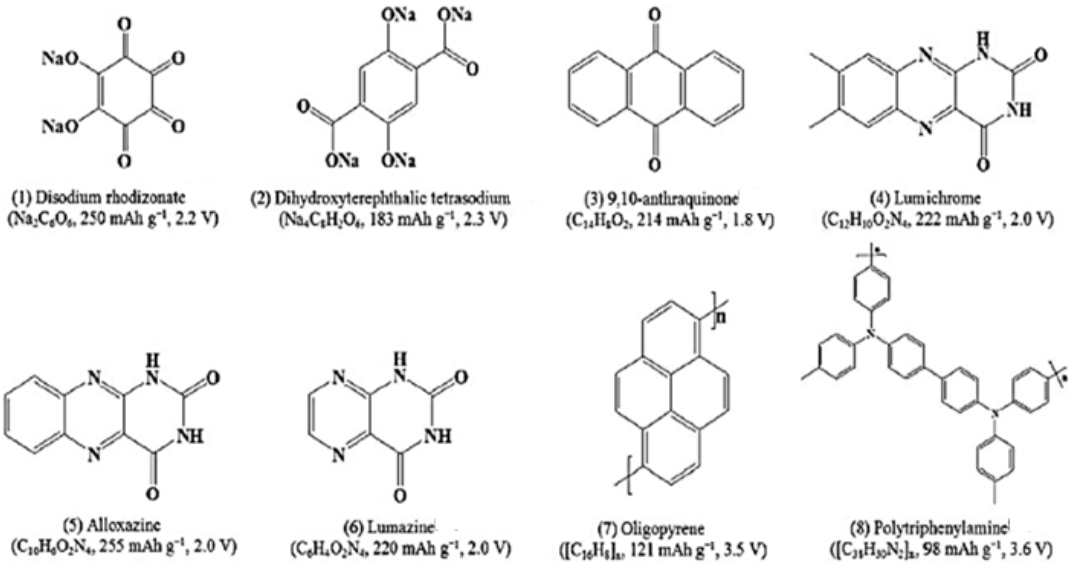


Figure 2.20: Organic cathode materials used in sodium-ion batteries [160].

3. Polyanions and pyrophosphates

Na-based polyanions includes olivine $NaFePO_4$, Na-based fluorophosphates such as Na_2FePO_4F and Na_2MnPO_4F, NASICON (Na Super Ionic CONductor) $Na_3V_2(PO_4)_3$ [154,161,162] They are good candidates for sodium ion batteries because of their structural, thermal stability and higher redox potential of transition metals. Sodium-based pyrophosphates such as $Na_2MP_2O_7$ (M = Fe, Mn or Co) have also been studied as cathode materials due to their structural stability and good sodium ion mobility, but these materials suffers from low capacity and poor cycle performance [154]. Figure 2.21 displays the structural framework of the different polyanions based cathode materials for sodium-ion batteries. Table 2.4 shows the electrochemical performance of polyanions and pyrophosphates based cathode materials.

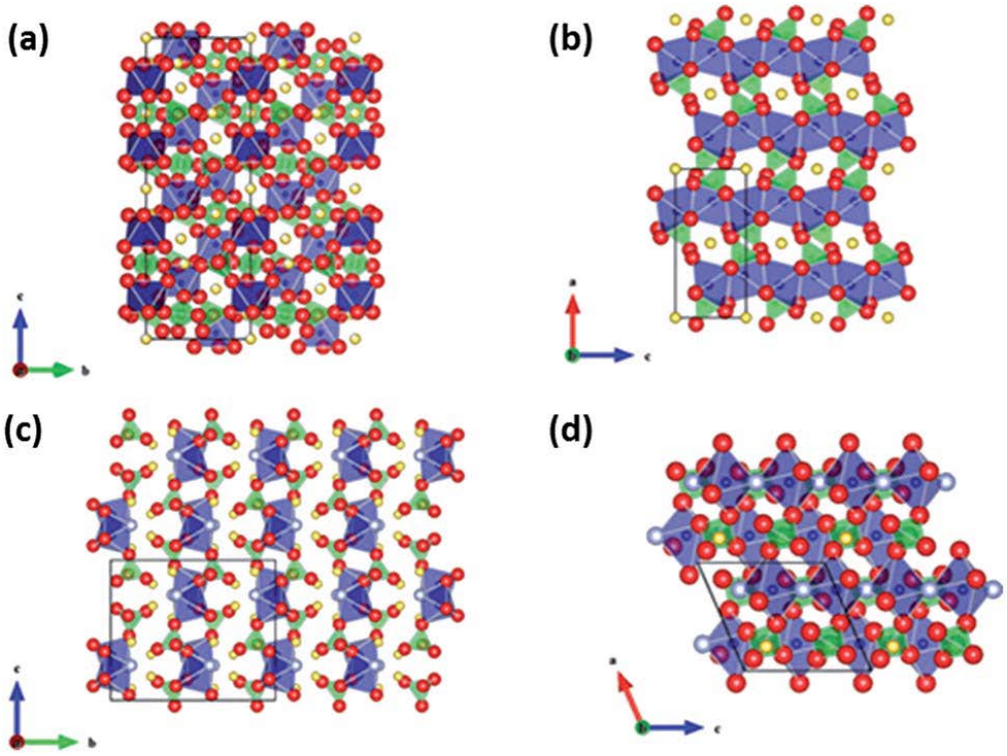


Figure 2.21: Crystal structure of polyanionic cathode material (a) NASICON $Na_3V_2(PO_4)_3$, (b) olivine $NaFePO_4$, (c) Na_2FePO_4F, (d) Na_2FeSO_4F [154].

Table 2.4: Electrochemical performance of polyanions and pyrophosphates based cathode materials [149].

Material	**Specific Capacity [mAh/g]**	**Potential of insertion [V *vs.* Na+/Na°]**
$NaFePO_4$ (maricite-type)	Inactive	-
$Na_3Fe_2(PO_4)_3$	~ 45	2.5
$Na_3Fe_3(PO_4)_4$	~80	2.5
$Na_3Fe_2(PO_4)_2F_3$	~ 45	2.8
$NaFePO_4F$	~ 110	3.0
$Na_2FeP_2O_7$	~ 80	2.8
$Na_2MnP_2O_7$	~ 80	3.3
$NaFeF_3$	~ 150	2.8

4. Layered Oxides

Layered oxides are the widely studied cathode materials for the sodium-ion batteries due to their high potential and energy density above 500 Wh/kg. The study of layered sodium transition metal oxides began in the 1970's. Fouassier et al studied the physical and structural properties of A_xMO_2 compounds (A = Na, K; M = Cr, Mn, Co) in the early 1970's and in 1985 Delmas et al. established the notation for the layered sodium transition metal oxides[163]. The crystal structures of the layered sodium transition metal oxides are built up by stacking sheets of edge-sharing MO_6 octahedra and the sodium ions are located between MO_6 sheets. Layered sodium transition metal oxides are classified according to the stacking arrangement of the sodium-ion between each interlayer in the structure [154,164]. Each layered oxide structure is denoted by Xn (X = the sodium-ion coordination and n = the number of MO_2 slabs in the unit cell). Layered sodium transition metal oxides are found as an O and P-type structure where the sodium-ion is in octahedral and trigonal (prismatic) coordination with the oxygen within the interstitial layer of the crystal structure, respectively [154]. In the P2-type phase, the sodium-ion is coordinated in the trigonal prismatic sites between the TMO_2 (TM = transition metal) sheets and there are two repeating MO_2 layers in the unit cell (Figure 2.22) [144,165,166]. In the O3-type the sodium ion is coordinated in the octahedral site and there are three repeating MO_2 layers in the unit cell. The stacking order in the P2-type is ABBA and the stacking order in O3 is ABCABC as shown in Figure 2.22. A prime indicates a distortion of an ideal structure (polytype) for example O'3 and P'2 represent the monoclinic distortion of O3 and P2 phase packing [167]. Sodium layered oxides are found as O- and P-type structures because of the large sodium ionic radius which prefers octahedral and trigonal (prismatic) coordination [167] . P2-type, P3-type, O3-type layered oxides are the most common structure types of layered sodium transition metal oxides. The difference in the stacking order results in different insertion sites for the sodium-ions [164]. This then results in different electrochemical performance. Figure 2.22 displays the different structures of sodium layered oxides.

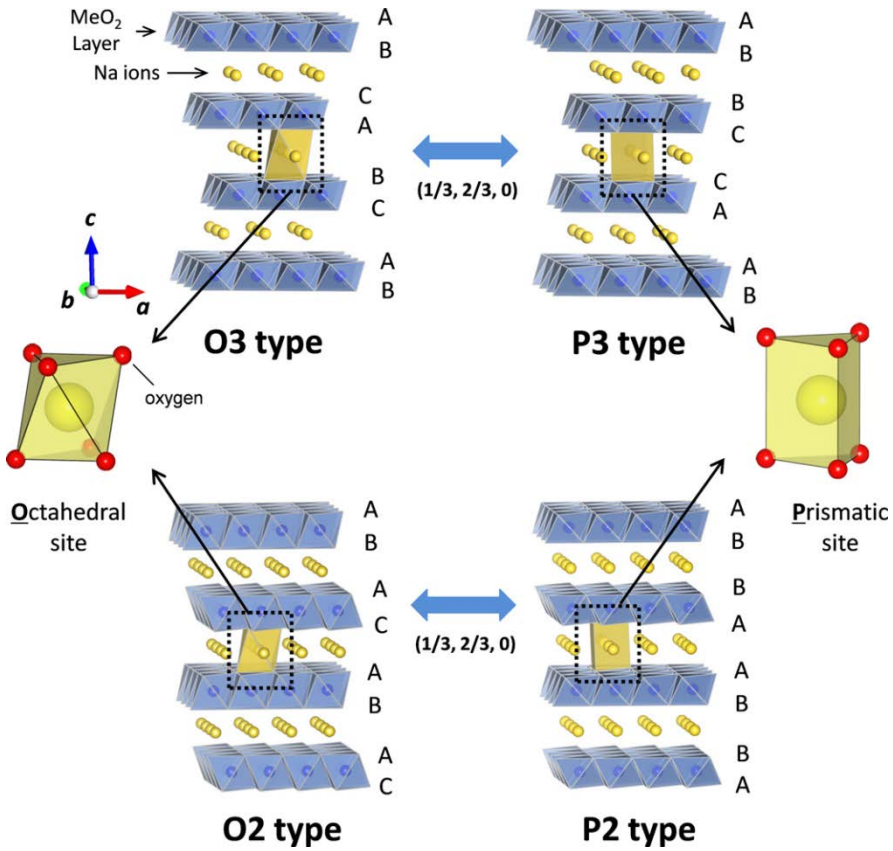


Figure 2.22: Structural classification of layered sodium transition metal oxide cathodes and phase transition processes induced by sodium extraction [149].

P2-type structures are obtained when xNa < 2/3, while O3-type structures are obtained at high Na contents [167]. P2-type structures are found to result in high capacity compared to O3-type structure. This is due to easy and fast intercalation and de-intercalation of sodium-ion in P2-type due to that the sodium ion sits in the prismatic site which is larger than the octahedral site for O3-type structure [144,168]. P2-type also has improved cycle performance compared to O3-type structure. This is due that the P2-type rarely undergoes structural changes from P2-type to other phases/structures during charge and discharge because the structural transformation involves complex processes which includes the rotation of MO_6 octahedra and the breaking of M–O bonds.

A wide range of transition metals are used for layered $NaMO_2$ compounds and their combination also results in layered $NaMO_2$ compounds. Each combination results in different electrochemical performance as seen in Figure 2.23. Figure 2.23 displays different layered $NaMO_2$ compounds and compares their electrochemistry with other types of sodium-ion cathode materials and lithium-ion cathode materials.

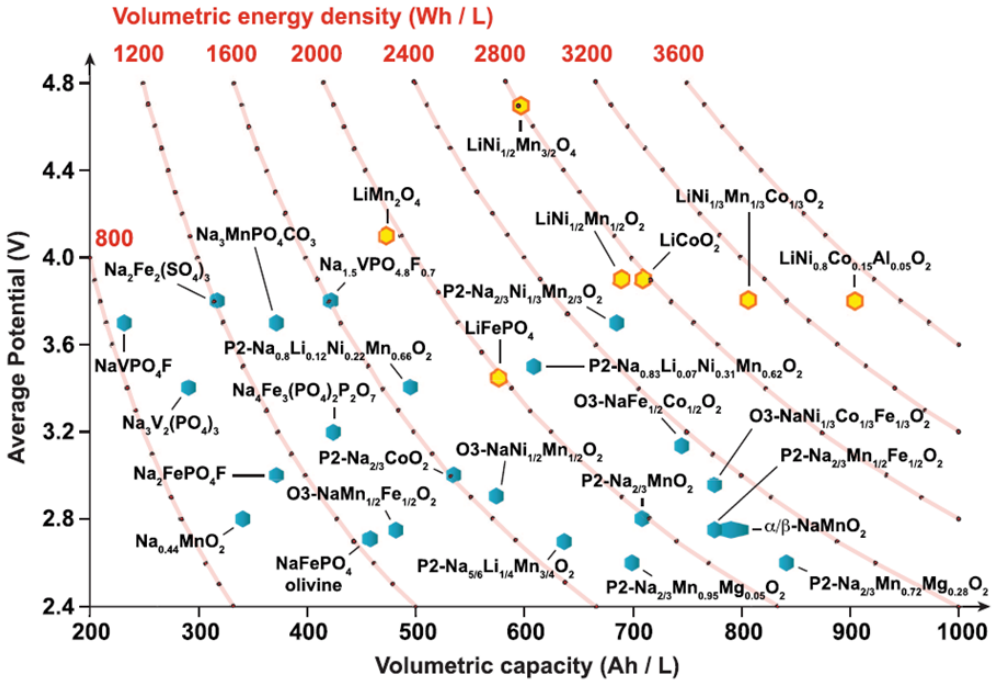


Figure 2.23: Average discharge potential and volumetric energy density (Wh/L) vs. volumetric capacity (Ah/L) for cathode materials for SIBs and LIBs [167].

2.3.5 P2-type $Na_{0.67}Mg_{0.28}Mn_{0.72}O_2$ cathode material

Layered P2-type manganese based oxides are the promising cathode materials for sodium-ion batteries [169-176]. This is because of the abundance of manganese, high capacities and larger tunnels that allow easy intercalation and de-intercalation of the sodium-ion [177-179].

In 2014, Bruce group reported Mg doping of P2-type $Na_{0.67}MnO_2$ cathode materials. The Mg doping of P2-type $Na_{0.67}MnO_2$ samples were prepared by solid state and co-precipitation methods. The work studied a series of $Na_{2/3}Mn_{1-x}Mg_xO_2$ (x = 0, 0.05, 0.1, 0.2) compounds and found out that Mg doping affected the structural phase transitions and Na-ordering [180]. In the same year, Komaba group reported that a P2-type $Na_{2/3}[Mg_{0.28}Mn_{0.72}]O_2$ prepared by solid state method capable of giving a large reversible capacity of >220 mAh/g [178]. The layered P2-type $Na_{2/3}[Mg_{0.28}Mn_{0.72}]O_2$ is abbreviated herein simply as NaMgMnO has a theoretical capacity of 260 mAh/g [181]. This cathode material is also interesting because it is cheap due to the huge natural abundance of Na, Mg and Mn precursor materials and that it is

also considered as a manganese rich layered oxide since the manganese content is $1.0 \leq Mn \leq 0.67$ [182].

2.3.5.1 Stucture of P2-type $Na_{0.67}Mg_{0.28}Mn_{0.72}O_2$ cathode material

The P2-type structure of NaMgMnO is composed of oxygen layers stacked in an ABBA arrangement, in which Mg and Mn occupy the octahedral sites between the AB oxide layers and Na occupies the trigonal prismatic sites between the AA and BB layers. The Mg and Mn ordering exists in the TM layers [183]. Figure 2.24 shows the structure of the P2-type $Na_{2/3}[Mg_{0.28}Mn_{0.72}]O_2$ cathode material.

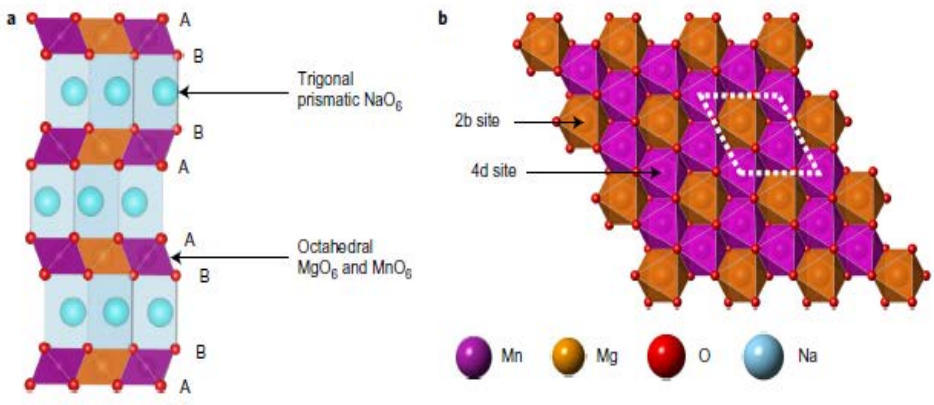


Figure 2.24: The structure of $Na_{2/3}[Mg_{0.28}Mn_{0.72}]O_2$, (a) shows the stacking of MO_2 in the structure and (b) shows the Mg-Mn ordering in the TM layers [183].

2.3.5.2 Disadvantages of $Na_{0.67}Mg_{0.28}Mn_{0.72}O_2$ cathode material

Sodium cathode materials based on P2-type manganese oxide intercalation materials can offer high capacity but they suffer from capacity fade during electrochemical cycling [143,184]. The capacity fade in these materials is due to the Jahn-Teller distortion of Mn^{3+} ions in the structure and manganese dissolution. Phase transition also occurs during cycling, whereby gliding of the oxygen layers result in structural distortion and rearrangement [164]. This also affects the cycle performance.

Sodium magnesium manganese oxides exhibit Jahn-Teller distortion because of the presence of Mn^{3+} ions in the structure. Manganese ions bonded to the weak field ligand such as oxygen results in a high spin complex with high spin 3d Mn^{3+} ions of electronic configuration t_{2g}^3-e_g^{*1}. Then Jahn-Teller distortion occurs in these complexes to lower the symmetry and thus remove

the degeneracy of the orbital. The electron in the e_g* orbital with orbital degeneracy will occupy the $d_{x^2-y^2}$ orbital resulting in the compression of the structure or occupy the d_{z^2} orbital resulting in the elongation of the structure [182]. Figure 2.25 shows the Jahn-Teller distortion of Mn^{3+} ions.

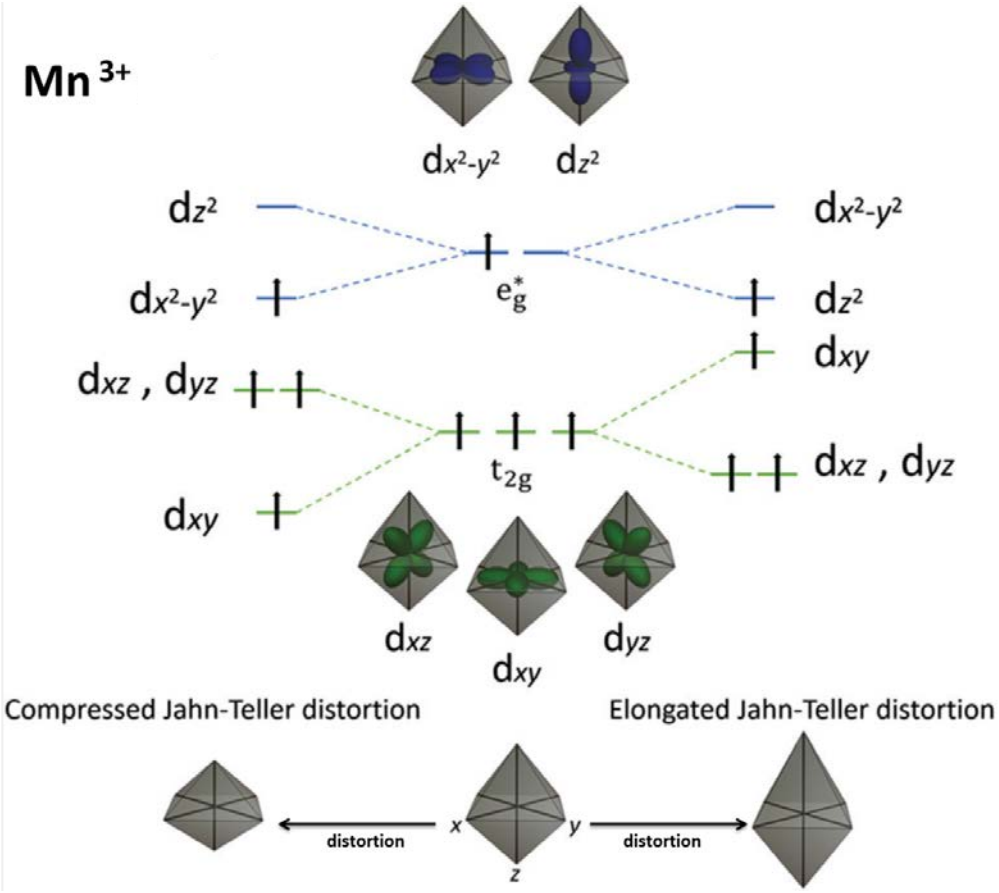


Figure 2.25: Jahn-Teller distortion of high spin Mn^{3+} ions [182].

2.3.5.3 Solution to the disadvantages of $Na_{0.67}Mg_{0.28}Mn_{0.72}O_2$ cathode material

To solve this problem of capacity fade in P2-type manganese oxide cathode materials strategies to decrease the Mn^{3+} ion content in the structure are employed. Magnesium (Mg) doping is one of the strategies reported in literature to reduce capacity fade in these materials [180,181]. Magnesium doping increases the Mn^{4+} ions (decreasing Mn^{3+} ions) and this reduces the Jahn-Teller distortion. However, Yabuuchi and co-workers reported the synthesis of $Na_{0.67}Mg_{0.28}Mn_{0.72}O_2$ exhibiting a high capacity of 220 mAh/g but this capacity reduced upon

cycling and was 150 mAh/g after 30 cycles (i.e. 32 % capacity loss after 30 cycles) [181]. This suggests that the capacity fade in Mg-doped P2-type manganese oxide could be further improved. Some strategies to be employed in improving the capacity fade in $Na_{0.67}Mg_{0.28}Mn_{0.72}O_2$ cathode materials include the following;

1. Doping of the materials with anions such as fluoride ions in the space of the oxygen can be used to improve the cycle performance. Surface fluorination also is beneficial for enhancing the rate capacity performance.
2. The electrochemical performance of electrode materials for SIBs can be also improved by employing using different synthesis methods and conditions. The $Na_{0.67}Mg_{0.28}Mn_{0.72}O_2$ cathode material has been only synthesized using solid state and co-precipitation methods. Therefore other methods need to be investigated to improve its electrochemical performance.
3. Coating strategies discussed above for lithium-ion batteries can be used to improve the cycle performance of the $Na_{0.67}Mg_{0.28}Mn_{0.72}O_2$ cathode materials.

2.4 Electrochemical characterization of cathode materials

Electrochemical characterization of the cathode materials is a very crucial part of the study of cathode materials. The results obtained from the electrochemical characterization give in details the performance of the cathode materials in lithium-ion or sodium-ion. The study of cathode materials is never complete without the electrochemical characterization techniques such cyclic voltammetry, galvanostatic charge-discharge measurements and electrochemical impedance spectroscopy.

2.4.1 Cyclic voltammetry

Cyclic voltammetry (CV) is an important electrochemical technique for the determination of the redox potentials and redox couples for electroactive species in the cathode materials. Therefore, it is useful in determining the potential window for the electrochemical cycling of the cathode materials. It then should be the first analysis performed in any electrochemical characterization of cathode materials, especially if the cathode material is newly discovered.

A typical CV experiment involves the sweeping of a potential applied to the working electrode from an initial potential (V_1) to an end potential (V_2) at a constant scan/sweep rate (ν). Then

the direction of the sweep is reversed and the potential is swept from V_2 back to V_1, to complete one scan or cycle. The scans can be repeated many times and performed at different scan rates. The scan rate may range from a few millivolts per seconds to a million volts per second. However, slower scan rates are used to study the redox couples for electroactive species in the cathode materials. During the potential sweep current due to the electrochemical reactions taking place at the electrode interface is measured. Then a cyclic voltammogram becomes a plot of measured current (y-axis) vs. applied potential (x-axis). Figure 2.26 displays the cyclic voltammogram of $Li[Li_{0.2}Mn_{0.54}Ni_{0.13}Co_{0.13}Al_{0.02}]O_2$ cathode material for lithium-ion battery.

Cyclic voltammetry is also used to investigate the kinetics, thermodynamics and mechanism of electrochemical reactions. The reversibility of the insertion ions (Li^+ or Na^+) is also investigated using CV.

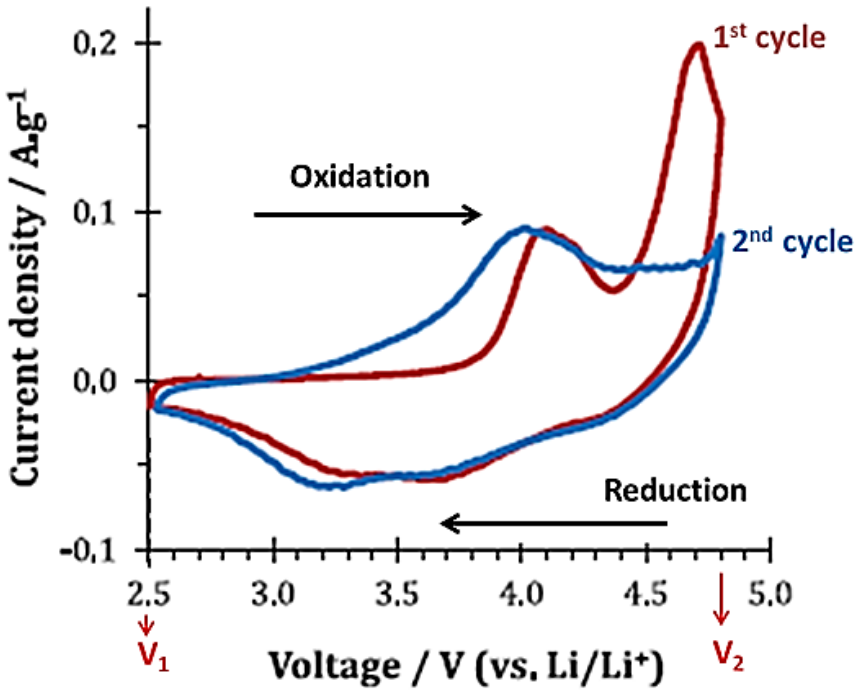


Figure 2.26: Typical cyclic voltammogram of LMR-NMC ($Li[Li_{0.2}Mn_{0.54}Ni_{0.13}Co_{0.13}Al_{0.02}]O_2$) cathode material cycled between 2.5 V and 4.8 V at 0.1 mV s^{-1} [185].

2.4.2 Galvanostatic charge-discharge

Galvanostatic charge-discharge studies are at the centre of the electrochemical characterization of cathode materials. This technique allows the cathode material to be tested under real battery working conditions. This technique can give us the specific capacity of the cathode material.

The capacity is an amount of energy the cathode material can store. The theoretical capacity (Q) can be calculated using the following equation (2.8):

$$Q = \frac{nF}{M \times 3.6} \tag{2.8}$$

where M is the molar mass of the active material (in g/mol), n is the number of moles of lithium ions that participate in the reaction and F is Faraday's constant (9.65×10^4 C mol^{-1}).

During galvanostatic charge-discharge measurements a constant current is applied between the set upper and lower potentials limits for the working electrode (cathode). When coin half cells are used, the working electrode is the cathode electrode and the lithium metal foil assumes the role of both a reference and counter electrode.

Galvanostatic charge-discharge studies are also used to determine the cycle performance of the cathode materials by charging and discharging the cell at a constant current for many cycles e.g. 100 cycles. Slow current rates are preferred for determination of the cycle performance. The cell can also be charge-discharged at different currents from low current rates to high current rates in order to study the rate capability of the cathode material. The rate capability studies determine how fast the cathode material can be charged and discharged.

2.4.3 Electrochemical impedance spectroscopy

Electrochemical Impedance Spectroscopy (EIS) is used in lithium-ion and sodium-ion batteries to study the impedance, aging effects and kinetics of cathode materials [186,187,187-190]. The impedance (Z) is measured by applying an AC potential (sinusoidal $V(t)$) to an electrochemical cell and measuring the resulting sinusoidal current, $I(t)$ [191]:

$$Z = \frac{V\,(t)}{I\,(t)} \tag{2.9}$$

where $V(t)$ is given by $V(t) = V_0 \sin \omega t$ and $I(t) = I_0 \sin(\omega t + \theta)$. V_0 is the maximum potential amplitude and ω is the radical frequency (rad s^{-1}), I_0 is the maximum applied current and θ represent the shift in phase by which the voltage lags the current [191,192]. The current response $I(t)$ can be analysed as a sum of sinusoidal functions at the same frequency but at a different phase. Therefore the impedance can be represented as follows:

$$Z = \frac{V(t)}{I(t)} = \frac{V_0 \sin(\omega t)}{I_0 \sin(\omega t + \theta)} = Z_0 \frac{\sin(\omega t)}{\sin(\omega t + \theta)} \tag{2.10}$$

For the expression of impedance in Euler's relation, the total impedance becomes:

$$Z_0 \exp(j\theta) = Z_0[\cos(\theta) + j\sin(\theta)] \tag{2.11}$$

Therefore the total impedance is written in complex notation as the following:

$$Z = Z' + j \cdot Z'' \tag{2.12}$$

where Z' is the real impedance, Z" is the imaginary impedance and j is the complex number. The EIS data is then represented using the Nyquist plots where the Z'' is plotted against Z' for different values of ω. The radical frequency is related to the frequency as $\omega = 2\pi f$.

The Nyquist plot usually comprises of a semi-circle at high frequencies corresponding to the kinectic processes and a straight-line at low frequencies corresponding to the diffusion processes in the cell. The EIS data is fitted using an equivalent circuit. Figure 2.27 shows a Nyquist plot and equivalent circuit for LMR-NMC cathode material.

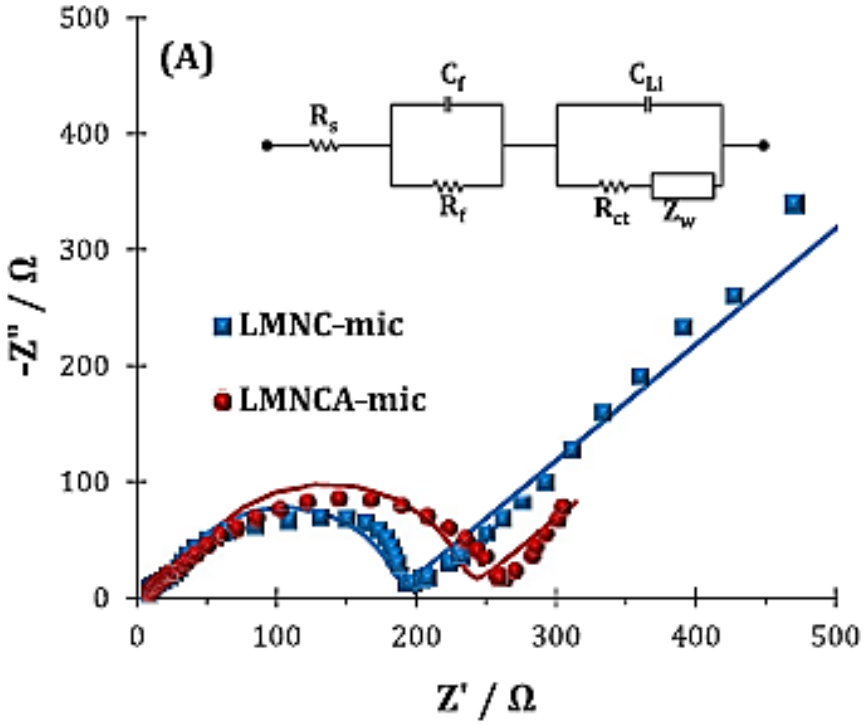


Figure 2.27: Nyquist plot and equivalent circuit (inset) of LMR-NMC cathode material [185].

In the equivalent circuit the fitting parameters involve the solution ohmic resistance of the electrode system (R_s), solid electrolyte interface (SEI) film resistance (R_f) and the

corresponding capacitance of the surface film (C_f), the charge transfer resistance (R_{ct}) due to the lithium intercalation/de-intercalation process and the corresponding interfacial capacitance (C_{Li}) and the Warburg element (Z_w) signified as the straight sloping line (45^o) at the low frequency region describing the solid state diffusion of lithium ions inside the active particles [185]. Figure 2.28 shows the EIS behaviour of cathode material at different frequency ranges.

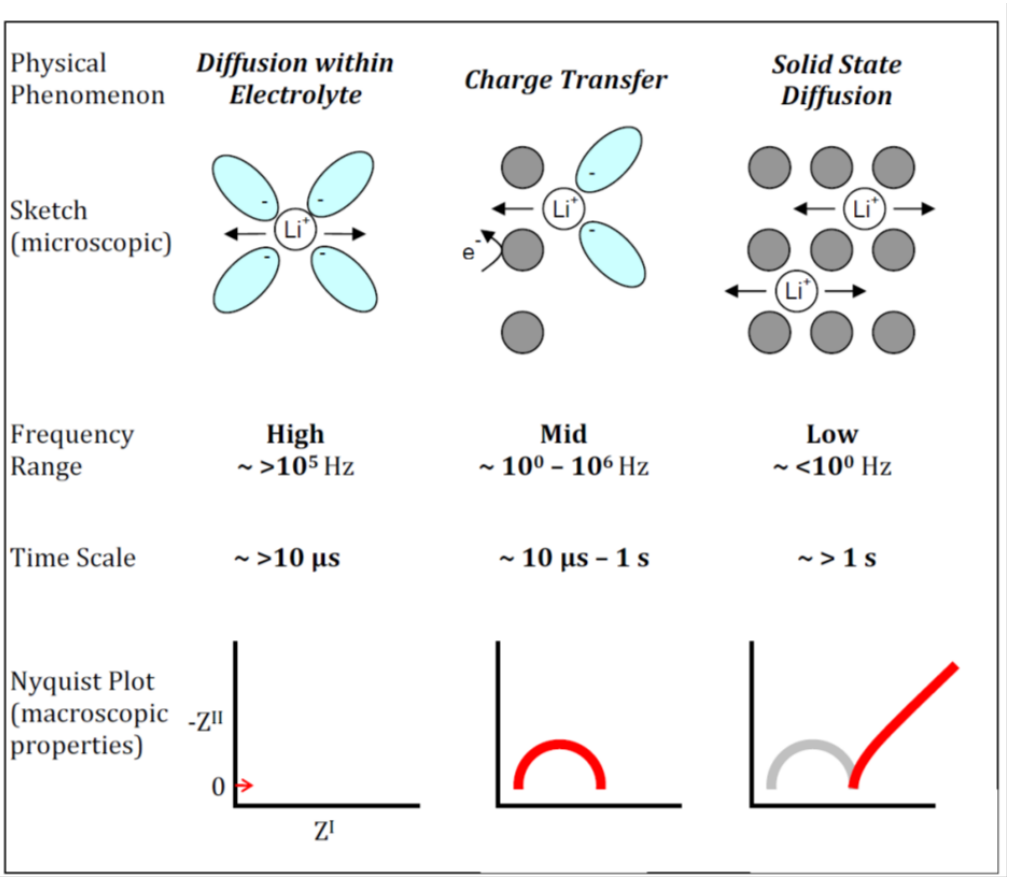


Figure 2.28: EIS behaviour of cathode material at different frequency ranges [193].

2.4.4 Diffusion coefficient of lithium-ions

The diffusion coefficient of lithium ions in this thesis was calculated using the Warburg parameter obtained from the EIS data. The following equation was used [95]:

$$D_{Li} = \frac{2R^2\ T^2}{n^4\ F^4\ \sigma^2 A^2\ C_{Li}^2} \tag{2.13}$$

where D_{Li} is the lithium ion diffusion coefficient, R is the gas constant, T is the absolute temperature, n is the number of electrons transferred, F is the Faraday constant, σ is the Warburg parameter, A is the geometric surface area of the cathode and C_{Li} is the concentration

of lithium in the cathode material. The Warburg factor (σ) is obtained from the slope of a plot of real impedance (Z′) vs. reciprocal square root of frequency ($\omega^{-1/2}$) in the low frequency region. The following equation is then used for the plot:

$$Z = \sigma\,(1 - j)\omega^{-1/2} \tag{2.14}$$

2.5 References

[1] M. Piccolino, M. Bresadola, Trends in Neurosciences, 25 (2002) 51-57.

[2] B. Scrosati, Journal of Solid State Electrochemistry, 15 (2011) 1623-1630.

[3] D. Linden, T.B. Reddy, New York, (2002).

[4] D.R. MacFarlane, J. Huang, M. Forsyth, Nature, 402 (1999) 792-794.

[5] X. Ji, K.T. Lee, L.F. Nazar, Nature Materials, 8 (2009) 500-506.

[6] F. Beck, P. Rüetschi, Electrochimica Acta, 45 (2000) 2467-2482.

[7] C. Chakkaravarthy, P. Periasamy, S. Jegannathan, K.I. Vasu, Journal of Power Sources, 35 (1991) 21-35.

[8] T. Sakai, H. Miyamura, N. Kuriyama, A. Kato, K. Oguro, H. Ishikawa, Journal of the Electrochemical Society, 137 (1990) 795-799.

[9] T. Nagaura, K. Tozawa, Prog.Batteries Solar Cells, 9 (1990) 209.

[10] M.S. Whittingham, Chemical Reviews, 104 (2004) 4271-4302.

[11] K. Ozawa, Solid State Ionics, 69 (1994) 212-221.

[12] J. Tarascon, M. Armand, Nature, 414 (2001) 359-367.

[13] R. Liu, J. Duay, S.B. Lee, Chemical Communications, 47 (2011) 1384-1404.

[14] J. Xu, S. Dou, H. Liu, L. Dai, Nano Energy, 2 (2013) 439-442.

[15] H.D. Yoo, E. Markevich, G. Salitra, D. Sharon, D. Aurbach, Materials Today, 17 (2014) 110-121.

[16] M. Reddy, G. Subba Rao, B. Chowdari, Chemical Reviews, 113 (2013) 5364-5457.

[17] P. Garcia, L.M. Fernandez, C.A. Garcia, F. Jurado, Industrial Electronics, IEEE Transactions on, 57 (2010) 4013-4023.

[18] A.M. Gets, Powering the Future: Renewable Energy Roll-out in South Africa, Greenpeace Africa (2013).

[19] J. Axsen, K.S. Kurani, A. Burke, Transport Policy, 17 (2010) 173-182.

[20] J. Gonder, A. Simpson, Measuring and reporting fuel economy of plug-in hybrid electric vehicles, National Renewable Energy Laboratory 2006.

[21] L. Lu, X. Han, J. Li, J. Hua, M. Ouyang, Journal of Power Sources, 226 (2013) 272-288.

[22] G. Wang, S. Bewlay, M. Lindsay, Z. Guo, J. Yao, K. Konstantinov, H.K. Liu,. S.X. Dou, Materials Forum 27 (2004) 33- 44.

[23] Brian Westenhaus. http://newenergyandfuel.com/http:/newenergyandfuel/com/2010/02/04/the-battery-explosion-is-coming-part-one/lithium-ion-battery-component-cost-shares/,(2013).

[24] B. Xu, D. Qian, Z. Wang, Y.S. Meng, Materials Science and Engineering: R: Reports, 73 (2012) 51-65.

[25] R. Chen, T. Zhao, X. Zhang, L. Li, F. Wu, Nanoscale Horizons, 1 (2016) 423-444.

[26] R.J. Gummow, A. de Kock, M.M. Thackeray, Solid State Ionics, 69 (1994) 59-67.

[27] A.K. Padhi, K. Nanjundaswamy, J.B.d. Goodenough, Journal of the Electrochemical Society, 144 (1997) 1188-1194.

[28] J.R. Croy, M. Balasubramanian, K.G. Gallagher, A.K. Burrell, Accounts of Chemical Research, 48 (2015) 2813-2821.

[29] J.R. Croy, K.G. Gallagher, M. Balasubramanian, B.R. Long, M.M. Thackeray, Journal of the Electrochemical Society, 161 (2014) A318-A325.

[30] M. Thackeray, S. Kang, C. Johnson, J. Vaughey, S. Hackney, Electrochemistry Communications, 8 (2006) 1531-1538.

[31] M.M. Thackeray, S. Kang, C.S. Johnson, J.T. Vaughey, R. Benedek, S. Hackney, Journal of Materials chemistry, 17 (2007) 3112-3125.

[32] Y. Wu, A. Manthiram, Electrochemical and Solid-State Letters, 9 (2006) A221-A224.

[33] J. Gao, J. Kim, A. Manthiram, Electrochemistry Communications, 11 (2009) 84-86.

[34] Z. Lu, J.R. Dahn, Journal of the Electrochemical Society, 149 (2002) A815-A822.

[35] D. Mohanty, A. Huq, E.A. Payzant, A.S. Sefat, J. Li, D.P. Abraham, D.L. Wood III, C. Daniel, Chemistry of Materials, 25 (2013) 4064-4070.

[36] D. Mohanty, S. Kalnaus, R.A. Meisner, K.J. Rhodes, J. Li, E.A. Payzant, D.L. Wood, C. Daniel, Journal of Power Sources, 229 (2013) 239-248.

[37] D. Mohanty, A.S. Sefat, S. Kalnaus, J. Li, R.A. Meisner, E.A. Payzant, D.P. Abraham, D.L. Wood, C. Daniel, Journal of Materials Chemistry A, 1 (2013) 6249-6261.

[38] D. Mohanty, A.S. Sefat, J. Li, R.A. Meisner, A.J. Rondinone, E.A. Payzant, D.P. Abraham, D.L. Wood III, C. Daniel, Physical Chemistry Chemical Physics, 15 (2013) 19496-19509.

[39] Isidor Buchmann, BU-1003: Electric Vehicle (EV), Battery University (2017).

[40] J. Zheng, S. Myeong, W. Cho, P. Yan, J. Xiao, C. Wang, J. Cho,J. G. Zhang, Advanced Energy Materials, 7 (2017) 1601284.

[41] H. Yu, H. Zhou, The Journal of Physical Chemistry Letters, 4 (2013) 1268-1280.

[42] J.R. Croy, K.G. Gallagher, M. Balasubramanian, Z. Chen, Y. Ren, D. Kim, S. Kang, D.W. Dees, M.M. Thackeray, The Journal of Physical Chemistry C, 117 (2013) 6525-6536.

[43] A. Boulineau, L. Simonin, J. Colin, C. Bourbon, S. Patoux, Nano Letters, 13 (2013) 3857-3863.

[44] C. Johnson, J. Kim, C. Lefief, N. Li, J. Vaughey, M. Thackeray, Electrochemistry Communications, 6 (2004) 1085-1091.

[45] C. Lei, J. Bareno, J. Wen, I. Petrov, S. Kang, D. Abraham, Journal of Power Sources, 178 (2008) 422-433.

[46] J. Bareno, C. Lei, J. Wen, S. Kang, I. Petrov, D. Abraham, Advanced Materials, 22 (2010) 1122-1127.

[47] M. Gu, I. Belharouak, J. Zheng, H. Wu, J. Xiao, A. Genc, K. Amine, S. Thevuthasan, D.R. Baer, J. Zhang, ACS nano, 7 (2012) 760-767.

[48] S. Kang, M.M. Thackeray, Electrochemistry Communications, 11 (2009) 748-751.

[49] J. Yan, X. Liu, B. Li, Rsc Advances, 4 (2014) 63268-63284.

[50] A.R. Armstrong, M. Holzapfel, P. Novák, C.S. Johnson, S. Kang, M.M. Thackeray, P.G. Bruce, Journal of the American Chemical Society, 128 (2006) 8694-8698.

[51] N. Yabuuchi, K. Yoshii, S. Myung, I. Nakai, S. Komaba, Journal of the American Chemical Society, 133 (2011) 4404-4419.

[52] Z. Lu, J.R. Dahn, Journal of the Electrochemical Society, 149 (2002) A815-A822.

[53] N. Tran, L. Croguennec, M. Ménétrier, F. Weill, P. Biensan, C. Jordy, C. Delmas, Chemistry of Materials, 20 (2008) 4815-4825.

[54] J.R. Croy, D. Kim, M. Balasubramanian, K. Gallagher, S. Kang, M.M. Thackeray, Journal of the Electrochemical Society, 159 (2012) A781-A790.

[55] A.R. Armstrong, M. Holzapfel, P. Novák, C.S. Johnson, S. Kang, M.M. Thackeray, P.G. Bruce, Journal of the American Chemical Society, 128 (2006) 8694-8698.

[56] C.S. Johnson, N. Li, C. Lefief, M.M. Thackeray, Electrochemistry Communications, 9 (2007) 787-795.

[57] K. Kang, Y.S. Meng, J. Breger, C.P. Grey, G. Ceder, Science (New York, N.Y.), 311 (2006) 977-980.

[58] B.R. Long, J.R. Croy, J.S. Park, J. Wen, D.J. Miller, M.M. Thackeray, Journal of the Electrochemical Society, 161 (2014) A2160-A2167.

[59] C. Johnson, J. Kim, C. Lefief, N. Li, J. Vaughey, M. Thackeray, Electrochemistry Communications, 6 (2004) 1085-1091.

[60] C.S. Johnson, N. Li, C. Lefief, M.M. Thackeray, Electrochemistry Communications, 9 (2007) 787-795.

[61] B. Xu, C.R. Fell, M. Chi, Y.S. Meng, Energy and Environmental Science, 4 (2011) 2223-2233.

[62] M. Jiang, B. Key, Y.S. Meng, C.P. Grey, Chemistry of Materials, 21 (2009) 2733-2745.

[63] A.D. Robertson, P.G. Bruce, Electrochemical and Solid-State Letters, 7 (2004) A294-A298.

[64] Z. Lu, L. Beaulieu, R. Donaberger, C. Thomas, J. Dahn, Journal of the Electrochemical Society, 149 (2002) A778-A791.

[65] Z. Lu, J.R. Dahn, Journal of the Electrochemical Society, 149 (2002) A815-A822.

[66] Z. Lu, D. MacNeil, J. Dahn, Electrochemical and Solid-State Letters, 4 (2001) A191-A194.

[67] S. Guo, H. Yu, P. Liu, X. Liu, M. Chen, M. Ishida, H. Zhou, Journal of Materials Chemistry A, 2 (2014) 4422-4428.

[68] K. Jiang, X. Wu, Y. Yin, J. Lee, J. Kim, Y. Guo, ACS Applied Materials and Interfaces, 4 (2012) 4858-4863.

[69] Y. Wu, A.V. Murugan, A. Manthiram, Journal of the Electrochemical Society, 155 (2008) A635-A641.

[70] F. Lin, I.M. Markus, D. Nordlund, T. Weng, M.D. Asta, H.L. Xin, M.M. Doeff, Nature Communications, 5 (2014) 3529.

[71] N. Tran, L. Croguennec, M. Ménétrier, F. Weill, P. Biensan, C. Jordy, C. Delmas, Chemistry of Materials, 20 (2008) 4815-4825.

[72] J.B. Goodenough, Y. Kim, Journal of Power Sources, 196 (2011) 6688-6694.

[73] A. Ito, K. Shoda, Y. Sato, M. Hatano, H. Horie, Y. Ohsawa, Journal of Power Sources, 196 (2011) 4785-4790.

[74] Y. Zhu, Y. Li, M. Bettge, D.P. Abraham, Journal of the Electrochemical Society, 159 (2012) A2109-A2117.

[75] S. Shi, J. Tu, Y. Tang, Y. Yu, Y. Zhang, X. Wang, Journal of Power Sources, 221 (2013) 300-307.

[76] K.G. Gallagher, J.R. Croy, M. Balasubramanian, M. Bettge, D.P. Abraham, A.K. Burrell, M.M. Thackeray, Electrochemistry Communications, 33 (2013) 96-98.

[77] J. Liu, A. Manthiram, Journal of Materials Chemistry, 20 (2010) 3961-3967.

[78] Z. Deng, A. Manthiram, The Journal of Physical Chemistry C, 115 (2011) 7097-7103.

[79] J. Zheng, J. Li, Z. Zhang, X. Guo, Y. Yang, Solid State Ionics, 179 (2008) 1794-1799.

[80] G. Kim, Y.J. Park, K.H. Jung, D. Yang, J.W. Lee, H. Kim, Journal of Applied Electrochemistry, 38 (2008) 1477-1481.

[81] L. Zhou, M. Tian, Y. Deng, Q. Zheng, C. Xu, D. Lin, Ceramics International, 42 (2016) 15623-15633.

[82] E. Han, Y. Li, L. Zhu, L. Zhao, Solid State Ionics, 255 (2014) 113-119.

[83] X. Liu, T. Huang, A. Yu, Electrochimica Acta, 163 (2015) 82-92.

[84] R. Yu, Y. Lin, Z. Huang, Electrochimica Acta, 173 (2015) 515-522.

[85] J. Kong, H. Zhai, X. Qian, M. Wang, Q. Wang, A. Li, H. Li, F. Zhou, Journal of Alloys and Compounds, 694 (2017) 848-856.

[86] K. Gao, S. Zhao, S. Guo, C. Nan, Electrochimica Acta, 206 (2016) 1-9.

[87] Y. Sun, M. Lee, C.S. Yoon, J. Hassoun, K. Amine, B. Scrosati, Advanced Materials, 24 (2012) 1192-1196.

[88] S. Sun, N. Wan, Q. Wu, X. Zhang, D. Pan, Y. Bai, X. Lu, Solid State Ionics, 278 (2015) 85-90.

[89] C. Li, J. Xu, J. Xia, W. Liu, X. Xiong, Z. Zheng, Solid State Ionics, 292 (2016) 75-82.

[90] Y. Zuo, B. Huang, C. Jiao, R. Lv, G. Liang, Journal of Materials Science: Materials in Electronics, (2017) 1-11.

[91] X. Liu, J. Liu, T. Huang, A. Yu, Electrochimica Acta, 109 (2013) 52-58.

[92] C. Johnson, J. Kim, C. Lefief, N. Li, J. Vaughey, M. Thackeray, Electrochemistry Communications, 6 (2004) 1085-1091.

[93] J. Kim, C. Johnson, J. Vaughey, M. Thackeray, Journal of Power Sources, 153 (2006) 258-264.

[94] S. Kim, B. Jin, S. Lee, H. Kim, Electrochimica Acta, 171 (2015) 35-41.

[95] C.J. Jafta, K.I. Ozoemena, M.K. Mathe, W.D. Roos, Electrochimica Acta, 85 (2012) 411-422.

[96] T. Tang, H. Zhang, Electrochimica Acta, 191 (2016) 263-269.

[97] C.W. Lee, Y. Sun, J. Prakash, Electrochimica Acta, 49 (2004) 4425-4432.

[98] X. Jin, Q. Xu, H. Liu, X. Yuan, Y. Xia, Electrochimica Acta, 136 (2014) 19-26.

[99] Z. Huang, X. Li, Y. Liang, Z. He, H. Chen, Z. Wang, H. Guo, Solid State Ionics, 282 (2015) 88-94.

[100] L.F. Jiao, M. Zhang, H.T. Yuan, M. Zhao, J. Guo, W. Wang, X. Di Zhou, Y.M. Wang, Journal of Power Sources, 167 (2007) 178-184.

[101] H. Yu, H. Zhou, Journal of Materials Chemistry, 22 (2012) 15507-15510.

[102] B. Song, M.O. Lai, L. Lu, Electrochimica Acta, 80 (2012) 187-195.

[103] J. Park, J. Lim, J. Yoon, K. Park, J. Gim, J. Song, H. Park, D. Im, M. Park, D. Ahn, Dalton Transactions, 41 (2012) 3053-3059.

[104] S. Kang, H. Qin, Y. Fang, X. Li, Y. Wang, Electrochimica Acta, 144 (2014) 22-30.

[105] Y. Zhao, M. Xia, X. Hu, Z. Zhao, Y. Wang, Z. Lv, Electrochimica Acta, 174 (2015) 1167-1174.

[106] C. Lu, S. Yang, H. Wu, Y. Zhang, X. Yang, T. Liang, Electrochimica Acta, 209 (2016) 448-455.

[107] Z. He, Z. Wang, H. Chen, Z. Huang, X. Li, H. Guo, R. Wang, Journal of Power Sources, 299 (2015) 334-341.

[108] J. Zhao, Z. Wang, H. Guo, X. Li, Z. He, T. Li, Ceramics International, 41 (2015) 11396-11401.

[109] H. Li, L. Fan, Electrochimica Acta, 113 (2013) 407-411.

[110] J. Zheng, X. Wu, Y. Yang, Electrochimica Acta, 105 (2013) 200-208.

[111] S. Kang, K. Amine, Journal of Power Sources, 146 (2005) 654-657.

[112] J. Zheng, Z. Zhang, X. Wu, Z. Dong, Z. Zhu, Y. Yang, Journal of the Electrochemical Society, 155 (2008) A775-A782.

[113] J. Lim, H. Bang, K. Lee, K. Amine, Y. Sun, Journal of Power Sources, 189 (2009) 571-575.

[114] X. Guo, Y. Li, M. Zheng, J. Zheng, J. Li, Z. Gong, Y. Yang, Journal of Power Sources, 184 (2008) 414-419.

[115] S. Shi, J. Tu, Y. Tang, Y. Yu, Y. Zhang, X. Wang, C. Gu, Journal of Power Sources, 228 (2013) 14-23.

[116] J. Zheng, X. Wu, Y. Yang, Electrochimica Acta, 56 (2011) 3071-3078.

[117] S. Kang, P. Kempgens, S. Greenbaum, A. Kropf, K. Amine, M. Thackeray, Journal of Materials Chemistry, 17 (2007) 2069-2077.

[118] S.J. Jin, K.S. Park, M.H. Cho, C.H. Song, A.M. Stephan, K.S. Nahm, Solid State Ionics, 177 (2006) 105-112.

[119] S. Kang, K. Amine, Journal of Power Sources, 146 (2005) 654-657.

[120] J. Zheng, X. Wu, Y. Yang, Electrochimica Acta, 56 (2011) 3071-3078.

[121] X. Wei, S. Zhang, Z. Du, P. Yang, J. Wang, Y. Ren, Electrochimica Acta, 107 (2013) 549-554.

[122] J. Fan, G. Li, D. Luo, C. Fu, Q. Li, J. Zheng, L. Li, Electrochimica Acta, 173 (2015) 7-16.

[123] C.J. Jafta, K. Raju, M.K. Mathe, N. Manyala, K.I. Ozoemena, Journal of the Electrochemical Society, 162 (2015) A768-A773.

[124] X. Miao, Y. Yan, C. Wang, L. Cui, J. Fang, G. Yang, Journal of Power Sources, 247 (2014) 219-227.

[125] W. West, J. Soler, B. Ratnakumar, Journal of Power Sources, 204 (2012) 200-204.

[126] J. Zheng, X. Wu, Y. Yang, Electrochimica Acta, 56 (2011) 3071-3078.

[127] X. Jin, Q. Xu, X. Yuan, L. Zhou, Y. Xia, Electrochimica Acta, 114 (2013) 605-610.

[128] W. He, J. Qian, Y. Cao, X. Ai, H. Yang, RSC Advances, 2 (2012) 3423-3429.

[129] S. Shi, J. Tu, Y. Tang, X. Liu, X. Zhao, X. Wang, C. Gu, Journal of Power Sources, 241 (2013) 186-195.

[130] C.J. Jafta, K.I. Ozoemena, M.K. Mathe, W.D. Roos, Electrochimica Acta, 85 (2012) 411-422.

[131] M.Y. Son, Y.J. Hong, S.H. Choi, Y.C. Kang, Electrochimica Acta, 103 (2013) 110-118.

[132] S. Chitra, P. Kalyani, T. Mohan, R. Gangadharan, B. Yebka, S. Castro-Garcia, M. Massot, C. Julien, M. Eddrief, Journal of Electroceramics, 3 (1999) 433-441.

[133] W. Yang, G. Zhang, J. Xie, L. Yang, Q. Liu, Journal of Power Sources, 81 (1999) 412-415.

[134] K. Lee, H. Choi, J. Lee, Journal of Materials Science Letters, 20 (2001) 1309-1311.

[135] H. Li, S. Zhang, X. Wei, P. Yang, Z. Jian, J. Meng, RSC Advances, 6 (2016) 79050-79057.

[136] F.P. Nkosi, C.J. Jafta, M. Kebede, L. le Roux, M.K. Mathe, K.I. Ozoemena, RSC Advances, 5 (2015) 32256-32262.

[137] K.C. Stella, A.S. Nesaraj, Iranian Journal of Materials Science and Engineering, 7 (2010) 36-44.

[138] S. Das, A. Mukhopadhyay, S. Datta, D. Basu, Bulletin of Materials Science, 32 (2009) 1-13.

[139] E. Thostenson, T. Chou, Composites Part A: Applied Science and Manufacturing, 30 (1999) 1055-1071.

[140] M.H. Bhat, B. Chakravarthy, P. Ramakrishnan, A. Levasseur, K. Rao, Bulletin of Materials Science, 23 (2000) 461-466.

[141] P.K. Nayak, J. Grinblat, M. Levi, E. Levi, S. Kim, J.W. Choi, D. Aurbach, Advanced Energy Materials, 6 (2016).

[142] M. Iftekhar, N. Drewett, A. Armstrong, D. Hesp, F. Braga, S. Ahmed, L. Hardwick, Journal of the Electrochemical Society, 161 (2014) A2109-A2116.

[143] H. Pan, Y. Hu, L. Chen, Energy and Environmental Science, 6 (2013) 2338-2360.

[144] N. Yabuuchi, K. Kubota, M. Dahbi, S. Komaba, Chemical Reviews, 114 (2014) 11636-11682.

[145] M.D. Slater, D. Kim, E. Lee, C.S. Johnson, Advanced Functional Materials, 23 (2013) 947-958.

[146] B.L. Ellis, L.F. Nazar, Current Opinion in Solid State and Materials Science, 16 (2012) 168-177.

[147] M. Hana, E. Gonzalo, G. Singh, T. Rojo, Energy and Environmental Science, 8 (2015) 81.

[148] H. Pan, Y. Hu, L. Chen, Energy and Environmental Science, 6 (2013) 2338-2360.

[149] N. Yabuuchi, S. Komaba, Science and Technology of Advanced Materials, 15 (2014) 043501.

[150] W. Craft, Solar Energy: The Pros and the Cons. http://www.solarenergyformyhome.com/home-solar-energy/solar-energy-the-pros-and-the-cons/ (2017).

[151] S. Guo, H. Yu, P. Liu,Y. Ren,T. Zhang, M. Chen, M. Ishida, H. Zhou, Energy and Environmental Science, 8 (2015) 1237-1244.

[152] V. Palomares, P. Serras, I. Villaluenga, K.B. Hueso, J. Carretero-González, T. Rojo, Energy and Environmental Science, 5 (2012) 5884-5901.

[153] D. Kim, E. Lee, M. Slater, W. Lu, S. Rood, C.S. Johnson, Electrochemistry Communications, 18 (2012) 66-69.

[154] L.P. Wang, L. Yu, X. Wang, M. Srinivasan, Z.J. Xu, Journal of Materials Chemistry A, 3 (2015) 9353-9378.

[155] H. Lee, R.Y. Wang, M. Pasta, S.W. Lee, N. Liu, Y. Cui, Nature Communications, 5 (2014) 6280.

[156] Y. Lu, L. Wang, J. Cheng, J.B. Goodenough, Chemical Communications, 48 (2012) 6544-6546.

[157] Y. You, X. Wu, Y. Yin, Y. Guo, Energy and Environmental Science, 7 (2014) 1643-1647.

[158] L. Wang, Y. Lu, J. Liu, M. Xu, J. Cheng, D. Zhang, J.B. Goodenough, Angewandte Chemie International Edition, 52 (2013) 1964-1967.

[159] H. Lee, Y. Kim, J. Park, J.W. Choi, Chemical Communications, 48 (2012) 8416-8418.

[160] W. Li. PhD, University of Wollongong,(2015).

[161] K. Saravanan, C.W. Mason, A. Rudola, K.H. Wong, P. Balaya, Advanced Energy Materials, 3 (2013) 444-450.

[162] B. Ellis, W. Makahnouk, Y. Makimura, K. Toghill, L. Nazar, Nature materials, 6 (2007) 749.

[163] A. Mendiboure, C. Delmas, P. Hagenmuller, Journal of Solid State Chemistry, 57 (1985) 323-331.

[164] L.P. Wang, L. Yu, X. Wang, M. Srinivasan, Z.J. Xu, Journal of Materials Chemistry A, 3 (2015) 9353-9378.

[165] R. Berthelot, D. Carlier, C. Delmas, Nature Materials, 10 (2011) 74.

[166] M. Guignard, C. Didier, J. Darriet, P. Bordet, E. Elkaïm, C. Delmas, Nature Materials, 12 (2013) 74.

[167] R.J. Clément, P.G. Bruce, C.P. Grey, Journal of the Electrochemical Society, 162 (2015) A2589-A2604.

[168] X. Wu, J. Guo, D. Wang, G. Zhong, M.J. McDonald, Y. Yang, Journal of Power Sources, 281 (2015) 18-26.

[169] R. Shanmugam, W. Lai, Journal of the Electrochemical Society, 162 (2015) A8-A14.

[170] K. Kubota, S. Komaba, Journal of the Electrochemical Society, 162 (2015) A2538-A2550.

[171] J. Zheng, P. Yan, W.H. Kan, C. Wang, A. Manthiram, Journal of the Electrochemical Society, 163 (2016) A584-A591.

[172] J. Kim, G. Amatucci, Journal of the Electrochemical Society, 163 (2016) A696-A705.

[173] G. Venkatesh, B. Kishore, R. Viswanatha, D. Aurbach, N. Munichandraiah, Journal of the Electrochemical Society, 164 (2017) A2176-A2182.

[174] N. Nguyen, K. Kim, K.H. Choi, H. Jeon, K. Lee, M. Ryou, Y.M. Lee, Journal of the Electrochemical Society, 164 (2017) A6308-A6314.

[175] C. Ma, J. Alvarado, J. Xu, R.J. Clément, M. Kodur, W. Tong, C.P. Grey, Y.S. Meng, Journal of the American Chemical Society, 139 (2017) 4835-4845.

[176] W. Pang, X. Zhang, J. Guo, J. Li, X. Yan, B. Hou, H. Guan, X. Wu, Journal of Power Sources, 356 (2017) 80-88.

[177] H. Wang, B. Yang, X. Liao, J. Xu, D. Yang, Y. He, Z. Ma, Electrochimica Acta, 113 (2013) 200-204.

[178] N. Yabuuchi, M. Kajiyama, J. Iwatate, H. Nishikawa, S. Hitomi, R. Okuyama, R. Usui, Y. Yamada, S. Komaba, Nature Materials, 11 (2012) 512-517.

[179] S. Kim, D. Seo, X. Ma, G. Ceder, K. Kang, Advanced Energy Materials, 2 (2012) 710-721.

[180] J. Billaud, G. Singh, A.R. Armstrong, E. Gonzalo, V. Roddatis, M. Armand, T. Rojo, P.G. Bruce, Energy and Environmental Science, 7 (2014) 1387-1391.

[181] N. Yabuuchi, R. Hara, K. Kubota, J. Paulsen, S. Kumakura, S. Komaba, Journal of Materials Chemistry A, 2 (2014) 16851-16855.

[182] N. Ortiz-Vitoriano, N.E. Drewett, E. Gonzalo, T. Rojo, Energy and Environmental Science, 10 (2017) 1051-1074.

[183] U. Maitra, R.A. House, J.W. Somerville, N. Tapia-Ruiz, J.G. Lozano, N. Guerrini, R. Hao, K. Luo, L. Jin, M.A. Pérez-Osorio, Nature Chemistry, (2018).

[184] X. Xu, S. Ji, R. Gao, J. Liu, RSC Advances, 5 (2015) 51454-51460.

[185] C.J. Jafta, K. Raju, M.K. Mathe, N. Manyala, K.I. Ozoemena, Journal of the Electrochemical Society, 162 (2015) A768-A773.

[186] M. Itagaki, N. Kobari, S. Yotsuda, K. Watanabe, S. Kinoshita, M. Ue, Journal of Power Sources, 135 (2004) 255-261.

[187] M. Itagaki, S. Yotsuda, N. Kobari, K. Watanabe, S. Kinoshita, M. Ue, Electrochimica Acta, 51 (2006) 1629-1635.

[188] Ozan Toprakci. PhD,North Carolina State University, (2012).

[189] D. Song, H. Ikuta, T. Uchida, M. Wakihara, Solid State Ionics, 117 (1999) 151-156.

[190] J. Song, H. Lee, Y. Wang, C. Wan, Journal of Power Sources, 111 (2002) 255-267.

[191] J. Wang, Analytical Electrochemistry, John Wiley and Sons 2006.

[192] Pillay Jeseelan. PhD,University of Pretoria,(2009).

[193] T.J. Patey, PhD, ETH Zurich, (2009).

CHAPTER 3

Experimental Method

3.1 Introduction

This chapter discusses the experimental and characterization techniques used in this thesis. This chapter outlines the chemicals and materials used for the preparation of cathode materials and fabrication of coin cells, the methods for synthesis of the cathode materials and discusses the characterization techniques used in studying the properties of the materials and their performance in the coin cells.

3.2 Chemicals and Materials

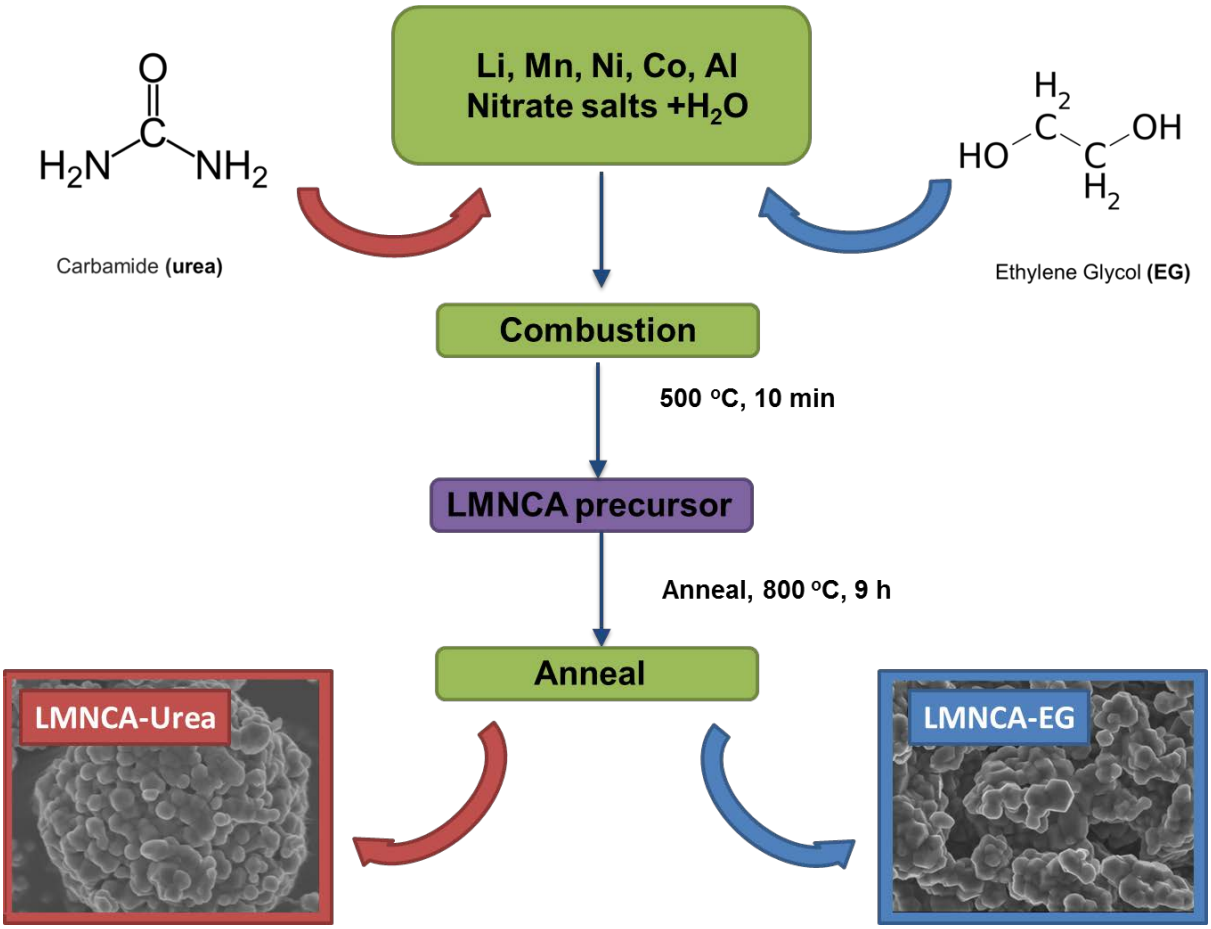
Table 3.1 shows all the chemicals and materials used in this thesis work. All chemicals were used without further purification.

3.3 Synthesis Procedures

3.3.1 Combustion synthesis of LMNCA powders using urea and ethylene glycol fuels

Combustion synthesis method was used to prepare the composite layered-layered LMNCA samples. Stoichiometric amounts of lithium nitrate (10 % excess lithium), manganese (II) nitrate tetrahydrate, nickel (II) nitrate hexahydrate, cobaltous nitrate hexahydrate and aluminum nitrate nonahydrate were dissolved completely in de-ionized water along with the appropriate quantity of urea or EG as fuels. The molar ratio of Li:fuel was 1:3. The mixture was stirred for 1 h using a magnetic stirrer at room temperature. The resultant solution was transferred into a crucible and introduced into a muffle furnace maintained at 500 ℃. In the muffle furnace, the solution initially boils and dehydrates, followed by the decomposition with evolution of gases. Then it burns to incandescence to form a foamy homogeneous residue. The combustion reaction was completed within 10 minutes. The residue was cooled to room temperature and ground into a fine powder before subjected to further heat treatment at 800 ℃ for 9 h in air. The powder is further annealed to complete the crystallisation of the material and

to get a pure powder by decomposing unreacted organic residues and carbon deposits. The schematic representation of the preparation of the LMNCA powders is shown in Scheme 3.1. The sample synthesized using urea as a fuel, will be referred to as LMNCA-urea sample and the sample synthesized using EG as a fuel will be referred to as LMNCA-EG sample.



Scheme 3.1: Combustion synthesis of LMNCA using EG and urea as a fuels.

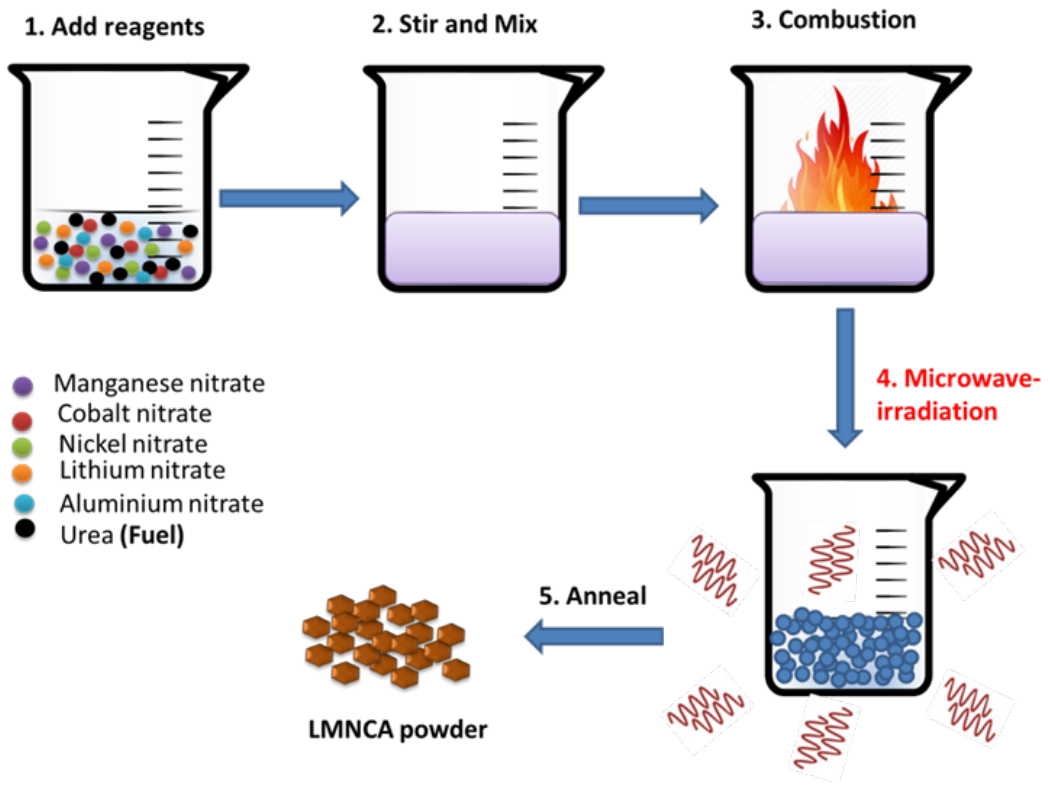
Table 3.1: List of materials and reagents used in this thesis.

Reagents and materials	Purity and specifications	Supplier
Acetone $(CH_3)_2CO$	≥ 99.5 %	Sigma Aldrich
Aluminum nitrate nonahydrate $(Al(NO_3)_3 \cdot 9H_2O)$	≥ 98 %	Fluka Analytical
Aluminum foil	50 μm thick	MTI corporation USA
Ammonium fluoride (NH_4F)	≥ 98 %	Sigma Aldrich
Carbon Black	Control number: 030520	PRINTEX XE-2-B
Microfiber filter paper	Grade. GF/A	Whatman
Cobaltous nitrate hexahydrate $Co(NO_3)_2 \cdot 6H_2O$	≥ 98 %	Associated Chemical Enterprises (ACE)
Diethyl carbonate (DEC) $OC(OCH_2CH_3)_2$	≥ 99 %	Sigma Aldrich
Dimethyl carbonate (DMC) $OC(OCH_3)_2$	≥ 99 %	Sigma Aldrich
Ethylene carbonate (EC) $(CH_2O)_2CO$	99 %	Sigma Aldrich
Ethylene glycol $(CH_2OH)_2$	≥ 99 %	Sigma Aldrich
Lithium nitrate ($LiNO_3$)	≥ 99 %	Sigma Aldrich
Lithium hexafluorophosphate ($LiPF_6$)	99.99 %	Sigma Aldrich
Manganese (II) nitrate tetrahydrate $(Mn(NO_3)_2 \cdot 4H_2O)$	≥ 97 %	Sigma Aldrich
Manganese sulphate monohydrate $(MnSO_4.H_2O)$	≥ 99 %	Sigma Aldrich
Manganese (II,III) oxide (Mn_3O_4)	97 %	Sigma Aldrich
Magnesium oxide (MgO)	≥ 97 %	Sigma Aldrich
Nickel (II) nitrate hexahydrate $(Ni(NO_3)_2 \cdot 6H_2O)$	≥ 98.5 %	Sigma Aldrich
N-methyl-2-pyyolidone (NMP)	99.5 %	Sigma Aldrich
Polycarbonate (PC)	≥ 99 %	Sigma Aldrich
Potassium nitrate (KNO_3)	>99 %	Sigma Aldrich

Polyvinylidene fluoride (PVDF)	≥ 99.5 %	MTI Corp
Pluronic acid (PA)	Pluronic F-127	Sigma Aldrich
Sodium carbonate (Na_2CO_3)	99.95 %	Sigma Aldrich
Sodium nitrate ($NaNO_3$)	97 %	Sigma Aldrich
Sodium perchlorate ($NaClO_4$)	98 %	Sigma Aldrich
Urea ($CO(NH_2)_2$)	≥ 99 %	Merck

3.3.2 Microwave irradiation of LMNCA prepared using urea and ethylene glycol combustion synthesis.

Stoichiometric amounts of lithium nitrate (10 % excess lithium), manganese (II) nitrate tetrahydrate, nickel (II) nitrate hexahydrate, cobaltous nitrate hexahydrate, aluminum nitrate nonahydrate and ethylene glycol were dissolved completely in de-ionized water. The mixture was stirred for 1 h using a magnetic stirrer at room temperature. The resultant solution was put into a crucible and combusted at 500 ℃ for 10 min using a muffle furnace. Then the resultant powders were allowed to cool to room temperature. The powders were then ground into a fine powder and were subjected to microwave irradiation (Anton Paar Multiwave 3000 system, λ = 0.12236 m) at 600 W for 20 min before annealing at 800 ℃ for 9 h in air. The schematic representation of the preparation of the LMNCA powders is shown in Scheme 3.2. Similar synthesis procedure was used for the urea combustion synthesis where urea instead of EG was used as a fuel. Urea is a common fuel used for combustion synthesis of electrode materials.



Scheme 3.2: Hybrid microwave irradiation-combustion synthesis of LMNCA powders.

3.3.3 Preparation of LMNCA from α-MnO_2 nanowires

3.3.3.1 Preparation of α-MnO_2 nanowires

Stoichiometric amounts of manganese sulphate monohydrate, lithium nitrate, sodium nitrate and potassium nitrate were mixed by grinding using a pestle and mortar until mixed well. The mixture was heated at 380 ℃ for 3 h in air using a muffle furnace. The resultant precursor was cooled naturally before washing several times with de-ionized water. Then it was dried in the oven 80 ℃ overnight.

3.3.3.2 Preparation of $Li[Li_{0.2}Ni_{0.13}Mn_{0.52}Co_{0.13}Al_{0.02}]$ composite

Stoichiometric amounts of MnO_2 nanomaterials, nickel (II) nitrate hexahydrate, cobaltous nitrate hexahydrate and aluminum nitrate nonahydrate were dispersed in de-ionized water. Then the Pluronic Acid (PA) was added to the mixture and stirred for 3 h using a magnetic stirrer at room temperature. The resultant solution mixture was dried in vacuum at 120 ℃ for 8 h using a vacuum oven. The dried powder was lithiated using lithium nitrate (10 % excess lithium) before annealing at 800 ℃ for 9 h.

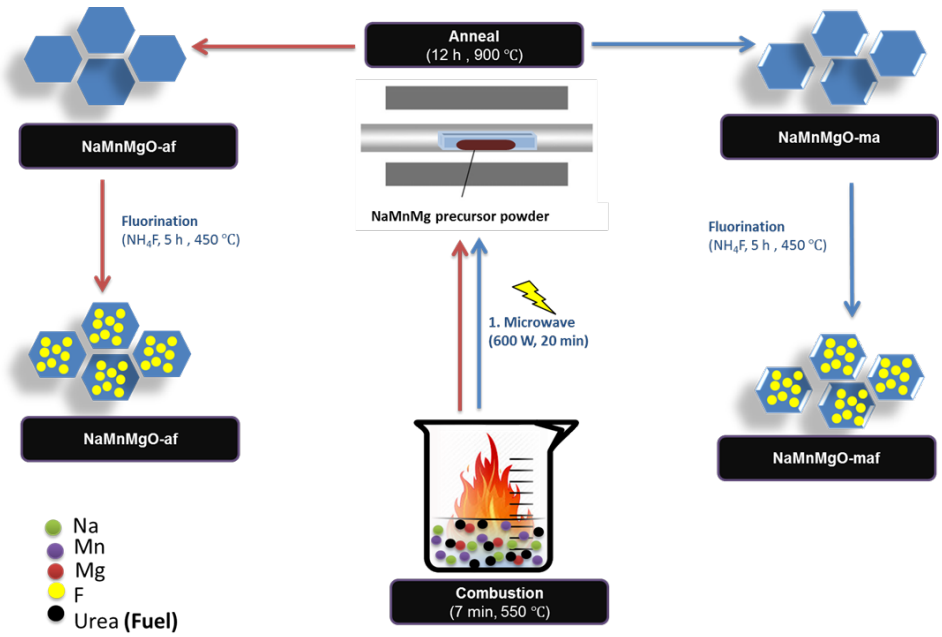
3.3.4 Preparation of NaMgMnO cathode materials

3.3.4.1 Combustion synthesis of NaMgMnO cathode materials and microwave irradiation

Stoichiometric amounts of sodium carbonate, manganese (II, III) oxide and magnesium oxide were thoroughly mixed using ball milling for 12 h under wet conditions with acetone. The mixture was then properly ground using pestle and mortar and dried in air for 30 min. The resultant mixture was mixed with the appropriate amount of urea, ground and dispersed in de-ionized water, ignited at 500 ^{o}C in air for ca. 10 min and then left to cool naturally at room temperature. The resultant product was ground into a very fine precursor powder, which was then divided into two batches. One batch was directly annealed at 900 ^{o}C for 12 h (abbreviated herein as NaMgMnO-a) while the other was first subjected to microwave irradiation (Anton Paar Multiwave 3000 system, $\lambda = 0.12236$ m) for 10 min at 600 W before annealing at 900 ^{o}C for 12 h (product abbreviated herein as NaMgMnO-ma).

3.3.4.2 Fluorination of NaMgMnO cathode materials

Portions of each of the NaMgMnO-a and NaMgMnO-ma prepared above were fluorinated by calcining the powders with the required amount of NH_4F at 450 ^{o}C for 5 h, and the resultant products abbreviated herein as NaMgMnO-af and NaMgMnO-maf, respectively. The general scheme for the synthesis is given in Scheme 3.3.



Scheme 3.3: Schematic representation of NaMgMnO samples including fluorination and microwave irradiation treatments.

3.4 Materials Characterization

The prepared samples were characterized using the following techniques: Powder X-ray Diffraction (PXRD), Scanning Electron Microscopy (SEM), Electron Dispersive X-ray Spectroscopy (EDX), Transmission Electron Microscopy (TEM), X-ray Photoelectron spectroscopy (XPS), Raman Spectroscopy (RS), Brunauer Emmett Teller surface area and these techniques are discussed briefly below. All the measurements were taken at room temperature.

3.4.1 Powder x-ray diffraction

X-ray diffraction (PXRD) is an analytical technique used to determine and identify the phase(s) and structure type of crystalline materials. The Rietveld refinement of the PXRD data provides information about the lattice parameters, d-spacing, and crystal density. A PANalytical X'Pert Pro diffractometer with CuKα radiation (λ=1.5046 Å, 45 kV, 40 mA, step size = 0.02°) was used. The XRD diffractograms were obtained in a scan range between 0 and 90°. The lattice parameters and crystal information were obtained by Rietveld refinement using a Topas software.

3.4.2 Scanning electron microscopy and Energy dispersive x-ray spectroscopy

The scanning electron microscope (SEM) is a form of an electron microscope that images the sample by scanning it with a focused high-energy electron beam in a raster scan pattern. This technique can be used to determine the morphology, particle size, and shape of the sample particles. The prepared samples were examined using the field emission scanning electron microscope (FE-SEM) (JSM-7500F, JEOL) with the acceleration voltage of 2.00 kV. The samples were coated with carbon during sample preparation to prevent charging.

Energy Dispersive X-ray Spectroscopy (EDX) is used for the elemental analysis of the sample. A SEM/EDX combined equipment was used for the analysis of the sample.

3.4.3 Transmission electron microscopy

The transmission electron microscope (TEM) is a type of electron microscope used for directly imaging materials in the nanometer range with maximum thickness of sample of 10 nm. TEM is also used to determine the morphology and particle size of the materials. Additionally, high resolution TEM is used to determine crystallinity and calculate d-spacings from lattice fringes.

A drop of sample particles dispersed in ethanol was spread on a carbon copper grid (200 meshes) and then allowed to dry at room temperature before the analysis. TEM analyses of the samples were carried out on a Joel HRJEM-2100 microscope using LaB6 filament as an electron source with the electron beam at 200 kV.

3.4.4 X-ray photoelectron spectroscopy

X-ray photoelectron spectroscopy (XPS) is a quantitative surface technique used to measure elemental composition and oxidation states of elements present in the sample. XPS measurements were carried out using the Thermo ESCA lab 250Xi with monochromatic Al Kα radiation (1486.7 eV). X-ray power of 300 W and X-ray spot size 900 μm were used. The binding energy was calibrated with reference to the C 1s level of the carbon (284.6 eV).

3.4.5 Raman spectroscopy

Raman spectroscopy is a fast and non-destructive spectroscopy technique based on the inelastic scattering of light (laser) by materials. The Raman spectra were acquired using a Horiba LabRAM HR Raman spectrometer with an Olympus BX41 microscope attachment. The excitation wavelength was the 514.5 nm line and the beam power at the sample was 0.4 mW. Raman spectra were measured up to 1000 cm^{-1} on the stokes side, with a spectral resolution of about 3 cm^{-1}.

3.4.6 Brunauer- Emmett-Teller (BET) surface area

Brunauer- Emmett-Teller (BET) surface area is used to determine the surface area and porosity of the materials. The surface area of the materials was determined using a Micromeritics Tristar 3000 surface area and porosity analyzer. The N_2 adsorption–desorption experiments were conducted at -195 ℃. Prior to the experiment, the sample was outgassed at 150 ℃ for 4 h under nitrogen gas. The BET surface areas were obtained from the adsorption data in a relative pressure range from 0.05 to 0.30.

3.5 Coin cells

3.5.1 Electrode fabrication for lithium-ion and sodium-ion batteries

The cathodes for sodium-ion and lithium-ion cells were prepared using the same procedure. The cathodes were prepared by the making up of slurry containing 80 % active material (prepared sample), 10 % carbon black and 10 % polyvinylidene fluoride (PVDF) binder in N-methyl-2-pyrrolidone (NMP) solvent. The slurry is stirred overnight to perfectly mix the

contents. The slurry was coated onto an aluminum current collector using a doctor-blade method. The coated aluminum foil was then dried under vacuum at 110 ^{o}C for 12 h, before being pressed to form a uniform layer and cut into circular disk electrodes. The electrodes were heated at 80 ^{o}C for at least 6 h before put into the glove box.

3.5.2 Fabrication of coin cells

The electrochemical performance of the prepared materials was evaluated using a two-electrode coin-type cell. The coin cells consist of the prepared powders as cathode, lithium foil as an anode and the electrolyte. The coin cells also contain a spacer which provides an electrical connection from the electrode to the case and a spring to allow maximum contact of the cathode and anode when the coin cell is sealed. A 1 M $LiPF_6$ in EC/DEC/DMC in 1:1:1 volume ratio solution was used as the electrolyte and a micro-porous polypropylene Celgard 2400 was used as a separator. The electrolyte was put on the separator, between the cathode and the anode. The cells were fabricated in a glove box with ultra-high purity argon gas (MBRAUN MB10 compact). The concentration of H_2O and O_2 was maintained at < 0.5 ppm because lithium and sodium metal are highly reactive and react rapidly with water, and also the electrolyte is affected by water. Figure 3.1 shows the components of the coin-cells and the coin cells before electrochemical characterization. The sodium-ion coin cells were fabricated in the same way as the lithium-ion coin cells, except that the anode is sodium metal, a 1 M $NaClO_4$ in Polycarbonate (PC) is used as an electrolyte and a Whatman microfiber filter paper is used as a separator. The coin cells were sealed with a Compact Hydraulic Crimping Machine (MSK-110). The pressure on the crimper was set at 750 psi to seal the coin cells. The coin cells were allowed to stand for 24 h before performing the electrochemical measurements.

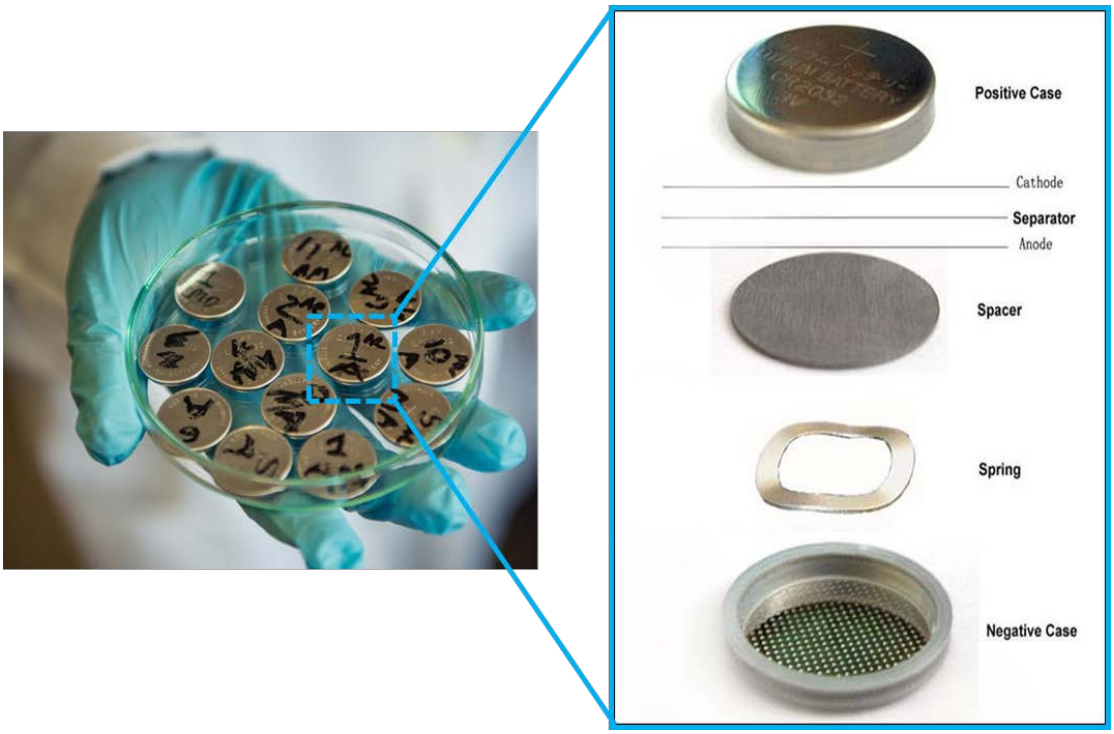


Figure 3.1: Components of a coin cells and coin cells fabricated from the prepared cathode materials.

3.5.1 Characterization of coin cells

All of the electrochemical performance measurements were carried out at room temperature.

3.5.1.1 Cyclic voltammetry

Cyclic voltammetry (CV) was conducted using the coin cell wherein the prepared cathode samples were used as the working electrode and lithium/sodium metal was used as the counter and reference electrodes. The CV was measured using a Bio-Logic Science VMP3-based instrument. CV scans were recorded at a scan rate of 0.1 mV s^{-1} between 2.0 and 4.8 V (vs. Li^+/Li) for the LMNCA cathodes and 1.5 to 4.4 V (vs. Na^+/Na) for NaMgMnO cathodes.

3.5.1.2 Galvanostatic charge-discharge measurements

Galvanostatic charge-discharge measurements were carried using a Maccor 4000 battery tester. The charge-discharge measurements were recorded at 0.1 C between between 2.0 and 4.8 V (vs. Li^+/Li) for the LMNCA cathodes and 1.5 to 4.4 V (vs. Na^+/Na) for NaMgMnO cathodes.

The rate capability was measured at different C-rates (charge-discharge rates) also using a Maccor 4000 battery tester. The different C-rates are 0.1 C, 0.5 C, 1 C, 2 C, 3 C and 5 C.

3.5.1.3 Electrochemical impendence spectroscopy

Electrochemical impedance spectroscopy (EIS) studies were carried out using a Bio-Logic Science VMP3-based instrument. The EIS measurements were performed in the range from 100 kHz to 1 MHz with an AC signal amplitude of 10 mV. The data acquisition and analysis were done using the EC-lab V10.32 software.

CHAPTER 4

Investigating the effect of combustion fuel on the synthesis of lithium manganese rich – transition metal oxides: Comparative studies of structure and electrochemistry

4.1 Introduction

Intensive efforts have been made in the development of lithium-manganese-rich nickel-manganese-cobalt oxides (LMR-NMC) as cathode materials for lithium-ion batteries. This is because these materials deliver a high reversible capacity of ca. 250 mAh/g when charged to > 4.4 V vs. Li^+/ Li, they have high energy density (above 900 Wh/kg), high operating potential (> 3.5 V vs. Li^+/Li), low cost and better thermal stability compared to commercial $LiCoO_2$ cathode material [1-12]. These remarkable characteristics make LMR-NMCs attractive for application in electric vehicles. However, these cathode materials are faced with various problems such as poor rate capability, voltage fade, low first cycle efficiency (< 80 %), capacity fade and transition-metal ion solubility [1,9,13-17]. Many of these short comings are related to the synthesis method. The synthesis method and conditions impact the stoichiometry, crystal structure, and morphology which in turn have an effect on the electrochemical performance [18-21]. Therefore, it is important to understand how the synthesis routes affect the electrochemical properties of these materials. This could lead to solving the problems inhibiting the performance of these materials.

Combustion synthesis is an alternative method for preparing pure crystalline electrode materials at low external temperatures in a short time [22,23]. Unlike methods such as sol-gel and co-precipitation, the combustion method does not have long stirring, washing and drying steps. These methods are also accompanied by the loss of nickel and manganese ions during filtering and washing [24]. Combustion method is also desirable compared to high temperature

solid state methods because it requires lower temperatures (< 500 ℃) and shorter reaction times (<10 min) [23,25]. Combustion method involves a highly exothermic reaction between oxidizers (such as metal nitrates) and fuel as a reducing reagent [26]. This exothermic reaction is accompanied by the rapid evolution of gases, which is useful in controlling the increase in flame temperature (> 1000 ℃) to avoid local sintering among the crystallites [27]. The exothermic heat (flame) produced determines the powder properties of the sample and is influenced by the fuel used for the combustion synthesis [27].

In this work we investigate the effect of the fuel (urea and ethylene glycol) in the combustion synthesis of $Li_{1.2}Mn_{0.52}Co_{0.13}Ni_{0.13}Al_{0.02}O_2$ (LMNCA). Doping with aluminium in LMR-NMC is employed to improve the structural stability and rate capability performance. Urea, also known as a carbamide, reacts rapidly with the nitrate reagents often used in the combustion synthesis but it is a weak complexing agent and thus results in poor gel stability. Ethylene glycol (EG), a dihydroxyl alcohol, is a controllable oxidant for combustion, a good complexing agent and thus forms a stable gel. The gel stability is one of the important parameters of the combustion synthesis and has an effect in the flame temperature. The effect of urea and EG fuels in the electrochemical performance of LMNCA is also investigated and discussed in this work. The experimental procedure is outlined in Chapter 3 Section 3.3.1 of this thesis.

4.2 Results and Discussions

4.2.1 Powder X-ray Diffraction Characterization

The effect of the different fuels on the structure of the samples was investigated using X-ray analysis. Figure 4.1 shows the X-ray diffraction pattern of the samples. The diffraction peaks of the samples were indexed to a hexagonal structure with the space group $R\bar{3}m$ corresponding to the $LiMO_2$ major phase (M =Ni, Mn, Co, Al) and to a monoclinic structure with the space group (C_2/m) corresponding to the Li_2MnO_3 minor phase [8,16,28,29]. Therefore both samples show the formation of a ‘layered-layered’ composite. The samples are pure as there are no peaks from any impurities (such as NiO, CoO or Al_2O_3) observed. The samples are both of good crystalline quality as they produce narrow peaks and there is clear splitting of the (006)/(012) and (108)/(110) doublet peaks.

The increase in the intensity of the peak between 2 Theta = 20-25° (shown in the insert) is due to the superlattice structure of Li_2MnO_3 in LMNCA-EG compared to LMNCA-urea indicates a more stable Li_2MnO_3 phase.

The peak intensity ratio of $I_{(003)}/I_{(104)}$ for the samples, listed in Table 4.1, was calculated to determine the cation mixing in the $LiMO_2$ layer. Cation mixing causes the deterioration of the electrochemical performance in the LMR-NMC material and it is small and negligible when the $I_{(003)}/I_{(104)}$ value is >1.2. LMNCA-EG has a larger $I_{(003)}/I_{(104)}$ value of 1.4705 compared to LMNCA-Urea at 1.3669, suggesting that EG is beneficial for reducing cation mixing compared to urea.

The lattice parameters *a* and *c* were determined by Rietveld refinement and are reported in Table 4.1. The lattice parameters are comparable to those reported in literature for lithium manganese rich- transition metal oxides [30,31]. The lattice parameter *a* represents the metal to metal distance while the *c* parameter represents the inter-slab distance. The high *c* lattice parameter and axis ratio *c/a* values for LMNCA-urea suggests faster lithium ion diffusion compared to LMNCA-EG. A high axis ratio *c/a* value indicates better hexagonal ordering and high *c*-lattice parameter decreases the activation of lithium-ion hoping; and that allows for fast lithium intercalation and de-intercalation [32].

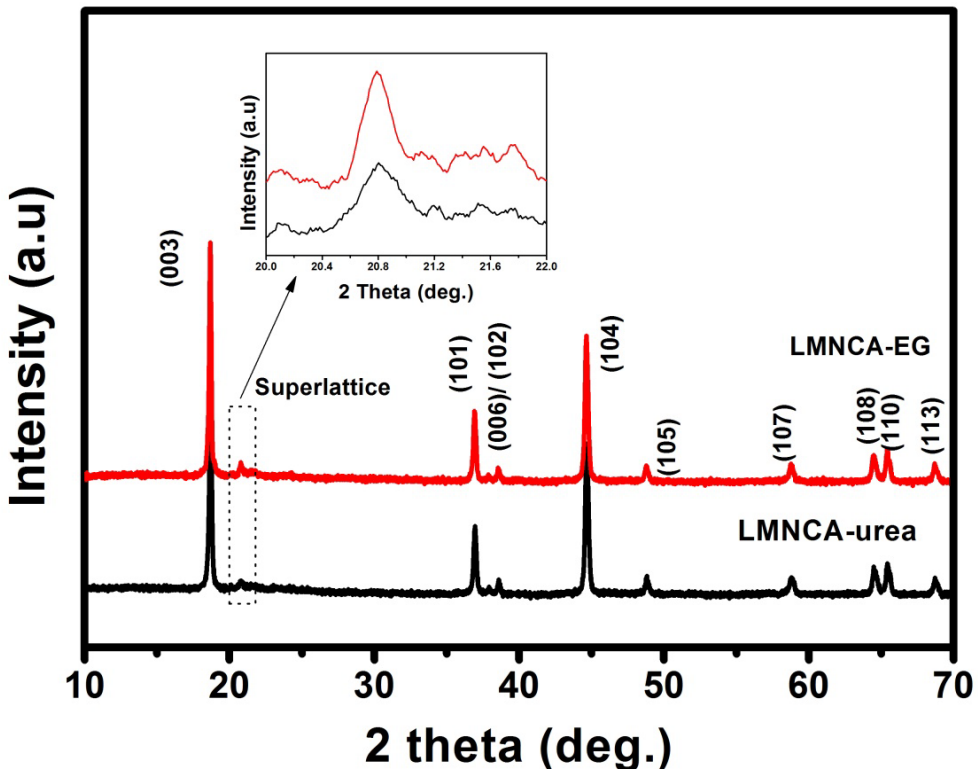


Figure 4.1: PXRD pattern of LMNCA-urea and LMNCA-EG samples.

Table 4.1: Summary of crystallographic parameters

Materials	Lattice parameter ±0.003 (Å)	Axis ratio *(c/a)*	$I_{(003)}/I_{(104)}$ ratio	Cell volume ±0.002 ($Å^3$)	Crystal density ±0.002 (g cm^{-3})	R_p (%)	R_{wp} (%)	R_{bragg} (%)
LMNCA-EG	***a***-2.860 ***c***-14.227	4.97	1.4705	100.780	482.253	1.91	2.47	1.323
LMNCA-urea	***a***-2.852 ***c***-14.239	4.99	1.3669	100.304	231.555	1.97	2.58	1.529

4.2.2 X-ray Photoelectron Spectroscopy Characterization (XPS)

X-ray photoelectron spectroscopy (XPS) of the samples is shown in Figure 4.2 (a-c) and was done to investigate the oxidation states of the manganese ions. Figure 4.2 (a) shows the Mn 3s spectra of the samples. The Mn 3s spectra give two intense peaks at about 84 and 88 eV and their energy separation (ΔE_{3s}) is ~ 4.4 eV. This suggests that the majority of the manganese ions are in the Mn^{4+} oxidation state for both samples [29,33]. Figure 4.2 (b,c) shows the Mn $2p_{3/2}$ spectra of the samples. The broad nature of the Mn $2p_{3/2}$ peak suggests the existence of more than one manganese oxidation state. The Mn $2p_{3/2}$ peak was deconvoluted into the Mn^{3+} and Mn^{4+} states and their distributions are reported in Table 4.2. The binding energies of the Mn^{4+} and Mn^{3+} ions are consistent with the literature [29,33,34]. The XPS results reveal

The average oxidation state of manganese ions (V_{Mn}) in both samples was calculated from the following linear equation (Equation 4.1) between V_{Mn} and ΔE_{3s} [35,36].

$$V_{Mn} = 7.875 - 0.893\Delta E_{3s} \quad (4.1)$$

Table 4.2: XPS analysis of LMNCA-urea and LMNCA-EG samples

Sample	Binding energy position (eV)		Cation distribution			Average oxidation state of Mn
	Mn^{4+}	Mn^{3+}	Mn^{4+} (%)	Mn^{3+} (%)	Mn^{3+}/Mn^{4+}	
LMNCA-urea	643.0	641.9	79	21	0.26	3.95
LMNCA-EG	643.1	641.9	77	23	0.29	3.95

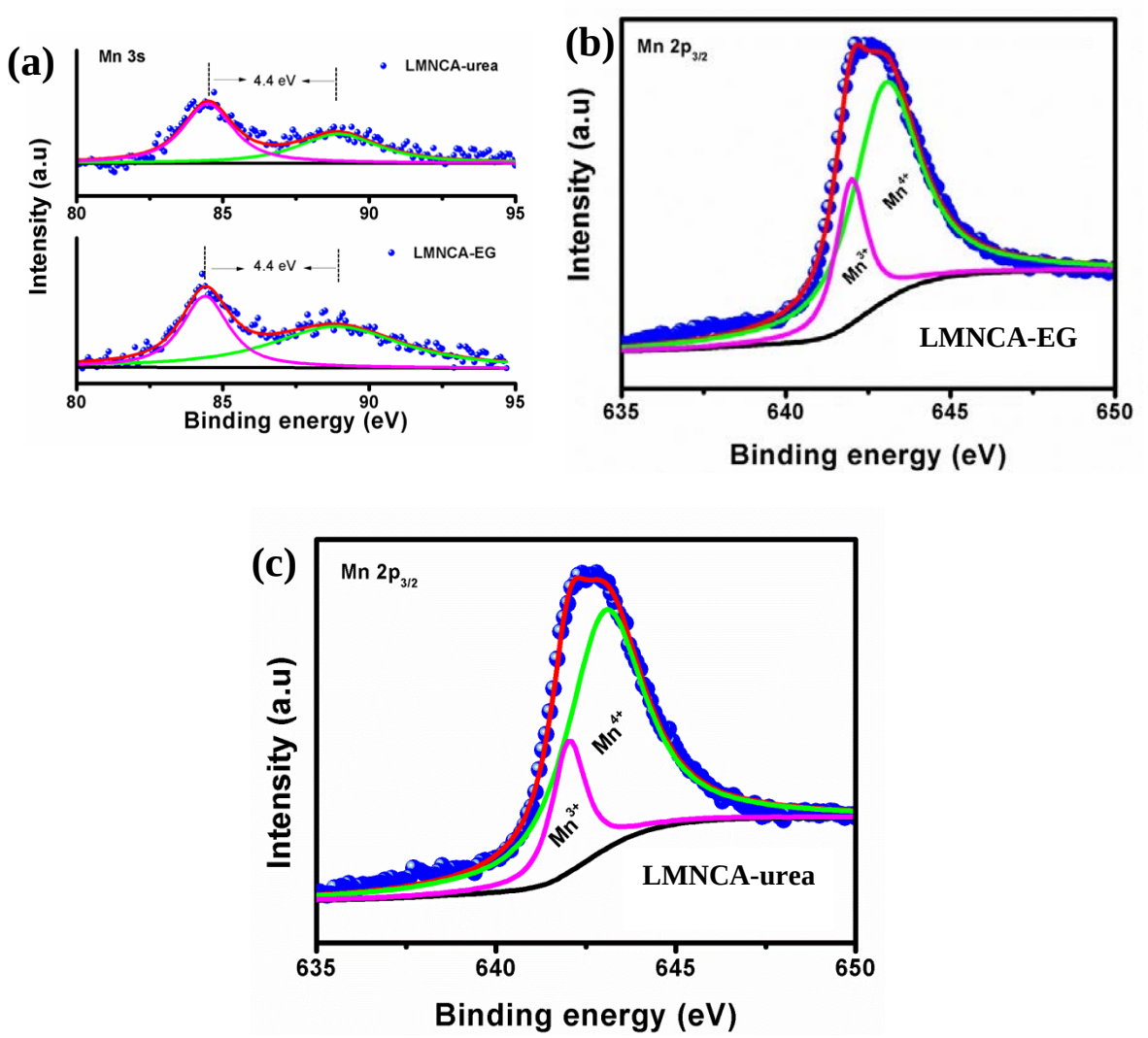


Figure 4.2: XPS of LMNCA powders prepared from urea and EG combustion methods.

4.2.3 Raman Spectroscopy Characterization

Furthermore, Raman analysis shown in Figure 4.3 was performed to investigate the effect of the fuels in the local structure of the samples [9]. The assignment of the observed Raman bands is summarized in Table 4.3 and these results are consistent with previously reported Raman spectra of LMR-NMC material [9]. The Raman peaks of the LMNCA-EG sample are slightly shifted to higher wavenumbers compared to the LMNCA-urea sample. The peak shift to higher wavenumbers suggests an increase in the bond strength for the Li_2MnO_3 phase for LMNCA-EG compared to LMNCA-urea.

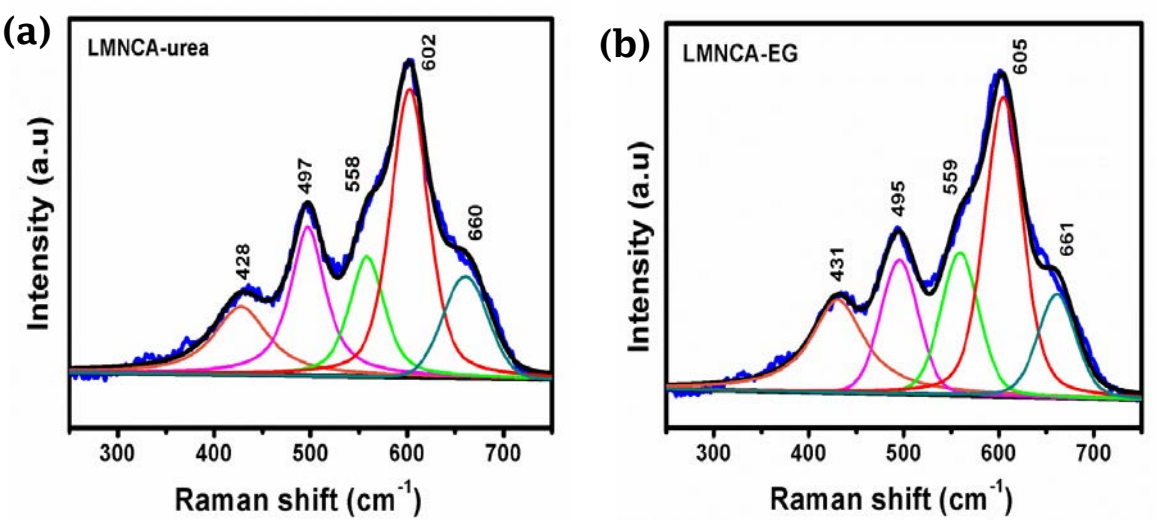


Figure 4.3: Raman analysis of LMNCA-urea and LMNCA-EG samples.

Table 4.3: Raman analysis of LMNCA materials synthesis by urea and EG combustion

Peak position (cm^{-1}) -Urea-	Peak position (cm^{-1}) -EG-	Assignment	Symmetry
428	431	B_g, A_g	Li_2MnO_3
497	495	E_g, M-O bend	$LiMO_2$
558	559	B_g, A_g	Li_2MnO_3
602	605	$A1_g$, M-O stretch	$LiMO_2$
660	661	Mn-O	Spinel-like

4.2.4 Scanning Electron Microscopy Characterization (SEM)

FE-SEM analysis (Figure 4.4) was carried out to study the effect of the fuels on the morphology of the LMNCA samples. LMNCA-urea exhibits octahedral shaped particles with particle size distribution between 50-90 nm (shown in inset of Figure 4.4 (c)) and average size is 56 nm. LMNCA-EG exhibit hexagonal shaped particles with particle size between 80-200 nm (shown in inset of Figure 4.4 (a)) and average size 102 nm. Particle size distribution was also calculated and the LMNCA-urea exhibit a narrow particle size distribution compared to the LMNCA-EG. These results are due to different flame properties and gas evolution processes for urea and EG, which impacts the particle size, surface area and morphology.

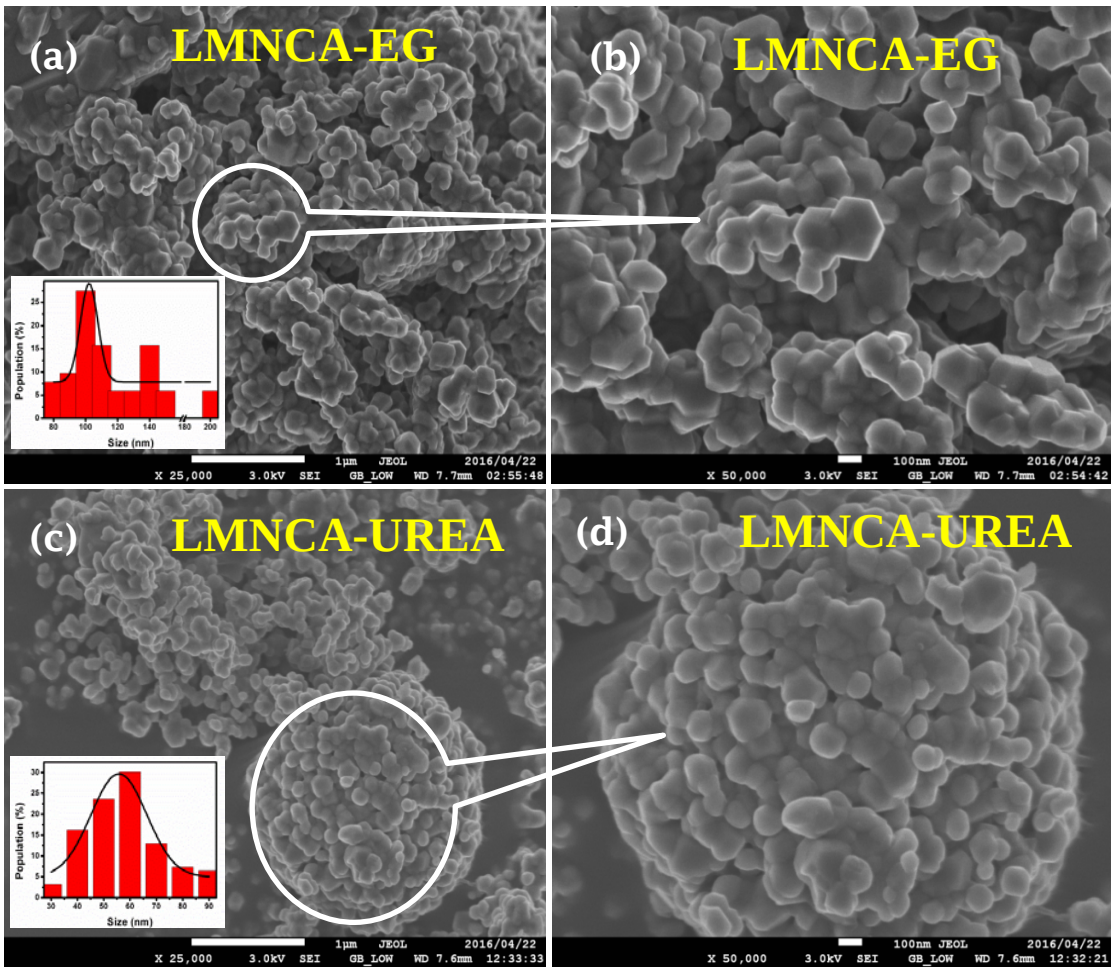


Figure 4.4: SEM images and particle size distribution histogram of urea-combustion and EG-combustion samples.

Urea is beneficial to the combustion reaction because it reacts rapidly with the nitrates reagents. During the combustion synthesis the solution mixture of the reagent nitrates and urea rapidly undergoes dehydration, followed by the gel formation which results in the hypergolic mixture

of NO_x, NH_3 and HNCO gas emissions. But EG acts as both a fuel and a complexing agent. EG complexes the metal cations (Ni, Mn, Co, Al), increases their solubility, and prevents them from precipitating. A different gel with high viscosity honey-like consistency results and CO_2, N_2 and H_2O gas evolutions are expected. The different gel properties results in different flame properties. LMNCA-urea shows increased agglomeration compared to LMNCA-EG sample. Agglomeration is generally expected from combustion synthesis because of the Van Der Waals forces existing between the nanoparticles [37]. However, the reduced agglomeration in EG is due to the complexing ability of EG [37].

4.2.5 Transmission Electron Microscopy Characterization (TEM)

Figure 4.5 shows typical TEM images of LMNCA material at low magnification (Figure 4.5 (a)) and high magnification (Figure 4.5 (b)). The HRTEM image (Figure 4.5 (b)) confirms that the sample is highly crystalline with distinct lattice fringes of d-spacing of ca. 0.474 nm corresponding to (003) lattice planes of the hexagonal layered phase.

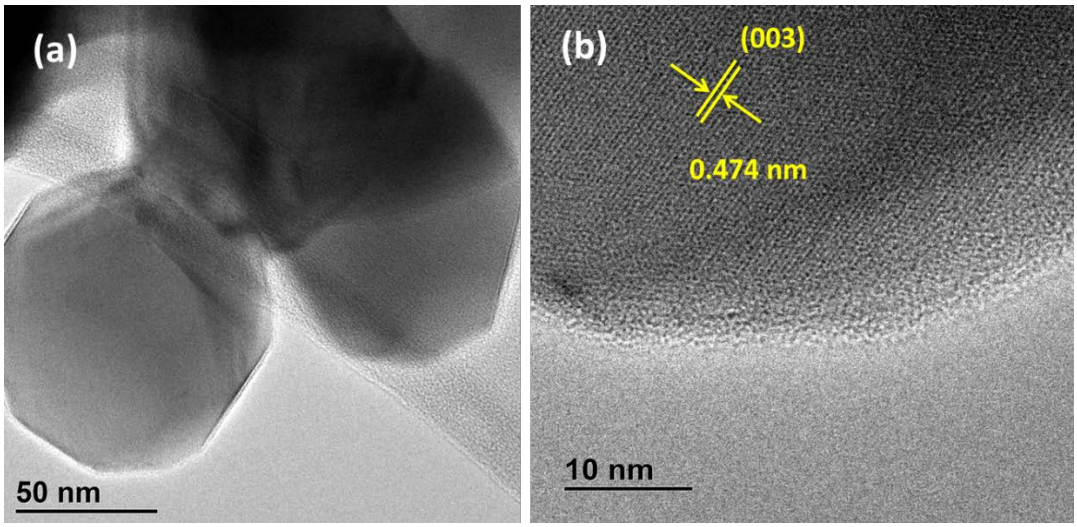


Figure 4.5: TEM images of LMNCA-urea sample.

4.2.6 Brunuar Emmett Teller (BET) Surface Area

Figure 4.6 shows the surface area of the samples determined using the BET surface area analysis. LMNCA-urea shows high surface area and pore volume compared to the LMNCA-EG sample. This will be beneficial for increased reaction with the electrolyte and thus will improve the electrochemical performance. Table 4.4 shows the BET analysis results.

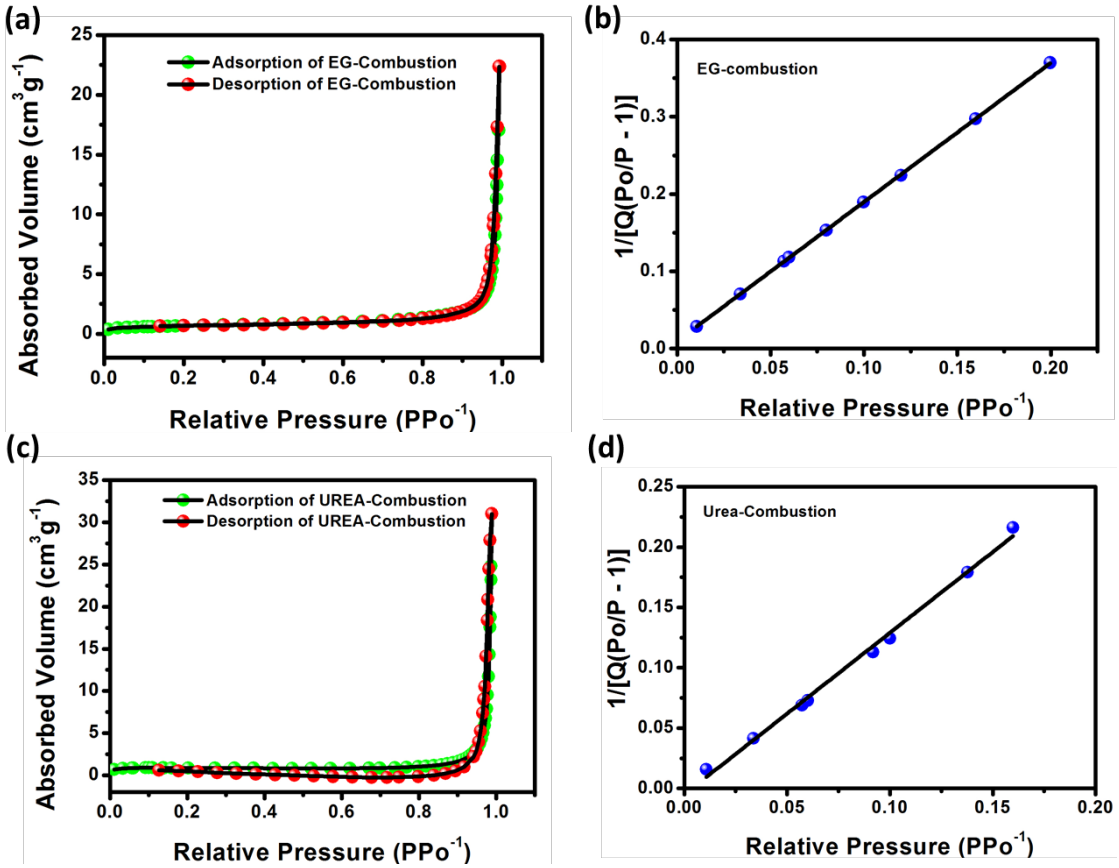


Figure 4.6: BET surface area analysis of LMNCA-urea and LMNCA-EG samples.

Table 4.4: Summary of particle surface area, pore volume and average particle size

Material (cm^{-1})	BET surface area (m^2/g)	Pore volume (cm^3/g)
LMNCA-urea	2.55 ± 0.14	0.038
LMNCA-EG	2.32 ± 0.03	0.026

4.2.7 Electrochemical Characterization

4.2.7.1 Cyclic voltammetry

Cyclic voltammetry of the samples was studied to investigate the redox reactions in the samples. Figure 4.7 (a) shows the cyclic voltammograms of the LMNCA-urea and LMNCA-EG samples at a scan rate of 0.1 mV s^{-1} in the voltage range of 2.0 – 4.8 V. The cyclic voltammograms are similar to each other and show two oxidation peaks in the first cycle appearing at ~4.2 V and ~4.7 V. The broad peak at about 4.2 V corresponds to the oxidation of both the Ni^{2+} to Ni^{4+} and Co^{3+} to Co^{4+} in the structure [29,31,33]. The peak at ~4.7 V

corresponds to the extraction of Li_2O (in the form of Li^+ and O_2) due to the activation of the Li_2MnO_3 phase, which results in the formation of the spinel-like MnO_2 phase. The reduction peaks between 3.7 and 4.5 V corresponds to the reduction of Ni^{4+} to Ni^{2+} and Co^{4+} to Co^{3+} due to the lithium reintercalation in the tetrahedral and octahedral sites. The reduction peak at ~3.2 V is due to the reduction of Mn^{4+} in the spinel-like MnO_2 phase and . This peak shifts to lower potentials for LMNCA-urea compared to LMNCA-EG, indicating increased activation of the Li_2MnO_3 phase in LMNCA-urea [31,38]. LMNCA-urea also shows more intense redox peaks compared to the LMNCA-EG sample confirming the faster Li-ion intercation and de-intercalation kinetics as suggeted by the X-ray diffraction analysis. However, Figure 4.7 (b) shows more intense redox peaks after 100 cycles for LMNCA-EG compared to LMNCA-urea, revealing faster Li-ion intercation and de-intercalation kinetics for LMNCA-EG after cycling. Figure 4.7 (b) also shows an oxidation peak around 3.25 V due to the oxidation of the spinel-like MnO_2 phase, but this is only observed in LMNCA-urea.

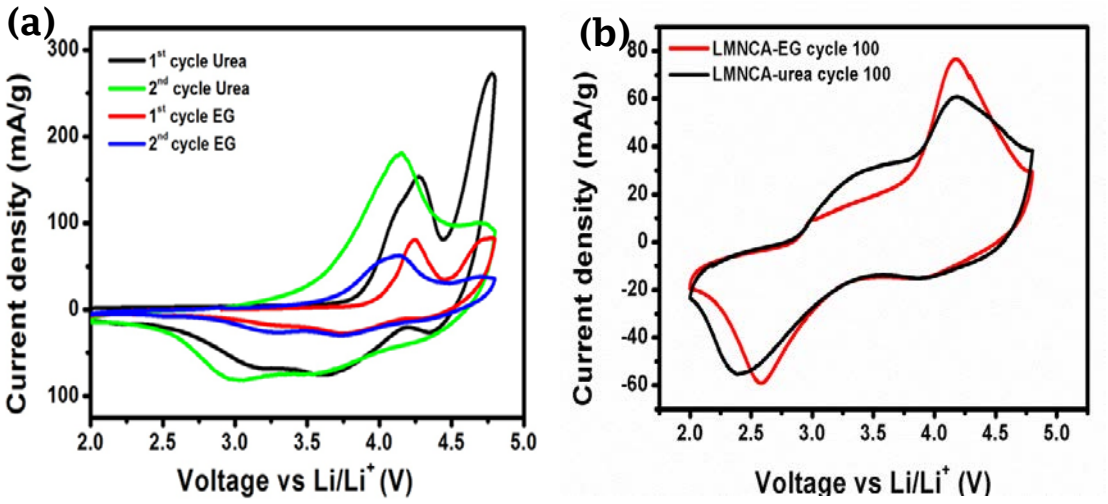


Figure 4.7: Cyclic voltammograms between 2.0 V - 4.8 V at 0.1 mV s^{-1} at room temperature.

4.2.7.2 Galvanostatic charge-discharge.

Galvanostatic charge-discharge studies were performed to investigate the lithium-ion battery performance of LMNCA-urea and LMNCA-EG. Figure 4.8 (a-b) displays the charge-discharge cycle results of the samples cycled between 2.0 and 4.8 V at 0.1 C (vs. Li^+/Li) at room temperature. Figure 4.8 (a-b) shows two defined voltage plateaus in the first charge curves of

both materials due to the two-step charging process from the two different lithium extraction processes. The first voltage plateau around 4.1 V is attributed to the de-lithiation of the $LiMO_2$ (M = Mn, Ni, Co) phase corresponding to the oxidation of the Ni^{2+} to Ni^{4+} and Co^{3+} to Co^{4+}. The long second voltage plateau above 4.4 V is due to the activation of the Li_2MnO_3 phase and disappears after the 1st cycle. These results are consistent with the electrochemical redox reactions observed in the cyclic voltammogram studies.

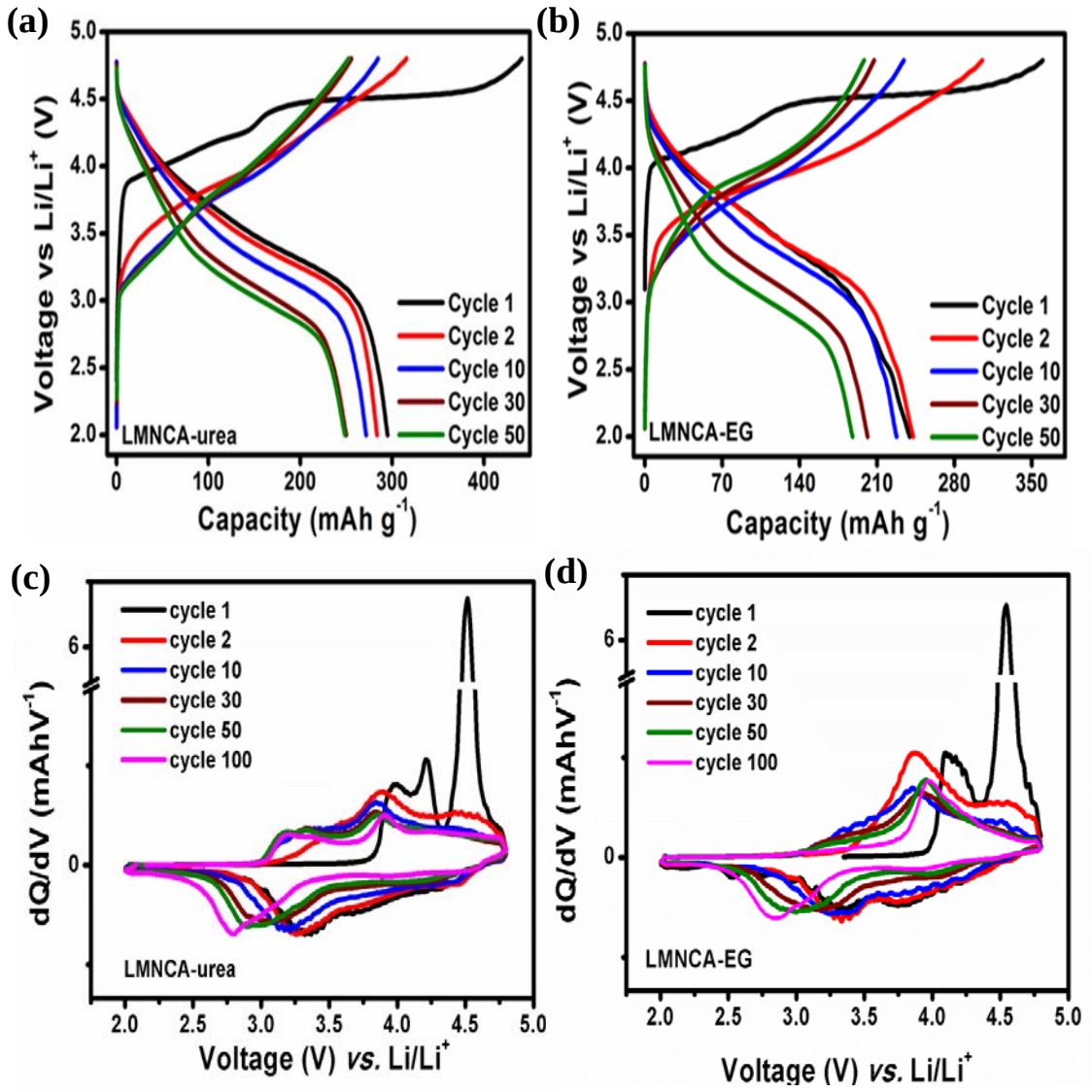


Figure 4.8: (a-b) Charge-discharge at 0.1 C between 2.0 - 4.8 V, and (c-d) corresponding differential capacity curves (dQ/dV vs. V) plots for the LMNCA-urea and -EG samples.

LMNCA-urea exhibits a higher discharge capacity of 295 mAh/g compared to the LMNCA-EG which exhibits a discharge capacity of 240 mAh/g. The high capacity for LMNCA-urea is

due to the longer second voltage plateau at > 4.4 V, indicating more activation of the Li_2MnO_3 phase in LMNCA-urea. The charge capacity in the first cycle is 442 mAh/g and 360 mAh/g for LMNCA-urea and LMNCA-EG, respectively. The length of the second voltage plateau is 282 mAh/g and 235 mAh/g for LMNCA-urea and LMNCA-EG, respectively.

The activation process transforms the Li_2MnO_3 phase to a MnO_2 phase which also contributes to the high discharge capacity [39]. Differential capacity curves (dQ/dV vs. V) were plotted to investigate the transformation of the Li_2MnO_3 phase to MnO_2 phase in the samples. Figure 4.8 (c-d) shows the differential capacity curves of the samples at different charge-discharge cycles (1, 2, 10, 30, 50,100 cycles). The dQ/dV redox couples around 3.7-4.2 V corresponds to the reversible redox process of Ni^{2+} to Ni^{3+} to Ni^{4+} and Co^{3+} to Co^{4+} redox process [34]. In the first cycle, the intense oxidation peak around 4.5 V is due to the activation of Li_2MnO_3 phase and gives no corresponding reduction peaks since this process is irreversible. However, the activation process induces a new reduction peak ~3.3 V which is due to the transformation of the Li_2MnO_3 phase to a spinel–like MnO_2 phase. The reduction peak ~3.3 V is due to the Mn^{4+} to Mn^{3+} reduction in the MnO_2 activation product. LMNCA-urea shows a more pronounced Mn^{4+}/Mn^{3+} reduction peak at ~3.3 V compared to LMNCA-EG and this indicates more activation of Li_2MnO_3 in LMNCA-urea. The shift of this peak to lower potentials upon cycling confirms the formation of the spinel-like MnO_2 phase. For LMNCA-urea the potential difference between the 1st and 100th cycle is 550 mV, while for LMNCA-EG the difference is 490 mV. These findings show the formation of the spinel-like MnO_2 phase is adverse in LMNCA-urea compared to LMNCA-EG. Figure 4.8 (c) displays the formation of new oxidation peaks between 3.1- 3.4 V upon cycling for the LMNCA-urea sample, while these peaks do not appear in the LMNCA-EG sample in Figure 4.8 (d). These new peaks demonstrate the transformation of the structure from ‘layered-layered’ to ‘layered-spinel’. The existence of these new peaks also demonstrate the increase in the Mn^{3+} ion content upon cycling in LMNCA-urea [34,40].

However, these results also suggest that EG can be used to suppress or reduce the activation of the Li_2MnO_3 phase which affects the average discharge voltage stability upon cycling and causes a voltage fade. The LMNCA-EG showed resistance to the formation of the spinel phase because of the improved the Li_2MnO_3 local structure or framework stability. To get more information on the voltage fade of the materials, the mid-point voltages of these materials are plotted in Figure 4.9 (a). Figure 4.9 (a) shows a similar mid-point voltage in the second cycle for the materials but the mid-point voltage fades fast for LMNCA-urea compared to the

LMNCA-EG. The mid-point voltage difference between the 2nd cycle and 100th cycle is ΔE_{mid} = 0.15 V and ΔE_{mid} = 0.33 V for LMNCA-EG and LMNCA-urea, respectively. These results illustrate the suppression of the voltage fade in LMNCA-EG compared to LMNCA-urea.

4.2.7.3 Cycle performance and Coulombic efficiency (CE)

Figure 4.9 (b-c) displays the cyclic performance with coulombic efficiency curves of the LMNCA-urea and LMNCA-EG samples. Figure 4.9 (b-c) shows the cycle performance of the samples cycled at 0.1 C between 2.0-4.8 V at room temperature. The capacity retention after 50 cycles is 84 % and 76 % for LMNCA-urea and LMNCA-EG, respectively. The capacity retention after 100 cycles is 78 % and 70 % for LMNCA-urea and LMNCA-EG, respectively. Capacity fade in LMR-NMC materials is caused by the transformation of the layered-layered to layered-spinel structure, dissolution of the manganese in the electrolyte, electrode/electrolyte interface reaction and lattice rearrangement [14]. Interestingly, the layered-spinel formation did not deteriorate the electrochemical performance suggesting that small amounts of spinel phase were formed, especially for the urea sample which showed more spinel formation according to Figure 4.8 (c,d). The differential capacity curves (dQ/dV vs. V) in Figure 4.8 (c,d) also show that the intensity of the peak at ~3.3 V due to the newly formed MnO_2 spinel formation is not reduced upon cycling; this means that the spinel phase formed did not lose its capacity upon cycling and therefore does not affect the capacity retention upon cycling. Figure 4.9 (b-c) also shows the coulombic effieciency of the LMNCA-urea and LMNCA-EG samples. Coulombic efficiency (CE) is 67 % for both the samples in the first cycle due to the activation of the Li_2MnO_3 phase, but stabilized to above 90 % after 6 cycles. This indicates good reversibility of the Li-ion intercalation and de-intercalation reactions in the materials after 6 cycles. The CE is 98 and 99 % after 100 cycles for LMNCA-urea and LMNCA-EG samples, respectively.

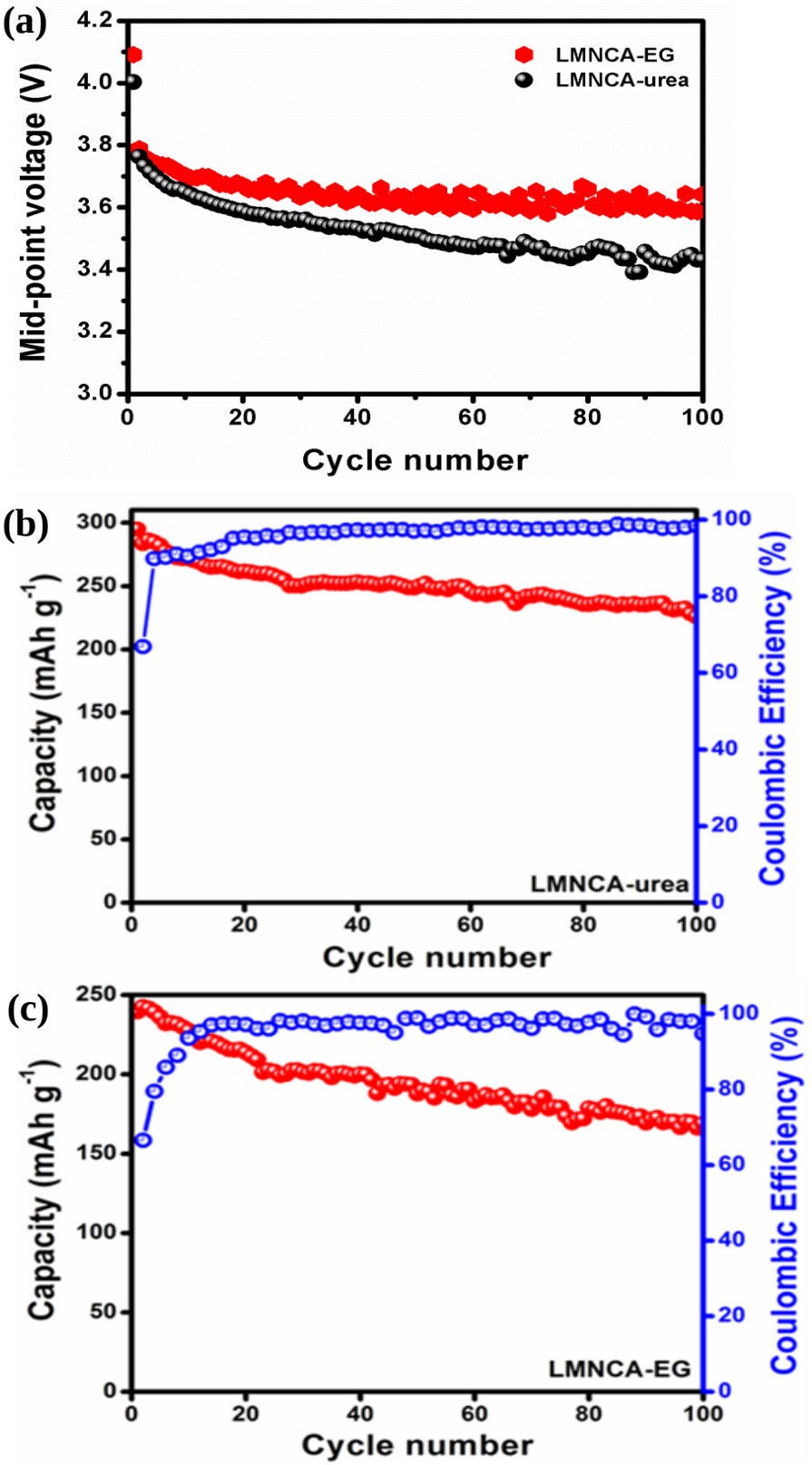


Figure 4.9: (a) Mid-point voltage curves at 0.1 C, (b-c) cycle performance and coulombic efficiency at 0.1 C between 2.0 - 4.8 V for LMNCA-urea and LMNCA-EG samples.

4.2.7.4 Rate capability

Figure 4.10 (d) shows the rate capability performance of the samples, cycled at different current rates of 0.5, 1, 2, and 5 C between 2.0 - 4.8 V (vs. Li^+/Li) at room temperature. The LMNCA-urea shows better and more stable cycle performance and rate capability compared to the LMNCA-EG. This is due to smaller particles, narrower particle size distribution and higher surface area for LMNCA-urea.

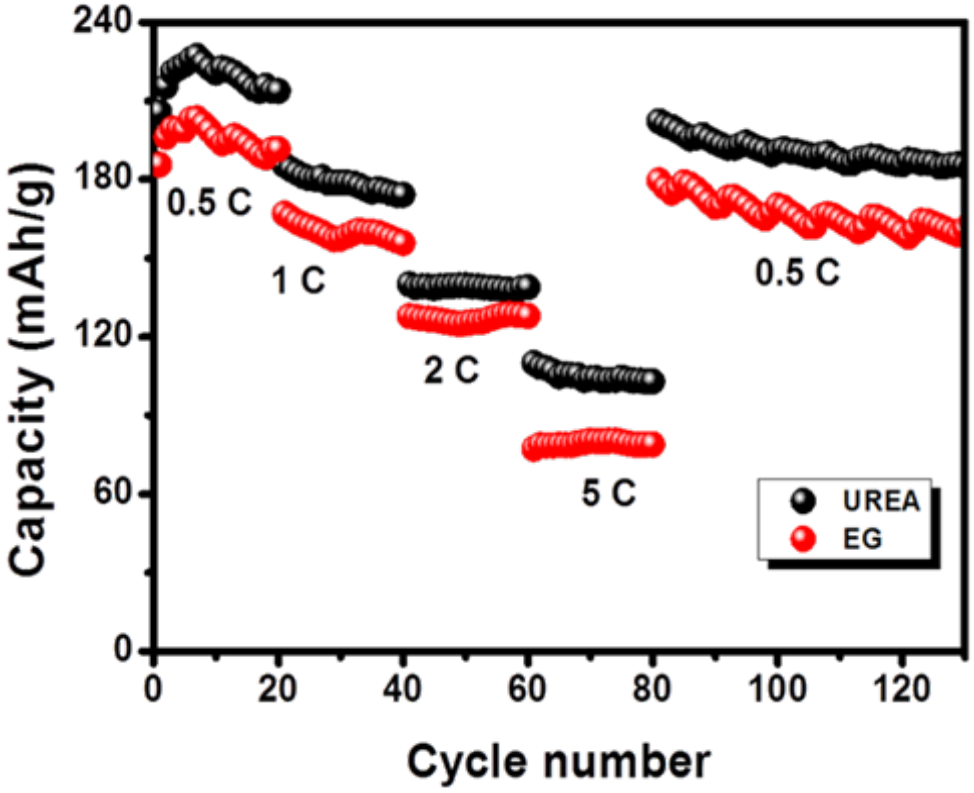


Figure 4.10: Rate capability at different current densities for LMNCA-urea and LMNCA-EG samples.

4.2.7.5 Post-cycling analysis

The structure of the LMNCA-urea and LMNCA-EG samples after 100 cyles at 0.1 C was examined by XRD analysis. The coin cells were disassembled in the Ar filled glove box after the cyclic analysis. Figure 4.11 shows the XRD analysis of LMNCA-urea and LMNCA-EG samples after 100 cycles at 0.1 C. The XRD results show that the materials still display a layered structure as the XRD patterns of the cycled electrodes are comparable to the fresh powders of the samples. However, the superlattice peaks between 2 Theta = 20-22° disappeared, confirming the activation of the Li_2MnO_3 phase upon cycling. Though the spinel

formation was confirmed by the differential capacity curves (dQ/dV vs. V) curves, the XRD analysis could not detect the spinel phase diffraction peaks and this confirms that only small amounts of the spinel phase is formed.

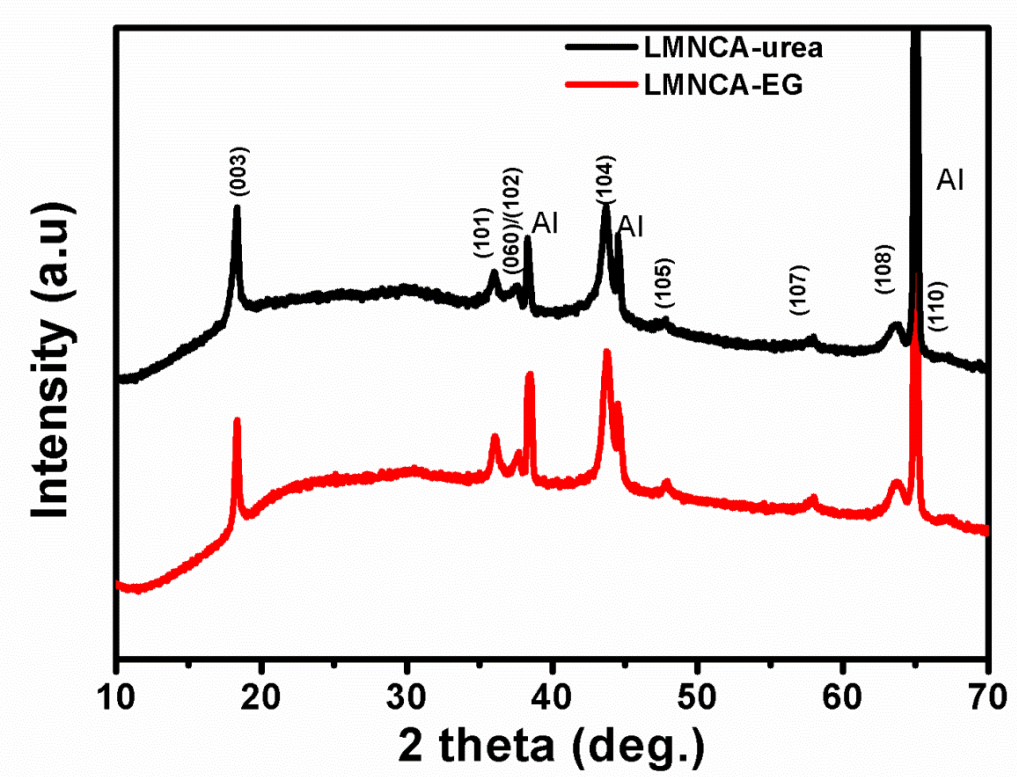


Figure 4.11: XRD patterns of LMNCA-urea and LMNCA-EG electrodes after 100 cycles.

SEM analysis of the electrodes was also peformed to determine the change in morphology upon cycling. The SEM images of the electrodes after cycling for 100 cycles at 0.1 C were taken ex-situ. Figure 4.12 shows the SEM images of both samples and reveal that the morphology of the electrode materials was maintained, except for some agglomeration due to the redox reactions occuring during cycling [41]. The SEM images also show the coverage of the particles of both samples by the solid electrolyte interphase (SEI) layer. The SEI layer is due to the interfacial reactions between the surface of the electrodes and the electrolyte solution [42]. Charging above 4.5 V results in severe oxidative decomposition of electrolyte and contributes to SEI formation [43-45]. However, a thicker SEI layer was formed on the surface of the cycled LMNCA-EG electrode compared to that of LMNCA-urea electrode (Figure 4.12 inset). This could be the cause of the unstable cycle performance and rate capability in LMNCA-EG. This is because the SEI layer creates a barrier for Li-ions during cycling which increases the cell impedance and decreases cycle performance and the rate capability [43,46]. These results and

the XRD analysis in Figure 4.11 suggest that the capacity fade in the samples is not affected by the spinel formation but by the SEI layer growth.

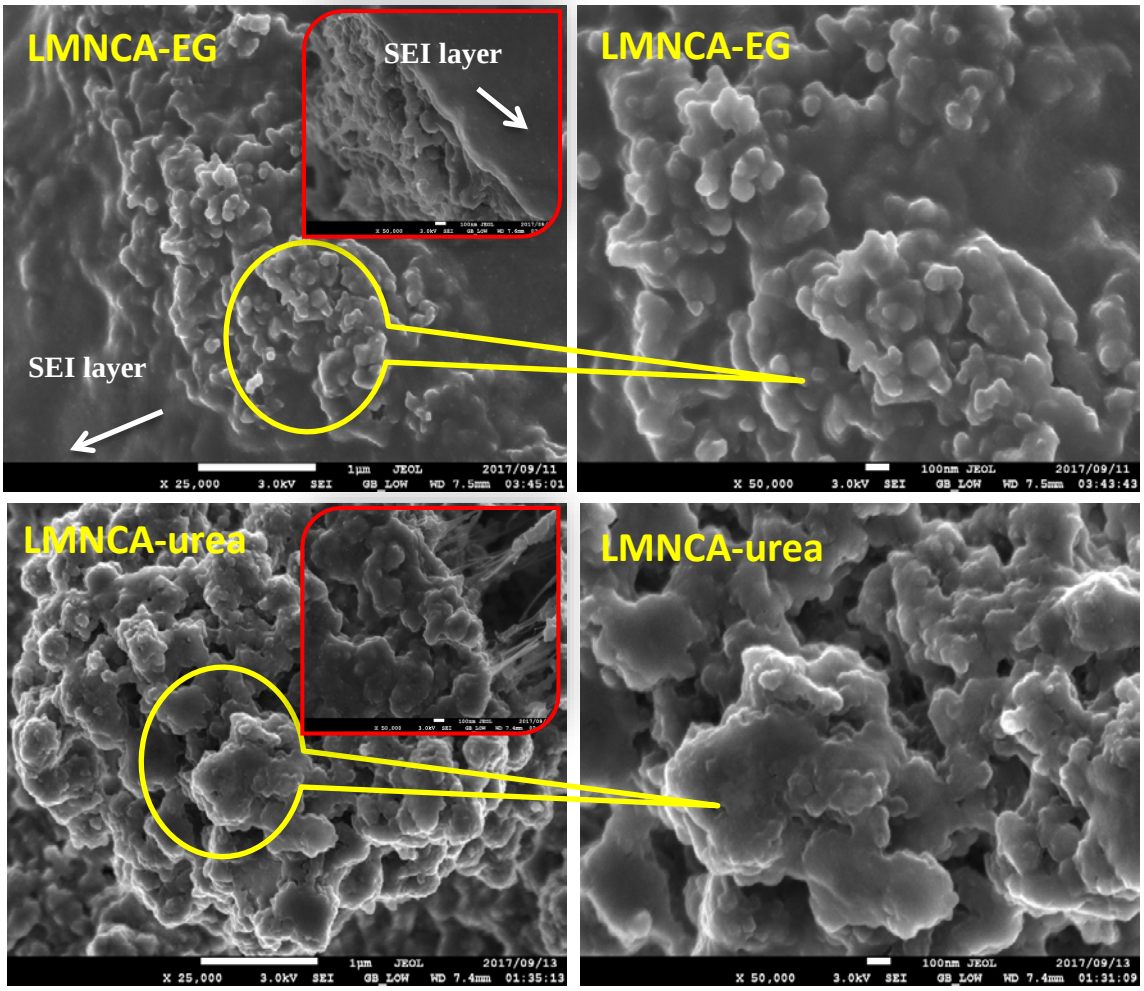


Figure 4.12: SEM analysis of the LMNCA-urea and LMNCA-EG electrodes after 100 cycles at 0.1 C.

To investigate the properties of the SEI layer the EDX and XPS analyses of the LMNCA-EG electrode after 100 cycles were performed. Figure 4.13 shows the EDX elemental analysis and mapping and reveal that the electrode contains fluorine (F), phosphorus (P), oxygen and carbon, additionally to some Mn, Ni, Co and Al due to LMNCA cathode. The EDX elemental analysis results are reported in Table 4.5. The obtained Mn:Ni:Co ratio is ca. 4.7:1:1 for LMNCA-EG and ca. 4.4:1:1 for LMNCA-urea and these values agree with the expected 4:1:1 Mn:Ni:Co ratio in LMNCA. This suggests that the Mn:Ni:Co composition was not changed during cycling.

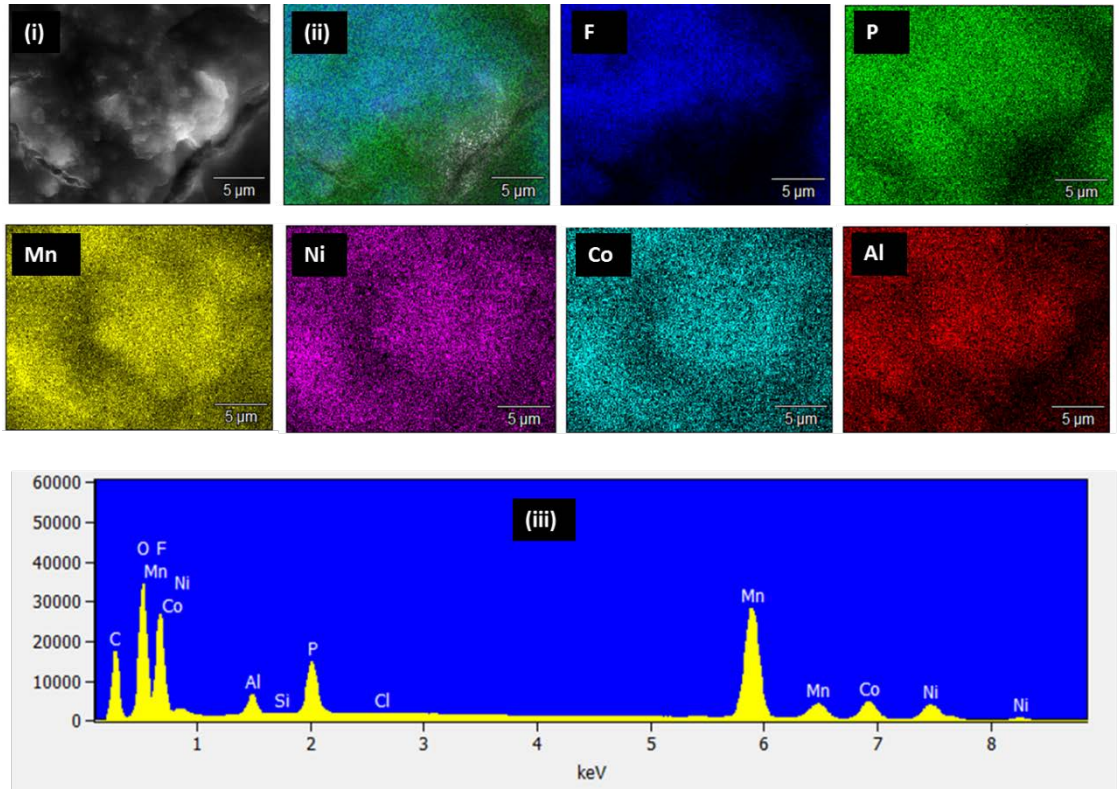


Figure 4.13: EDX mapping and elemental analysis of LMNCA-EG electrode after 100 cycles.

Table 4.5: EDX elemental composition of the LMNCA sample.

Element	Atomic percentage (%) LMNCA-EG	Atomic percentage (%) LMNCA-urea
C	42.81±0.17	42.98±0.16
O	21.08±0.34	21.77±0.12
F	24.83±0.76	21.96±0.18
Al	0.74±0.01	1.50±0.01
Si	0.07±0.01	0.09±0.01
P	1.68±0.01	2.16±0.01
Cl	0.01±0.01	0.07±0.01
Mn	6.15±0.02	6.67±0.02
Co	1.32±0.01	1.42±0.01
Ni	1.33±0.02	1.39±0.01

The XPS analysis in Figure 4.14 shows the O 1s, F 1s, P 2p, Li 1s and C 1s spectra for the LMNCA-EG electrode. Figure 4.14 a shows that the surface of the electrode is composed of the O, F, P, Li and C. The O 1s spectra shows peaks at 531.8 eV and 533.5 eV due to Li_2O together with Li_3PO_4, and organic O, respectively. The Li_2O is believed to be from the reaction of the electrode with the atmospheric oxygen and the Li_3PO_4 is due to the hydrolysis of $LiPF_6$ [43]. The F 1s spectrum shows peaks at 685.1 and 686.9 eV due to the LiF and PVDF binder, respectively. The P 2p spectrum shows peaks at 133.9 and 137.0 eV due to Li_3PO_4 and PVDF binder, respectively. The Li 1s spectrum shows peaks due to LiF, Li_2O and Li_3PO_4 which cannot be resolved because they have very similar binding energies. The LiF is due to the decomposition of the $LiPF_6$ [46,47].

The C 1s spectrum shows peaks at 285.1, 286.7, 288.4 and 290.0 eV corresponding to the polymeric phase of the surface, ether functional groups, carbonate functional groups and PVDF, respectively [46]. The ether and carbonate functional groups are due to the decomposition of the solvent [43,48]. The assignment of the ether and functional groups is supported by the peak at 532.8 eV in the O 1s spectrum. Table 4.6 reports the quantitative analysis of the XPS electrode surface data of LMNCA-EG and LMNCA-urea and reveals that the SEI layer consists mostly of Li_3PO_4, polycarbonates, LiF and PVDF compounds.

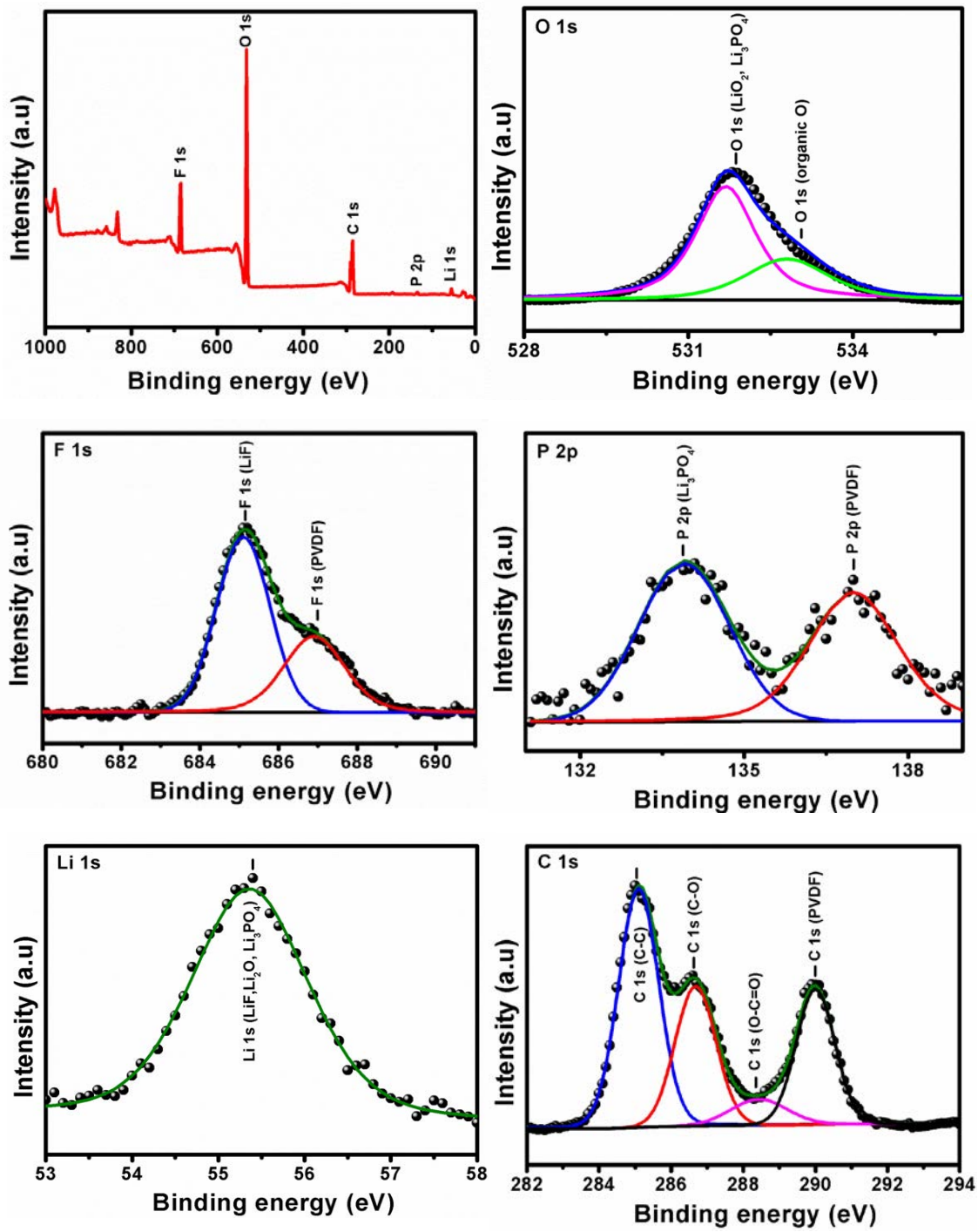


Figure 4.14: O 1s, F 1s, P 2p, Li 1s and C 1s XPS spectra for LMNCA-EG electrode after 100 cycles.

Table 4.6: Elemental identification and quantification of LMNCA-EG and LMNCA-urea.

Name	Peak BE (eV) [LMNCA-EG]	Atom (%) [LMNCA-EG]	Peak BE (eV) [LMNCA-urea]	Atom (%) [LMNCA-urea]
Li 1s (LiF; Li_2O; Li_3PO_4)	55.4	1.9	55.5	27.2
P 2p (Li_3PO_4)	133.9	0.0	133.9	0.5
P 2p (PVdF)	137.0	0.0	136.9	0.8
C 1s (C-C)	285.1	0.9	284.9	13.6
C 1s (C-O)	286.6	0.7	286.6	9.4
C 1s (O-C=0)	288.6	0.1	288.6	2.0
C 1s (PVdF)	290.0	0.6	289.9	5.8
O1s (Li_2O; Li_3PO_4)	531.8	94.9	531.8	24.0
O 1s (Organic O)	533.5	0.3	533.4	4.8
F 1s (LiF)	685.1	0.4	685.0	4.9
F 1s (PVdF)	686.9	0.2	686.8	6.1

Although a thick SEI layer was observed in LMNCA-EG, LMNCA-urea also exhibited decomposition of the electrolyte upon cycling. Figure 4.15 (a) shows a dark compound on the surface of the LMNCA-urea electrode assumed to be the electrolyte decomposition product. Wang and co-workers also reported the existence of this surface compound after 100 cycles in $Li_{1.2}Mn_{0.54}Co_{0.13}Ni_{0.13}O_2$ based electrodes [14]. The EDX analyses (Figure 4.15 (a-f)) reveal that this surface compound consists of P and F ions. This surface compound is due to the insoluble $Li_xPF_yO_z$ and LiF precipitates due to the decomposition of electrolyte. The XPS analyses in Figure 4.15 (g-h) compares the F 1s and P 2p spectra of LMNCA-urea and LMNCA-EG and shows that the LiF and Li_3PO_4 decomposition peaks are also present in LMNCA-urea. The LMNCA-urea shows stronger PVDF binder peaks in both F 1s and P 2p spectra suggesting more decomposition in LMNCA-urea compared to LMNCA-EG.

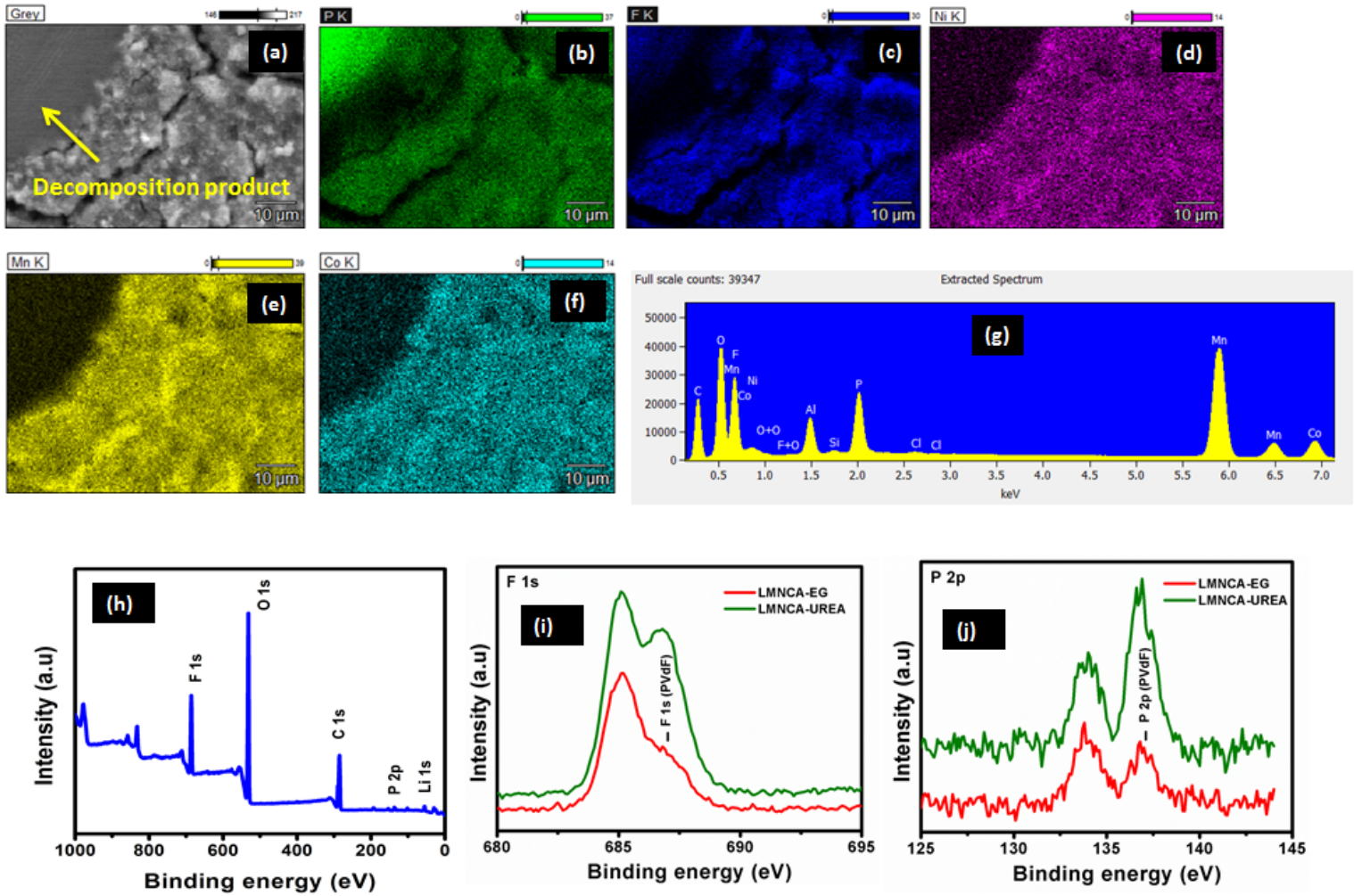


Figure 4.15: Post-morterm studies- (a-g) EDX analysis of LMNCA-urea, (h) XPS analysis of LMNCA-urea and (i,j) XPS of F 1s and P 2p peaks for LMNCA-urea and LMNCA-EG.

4.2.7.6 Electrochemical impedance spectroscopy (EIS)

Figure 4.16 (a-b) shows the Nyquist plots (-Z″ vs. Z′) and Z′ vs. $\omega^{-1/2}$ curves obtained from the electrochemical impedance spectroscopy analysis. The coin cells were analyzed before and after 100 cycles at the open circuit voltage, where OCV ~3.0 V vs. Li/Li^+.The spectra were fitted with the equivalent circuit shown as the insert in Figure 4.16 (a). The fitting parameters involved: the solution ohmic resistance of the electrode system (R_s) due to electric conductivity of the electrolyte, separator and electrodes; the surface film resistance (R_f) and constant phase element (CPE_f), referring to the resistance and capacitance due to the solid-electrolyte interphase layer formed on the electrode surface; the charge transfer resistance (R_{ct}) and interfacial capacitance (CPE_{Li}), corresponding to lithium intercalation/de-intercalation processes arising at the interface between the electrode and the electrolyte, and the Warburg element (Z_w) describing the solid state diffusion of Li-ion between the particles of active materials and electrolyte, signified by the straight sloping line (~45°) at the low frequency region

The impedance spectra for both the samples consists of one clear semicircle in the high frequency region and a straight line with an inclined slope in the low frequency region. Table 4.7 summerises the EIS results of the samples. The EIS data measured before cycling indicate that LMNCA-urea exhibits lower R_f and R_{CT} impedance values compared to the LMNCA-EG. This suggests that LMNCA-urea has higher electronic conductivity compared to LMNCA-EG. The R_f and R_{ct} values are 57.5 and 544.0 ohm, and 645.6 and 719.9 ohm for LMNCA-urea and LMNCA-EG, respectively. Interestingly, the R_f and R_{ct} values increases for LMNCA-urea after 100 cycles, while they decrease for the LMNCA-EG. The increase in R_{ct} values after 100 cycles is expected because of the spinel phase formation and rearrangement of the lattice upon cycling. The increase in the R_f value after 100 cycles is due to the formation of a SEI layer and changes in surface structure as the extensive removal of Li_2O from the Li_2MnO_3 activation process damages the electrode surface [49].

Figure 4.16 (b) represents the relationship of impedance and frequency used to determine the diffusion coefficient for the samples. The Li-ion diffusion co-efficient (D_{Li^+}) was calculated as reported in literature [31]. It was calculated to be 1.22 x 10^{-16} and 0.62 x 10^{-16} cm^2s^{-1} at 3.0 V for LMNCA-urea and LMNCA-EG, respectively. The Li-ion diffusion coefficient of the LMNCA-urea is double that of the LMNCA-EG before prolonged cycling and this explains the high Li-ion intercalation and de-intercalation kinectics observed for the LMNCA-urea

confirmed by the higher hexagonal ordering calculated in the XRD analysis. However, the diffusion coeffcient increases after 100 cycles for both the samples due to the MnO_2-spinel formation product, this suggests that the diffusion of lithium ions in the layered-spinel is easier compared to that of the layered-layered structure.

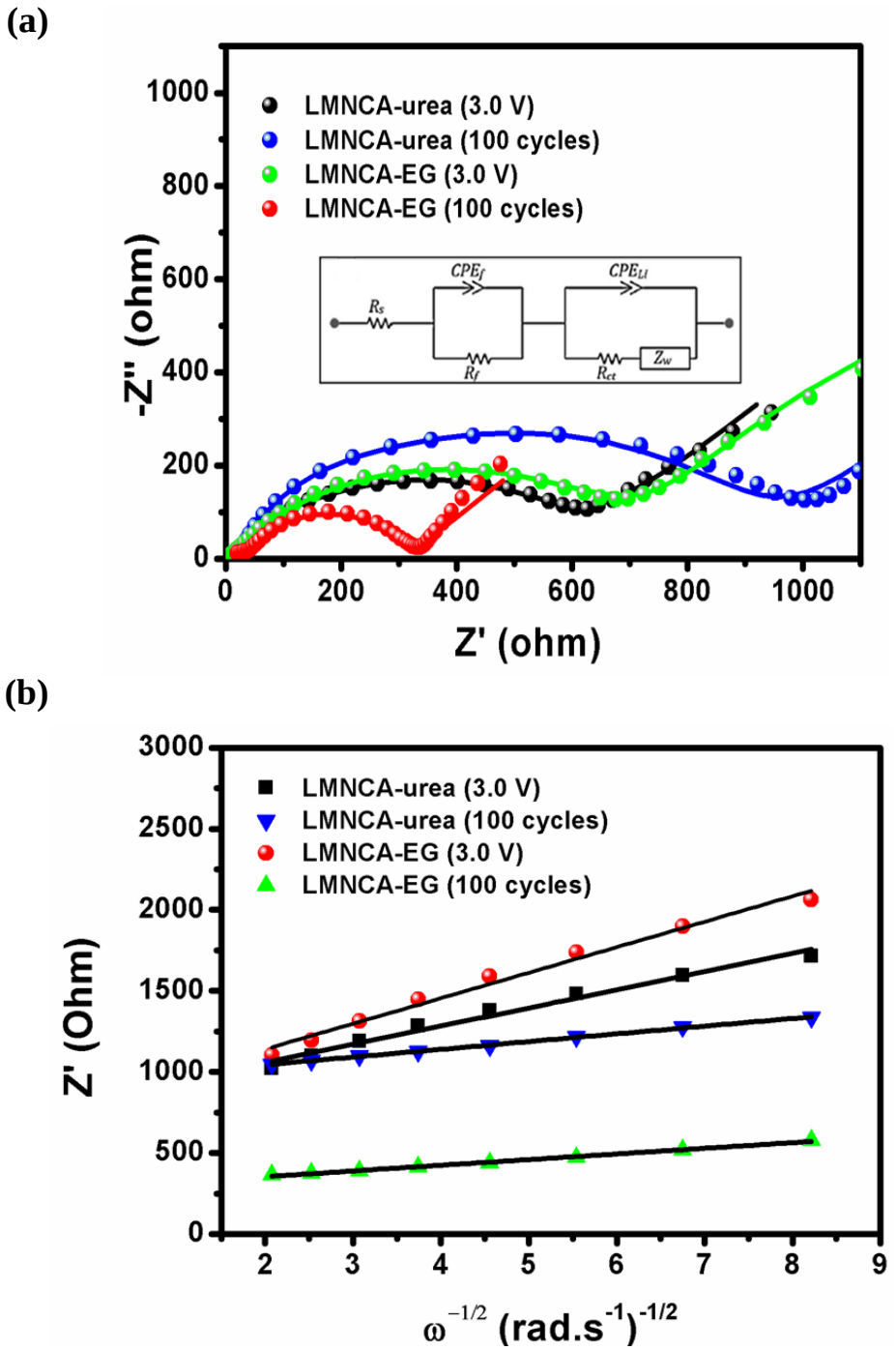


Figure 4.16: (a) Nyquist plots (-Z″ vs. Z′) and (b) Z′ vs. $\omega^{-1/2}$ curves of LMNCA-urea and LMNCA-EG samples.

Table 4.7: Electrochemical impedance spectroscopy fitted parameters

	R_{SEI} (Ω)	R_f (Ω)	R_{CT} (Ω)	CPE_f		CPE_{CT}		Z_w $\Omega.s^{-1/2}$	D_{Li^+} cm^2s^{-1}
				CPE_f ($F.s^{(a-1)}$)	a	CPE_{CT} ($F.s^{(a-1)}$)	a		
LMNCA-urea (OCV)	13.6	57.5	544.0	6.6e-6	0.91	25.4e-6	0.67	322	1.2e-16
LMNCA-urea (100 cyc)	16.7	112.2	806.4	9.4e-6	1.00	37.8e-6	0.70	152	6.8e-16
LMNCA-EG (OCV)	3.2	645.6	719.9	3.1e-3	0.78	27.2e-6	0.81	216	0.6e-16
LMNCA-EG (100 cyc)	10.1	26.6	275.9	0.9e-6	0.84	14.6e-6	0.78	76	12.e-16

The obtained lithium-ion diffusion coefficients are lower compared to layered oxides such as LCO and NMC ($LiNi_{1/3}Mn_{1/3}Co_{1/3}O_2$), this is due to the existence of Li_2MnO_3 phase [50]. The diffusion coefficient of LCO and NMC is 10^{-8} - 10^{-10} cm^2 s^{-1} and 10^{-9} - 10^{-10} cm^2 s^{-1}, respectively [51,52].

4.3 Conclusions

LMNCA-urea and LMNCA-EG were successfully prepared using urea and EG fuel, respectively. The samples both exhibit pure and crystalline powders. LMNCA-urea sample shows high capacity, improved cycle performance and rate capability compared to LMNCA-EG. This is due to the narrower particle size distribution, high surface area and high hexagonal ordering compared to LMNCA-EG. However, the LMNCA-EG displays the suppression of the voltage fade due the resistance to the formation of spinel phase. This is attributed to the strong complexing ability of EG which improved the Li_2MnO_3 structure stability.

4.4 References

[1] M. Bettge, Y. Li, B. Sankaran, N.D. Rago, T. Spila, R.T. Haasch, I. Petrov, D.P. Abraham, Journal of Power Sources, 233 (2013) 346-357.

[2] J.R. Croy, J.S. Park, F. Dogan, C.S. Johnson, B. Key, M. Balasubramanian, Chemistry of Materials, 26 (2014) 7091-7098.

[3] B.R. Long, J.R. Croy, J.S. Park, J. Wen, D.J. Miller, M.M. Thackeray, Journal of the Electrochemical Society, 161 (2014) A2160-A2167.

[4] W. Lu, Q. Wu, D.W. Dees, Journal of the Electrochemical Society, 160 (2013) A950-A954.

[5] D. Mohanty, A. Huq, E.A. Payzant, A.S. Sefat, J. Li, D.P. Abraham, D.L. Wood III, C. Daniel, Chemistry of Materials, 25 (2013) 4064-4070.

[6] D. Mohanty, S. Kalnaus, R.A. Meisner, K.J. Rhodes, J. Li, E.A. Payzant, D.L. Wood III, C. Daniel, Journal of Power Sources, 229 (2013) 239-248.

[7] D. Mohanty, A.S. Sefat, J. Li, R.A. Meisner, A.J. Rondinone, E.A. Payzant, D.P. Abraham, D.L. Wood III, and C Daniel, Physical Chemistry Chemical Physics, 15 (2013) 19496-19509.

[8] P.K. Nayak, J. Grinblat, M. Levi, E. Levi, S. Kim, J.W. Choi, D.Aurbach, Advanced Energy Materials, 6 (2016).

[9] R.E. Ruther, A.F. Callender, H. Zhou, S.K. Martha, J. Nanda, Journal of the Electrochemical Society, 162 (2015) A98-A102.

[10] A. Vu, L.K. Walker, J. Bareño, A.K. Burrell, I. Bloom, Journal of Power Sources, 280 (2015) 155-158.

[11] C. Wang, A. Manthiram, Journal of Materials Chemistry A, 1 (2013) 10209-10217.

[12] H. Xu, S. Deng, G. Chen, Journal of Materials Chemistry A, 2 (2014) 15015-15021.

[13] D. Kim, G. Sandi, J.R. Croy, K.G. Gallagher, S. Kang, E. Lee, M. D. Slater, C. S. Johnson, M.M. Thackeray, Journal of the Electrochemical Society, 160 (2013) A31-A38.

[14] S. Wang, Y. Li, J. Wu, B. Zheng, M.J. McDonald, Y. Yang, Physical Chemistry Chemical Physics, 17 (2015) 10151-10159.

[15] N. Li, R. An, Y. Su, F. Wu, L. Bao, L. Chen, Y. Zheng, H. Shou, S. Chen, Journal of Materials Chemistry A, 1 (2013) 9760-9767.

[16] C.J. Jafta, K. Raju, M.K. Mathe, N. Manyala, K.I. Ozoemena, Journal of the Electrochemical Society, 162 (2015) A768-A773.

[17] C.J. Jafta, M.K. Mathe, N. Manyala, W.D. Roos, K.I. Ozoemena, ACS applied materials & interfaces, 5 (2013) 7592-7598.

[18] S. Balaji, D. Mutharasu, N.S. Subramanian, K. Ramanathan, Ionics, 15 (2009) 765-777.

[19] T. Zhao, S. Chen, L. Li, X. Zhang, R. Chen, I. Belharouak, F. Wu, K. Amine, Journal of Power Sources, 228 (2013) 206-213.

[20] J. Zheng, X. Wu, Y. Yang, Electrochimica Acta, 56 (2011) 3071-3078.

[21] S. Shi, J. Tu, Y. Tang, Y. Yu, Y. Zhang, X. Wang, C. D. Gu, Journal of Power Sources, 228 (2013) 14-23.

[22] W. Yang, G. Zhang, J. Xie, L. Yang, Q. Liu, Journal of Power Sources, 81 (1999) 412-415.

[23] F.P. Nkosi, C.J. Jafta, M. Kebede, L. le Roux, M.K. Mathe, K.I. Ozoemena, RSC Advances, 5 (2015) 32256-32262.

[24] Z. Zhong, N. Ye, H. Wang, Z. Ma, Chemical Engineering Journal, 175 (2011) 579-584.

[25] S. Chitra, P. Kalyani, T. Mohan, R. Gangadharan, B. Yebka, S. Castro-Garcia, M. Massot, C. Julien,M. Eddrief, Journal of electroceramics, 3 (1999) 433-441.

[26] K. Lee, H. Choi, J. Lee, Journal of Materials Science Letters, 20 (2001) 1309-1311.

[27] S.T. Mukherjee, V. Bedekar, A. Patra, P. Sastry, A. Tyagi, Journal of Alloys and Compounds, 466 (2008) 493-497.

[28] S. Yin, Y. Rho, I. Swainson, L. Nazar, Chemistry of materials, 18 (2006) 1901-1910.

[29] H. Li, S. Zhang, X. Wei, P. Yang, Z. Jian, J. Meng, RSC Advances, 6 (2016) 79050-79057.

[30] X. Zhang, D. Luo, G. Li, J. Zheng, C. Yu, X. Guan, C. Fu, X. Huang, L. Li, Journal of Materials Chemistry A, 1 (2013) 9721-9729.

[31] C.J. Jafta, K.I. Ozoemena, M.K. Mathe, W.D. Roos, Electrochimica Acta, 85 (2012) 411-422.

[32] C. Fu, G. Li, D. Luo, J. Zheng, L. Li, Journal of Materials Chemistry A, 2 (2014) 1471-1483.

[33] L. Li, X. Zhang, R. Chen, T. Zhao, J. Lu, F. Wu, K Amine, Journal of Power Sources, 249 (2014) 28-34.

[34] C. Fu, G. Li, D. Luo, J. Zheng, L. Li, Journal of Materials Chemistry A, 2 (2014) 1471-1483.

[35] J. Li, X. Wu, X. Zhang, H. Lü, G. Wang, J. Guo, F. Wan, R. Wang, Chemical Communications, 51 (2015) 14848-14851.

[36] J. Song, J. Gim, S. Kim, J. Kang, V. Mathew, D. Ahn, J. Kim, Chemistry–An Asian Journal, 9 (2014) 1550-1556.

[37] S.T. Mukherjee, V. Bedekar, A. Patra, P. Sastry, A. Tyagi, Journal of Alloys and Compounds, 466 (2008) 493-497.

[38] M. Iftekhar, N. Drewett, A. Armstrong, D. Hesp, F. Braga, S. Ahmed, L. J. Hardwick, Journal of the Electrochemical Society, 161 (2014) A2109-A2116.

[39] I. Bloom, L. Trahey, A. Abouimrane, I. Belharouak, X. Zhang, Q. Wu, W. L, D.P. Abraham, M. Bettge, J.W. Elam, X. Meng, Journal of Power Sources, 249 (2014) 509-514.

[40] M.N. Ates, Q. Jia, A. Shah, A. Busnaina, S. Mukerjee, K. Abraham, Journal of the Electrochemical Society, 161 (2014) A290-A301.

[41] S. Tao, W. Huang, H. Xie, J. Zhang, Z. Wang, W. Chu, B. Qian, L. Song, RSC Advances, 7 (2017) 39427-39433.

[42] D. Aurbach, Journal of Power Sources, 89 (2000) 206-218.

[43] N. Choi, J. Han, S. Ha, I. Park, C. Back, RSC Advances, 5 (2015) 2732-2748.

[44] L. Yang, B. Ravdel, B.L. Lucht, Electrochemical and Solid-State Letters, 13 (2010) A95-A97.

[45] R. Wagner, M. Korth, B. Streipert, J. Kasnatscheew, D.R. Gallus, S. Brox, M. Amereller, I. Cekic-Laskovic, M. Winter, ACS Applied Materials & Interfaces, 8 (2016) 30871-30878.

[46] A. Andersson, D. Abraham, R. Haasch, S. MacLaren, J. Liu, K. Amine, Journal of the Electrochemical Society, 149 (2002) A1358-A1369.

[47] M. Balasubramanian, H.S. Lee, X. Sun, X. Yang, A. Moodenbaugh, J. McBreen, D.A. Fischer, F. Ziwen Fu, Electrochemical and Solid-State Letters, 5 (2002) A22-A25.

[48] D. Aurbach, K. Gamolsky, B. Markovsky, G. Salitra, Y. Gofer, U. Heider, R. Oesten,M. Schmidt, Journal of the Electrochemical Society, 147 (2000) 1322-1331.

[49] M.M. Thackeray, S. Kang, C.S. Johnson, J.T. Vaughey, R. Benedek, S. Hackney, Journal of Materials chemistry, 17 (2007) 3112-3125.

[50] S. Shi, J. Tu, Y. Tang, Y. Yu, Y. Zhang, X. Wang, Journal of Power Sources, 221 (2013) 300-307.

[51] M. Park, X. Zhang, M. Chung, G.B. Less, A.M. Sastry, Journal of Power Sources, 195 (2010) 7904-7929.

[52] K. Shaju, G.S. Rao, B. Chowdari, Journal of the Electrochemical Society, 151 (2004) A1324-A1332.

CHAPTER 5

Effect of microwave irradiation on the LMNCA cathode materials prepared using urea and ethylene glycol combustion synthesis

5.1 Introduction

Previous studies have reported the influence of synthesis method and conditions on the physical and electrochemical properties of LMR-NMC cathode materials [1-3]. For example, Zheng and co-workers reported the direct correlation between voltage fade and atomic level spatial distribution of chemical species among lithium manganese- rich cathode materials prepared by several synthesis methods [1]. Iftekhar and co-workers revealed that the electrochemistry of lithium manganese - rich composite materials is significantly affected by the choice of synthetic route [2].

This chapter studies the effect of microwave irradiation on the $Li_{1.2}Mn_{0.52}Ni_{0.13}Co_{0.13}Al_{0.02}O_2$ (LMNCA) powders prepared using combustion methods, again using either urea or EG as fuel. In this work we employ the hybrid microwave irradiation- combustion synthesis to prepare LMNCA cathode materials. The effect of microwave irradiation on the electrochemisty of LMNCA cathode materials prepared using combustions synthesis is also investigated. The samples were exposed to microwave irradiation before the annealing step and the experimental procedure is outlined in Chapter 3 Section 3.3.2 of this thesis. Research efforts carried-out by our group and our previously reported work [4-8] revealed that microwave irradiation particularly with the following conditions; power = 600 W and irradiation time = 20 min, has the ability to improve the morphology, average manganese ion oxidation state and tune the electrochemical performance of electrode materials. These conditions were found to be optimum conditions for microwave irradiation treatment at the pre-annealling step during the synthesis of electrode materials.

5.2 Results and Discussions

5.2.1 Powder X-ray Diffraction Characterization

Figure 5.1 shows the PXRD patterns of the LMNCA-urea mic and LMNCA-EG mic samples. The relatively strong peaks were indexed to the $LiMO_2$ phase based on the hexagonal structure with the space group $R\bar{3}m$ [9,10], while the peak between 2 Theta= 20-25° was indexed to the Li_2MnO_3 phase based on the monoclinic structure with the space group (C_2/m) [11]. The peak between 2 Theta = 20-25° is due to the superlattice structure of Li_2MnO_3 as a result of the Li-TM (transition metal) cation ordering [10]. The PXRD patterns also show a clear splitting of the (018)/(110) doublet peaks for both the samples suggesting a highly ordered layered $R\bar{3}m$ structure [12]. The PXRD patterns also show that the samples are pure with no impurity phase such as Al_2O_3. These results confirm that microwave irradiation did not change the structure of the samples.

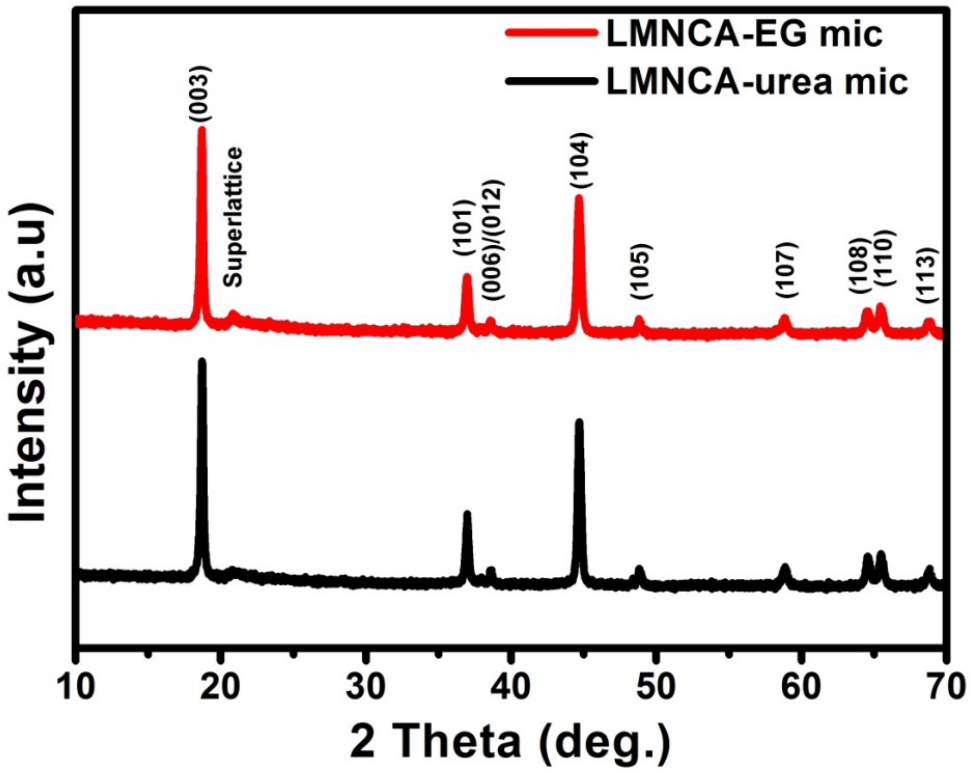


Figure 5.1: PXRD patterns of LMNCA-urea mic and LMNCA-EG mic samples.

The lattice parameters *a* and *c* for the samples were calculated using Rietveld refinement using the $R\bar{3}m$ space group. The calculated lattice parameters with other structural parameters are summarized in Table 5.1. The obtained lattice parameters are consistent with the values reported in literature [13]. The axis ratio *c/a* is close to 5, indicating that the samples exhibit good hexagonal ordering [12]. However, the peak intensity ratio $I_{(003)}/I_{(104)}$ is larger for LMNCA-EG mic compared to LMNCA-urea mic indicating reduced Li-Ni cation mixing effect in LMNCA-EG mic [14]. The PXRD analysis also reveals an increase in the lattice parameters and crystal density for LMNCA-EG mic compared to LMNCA-urea mic. This suggests that there is lower in Mn^{4+} ions in the LMNCA-EG mic sample compared to the LMNCA-urea mic sample. The Mn^{3+} ions are larger ionic radius (0.66 Å) compared to the Mn^{4+} (0.60 Å) ions [15], therefore the increase in lattice parameters and crystal density may suggest more Mn^{3+} and less Mn^{4+} ions.

Table 5.1: Summary of crystallographic results LMNCA-urea mic and LMNCA-EG mic samples

Materials	**Lattice parameter ±0.003 (Å)**	**Axis ratio *(c/a)***	**$I_{(003)}/I_{(104)}$ ratio**	**Cell volume ±0.002 ($Å^3$)**	**Crystal density ±0.002 (g cm^{-3})**	**R_p (%)**	**R_{wp} (%)**	**R_{bragg} (%)**
LMNCA-urea mic	***a***-2.852 ***c***-14.233	4.991	1.259	100.23	235.055	1.89	2.45	1.478
LMNCA-EG mic	***a***-2.853 ***c***-14.244	4.993	1.327	100.38	309.735	2.02	2.63	1.336

5.2.2 X-ray Photoelectron Spectroscopy Characterization (XPS)

X-ray photoelectron spectroscopy (XPS) analysis was used to determine the oxidation states of the transition metals especially for the manganese ions. Figure 5.2 (a-d) shows the XPS spectra of the Mn ions.

Figure 5.2 (a,b) shows the Mn 3s spectra of the samples. The Mn 3s spectra give two intense peaks at about 84 and 88 eV and their binding energy difference is 4.3 and 4.7 eV for LMNCA-urea mic and LMNCA-EG mic samples, respectively. This suggests that the majority of the manganese ions are in the Mn^{4+} oxidation state. To confirm this, the Mn 2p spectra of the

samples was examined and show two major peaks at around 642 and 654 eV, corresponding to the Mn $2p_{3/2}$ and Mn $2p_{1/2}$ peaks. The binding energy difference between the Mn $2p_{3/2}$ and $2p_{1/2}$ peak is around 11.5 eV and this confirms that most of the Mn ions in the samples are in Mn^{4+} oxidation state. These results are consistent to the XPS findings by Honglei Li *et al*. [16] and Li Li *et al*. [17] for $Li_{1.2}Mn_{0.54}Ni_{0.13}Co_{0.13}O_2$ (LMNC) materials.

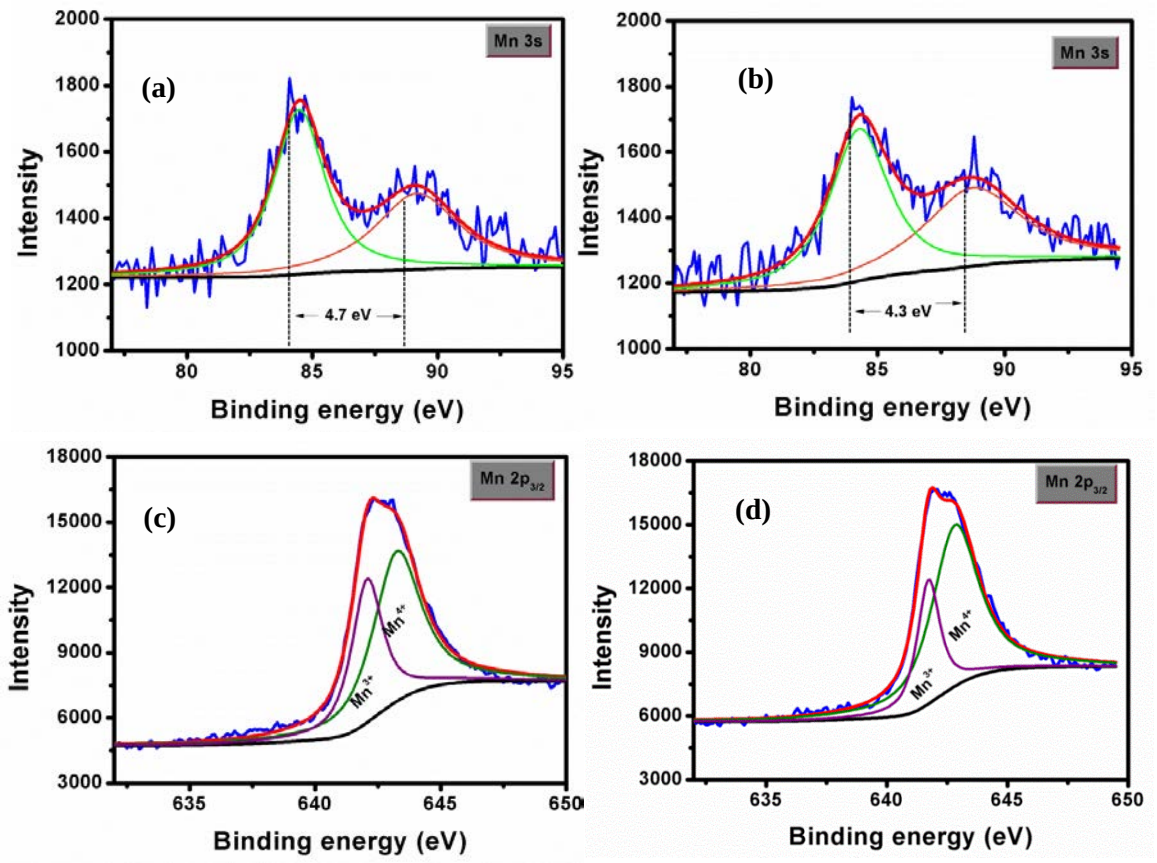


Figure 5.2: XPS data of Mn 3s and Mn $2p_{3/2}$ for (a,c) LMNCA-EG mic, and (b,d) LMNCA-urea mic samples.

However, the descrepancy in the binding energy difference of the Mn 3s peaks of the samples, suggests that the samples contain different amounts of the Mn^{4+} ions. The broadness of the Mn 2p peak indicates that there also exist some Mn^{3+} ions additionally to the Mn^{4+} ions [18]. Then the Mn $2p_{3/2}$ peak (Figure 5.2 (c,d)) was deconvoluted into two peaks at about 641 eV and 643 eV, corresponding to the Mn^{3+} and Mn^{4+} ions, respectively. The relative amounts of Mn^{3+} and Mn^{4+} ions in the samples were determined from their corresponding peak areas. Table 5.2 reports the Mn $2p_{3/2}$ peak position, Mn^{3+}/Mn^{4+} cation distribution, Mn^{3+}:Mn^{4+} ratio and the average manganese oxidation state. These XPS results reveal that the LMNCA-EG mic has lower Mn^{4+} ions compared to LMNCA-urea mic. The Mn^{4+} content is 59 and 72 % for

LMNCA-EG mic and LMNCA-urea mic, respectively. Comparing to non-microwave irradiated samples, the microwave irradiation resulted in the decrease of the Mn^{4+} content for both samples and thus decreased the average manganese oxidation state. The average oxidation state of manganese was calculated using Equation 4.1. The Mn^{4+} content is 77 and 79 % for the non-microwave irradiated LMNCA-EG and LMNCA-urea, respectively. Low Mn^{4+} content is beneficial for the reduction of Li_2MnO_3 phase activation for reduced voltage fade. Mn^{4+} ions are further decreased in the LMNCA-EG mic because during the synthesis the ethylene glycol also complexes the metal cations and this results in the incomplete oxidation of the manganese ions and thus decreases the Mn^{4+} ions.

Table 5.2: Summary of Mn $2p_{3/2}$ peak positions and cation distribution of the LMNCA-EG mic and LMNCA-urea mic samples

Sample	Binding energy position (eV)		Cation distribution			Average oxidation state of Mn
	Mn^{4+}	Mn^{3+}	Mn^{4+} (%)	Mn^{3+} (%)	Mn^{3+}/Mn^{4+}	
LMNCA-EG mic	643.3	642.1	59	41	0.70	3.77
LMNCA-urea mic	642.8	641.7	72	28	0.39	3.49

Figure 5.3 (a-d) shows the XPS spectra of the Co and Ni ions. General observations do not reveal any significant difference in the oxidation states of the Co and Ni between the samples and the non-microwave irradiated samples. Figure 5.3 (a,b) shows the Co 2p spectra and Figure 5.3 (c,d) shows the Ni 2p spectra of the samples. The Co 2p and Ni 2p spectra each exhibit four peaks than include the two intense peaks and their two corresponding satellite peaks denoted as "S" in the spectra. The two relatively intense Co 2p peaks at around 798 and 780 eV are assigned to Co $2p_{1/2}$ and Co $2p_{3/2}$, respectively. The binding energy difference between the Co $2p_{3/2}$ and Co $2p_{1/2}$ peaks for all the samples are about 15 eV indicating that the cobalt ions for all the samples are in the Co^{3+} oxidation state [12,18-20]. The binding energy of the two intense Ni 2p peaks, Ni $2p_{1/2}$ and Ni $2p_{3/2}$ peaks is 879 and 855 eV, respectively; and their binding energy difference is around 18 eV corresponding to the Ni^{2+} oxidation state in the samples [12,21].

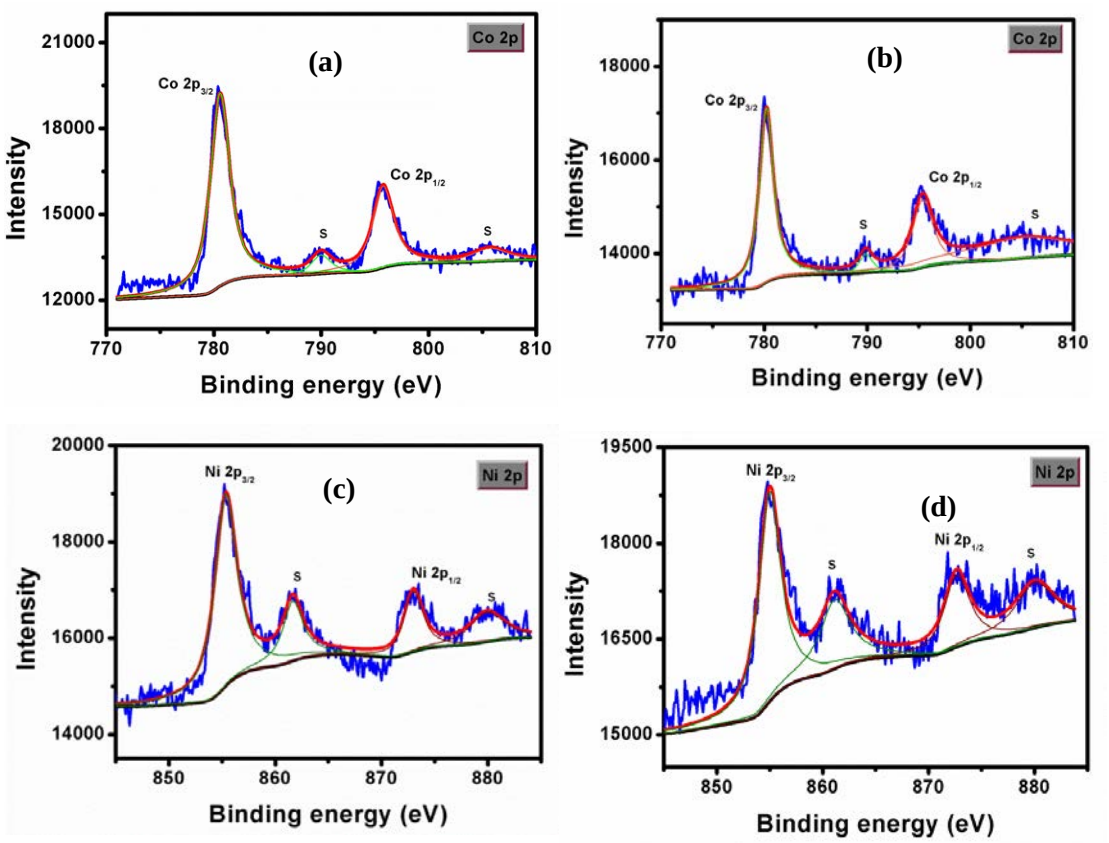


Figure 5.3: XPS data of Co 2p and Ni 2p for (a,c) LMNCA-EG mic, and (b,d) LMNCA-urea mic samples. Symbol "S" denotes the satellite signals for the corresponding metal ions.

5.2.3 Scanning Electron Microscopy Characterization (SEM)

Figure 5.4 shows the SEM images of the samples at high and low magnification. The LMNCA-EG mic sample exhibit polyhedral particles with particle size in the range of 50-100 nm and the average particle size is around 64 nm. The LMNCA-urea mic sample exhibit sphere-like particles with the particle size in the range of 60-110 nm and the average particle size is around 86 nm. The microwave irradiation in LMNCA-EG mic sample reduced the particle size, while it slightly increased the particle size for the LMNCA-urea mic. The particle size distribution was 50-90 nm and 80-200 nm for the unmicrowave irradiated LMNCA-urea and LMNCA-EG samples, respectively. The microwave irradiation did not change the shape of either of the samples.

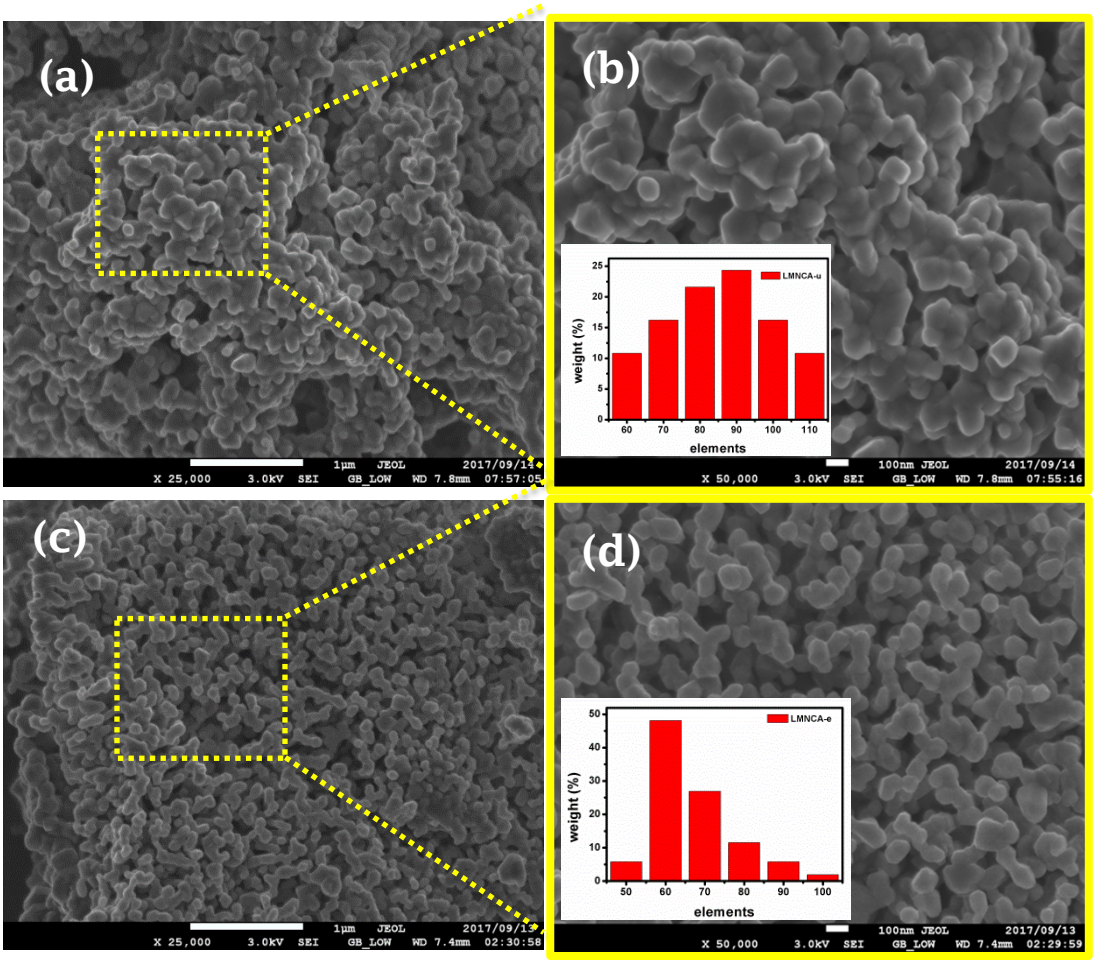


Figure 5.4: SEM images of (a-b) LMNCA-urea mic and (c-d) LMNCA-EG mic sample.

5.2.4 Electrochemical Characterization

5.2.4.1 Cyclic voltammetry

Cyclic voltammetry was carried out at 0.1 mV s^{-1} between 2.0 - 4.8 V. Figure 5.5 shows the cyclic voltammograms of cycles 1,2,5 and 10 of the samples. The microwave irradiated and unmicrowave irradiated samples have similar redox behaviour. The first cycle shows; (II) the oxidation of the Ni^{2+} and Co^{3+} transition metals at ~4.2 V and (III) the activation of the Li2MnO3 at 4.7 V. The reduction peaks at (II)' and (II)'' are due to the reduction of the Ni4+ and Co^{3+} in the octahedral and Ni^{4+} in the tetrahedral sites. In the second and third scans, the strong oxidation peak at (III) disappears, and the peak at (II) broadens indicating more oxidation of the Ni^{2+} and Co^{3+}. The activation of the Li_2MnO_3 induces a new peak at (I)' due to the Mn^{4+}/Mn^{3+} reduction from the spinel phase formed. The corresponding oxidation peak of this new peak at (I) is due to the Mn^{3+}/Mn^{4+} oxidation of the spinel phase as the material is

cycled. However, the Mn^{3+}/Mn^{4+} redox peaks are observed to be more intense for the LMNCA-urea mic compared to LMNCA-EG mic upon cycling.

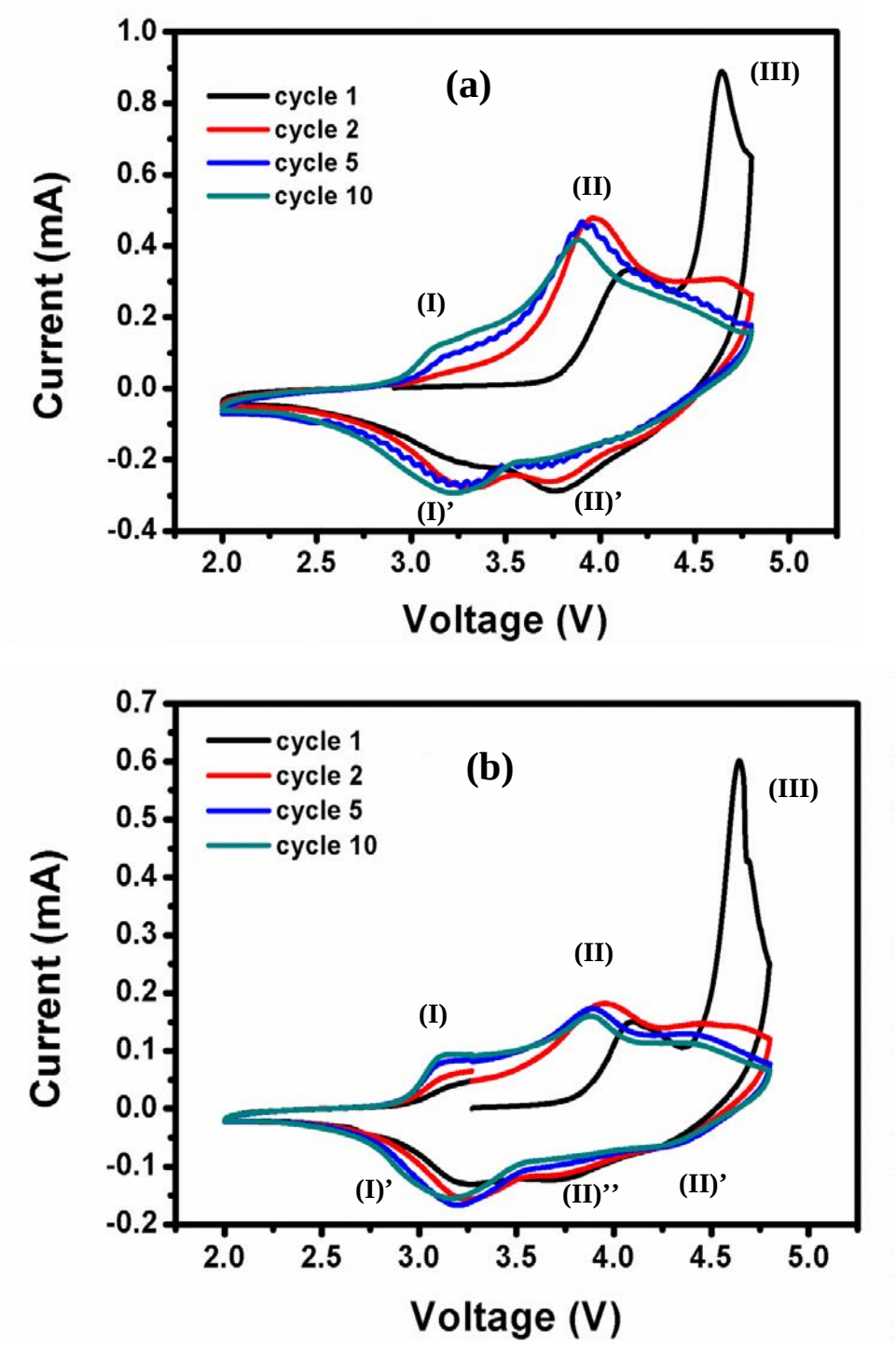


Figure 5.5: Cyclic voltammetry at 0.1 mV s^{-1} between 2.0 - 4.8 V (a) LMNCA-urea mic and (b) LMNCA-EG mic.

5.2.4.2 Galvanostatic charge-discharge

The galvanostatic charge-discharge studies were performed to determine the electrochemical performance of the LMNCA-urea mic and LMNCA-EG mic samples. Figure 5.6 (a,b) compares the 1st, 2nd, 10th, 30th and 50th cycles of the samples cycled between 2.0 and 4.8 V at 0.1 C at room temperature. The first charge curve shows two plateaus due to the two-step charging process from the two different lithium extraction processes. The first voltage plateau at ~4.0 V is due to the delithiation of the $LiMO_2$ phase corresponding to the oxidation of the Ni^{2+} to Ni^{4+} and Co^{3+} to Co^{4+}. The second voltage plateau at ~4.5 V is due to the activation of the Li_2MnO_3 phase due to the extraction of Li_2O (in the form of Li^+ and O_2) from the Li_2MnO_3 phase. This activation of the Li_2MnO_3 phase is only observed in the first cycle and disappears from the second cycle onwards.

LMNCA-urea mic shows a higher discharge capacity of ca. 361 mAh/g while LMNCA-EG mic exhibit a capacity of ca. 221 mAh/g. The capacity of LMNCA-urea mic is high compared to the LMNCA-EG mic because the former contains a higher content of Mn^{4+} ions at 72 % while the latter contains 59 % of Mn^{4+} ions. An increase in Mn^{4+} ions results in an increased in the activation of the Li_2MnO_3 phase which results in high capacity densities. As discussed before, the LMR-NMC materials get their high capacities from the activation of the Li_2MnO_3 phase.

To gain further insight into the Li_2MnO_3 activation, differential capacity vs. voltage curves are plotted in Figure 5.7 (a-f). The oxidation in the first cycle (Figure 5.7 (a,d)) reveals the activation of the Li_2MnO_3 phase at ca. 4.51 - 4.53 V. The activation peak is longer for LMNCA-urea mic compared to LMNCA-EG mic samples, confirming increased Li_2MnO_3 activation for LMNCA-urea mic. The activation of the Li_2MnO_3 phase results in the formation of the MnO_2-like spinel phase, which induces a new reduction peak at ca. 3.33 V upon cycling. The new Mn^{4+}/Mn^{3+} redox peaks are more pronounced for the LMNCA-urea mic. These redox peaks start appearing from cycle 1 and become intense upon cycling (Figure 5.7 (d-f)), especially for LMNCA-urea mic . Therefore, these results also confirm the increase in the Li_2MnO_3 activation in LMNCA-urea mic compared to LMNCA-EG mic.

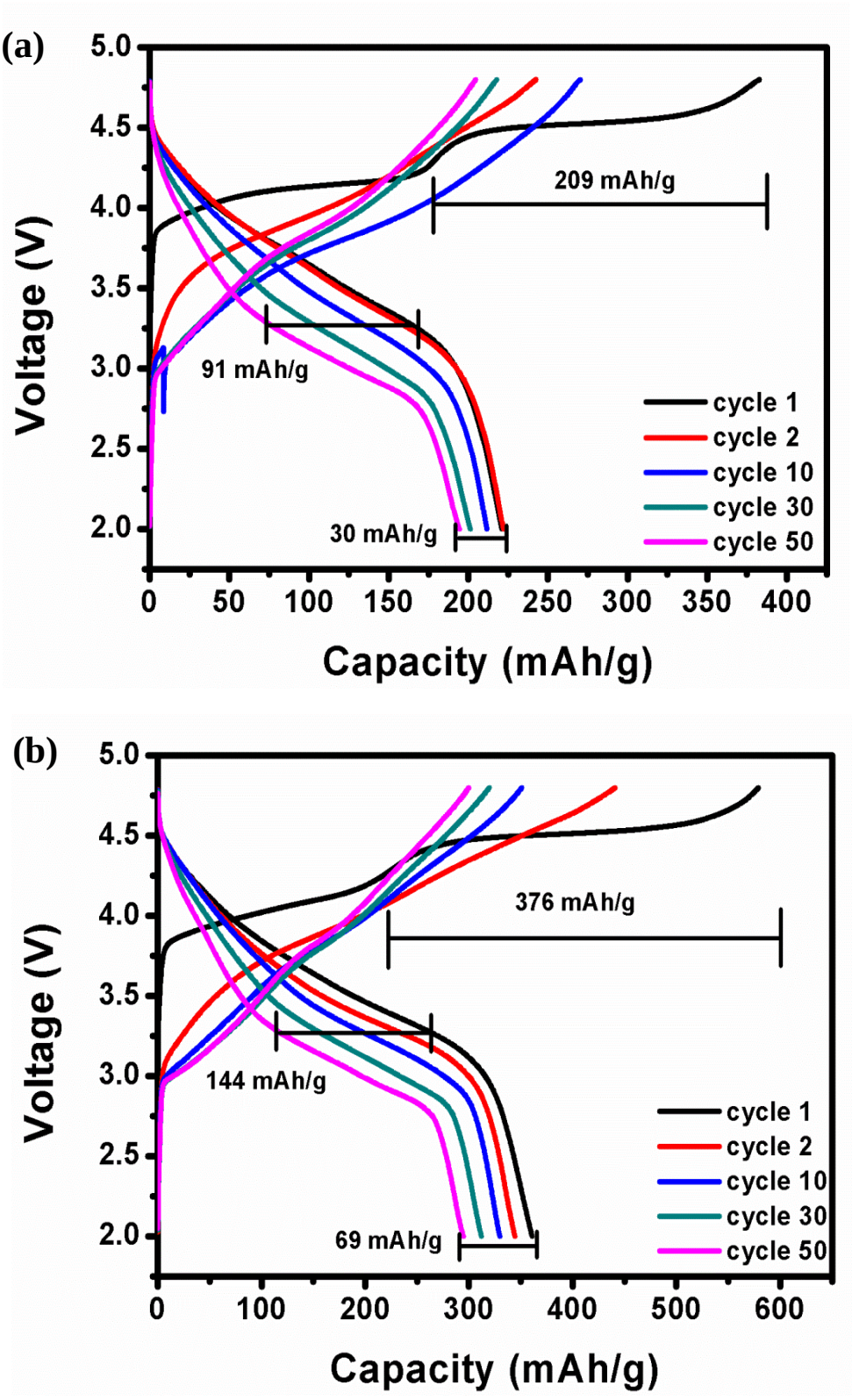


Figure 5.6: Galvanostatic charge-discharge at 0.1 C for (a) LMNCA-EG mic and (b) LMNCA-urea mic after 50 cycles.

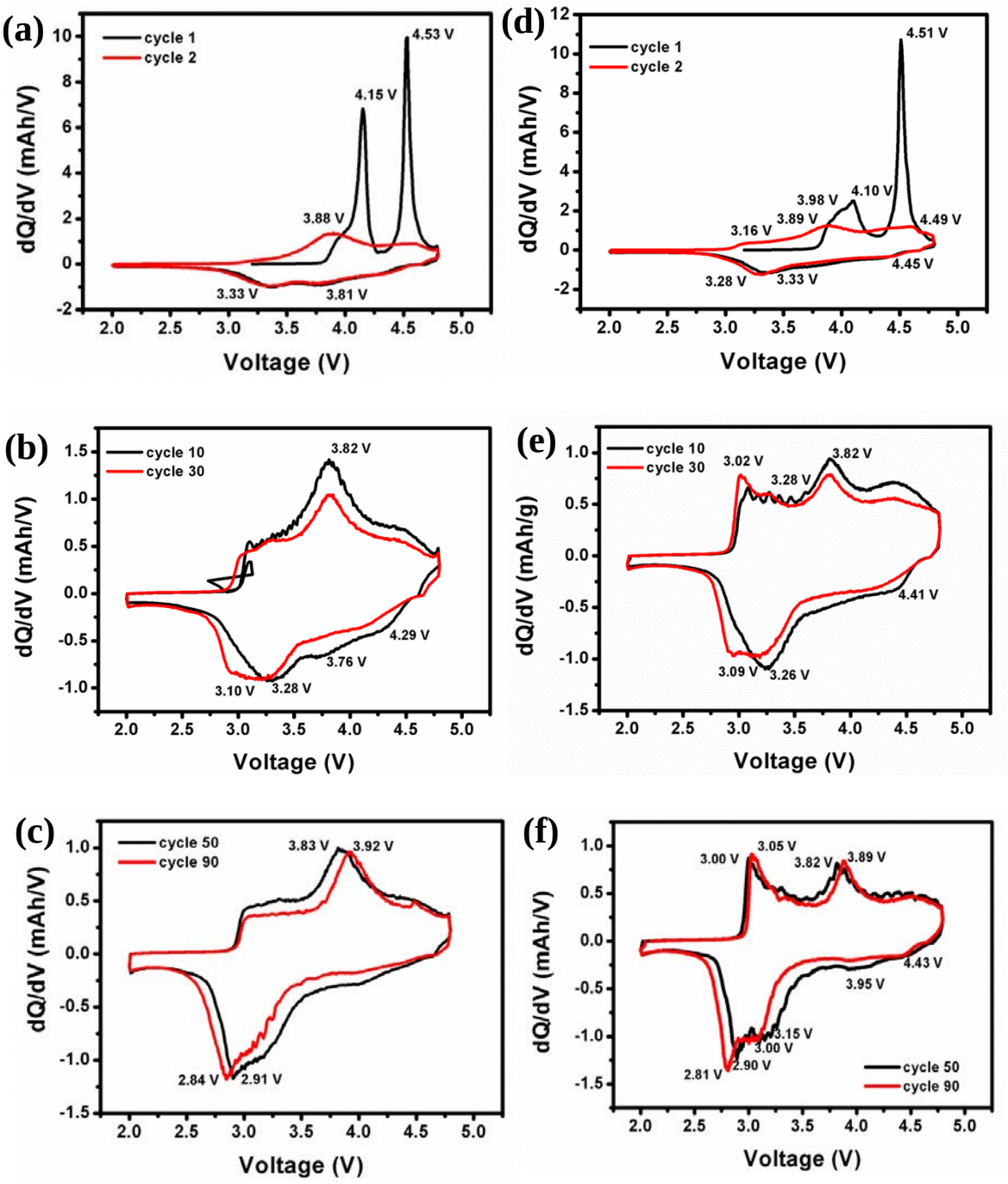


Figure 5.7: Differential capacity vs. voltage curves for (a-c) LMNCA-EG mic and (d-f) LMNCA-urea mic after 90 cycles.

Additionally, LMNCA-EG mic sample also shows that the oxidation and reduction of Ni occurs both from the tetrahedral and octahedral sites. This is observable by the intense oxidation peak between 4.12 - 3.82 V and the corresponding reduction peaks appearing at different voltages. The reduction at 3.76 (cycle 10) and 3.81 V (cycle 1 & 2) are due to the reduction in tetrahedral and the reduction at 4.18 and 4.29 V are due to the reduction in the octahedral sites. However, LMNCA-urea mic sample shows the reduction of Ni in the octahedral sites and the peaks are seen at 4.45 V (cycle 1 & 2), 4.41 V (cycle 10 & 30), 3.95 V (cycle 50) and 4.43 V (cycle 90). The oxidation of Co^{3+} to Co^{4+} and Ni^{2+} to Ni^{4+} is observed at 4.10 - 4.15 V.

5.2.4.3 Cycle Performance and Coulombic Efficiency (CE)

Figure 5.8 (a,b) shows the cycle performance and the coulombic efficiency of the LMNCA-urea mic and LMNCA-EG mic materials, respectively. The materials possess a good cycle performance at 0.1 C and 2 C. The capacity retention after 50 cycles at 0.1 C is 88 % and 82 % for LMNCA-EG mic and LMNCA-urea mic, respectively. Microwave irradiation increased the capacity retention of both microwave irradiated LMNCA-EG mic and LMNCA-urea mic. The capacity retention after 50 cycles is 84 % and 76 % for the non-microwave irradiated LMNCA-urea and LMNCA-EG samples, respectively. The microwave irradiated samples also have excellent capacity retention at high current rates. The capacity retention is 96 % and 102 % at 2 C after 50 cycles for LMNCA-EG mic and LMNCA-urea mic, respectively.

Coulombic efficiency (CE) at 0.1 C for the first cycle is reasonable at 58 % for LMNCA-EG mic and 62 % for LMNCA-urea mic. However, the coulombic efficiency reaches over 90 % for LMNCA-EG from the 2^{nd} cycle, while it stabilizes after 6 cycles for LMNCA-urea mic and this is due to rearrangement of the lattice upon cycling due to the increase in the spinel formation. The coulombic efficiency reaches to 95 % and 98 % for LMNCA-EG mic and LMNCA-urea mic, respectively, after 50 cycles. However, the coulombic efficiency of the first cycle is improved at 2 C and is 88 % and 89 % for LMNCA-EG mic and LMNCA-urea mic, respectively. The coulombic efficiency at 2 C after 50 cycles is 99 % for both samples. Table 5.3 displays the capacity, retention and coulombic efficiency at 0.1 C and 2 C for the samples. These results indicate that microwave irradiation results in good reversibility of the lithium-ion extraction and insertion reactions in the materials and also contributes to the good cycle performance of the materials.

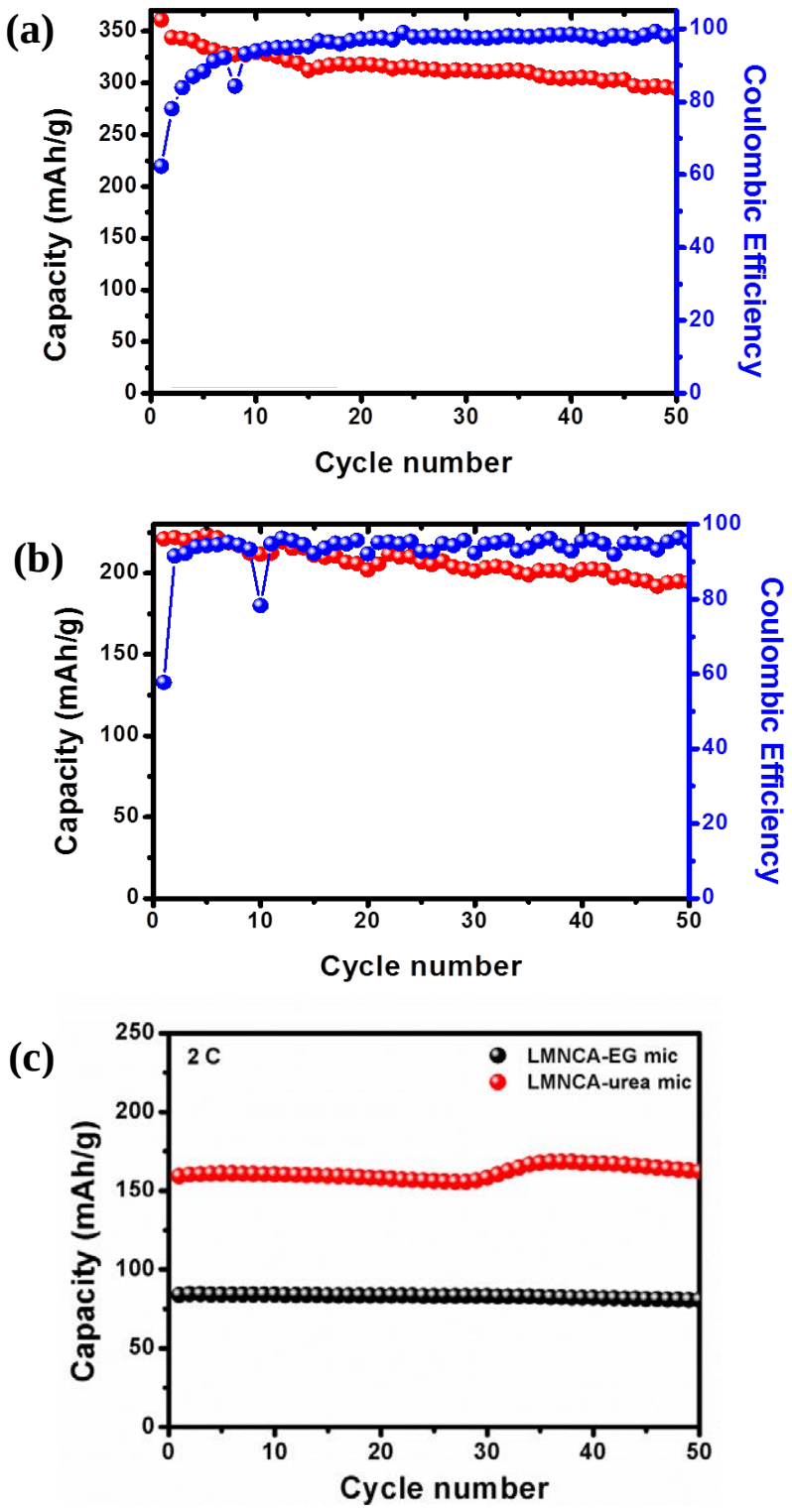


Figure 5.8: Cycle performance and the coulombic efficiency of the materials (a) LMNCA-urea mic and (b) LMNCA-EG mic, and (c) Cycle performance of both samples at 2 C.

Table 5.3: Capacity retention and coulombic efficiency at 0.1 C and 2 C of LMNCA-urea mic and LMNCA-EG mic samples.

Cycle performance	LMNCA-EG mic	LMNCA-urea mic
Charge capacity (mAh/g): 0.1 C, 1st cycle	383	579
Discharge capacity (mAh/g): 0.1 C, 1st cycle	221	361
Capacity Retention (%): 0.1 C, 50th cycle	88	82
Coulombic efficiency (%): 0.1 C, 1st cycle	58	62
Coulombic efficiency (%): 0.1 C, 50th cycle	95	98
Charge capacity (mAh/g): 2 C, 1st cycle	98	178
Discharge capacity (mAh/g): 2 C, 1st cycle	84	159
Capacity Retention (%): 2 C, 50th cycle	96	102
Coulombic efficiency(%): 2 C, 1st cycle	86	89
Coulombic efficiency (%): 2 C, 50th cycle	99	99

5.2.4.4 Rate capability

Figure 5.9 shows the rate capability of the samples. The cells were charge and discharged at 0.5, 1, 2, 3 C and again at 0.5 C. The microwave irradiation also improved the rate capacity of the LMNCA-urea mic and LMNCA-EG mic samples and this is due to that the microwave irradiation resulting in small particle size and high surface area.

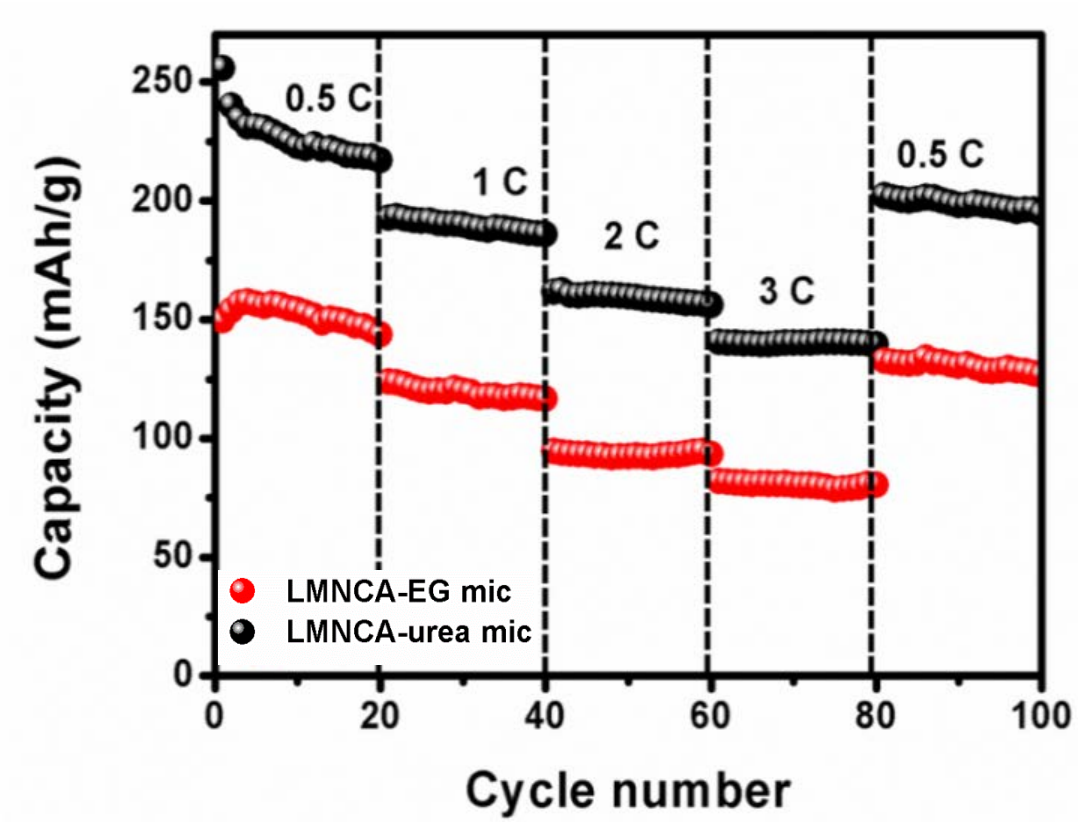


Figure 5.9: Rate capability of LMNCA-urea mic and LMNCA-EG mic materials.

5.2.4.5 Electrochemical impedance spectroscopy (EIS)

Figure 5.10 shows the Nyquist plots obtained from the electrochemical impedance spectroscopy (EIS) analysis of the materials. Figure 5.10 (a) compares the EIS data obtained before and after 100 cycles at the open circuit voltage, where OCV ~3.0 V vs. The equivalent circuit used for the EIS data fitting and the EIS fitting parameters are as defined in the previous chapter. Table 5.4 compares the R_{ct} and Z_w of microwave irradiated samples (LMNCA-urea mic and LMNCA-EG mic) with non-microwave irradiated samples (LMNCA-urea and LMNCA-EG materials), measured at OCV before and after cycling. These results show that microwave irradiation reduces the impedance of LMNCA materials.

Table 5.4: Comparison of R_{ct} and Z_w of LMNCA-urea mic and LMNCA-EG mic with non-microwave irradiated LMNCA-urea and LMNCA-EG samples.

Materials	R_{CT} (Ω)	Z_w $\Omega.s^{-1/2}$
LMNCA-urea (OCV)	544.0	322
LMNCA-urea (100 cyc)	806.4	152
LMNCA-urea mic (OCV)	257.1	94.2
LMNCA-urea mic (100 cyc)	1 171	119.2
LMNCA-EG (OCV)	719.9	216
LMNCA-EG (100 cyc)	275.9	76
LMNCA-EG mic (OCV)	142.2	38.2
LMNCA-EG mic (100 cyc)	152.8	86.8

Figure 5.10 (b) shows the EIS data obtained at 4.2 and 4.5 V to further understand the impact of the activation of the Li_2MnO_3 phase on the EIS performance. 4.2 V corresponds to the voltage before activation and the voltage around the oxidation of the transition metals (Ni and Co) and 4.5 V is the voltage of the Li_2MnO_3 activation. The impedance is similar at 4.2 and 4.5 V for the LMNCA-EG mic sample but slightly increases from 4.2 to 4.5 V for the LMNCA-urea mic sample. These results indicate that the increase in the Li_2MnO_3 activation increases the impedance. The R_s, R_f and R_{ct} values at 4.2 V and 4.5 V are lower for LMNCA-EG mic compared to LMNCA-urea mic. This is due to the resistance to the Li_2MnO_3 activation in the LMNCA-EG mic sample and improved particle morphology, i.e. small particles compared to LMNCA-urea mic. The R_s, R_f and R_{ct} values, especially the R_f, for LMNCA-urea mic increased upon charging from 4.2 V to 4.5 V. The increase in the R_f value is due to the formation of a surface film and the changes in surface structure and composition as the extensive removal of Li_2O from the Li_2MnO_3 activation process damages the electrode surface [9].

Figure 5.10 (c) shows the Z′ vs. $\omega^{-1/2}$ plots and shows clearly that the LMNCA-urea mic has higher impedance compared to LMNCA-EG mic. Figure 5.10 (d) studies the lithium diffusion coefficient (D_{Li^+}) at different voltages. It is found that the diffusion coefficient only changes very slightly when charging (1st cycle charge) from 3.0 V to 3.7 V; this is because as observed from the CV analysis no electrochemical reactions due to the lithium-ion intercalation and de-intercalation occurs in this range. But, the diffusion coefficient rapidly increases and then

decreases when charging from 4.0 V - 4.5 V, especially for LMNCA-urea mic and this is consistent with the oxidation of Ni, Co ions upon charging and Li_2MnO_3 activation. The lithium-ions diffuse faster at the 4.0 - 4.5 V region because the "c" lattice parameter is reported to be increasing upon charging towards 4.8 V [22] and this means that the space around the Li-layer also increases and the activation energy for Li motion is reduced [23]. This then allows the fast diffusion of the lithium ions. The lithium diffusion coefficient was also determined after 100 cycles. It is found to be higher for LMNCA-urea mic compared to the LMNCA-EG mic because of larger *c* lattice parameter and larger hexagonal ordering (Table 5.1). The lithium diffusion coefficient is higher for microwave irradiated samples compared to non-microwave irradiated samples. This shows that the microwave irradiation also increases the lithium diffusion coefficient resulting in faster lithium-ion kinectics. Table 5.5 summaries the EIS results of LMNCA-urea mic and LMNCA-EG mic samples.

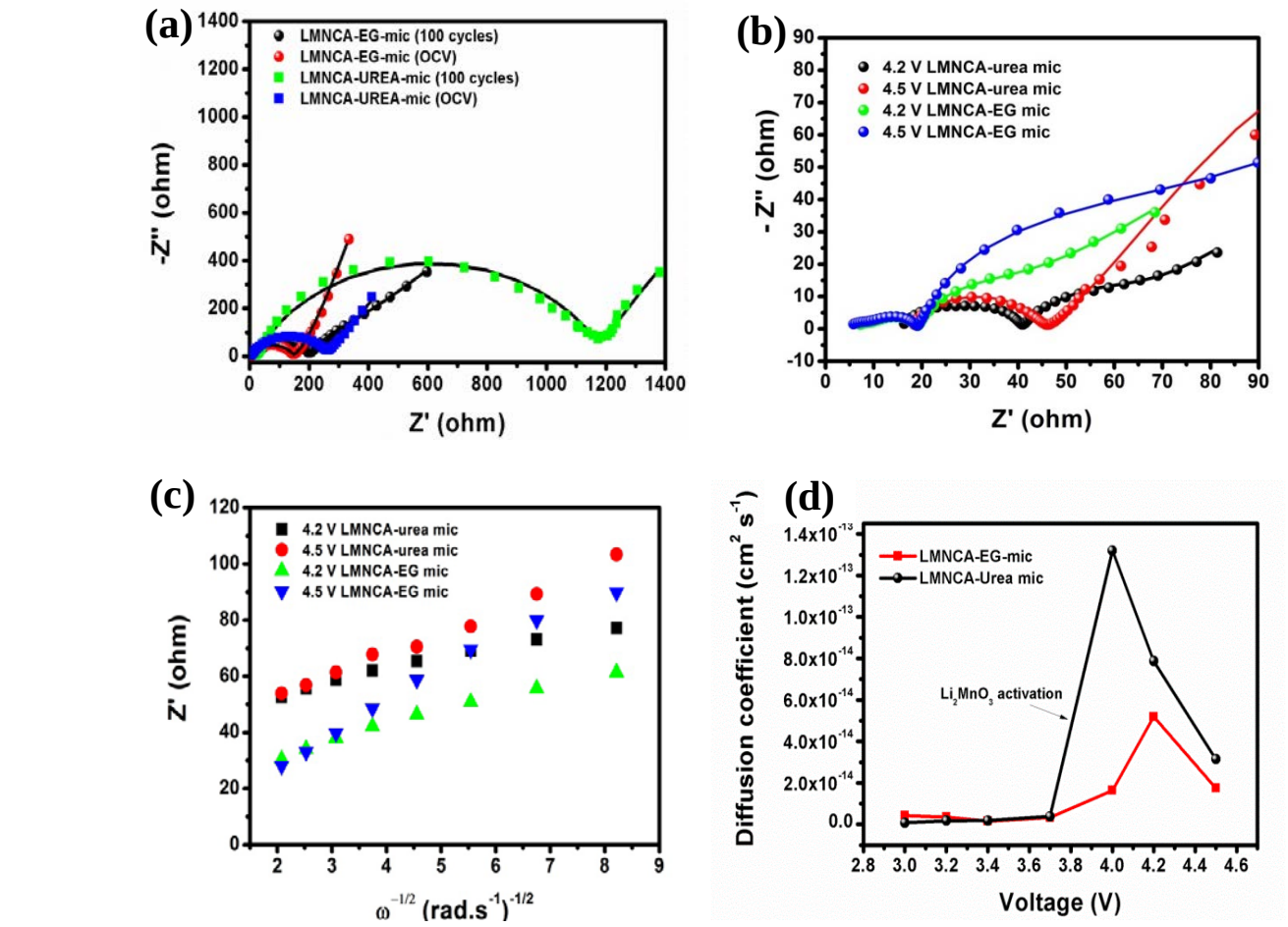


Figure 5.10: EIS and diffusion co-efficient analysis of LMNCA-urea mic and LMNCA-EG mic samples.

Table 5.5: Electrochemical impedance spectroscopy fitted parameters and diffusion coefficient.

	Charging Potential (V)	R_{SEI} (Ω)	R_f (Ω)	R_{CT} (Ω)	CPE_f		CPE_{CT}		Z (Ω $s^{-1/2}$)	D_{Li^+} (cm^2 s^{-1})
					CPE_f ($F.s^{(a-1)}$)	a	CPE_{CT} ($F.s^{(a-1)}$)	a		
LMNCA-urea mic	4.2	15.2	17.9	25.8	0.06	0.82	58.81e-6	0.67	5.6	9.94e-14
	4.5	17.8	121.0	27.4	0.24	0.99	16.36e-6	0.80	12.3	2.50e-14
	OCV	2.7	22 381	257.1	0.02	0.98	17.45e-6	0.70	94.2	7.83e-16
	100^{th} cycle	20.1	28.0	1171	0.02	0.90	21.37e-6	0.94	119.2	3.32e-15
LMNCA-EG mic	4.2	6.3	13.9	18.9	0.49e-3	0.54	0.03	0.98	8.8	6.23e-14
	4.5	4.4	16.1	55.8	0.68e-3	0.49	0.03	0.95	11.9	1.77e-14
	OCV	3.9	2 490	142.2	0.049	0.97	13.35e-6	0.74	38.2	4.34e-15
	100^{th} cycle	17.3	197.3	152.8	24.47e-6	0.67	4.77e-3	0.90	86.8	8.56e-16

5.3 Conclusions

LMNCA-urea mic and LMNCA-EG mic samples were successfully prepared using ethylene glycol and urea as fuels. Microwave irradiation was applied before the pre-annealing step and its effect on the electrochemical performance of LMNCA cathode materials was investigated. Microwave irradiation resulted in decreased Mn^{4+} ion and particle size, especially for LMNCA-EG mic. The microwave irradiation increased the capacity of LMNCA-urea mic due to increased Li_2MnO_3 activation, while the LMNCA-EG mic possessed a lower capacity and exhibited resistance to the Li_2MnO_3 activation. The Li_2MnO_3 activation is larger for LMNCA-urea mic because of the high content of Mn^{4+} ions at 72 % compared to LMNCA-EG mic with 59 % Mn^{4+} ions in the structure before cycling. The cycle performance and the rate capability of microwave irradiated LMNCA-urea mic and LMNCA-EG mic samples was improved because of reduced particle size. Microwave irradiation also resulted in decrease electrochemical impedance and higher lithium ion diffusion coefficients. Therefore this work showed that microwave irradiation improved the electrochemical performance for LMNCA materials prepared using either urea or EG as fuel during the combustion synthesis. However, there still exist differences in the electrochemical performance between urea and EG prepared samples, as observed in the study of non-microwave irradiated samples.

5.4 References

[1] J. Zheng, M. Gu, A. Genc, J. Xiao, P. Xu, X. Chen, Z. Zhu, W. Zhao, L. Pullan, C. Wang, J.G. Zhang, Nano letters, 14 (2014) 2628-2635.

[2] M. Iftekhar, N. Drewett, A. Armstrong, D. Hesp, F. Braga, S. Ahmed, L. J. Hardwick, Journal of the Electrochemical Society, 161 (2014) A2109-A2116.

[3] T. Zhao, S. Chen, L. Li, X. Zhang, R. Chen, I. Belharouak, F. Wu, K. Amine, Journal of Power Sources, 228 (2013) 206-213.

[4] C.J. Jafta, M.K. Mathe, N. Manyala, W.D. Roos, K.I. Ozoemena, ACS applied materials & interfaces, 5 (2013) 7592-7598.

[5] C.J. Jafta, K. Raju, M.K. Mathe, N. Manyala, K.I. Ozoemena, Journal of the Electrochemical Society, 162 (2015) A768-A773.

[6] F.P. Nkosi, C.J. Jafta, M. Kebede, L. le Roux, M.K. Mathe, K.I. Ozoemena, RSC Advances, 5 (2015) 32256-32262.

[7] F.P. Nkosi, K. Raju, N. Palaniyandy, M. Reddy, C. Billing, K.I. Ozoemena, Journal of the Electrochemical Society, 164 (2017) A3362-A3370.

[8] K. Raju, F.P. Nkosi, E. Viswanathan, M.K. Mathe, K. Damodaran, K.I. Ozoemena, Physical Chemistry Chemical Physics, 18 (2016) 13074-13083.

[9] M.M. Thackeray, S. Kang, C.S. Johnson, J.T. Vaughey, R. Benedek, S. Hackney, Journal of Materials chemistry, 17 (2007) 3112-3125.

[10] D. Mohanty, A.S. Sefat, S. Kalnaus, J. Li, R.A. Meisner, E.A. Payzant, D.P. Abraham, D.L. Wood III,C. Daniel, Journal of Materials Chemistry A, 1 (2013) 6249-6261.

[11] M. Thackeray, S. Kang, C. Johnson, J. Vaughey, S. Hackney, Electrochemistry Communications, 8 (2006) 1531-1538.

[12] X. Zhang, D. Luo, G. Li, J. Zheng, C. Yu, X. Guan, C. Fu, X. Huang, and L. Li, Journal of Materials Chemistry A, 1 (2013) 9721-9729.

[13] J.R. Croy, K.G. Gallagher, M. Balasubramanian, Z. Chen, Y. Ren, D. Kim, S. Kang, D.W. Dees, M.M. Thackeray, The Journal of Physical Chemistry C, 117 (2013) 6525-6536.

[14] X. Zhang, W. Jiang, A. Mauger, F. Gendron, C. Julien, Journal of Power Sources, 195 (2010) 1292-1301.

[15] S. Bao, Y. Liang, W. Zhou, B. He, H. Li, Journal of Power Sources, 154 (2006) 239-245.

[16] H. Li, S. Zhang, X. Wei, P. Yang, Z. Jian, J. Meng, RSC Advances, 6 (2016) 79050-79057.

[17] L. Li, X. Zhang, R. Chen, T. Zhao, J. Lu, F. Wu, K. Amine, Journal of Power Sources, 249 (2014) 28-34.

[18] C. Fu, G. Li, D. Luo, J. Zheng, L. Li, Journal of Materials Chemistry A, 2 (2014) 1471-1483.

[19] C. Yu, G. Li, X. Guan, J. Zheng, L. Li, T. Chen, Electrochimica Acta, 81 (2012) 283-291.

[20] L. Dahéron, R. Dedryvere, H. Martinez, M. Ménétrier, C. Denage, C. Delmas, D. Gonbeau, Chemistry of Materials, 20 (2007) 583-590.

[21] S. Kang, J. Kim, M.E. Stoll, D. Abraham, Y. Sun, K. Amine, Journal of Power Sources, 112 (2002) 41-48.

[22] D. Mohanty, A.S. Sefat, J. Li, R.A. Meisner, A.J. Rondinone, E.A. Payzant, D.P. Abraham, D.L. Wood III, C. Daniel, Physical Chemistry Chemical Physics, 15 (2013) 19496-19509.

[23] K. Kang, Y.S. Meng, J. Breger, C.P. Grey, G. Ceder, Science (New York, N.Y.), 311 (2006) 977-980.

CHAPTER 6

Preparation of LMNCA cathode materials from α-MnO_2 nanowires

6.1 Introduction

LMR-NMC materials are generally synthesised using the co-precipitation method which relies on precise control of synthesis conditions such as pH, feeding rate of the co-precipitator, temperature and stirring speed [1-5]. The preparation of $0.5Li_2MnO_3 \cdot 0.5LiNi_{1/3}Co_{1/3}Mn_{1/3}O_2$ cathode materials using co-precipitation results in spherical agglomerates with particle size between 5-10 microns [4,6]. However, these spherical agglomerates exhibit poor rate capability as they block the lithium intercalation and de-intercalation when charging above 4.4 V, especially at high current densities [7].

The synthesis employed in this Chapter involves the use of α-MnO_2 nanowires as the manganese source and pluronic acid as both a fuel and complexing agent to control the growth of the particles. The complexation of the metal cations by the pluronic acid prevents the precipitation of the metal cations and forms a stable precursor before the heating steps. MnO_2 materials have been used as manganese precursors in the preparation of cathode materials for lithium-ion batteries [8,9]. This is because MnO_2 is cheap, environmentally friendly, abundant and have good adsorption of lithium. It has been observed from previous studies that the structure and the morphology of the manganese based cathode materials are affected by the manganese precursor [8]. Therefore, α-MnO_2 nanowires were used in this work to influence the morphology of the LMNCA material in order to improve the electrochemical performance. This is because α-MnO_2 contains (2 × 2) + (1 × 1) one-dimensional (1D) tunnel structures with good absorption properties [10-12]. Therefore they can easily accommodate and absorb Li^+ into the structure [9]. α-MnO_2 nanowires also have high reactivity because they possess high surface area and this will facilitate the formation the LMNCA cathode material. Due to these remarkable properties α-MnO_2 nanowires make excellent manganese precursor for the

preparation of lithium-rich cathode materials. The experimental procedure is outlined in Chapter 3 Section 3.3.3 of this thesis.

The morphology, chemical composition and crystalline structure of the LMNCA powder prepared in this work were examined. The electrochemical performance of the materials as cathode materials in lithium-ion batteries was also studied.

6.2 Results and Discussions

6.2.1 Powder X-ray Diffraction Characterization

Figure 6.1 (a,b) shows the PXRD pattern of the α-MnO_2 wires and the LMNCA sample prepared. Figure 6.1 (a) was indexed to a α-MnO_2 phase which is based on the tetragonal crystal structure with the space group *I4/m*. No peaks from other phases such as the β- or γ-MnO_2 phases were detected. The lattice parameters for the samples were calculated using Rietveld refinement. The refined parameters are $a = b = 9.966$ Å and $c = 2.882$ Å which are consistent with the values reported in literature [13-15].

Figure 6.1 (b) was indexed to a $LiMO_2$ (M = Ni, Co, Mn) phase based on a hexagonal structure with the space group $R\bar{3}m$. The minor peak between 2 Theta = 20-25° is indexed using the Li_2MnO_3 phase based on the monoclinic structure with the space group (C_2/m). This peak is due to the superlattice structure of Li_2MnO_3 as a result of the Li-M (transition metal) cation ordering [16,17]. The prepared sample is of high purity as no extra peaks due to impurity phases are observed. The XRD pattern also shows a clear splitting of the (018)/(110) doublet suggesting a highly ordered and well crystalline layered $R\bar{3}m$ structure. The lattice parameters *a* and *c* for the samples were calculated using Rietveld refinement using the $R\bar{3}m$ space group. The calculated lattice parameters with other structural parameters are summarized in Table 6.1. The obtained lattice parameters are consistent with the values reported in literature [18]. The results reveal that the peak intensity ratio $I_{(003)}/I_{(104)}$ is > 1.2 suggesting a lower and negligible Li-Ni cation mixing [19]. The axis ratio *c/a* is almost the value 5 indicating good hexagonal ordering [20].

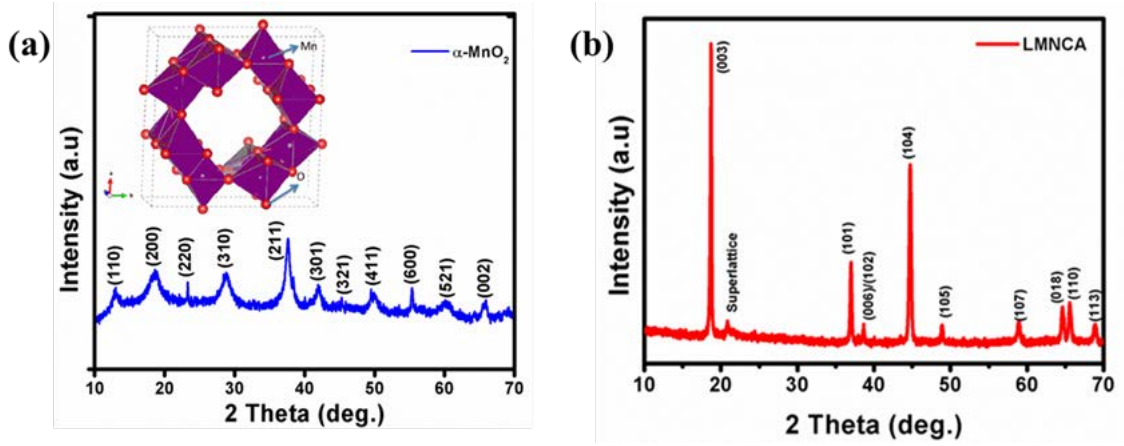


Figure 6.1: PXRD patterns of α-MnO_2 nanowires and LMNCA cathode materials.

Table 6.1: Summary of crystallographic results of α-MnO_2 nanowires and LMNCA cathode materials.

Materials	**Lattice parameter ±0.003 (Å)**	**Axis ratio *(c/a)***	**$I_{(003)}/I_{(104)}$ ratio**	**Cell volume ±0.002 ($Å^3$)**	**Crystal density ±0.002 (g cm^{-3})**	**R_p (%)**	**R_{wp} (%)**	**R_{bragg} (%)**
LMNCA	***a***-2.844 ***c***-14.208	4.996	1.435	99.5	220.696	1.91	2.47	1.280
MnO_2 wires	***a***-9.966 ***c***-2.882	-	-	286.2	34.223	3.20	5.19	1.420

6.2.2 X-ray Photoelectron Spectroscopy Characterization (XPS)

X-ray photoelectron spectroscopy (XPS) analysis was used to determine the oxidation states for the manganese ions. Figure 6.2 shows the XPS Mn $2p_{3/2}$ peak spectrum which was deconvoluted into two peaks at about 639 eV and 641 eV, corresponding to the Mn^{3+} and Mn^{4+} ions, respectively. Table 6.2 reports the Mn $2p_{3/2}$ peak position, Mn^{3+}/Mn^{4+} cation distribution, Mn^{3+}:Mn^{4+} ratio and the average manganese oxidation state. These XPS results reveal that the LMNCA prepared form α-MnO_2 nanowires has high Mn^{3+} ions compared to the LMNCA samples studied in Chapter 4 and Chapter 5. The high Mn^{3+} ion content in LMNCA prepared form α-MnO_2 nanowires explains its reduced discharge capacity compared to that of LMNCA samples studied in Chapter 4 and Chapter 5. Mn $^{3+}$ ions do not participate in the Li_2MnO_3 activation which contributes to the high capacity of LMNCA materials.

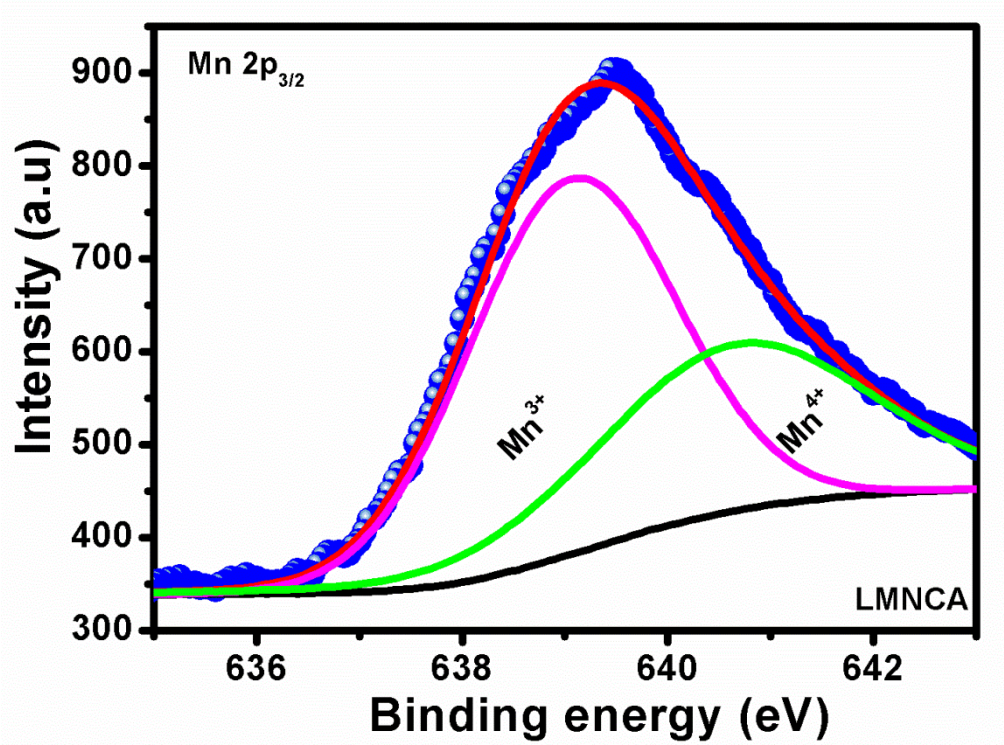


Figure 6.2: XPS data of Mn $2p_{3/2}$ for LMNCA sample prepared from α-MnO_2 nanowires..

Table 6.2: Summary of Mn $2p_{3/2}$ peak positions and cation distribution of the LMNCA sample prepared from α-MnO_2 nanowires.

Sample	Binding energy position (eV)		Cation distribution			Average oxidation state of Mn
	Mn^{4+}	Mn^{3+}	Mn^{4+} (%)	Mn^{3+} (%)	Mn^{3+}/Mn^{4+}	
LMNCA	642.8	641.7	39	61	1.56	3.61

6.2.3 Scanning Electron Microscopy Characterization (SEM)

The morphology of the α-MnO_2 nanowires was observed by scanning electron microscopy (SEM) and by transmission electron microscopy (TEM). Figure 6.3 (a,b) shows the SEM images of the MnO_2 wires at high and low magnifications. Figure 6.3 (c,d,e) shows the TEM images of the sample. The TEM images show nanowires with particle size in the range of 7-15 nm in diameter and their length is between 200 nm-1.65 μm. The MnO_2 wire sample is highly

crystalline showing the (200) lattice planes with d-spacing approximately 0.496 nm. The SAED pattern shown in Figure 6.3 (f) confirms that the sample is highly crystalline.

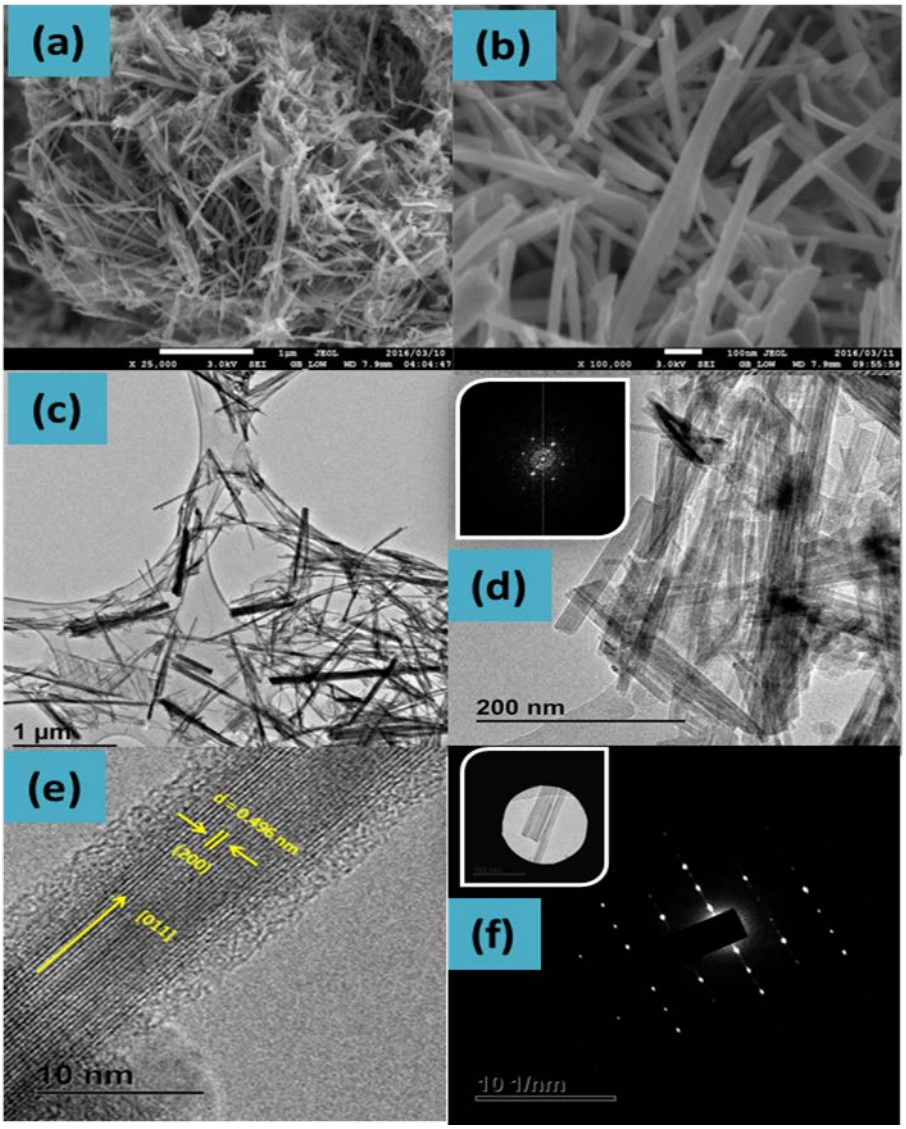


Figure 6.3: (a) Low magnification SEM images, (b) High magnification, (c) Low magnification TEM, (d) High magnification TEM, (e) High resolution TEM and (f) SAED image of α-MnO_2 nanowires.

Figure 6.4 (a,b) displays the morphology and the elemental analysis of the LMNCA sample. The image shows that the sample exhibits plate-like particles with smooth surfaces. The clean and smooth surface facets observed will improve the contact of the sample with the electrolyte and the transport of Li-ions and electrons during charge and discharge. The thickness of the plates is between 38-167 nm and the width of the particles is 135-922 nm. Figure 6.4 (c-d) shows the elemental analysis of the LMNCA sample. Figure 6.4 (c) confirms the purity and

elemental content of the sample. The EDX analysis confirms the composition of the samples and the results were found to be within 5 % of expected values. The elemental mapping in Figure 6.5 shows that the elements are homogeneously dispersed in the LMNCA particle.

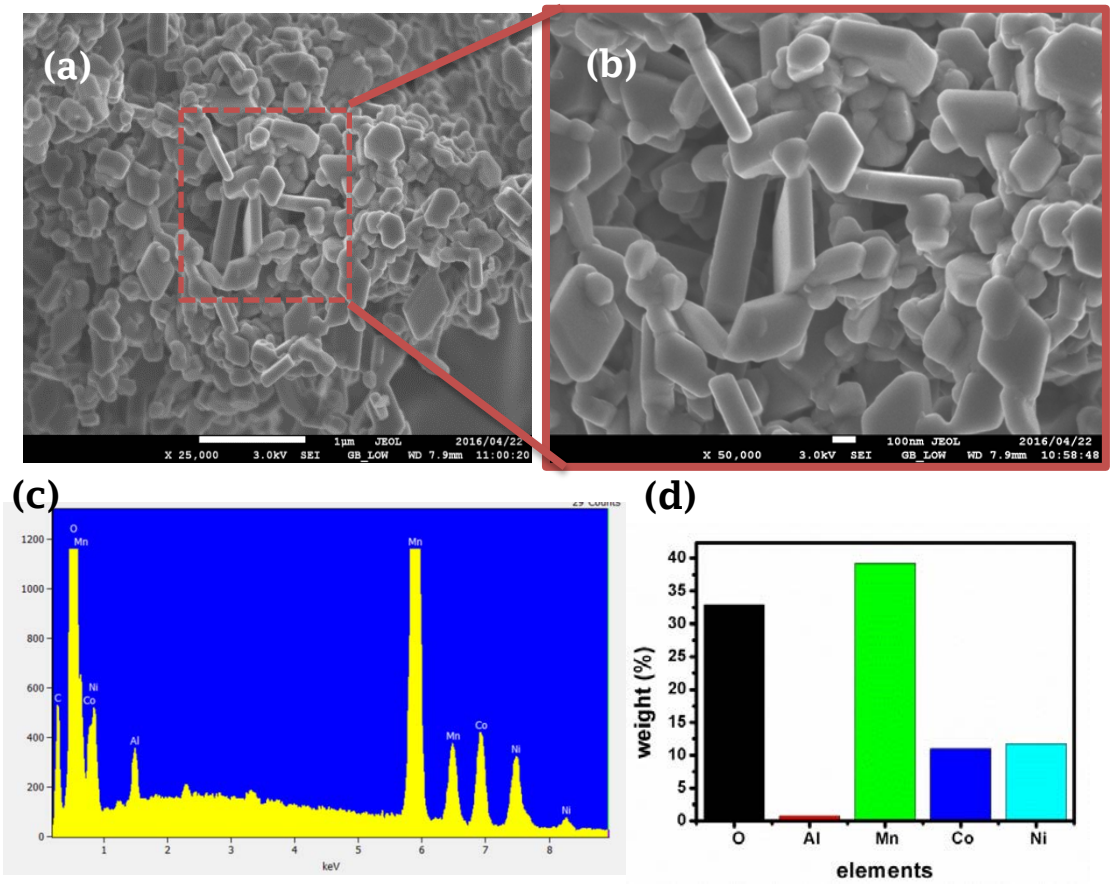


Figure 6.4: SEM images of LMNCA powders (a-b) and (c) EDX elemental analysis and composition.

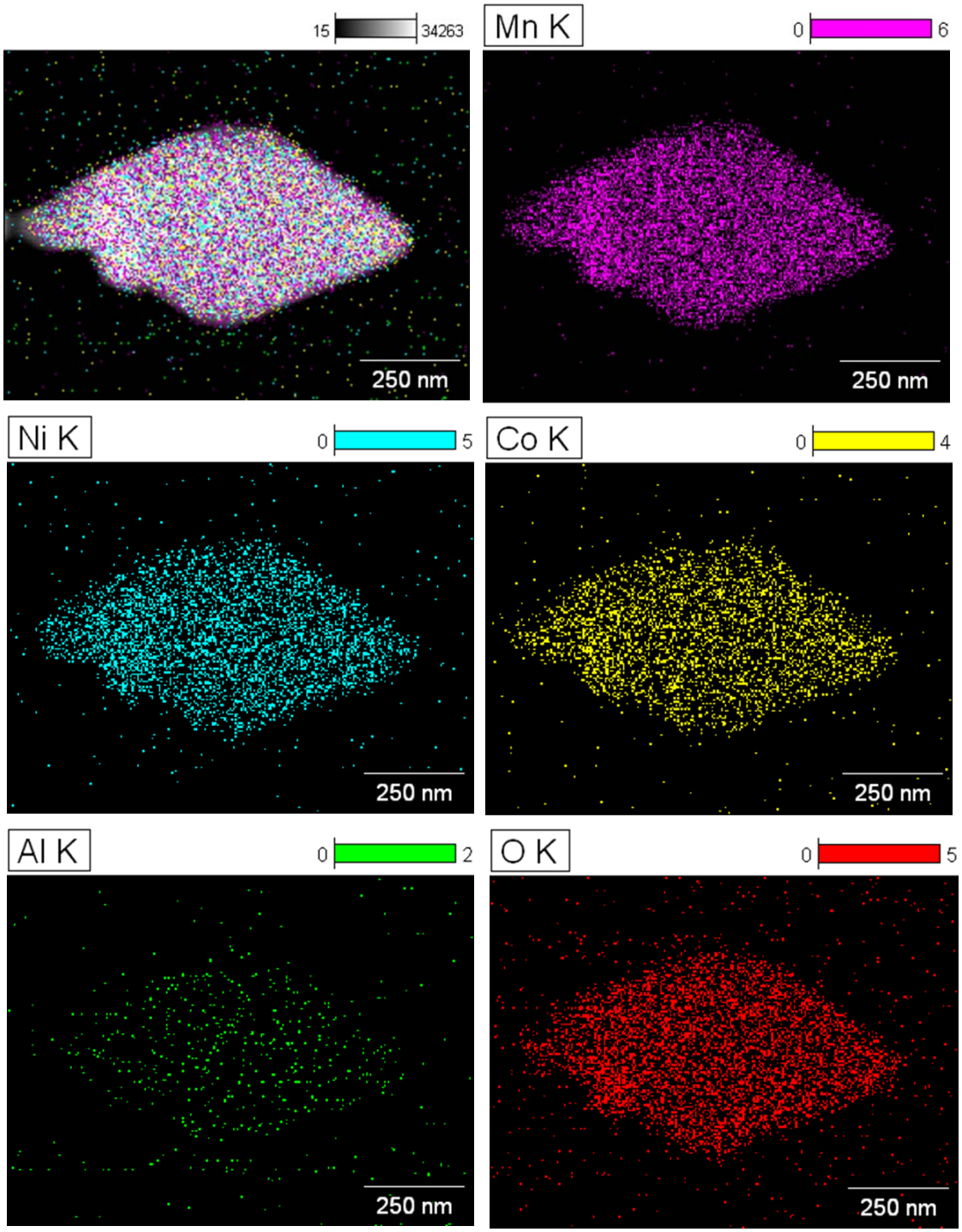


Figure 6.5: EDX elemental mapping of prepared LMNCA sample.

6.2.4 Transmission Electron Microscopy Characterization (TEM)

Figure 6.6 (a, c) shows the low magnification transmission electron microscopy (TEM) and high resolution TEM (HRTEM) images of the sample to further investigate the structure of the prepared LMNCA sample. The low magnification TEM of the frontal plane of the LMNCA sample and confirms the morphology of the sample as observed in the SEM analysis. The

HRTEM shows clearly the apparent lattice fringes with d spacing of 0.4725 nm corresponding to the (003) and/or (001) due to the $R\bar{3}m$ and C_2/m space groups, respectively. These planes are parallel to the c-axial direction parallel to the (100), (010), or (110) planes belonging to the {010} planes [21,22]. Figure 6.6 (b) shows the selected area electron diffraction (SAED) of the LMNCA particle and confirms the existence of the (110) planes belonging to the {010} planes. This suggest that the surface of the particle has exposed {010} planes which are known to be electrochemically active and results in rapid lithium- ion intercalation and de-intercalation leading to excellent electrochemical performance [21-24]. The (101) and (020) planes belong to the hexagonal and monoclinic phase, respectively.

The XRD, TEM and SAED pattern confirms that the LMNCA samples is highly crystalline and consists of the LMO_2 and Li_2MnO_3 phases.

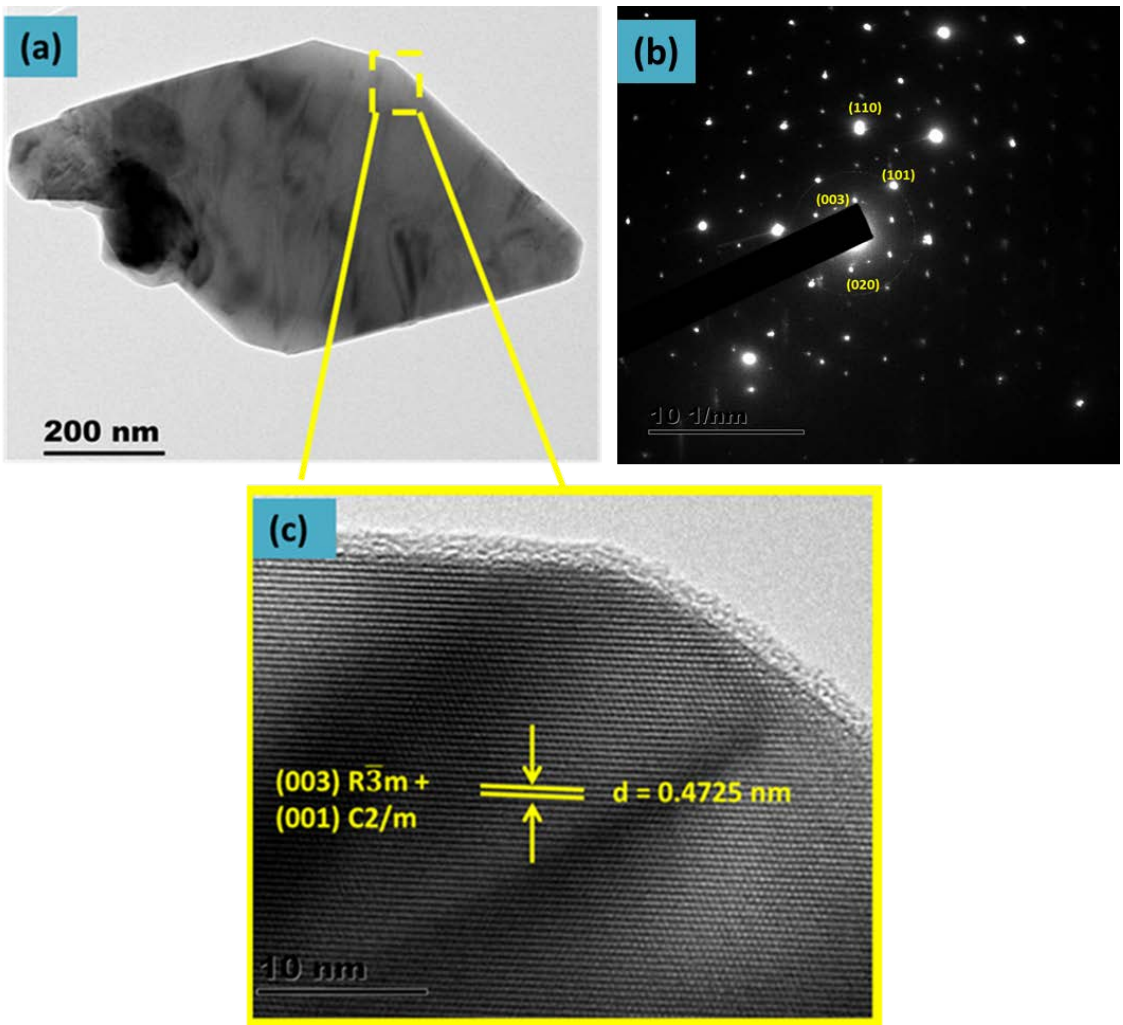


Figure 6.6: High resolution TEM and SAED pattern of the prepared LMNCA sample.

6.2.5 Electrochemical Characterization

6.2.5.1 Cyclic voltammetry

Figure 6.7 shows the cyclic voltammetric evolutions of the prepared samples for the 1st, 2nd, 4th, 6th, 8th and 10th cycles. The CV behaviour of the prepared samples is similar to that of the LMNCA samples studied in chapters four and five. The first cycle also shows an intense peak at >4.5 V due the Li_2MnO_3 activation. However, it is important to observe that there is not much change between the cycles, especially from the 3rd cycle onwards. This suggests good cycle performance of the prepared LMNCA sample.

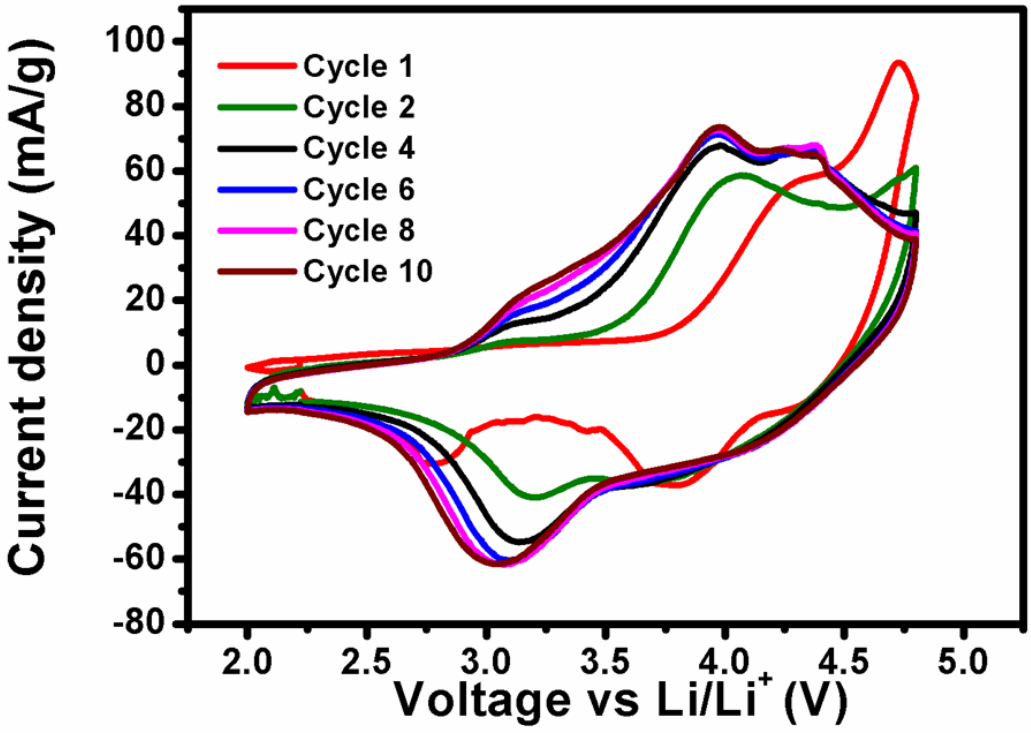


Figure 6.7: Cyclic voltammograms (current density vs. voltage) of the prepared LMNCA cathode. Scan rate: 0.1 mV s^{-1}; voltage range: 1.5 – 4.4 V vs. Li/Li^+.

6.2.5.2 Galvanostatic charge-discharge

Figure 6.8 (a,b) reports the cycle performance and the coulombic efficiency of the sample at 0.1 C and 5 C rate. The capacity retention is 95 % and 96 % after the 50th and 100th cycle at 0.1 C, while the capacity retention at 5 C is 98 % and 97 % after 100th and 300th cycles,

respectively. This indicates that the prepared LMNCA material possesses excellent cycle performance especially at 5 C rate due to the nanoplate structure, clean and smooth surface facets of the nanoplate and the exposed electrochemically active {010} planes. The prepared sample also possesses coulombic efficiency (CE) at 0.1 C of 62 % in the first cycle but increases to 94, 99 and 95 % in the 2nd, 50th and 100th cycle, while the CE at 5 C is 51 % and 99 % for 2nd and 300th cycle respectively.

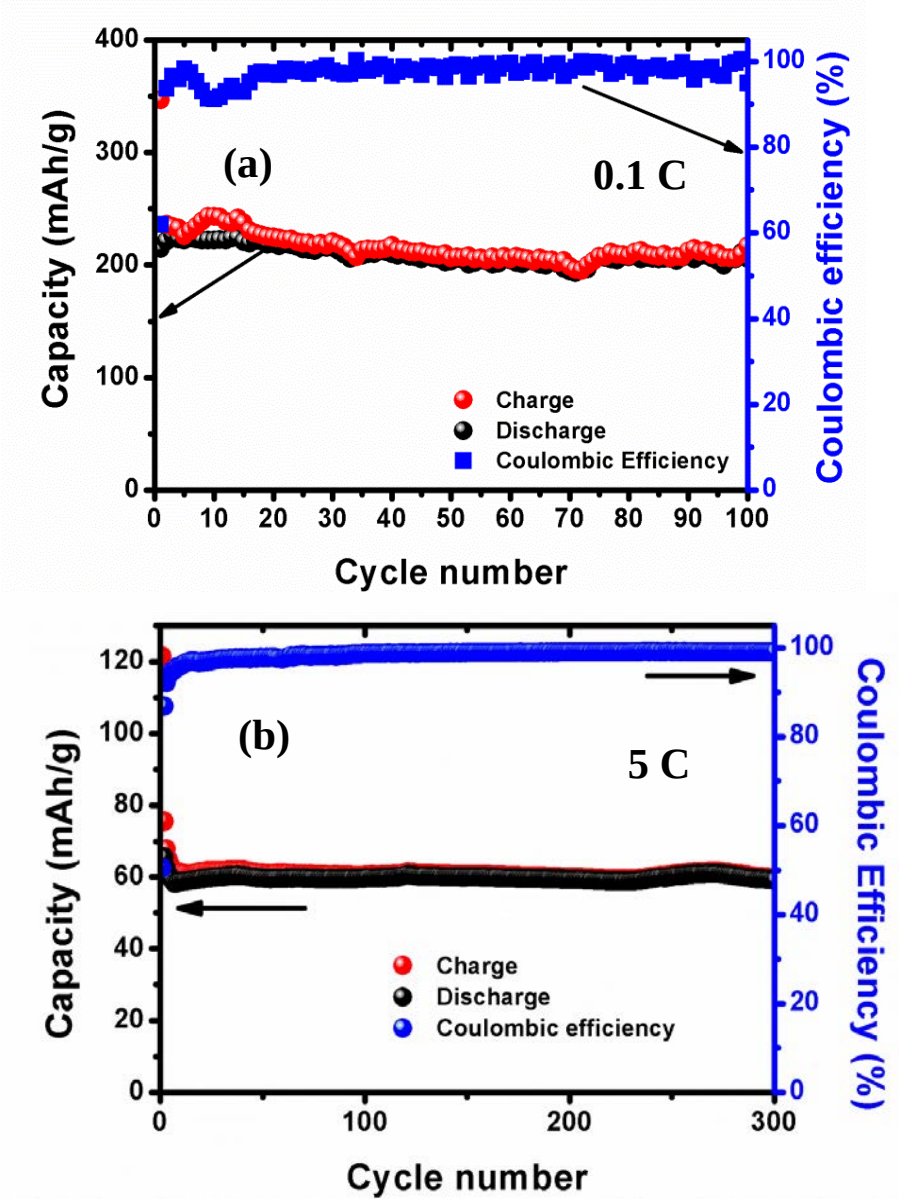


Figure 6.8: Cycle performance and coulombic efficiency at (a) 0.1 C and (b) 5 C rate.

6.2.5.3 Rate Capability

The sample exhibits a good rate capability when charge and discharged at different current rates at 0.5 C, 1 C, 2 C and 3 C as seen in Figure 6.9. Table 6.3 compares our results to reported values in literature and reveals that the LMNCA prepared in this work has better performance which is due to the nanoplate structure with exposed electrochemical active {010} planes and the nanoplates provide the short diffusion pathways and faster intercalation for the lithium-ions.

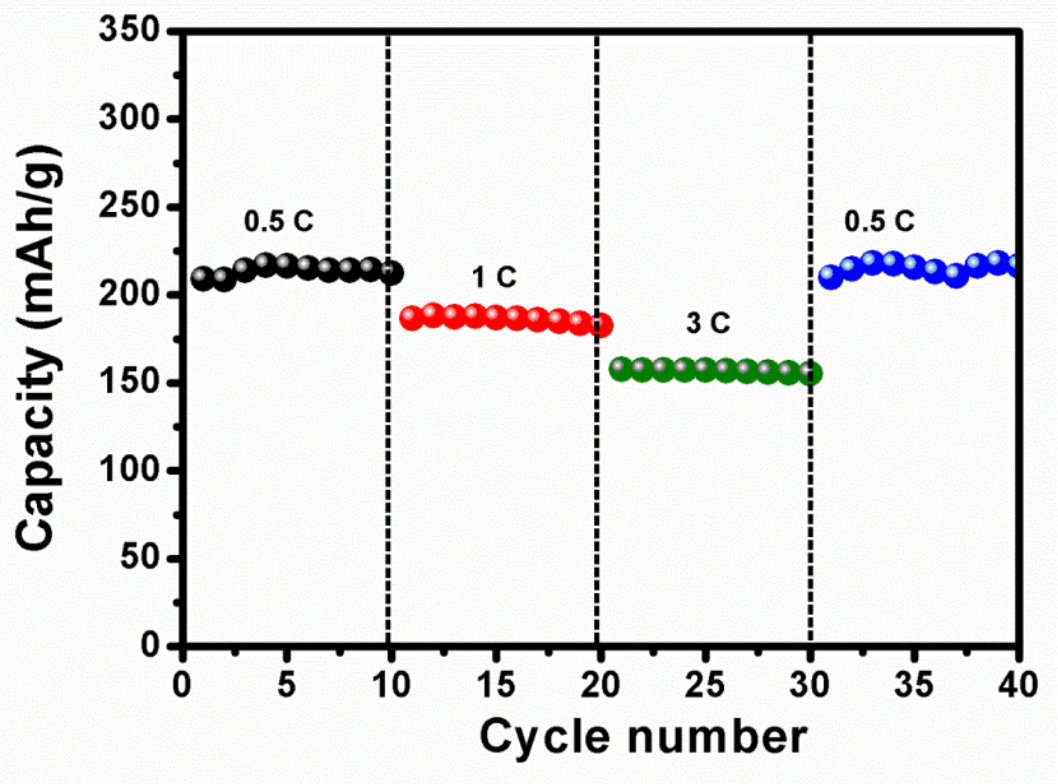


Figure 6.9: Rate capacity at different current rates.

Table 6.3: Comparison of the prepared LMNCA sample with literature.

Material	Synthesis method	Capacity	Capacity retention After 100 cycles	Reference
$Li_{1.2}Ni_{0.16}Mn_{0.52}Co_{0.16}Al_{0.02}O_2$	Self-combustion reaction (SCR)	255 mAh/g @0.1C	78 %	[25]
$Li_{1.2}Ni_{0.13}Mn_{0.52}Co_{0.13}Al_{0.02}O_2$	Pechini method	243 mAh/g @0.1C	62 % after 50 cycles	[26]
$Li_{1.2}Ni_{0.13}Mn_{0.52}Co_{0.13}Al_{0.02}O_2$	This work: LMNCA-prepared from α-MnO_2 nanowires	215 mAh/g @0.1 C	96 %	-

6.2.5.4 Electrochemical Impedance Spectroscopy (EIS)

Figure 6.10 shows the Nyquist plots obtained from electrochemical impedance spectroscopy (EIS) analysis of the prepared LMNCA material. The Nyquist plots were fitted with the electrical equivalent circuit and EIS fitting parameters as described in Chapter 4 of this thesis. The fitted data is shown in Table 6.4.

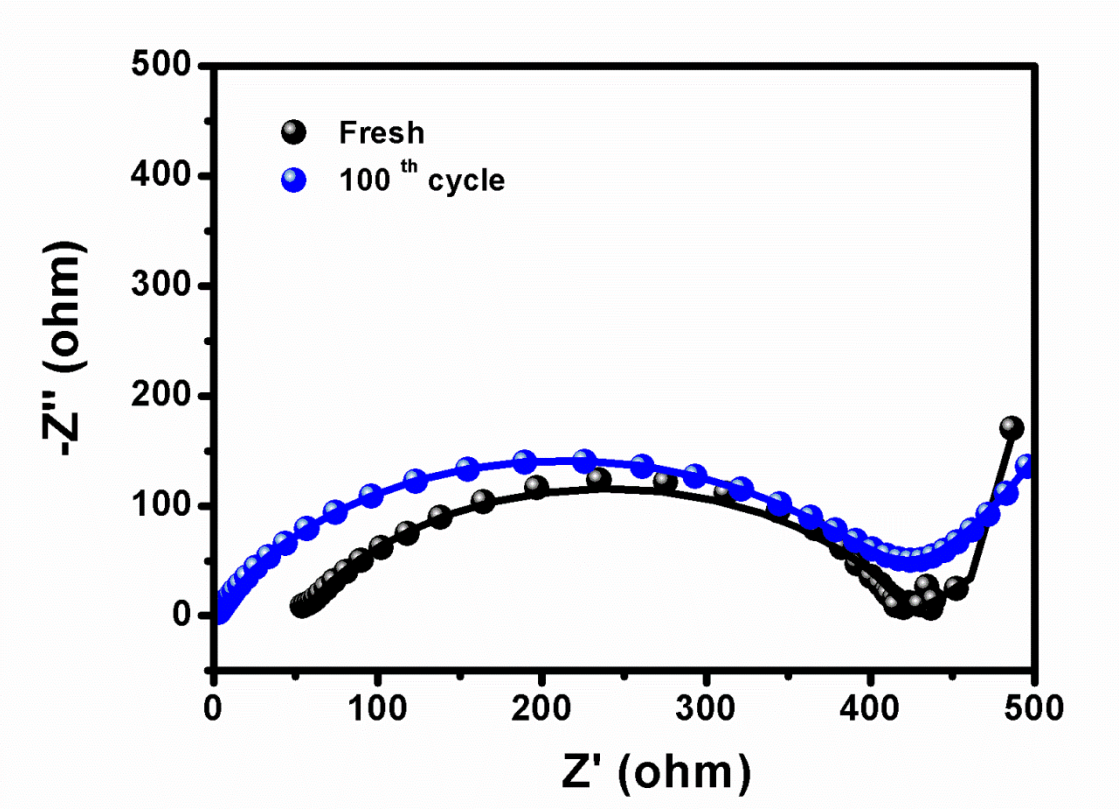


Figure 6.10: Electrochemical Impedance Spectroscopy of LMNCA sample.

Table 6.4: Impedimetric data of prepared LMNCA sample.

Aging cells	R_s (Ω)	R_f (Ω)	$R_{(ct)}$ (Ω)	Z_w (Ω)
Fresh cells	2.08	406.5	412.9	114.1
100th cycle	52.25	63.88	425.1	21.67

The R_s value increases upon cycling and this is expected due to that the electronic conductivity of the electrolyte changing/decomposing when charging at high potentials above 4.5 V. The R_{ct} values show a slight increase after 100 cycles and this confirms the good cycle stability of the materials. These results corroborate the charge-discharge results.

6.3 Conclusions

A new and simple synthesis method employing α-MnO_2 nanowires as precursor was used to prepare layered LMNCA cathode with exposed {010} planes. The α-MnO_2 nanowires were successfully prepared using the molten salt method. The prepared LMNCA sample is pure with highly crystalline and ordered structure. The LMNCA sample exhibits hexagonal nanoplates with exposed electrochemically active {010} planes. The mechanism of formation of the plates is such that the pluronic acid used during the synthesis as a surfactant chelated the transitional metal ions and also capped the surface of the highly reactive and absorptive α-MnO_2 nanowires. The capping of the α-MnO_2 nanowires surface then reduced the growing rate of the particles along the [001] direction to give a plate like morphology with exposed {010} planes. Nanoplates, which are two dimensional, possess high specific surface areas and large surface-to-volume ratios which are beneficial for improved electrochemical performance. Importantly, the exposed electrochemically active {010} planes results in improved cycle performance and rate capability due to that the lithium-ions can be easily intercalated and de-intercalated into LMNCA samples through the {010} planes. The capacity retention is 95 % and 96 % after the 50^{th} and 100^{th} cycle at 0.1 C, while the capacity retention at 5 C is 98 % and 97 % after 100^{th} and 300^{th} cycles, respectively. The simple synthesis strategy used in this work will be helpful in the development of other high voltage cathode materials especially those that suffer from capacity fade.

6.4 References

[1] R. Santhanam, B. Rambabu, Journal of Power Sources, 195 (2010) 4313-4317.

[2] C.S. Johnson, N. Li, C. Lefief, M.M. Thackeray, Electrochemistry Communications, 9 (2007) 787-795.

[3] T. Zhao, S. Chen, L. Li, X. Zhang, R. Chen, I. Belharouak, F. Wu, K. Amine, Journal of Power Sources, 228 (2013) 206-213.

[4] Y. Denis, K. Yanagida, H. Nakamura, Journal of the Electrochemical Society, 157 (2010) A1177-A1182.

[5] X. Liu, Z. Guo, Progress in Natural Science: Materials International, 22 (2012) 126-129.

[6] J. Lim, H. Bang, K. Lee, K. Amine, Y. Sun, Journal of Power Sources, 189 (2009) 571-575.

[7] J. Zheng, X. Wu, Y. Yang, Electrochimica Acta, 56 (2011) 3071-3078.

[8] H. Zou, B. Wang, F. Wen, L. Chen, Ionics, 23 (2017) 1083-1090.

[9] W. Xiao, W. Liu, X. Mao, H. Zhu, D. Wang, Electrochimica Acta, 88 (2013) 756-765.

[10] H. Fang, L. Li, Y. Yang, G. Yan, G. Li, Journal of Power Sources, 184 (2008) 494-497.

[11] M.M. Thackeray, Progress in Solid State Chemistry, 25 (1997) 1-71.

[12] X. Wang, Y. Li, Journal of the American Chemical Society, 124 (2002) 2880-2881.

[13] G. Cheng, L. Yu, B. Lan, M. Sun, T. Lin, Z. Fu, X. Su, M. Qiu, C. Guo, B. Xu, Materials Research Bulletin, 75 (2016) 17-24.

[14] L. Feng, Z. Xuan, H. Zhao, Y. Bai, J. Guo, C. Su, X. Chen, Nanoscale Research Letters, 9 (2014) 290.

[15] W. Li, X. Cui, R. Zeng, G. Du, Z. Sun, R. Zheng, S.P. Ringer, S.X. Dou, Scientific Reports, 5 (2015) 8987.

[16] D. Mohanty, S. Kalnaus, R.A. Meisner, K.J. Rhodes, J. Li, E.A. Payzant, D.L. Wood, C. Daniel, Journal of Power Sources, 229 (2013) 239-248.

[17] D. Mohanty, A. Huq, E.A. Payzant, A.S. Sefat, J. Li, D.P. Abraham, D.L. Wood III, C. Daniel, Chemistry of Materials, 25 (2013) 4064-4070.

[18] J.R. Croy, K.G. Gallagher, M. Balasubramanian, Z. Chen, Y. Ren, D. Kim, S. Kang, D.W. Dees, M.M. Thackeray, The Journal of Physical Chemistry C, 117 (2013) 6525-6536.

[19] X. Zhang, W. Jiang, A. Mauger, F. Gendron, C. Julien, Journal of Power Sources, 195 (2010) 1292-1301.

[20] X. Zhang, D. Luo, G. Li, J. Zheng, C. Yu, X. Guan, C. Fu, X. Huang, L. Li, Journal of Materials Chemistry A, 1 (2013) 9721-9729.

[21] L. Zhang, N. Li, B. Wu, H. Xu, L. Wang, X. Yang, F. Wu, Nano Letters, 15 (2014) 656-661.

[22] J. Zeng, Y. Cui, D. Qu, Q. Zhang, J. Wu, X. Zhu, Z. Li, X. Zhang, ACS Applied Materials and Interfaces, 8 (2016) 26082-26090.

[23] J. Li, C. Xu, J. Zhao, J. Chen, C. Cao, Journal of Alloys and Compounds, 734 (2018) 301-306.

[24] R. Yu, X. Zhang, T. Liu, X. Xu, Y. Huang, G. Wang, X. Wang, H. Shu, X. Yang, ACS Sustainable Chemistry and Engineering, 5 (2017) 8970-8981.

[25] P.K. Nayak, J. Grinblat, M. Levi, E. Levi, S. Kim, J.W. Choi, D. Aurbach, Advanced Energy Materials, 6 (2016).

[26] C.J. Jafta, K.I. Ozoemena, M.K. Mathe, W.D. Roos, Electrochimica Acta, 85 (2012) 411-422.

CHAPTER 7

The effect of microwave irradiation on the preparation of P2-type $Na_{0.67}Mg_{0.28}Mn_{0.72}O_2$ cathode materials for sodium-ion batteries

7.1 Introduction

The cheap P2-type $Na_{0.67}Mg_{0.28}Mn_{0.72}O_2$ cathode material is one of the promising cathode materials for sodium-ion batteries. P2-type $Na_{0.67}Mg_{0.28}Mn_{0.72}O_2$ cathode has shortcomings, such as capacity fade, large voltage hysteresis and is sodium deficient, which limit its implementation in practical systems. However, the results presented here in Chapter 7 and 8 advance our understanding of the effect of synthesis methodology and anion coating in improving the electrochemical performance of P2-type $Na_{0.67}Mg_{0.28}Mn_{0.72}O_2$ cathode materials. This chapter studies the shortcomings of this cathode material and discusses one of the solutions for enhanced electrochemical performance.

The P2-type $Na_{0.67}Mg_{0.28}Mn_{0.72}O_2$ (NaMgMnO) based cathode materials were prepared using a combustion synthesis method as outlined in Chapter 3 Section 3.3.4. This work reports for the first time the preparation of NaMgMnO cathode material using the urea-combustion method. Combustion method of synthesis is regarded an effective and fast method of preparing electrode materials [1-4]. Urea was chosen as suitable fuel for the synthesis of NaMgMnO materials because the urea synthesized cathodes were found in Chapter 4 and 5 of this thesis to result in improved capacity. Two samples were considered: a pristine sample (NaMgMnO-a) and a microwave-irradiated sample (NaMgMnO-ma).

P2-type $Na_{0.67}Mg_{0.28}Mn_{0.72}O_2$ cathode materials suffers from poor cycle performance, i.e. their capacity decreases rapidly during charge and discharge. The poor cycle performance is due to various factors including high Mn^{3+} ion concentration, poor morphological integrity, manganese dissolution in the electrolyte during cycling, Jahn-Teller distortion of the high-spin Mn^{3+} and phase transformation from P2 to O2-type.

This chapter investigates the effect of microwave irradiation in the electrochemical performance of P2-type $Na_{0.67}Mg_{0.28}Mn_{0.72}O_2$ cathode material. The effect of microwave irradiation was investigated particularly with the aim to improve the cycle performance of this cathode material. The same microwave irradiation conditions used in Chapter 5 were also employed in this chapter. This thesis also aims to extends the study of microwave irradiation on the electrode materials to sodium-ion batteries and also reports for the first time the study of microwave irradiation for P2-type $Na_{0.67}Mg_{0.28}Mn_{0.72}O_2$ cathode materials.

7.2 Results and discussion

7.2.1 Powder X-ray Diffraction Characterization

Figure 7.1 reports the PXRD results of the NaMgMnO-a and NaMgMnO-ma materials. PXRD patterns were indexed to a P2-type hexagonal structure with the space group *P6$_3$/mmc*. [8]. The patterns also show a diffraction peak at ca. 21° due to the presence of stacking faults of the superlattice layers along the c-axis direction. This is a (1/3, 1/3, 0) peak of superstructure due to the formation of $(\sqrt{3})$a by $(\sqrt{3})$a in-plane ordering between (Mg^{2+} and Mn^{3+}) and Mn^{4+} [8]. The NaMgMnO materials have the $A_1A_1A_1A_1$ stacking of ordered Mg-Mn layers ($Mg_xMn_{1-x}O_2$ sheets).

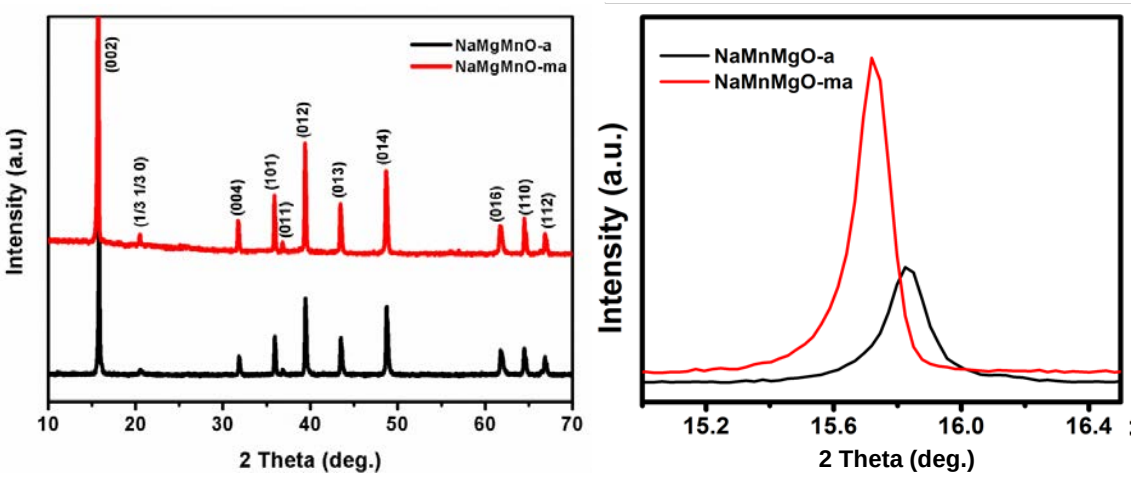


Figure 7.1: XRD patterns of the prepared NaMgMnO samples.

The Rietveld refinement was used to calculate the lattice parameters (*a* and *c*) and cell volume. The R_p , R_{wp} and R_{bragg} are refinement parameters and the reasonably small (< 5%) R_p , R_{wp} and R_{bragg} demonstrates a very good refinement. The observed and calculated patterns match well, also confirming a good fit. For layered materials, lattice parameter *a* represents the interlayer metal-metal distance and lattice parameter *c* represents the inter-slab distance. The

crystallographic data is summarised in Table 7.1. There lattice parameters *a* and *c* of NaMgMnO-a and NaMgMnO-ma are similar and the values obtained are comparable to those obtained in literature [9,10].

Table 7.1: Summary of refined crystallographic parameters for the prepared NaMgMnO samples

Materials	**Lattice parameter ±0.002 (Å)**	**d-spacing (002) ±0.002 (nm)**	**Cell volume ±0.002 (Å^3)**	**Crystal density ±0.002 (g cm^{-3})**	**R_p (%)**	**R_{wp} (%)**	**R_{bragg} (%)**
NaMgMnO-a	***a***-2.895 ***c***-11.265	5.632	245.259	67.894	2.86	3.82	1.761
NaMgMnO-ma	***a***-2.893 ***c***-11.248	5.624	244.639	77.606	2.32	3.64	2.051

Figure 7.1 (b) reveals that the microwave irradiation increased the intensity and slightly shifted the (002) peak to lower angles. This confirms the slight decrease in the lattice parameter, d-spacing and the cell volume by microwave irradiation suggesting a decrease in the concentration ratio of Mn^{3+}/Mn^{4+}.

7.2.2 X-ray Photoelectron Spectroscopy Characterization (XPS)

Figure 7.2 compares the XPS of the deconvoluted peaks of the Mn $2p_{3/2}$ of (a) NaMgMnO-a and (b) NaMgMnO-ma. The Mn $2p_{3/2}$ peak is deconvoluted into two peaks occurring at the expected positions for Mn^{3+} and Mn^{4+} oxidation states.

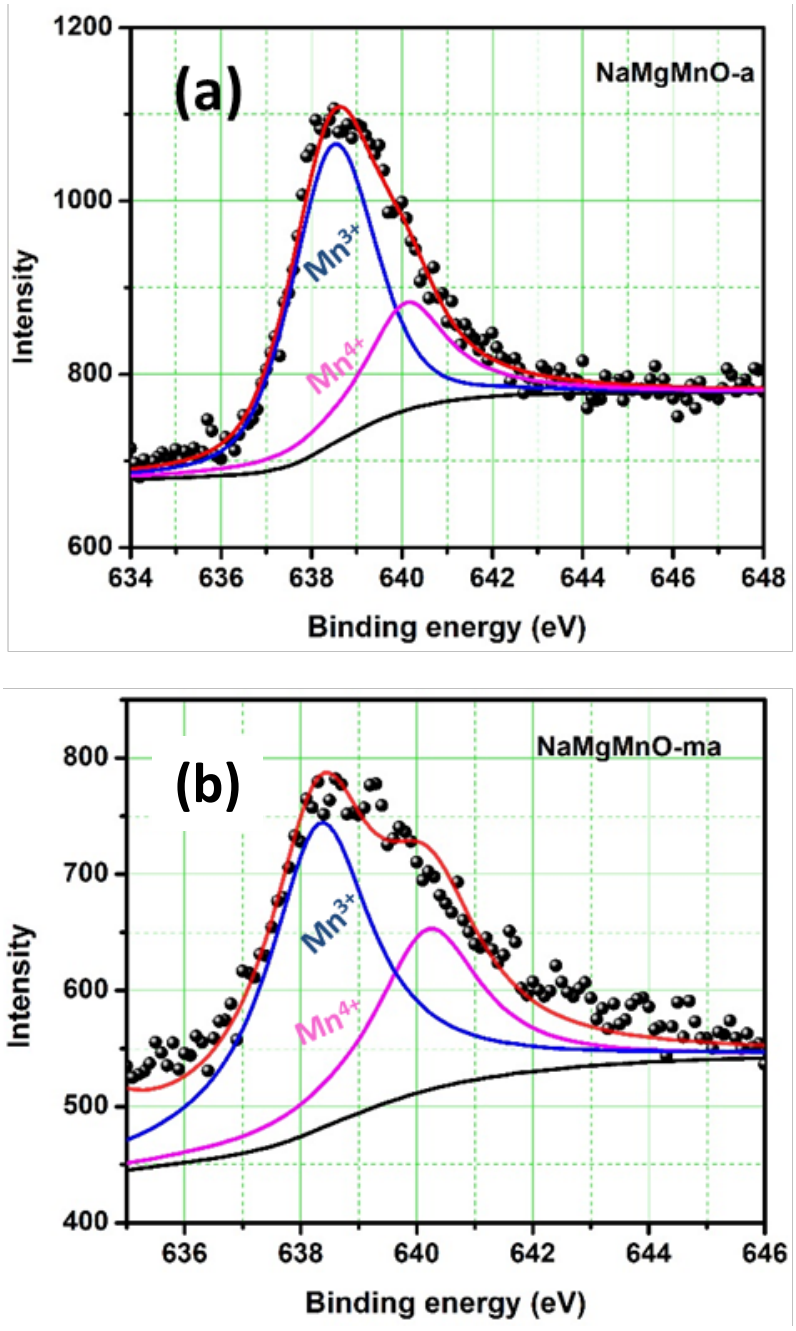


Figure 7.2: XPS spectra for the (a) NaMgMnO-a and (b) NaMgMnO-ma samples.

Table 7.2 displays the XPS (Mn $2p_{3/2}$ spectra) data of the NaMgMnO-a and NaMgMnO-ma samples. The results show some unique changes in the percentage concentration ratio of Mn^{3+}/Mn^{4+} upon microwave irradiation, i.e. the Mn^{3+}/Mn^{4+} ratio decreases by about 29 % upon microwave irradiation. The Mn^{3+} content is much higher than that of its Mn^{4+} counterpart in both samples, resulting in an average valence state of Mn atoms (V_{Mn}) of ca. 3.3+ for each sample (this value would be 3.5+ for a 50:50 ratio of Mn^{3+} and Mn^{4+}). This value is lower than

the 3.74+ obtained for $Na_{0.53}MnO_2$ by Li *et al*. [11] which may be related to the substitution of some Mn atoms by Mg in our work. In summary, this result suggests that microwave irradiation can decrease the amount of the redox-active Mn^{3+}, but without affecting the average valence state of the manganese significantly. The decrease in the Mn^{3+} ions results in an increase in the Mn^{4+} ions and thus decreases the cell volume and d-spacing since the Mn^{3+} ions are bigger than the Mn^{4+} ions [12]. These results corroborate the XRD results.

Table 7.2: XPS (Mn $2p_{3/2}$ spectra) data of the NaMgMnO-a and NaMgMnO-ma samples

Sample	Binding energy position (eV)		Cation distribution			Mn valence (average redox state)
	Mn^{4+}	Mn^{3+}	Mn^{4+} (%)	Mn^{3+} (%)	Mn^{3+}/Mn^{4+}	
NaMgMnO-a	640.1	638.5	30.9	69.1	2.24	3.31
NaMgMnO-ma	639.8	638.2	38.8	61.2	1.58	3.39

7.2.3 Scanning Electron Microscopy Characterization (SEM)

The SEM images shown in Figure 7.3 reveal that both the samples exhibit hexagonal plate-like shaped micron-sized particles (1–3 μm diameters). The microwave irradiation did not affect the particle size but resulted in clean and smooth surface facets, confirming that the microwave irradiated particles are well-crystalline. This is important for improving the electrochemical properties because the transport of Na-ions and electrons upon cycling occurs on the surface of the electrode sample.

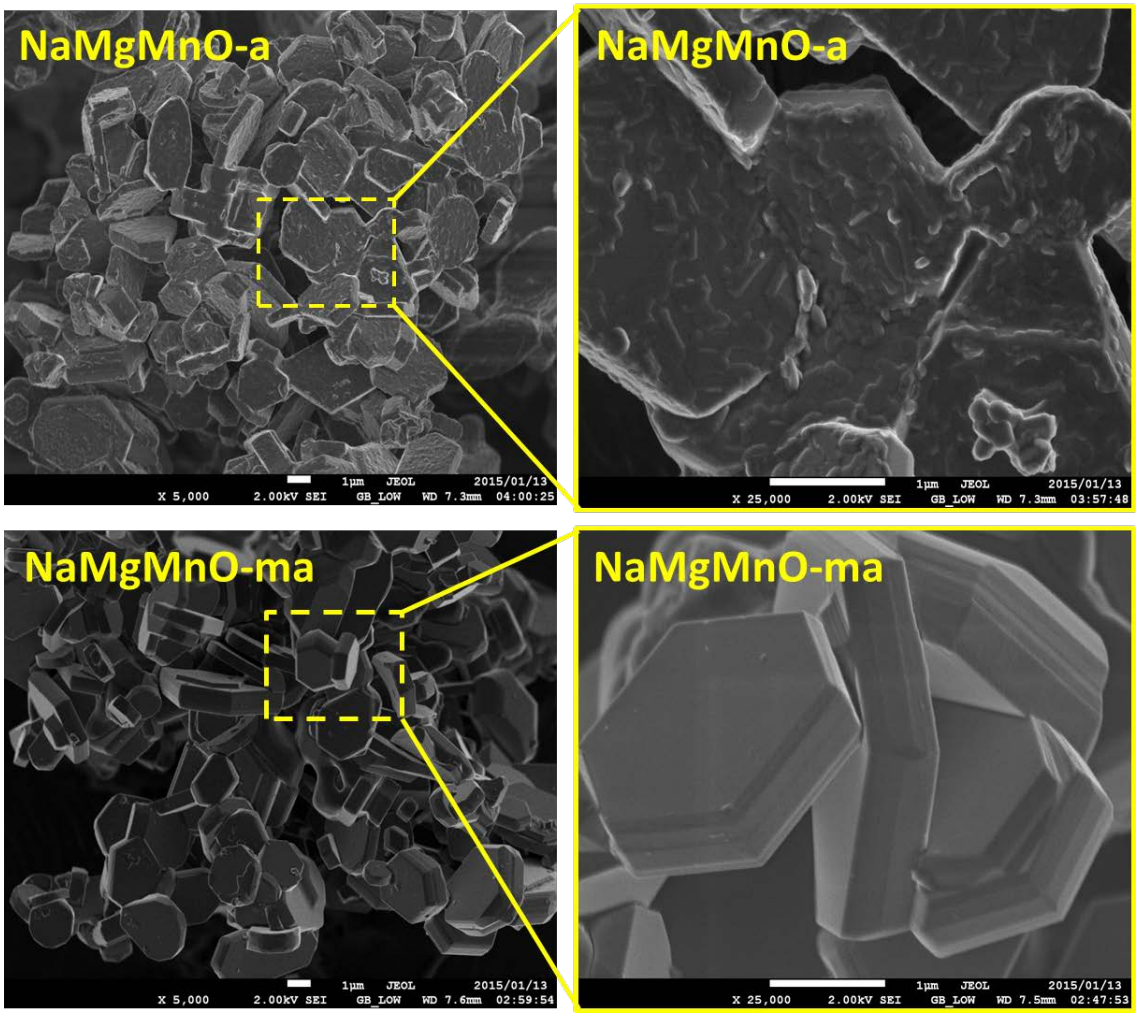


Figure 7.3: SEM images of (a) NaMgMnO-a and (b) NaMgMnO-ma samples.

7.2.4 Energy–Dispersive X-ray Spectroscopy (EDX)

Energy–Dispersive X-ray Spectroscopy (EDX) was carried out to determine the elemental composition of the prepared samples. Figure 7.4 shows the EDX analysis of NaMgMnO-a and Figure 7.5 shows the EDX analysis of NaMgMnO-ma.

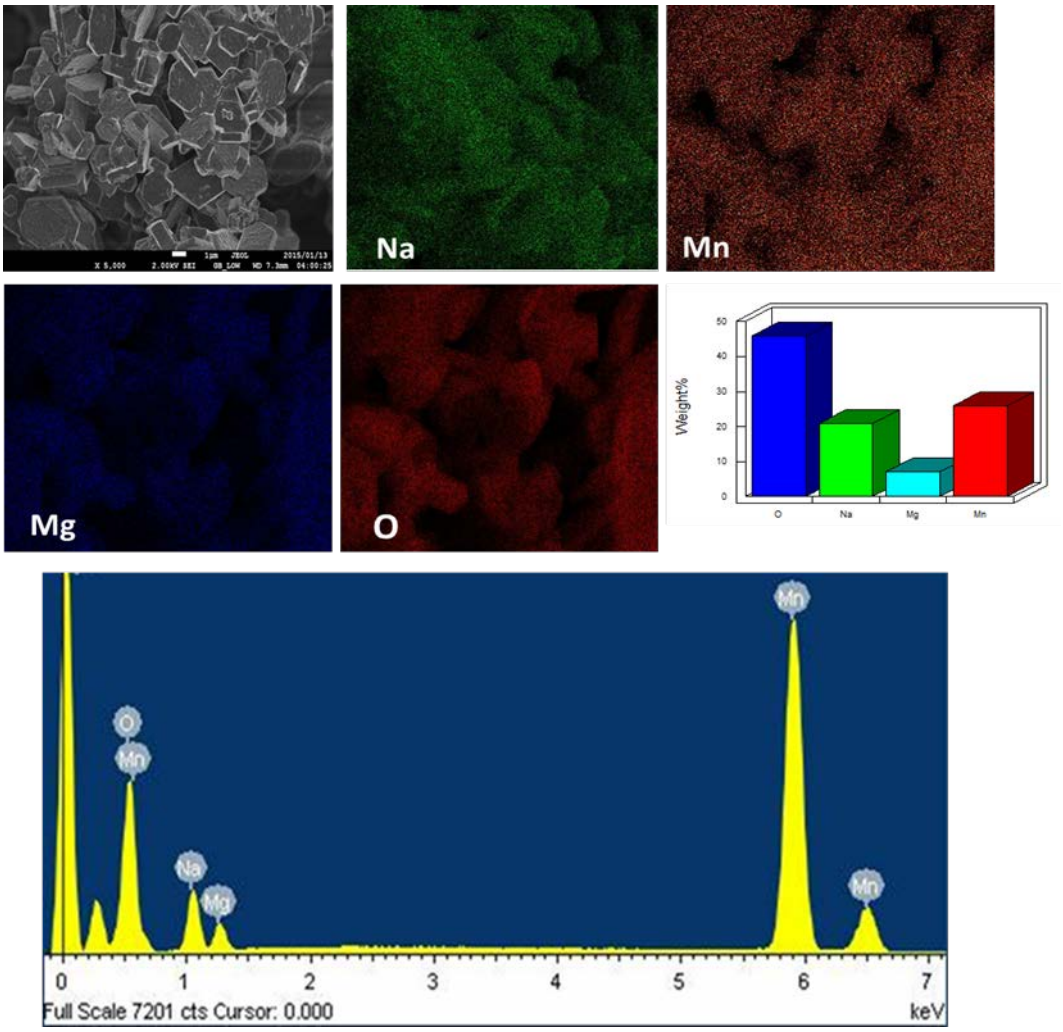


Figure 7.4: EDX analysis of NaMgMnO-a.

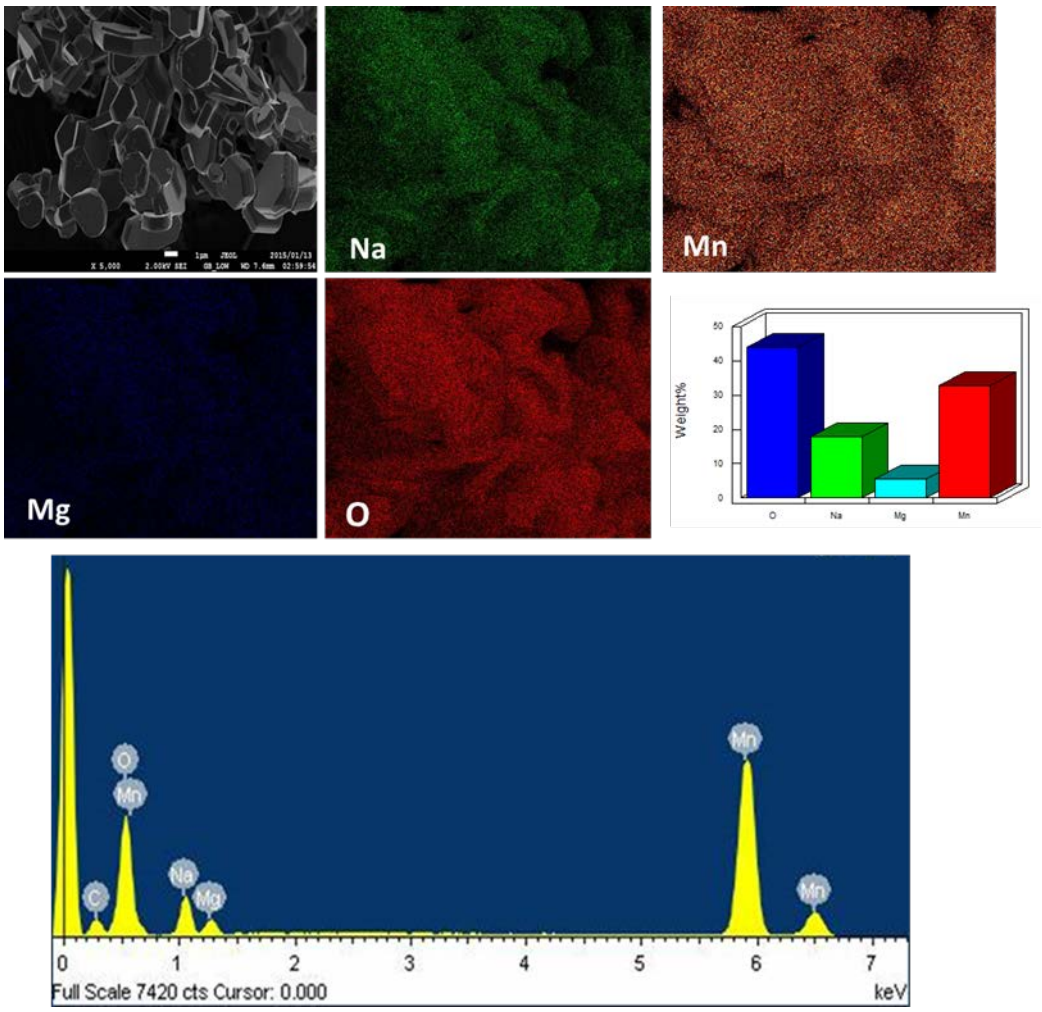


Figure 7.5: EDX analysis of NaMgMnO-ma.

The EDX profiles show peaks at ca. 5.9 keV and 6.5 keV due to the characteristic K_α and K_β X-rays, respectively, emitted from manganese atoms. The incident beam used had sufficient energy to produce both K_α X-rays and K_β X-rays. The K_α X-ray is emitted when the filling electron drops from the L shell to the K shell where the initial vacancy occurs [13]. The K_β X-ray is emitted when the filling electron drops from the M shell to the K shell and therefore the K_β radiation peak is higher in energy than K_α radiation as the energy between the M and K shell is greater than the energy between the L and K shell.

The Na and Mg peaks are observed at about 1.1 keV and 1.3 keV, respectively. The O and C peaks are observed at about 0.6 keV and 0.3 keV, respectively. The C peaks are due to the carbon coating used for sample preparation for the analysis. Therefore the EDX analyses confirm that the samples are pure and contain only the expected elements. The EDX results are summarised in Table 7.3. These results confirm the elemental composition of the samples to

within the expected 3 %. EDX elemental mapping of the samples also show that the elements are homogenously disperse in the samples.

Table 7.3: Elemental composition obtained from EDX

Elements	NaMgMnO-a		NaMgMnO-ma	
	Weight %	Atomic %	Weight %	Atomic %
O	45.93	63.13	45.15	63.1
Na	20.92	20.01	19.99	19.45
Mg	7.14	6.45	6.39	5.88
Mn	26.01	10.41	28.23	11.49
C	-	-	0.24	0.08

7.2.5 Electrochemical Characterization

7.2.5.1 Cyclic voltammetry

Figure 7.6 compares the cyclic voltammograms of the coin cells made using the synthesized cathode materials for the fresh cell and after the 100th cycle. The cyclic voltammograms show ill-defined and broad redox peaks suggesting multi-step reversible reaction processes. NaMgMnO-a (Figure 7.6 (a)) displays redox couples that are broad and nearly indistinguishable indicating that the reactions occur very close to each other. NaMgMnO-ma (Figure 7.6 (b)) displays improved peak intensity compared to NaMgMnO-a. This indicates a lower internal resistance, better electrochemical performance and good reversibility between charge and discharge processes. There are three prominent pairs of redox peaks: (I) at ca. 2.7 V vs. Na/Na$^+$ ascribed to the Mn^{3+}/Mn^{4+} redox couple, (II) at 3.0 – 3.3 V vs. Na/Na$^+$ gives broad peaks due to the complicated de-sodiation/sodiation processes in the crystal lattice structure, and (III) at ca. 4.2 V vs. Na/Na$^+$, observed only in the initial cycle, is due to the P2 – O2 phase transformation and the resultant gliding and expansion of the transition metal layers [10]. After the 100th cycle, the redox processes in NaMgMnO-a (Figure 7.6 (a)) have almost completely disappeared, indicating poor cycling performance. These results suggest that the microwave irradiation gives faster sodium extraction/insertion kinetics and improved cycle performance.

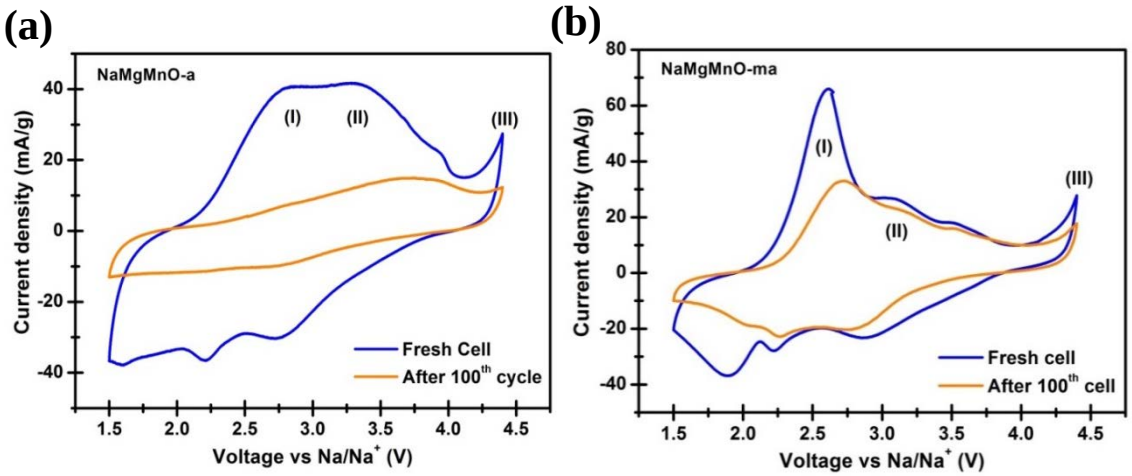


Figure 7.6: Cyclic voltammograms (current density vs. voltage) of the cells of (a) NaMgMnO-a and (b) NaMgMnO-ma. Scan rate: 0.1 mV s^{-1}. Voltage range: 1.5 – 4.4 V vs. Na/Na^+.

7.2.5.2 Galvanostatic charge-discharge

Figure 7.7 displays the charge-discharge performances of the materials (selected cycles between 1 – 100), cycled between 1.5 and 4.4 V at 0.1 C (1C = 260 mA/g). The first charge cycle to 4.4 V corresponds to the extraction (de-sodiation or de-intercalation) of small amounts of sodium ions (low charge capacity). However, upon discharge (sodiation or intercalation) more sodium ions from the sodium source (sodium metal anode) are inserted back into the structure giving rise to higher capacity. The long plateau which appeared around 4.2 V vs. Na/Na^+ in the charge curve of both the cells is due to the phase transition from the P2-type to the O2-type structure, with the resultant gliding and expansion of the transition metal layers which leads to irreversible capacity loss, whilst the voltage plateau below 4.0 V is due to the Na^+ and vacancy ordering taking place within the sodium layer. In the O2-type structure, the Na ions sit in the small octahedral sites in the lattice structure while in the P2-type they sit in the large prismatic sites, as shown in Figure 2.17. Therefore, there is a change in the unit cell as the structure changes from a P2-type to O2-type and this induces capacity fade upon cycling. The microwave irradiation is observed to increase the capacity of the NaMgMnO material. The discharge capacity for the first cycle is ca. 116 and 125 mAh/g for NaMgMnO-a and NaMgMnO-ma, respectively. The microwave irradiation increased the capacity due to the improved the morphology and crystallinity, as observed in the SEM and XRD analyses. Microwave irradiation also reduced the voltage fade in the NaMgMnO samples. NaMgMnO-a exhibited voltage fade with unstable mid-voltage.

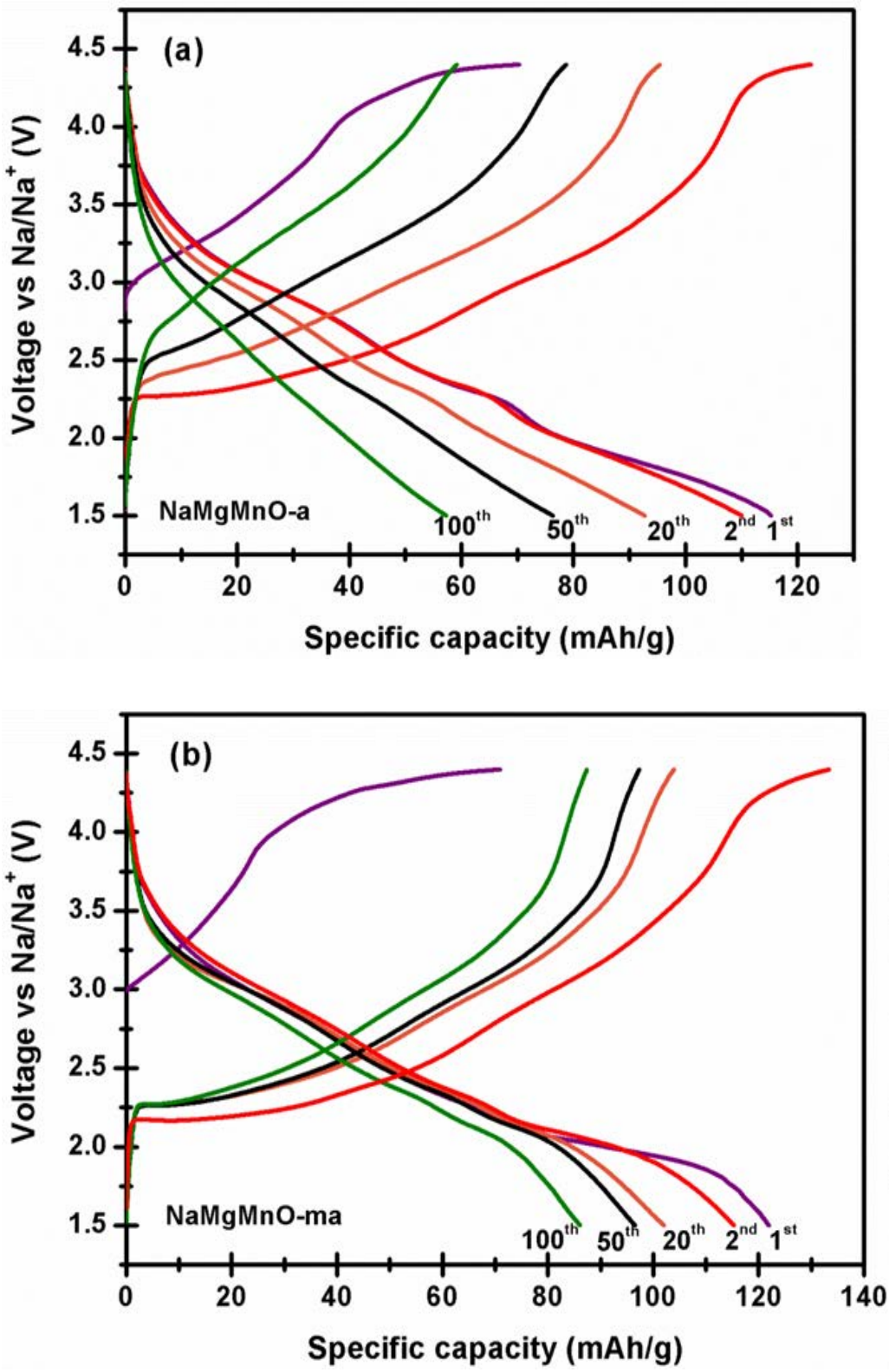


Figure 7.7: Galvanostatic charge-discharge graphs (voltage vs. specific capacity) of the cells containing the following cathode materials (a) NaMgMnO-a and (b) NaMgMnO-ma.

7.2.5.3 Cycle performance and Coulombic efficiency (CE)

Figure 7.8 shows the cycling performance and the coulombic efficiency profiles of the NaMgMnO-a and NaMgMnO-ma samples. The capacity retention and coulombic efficiency data are summarised in Table 7.4. NaMgMnO-a shows a good coulombic efficiency above 95 %, however, NaMgMnO-ma exhibits enhanced coulombic efficiency of 100 % from the 5^{th} – 100^{th} cycles. NaMgMnO-a shows poor capacity retention, only 50 % (i.e. 54 mAh/g) of its initial capacity of 108 mAh/g after 100 cycles. At the end of the 100^{th} cycle, NaMgMnO-ma, gave capacity retention of 71 %. The result clearly shows that microwave irradiation is able to stabilize the structure of the materials upon continuous cycling. Aside from the phase transformation, the reason for the observed capacity fading may be related to the Jahn-Teller distortion of the high-spin Mn^{3+} [20-22]. XPS revealed that the NaMgMnO-a has more Mn^{3+} ions compared to the NaMgMnO-ma, i.e. 69.1 % and 61.2 % for NaMgMnO-a and NaMgMnO-ma, respectively.

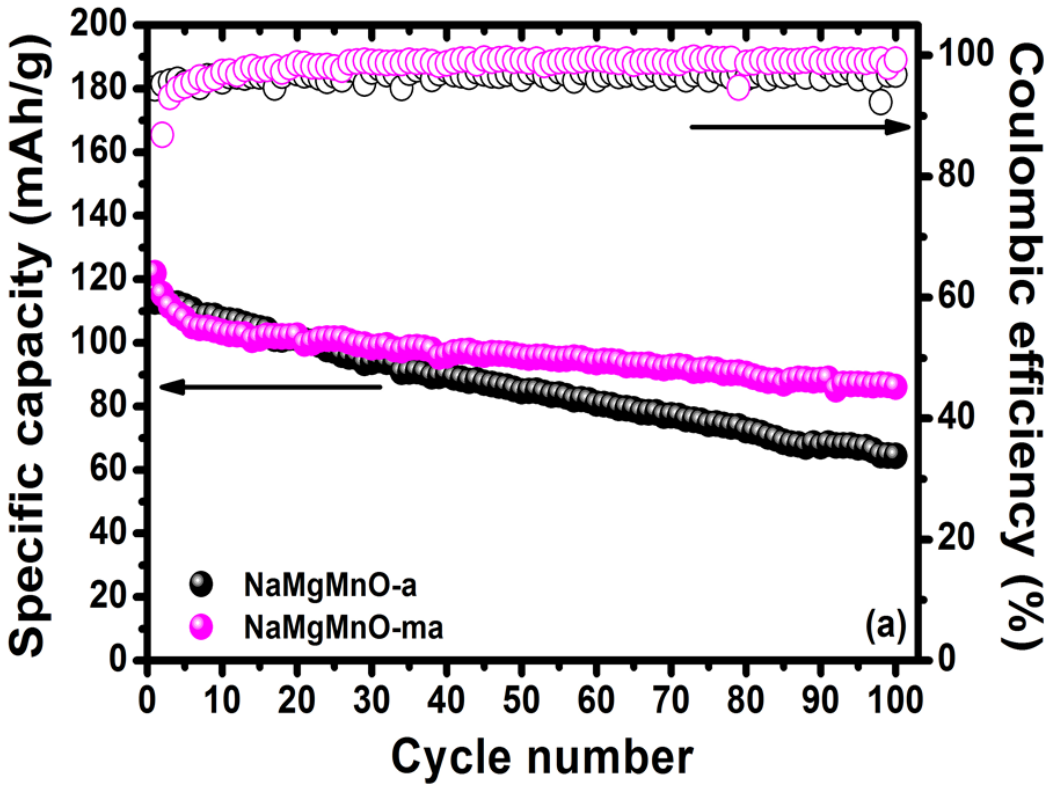


Figure 7.8: Discharge capacity and coulombic efficiency vs. cycle number graphs of NaMgMnO-a and NaMgMnO-ma containing cells.

Table 7.4: Summary of discharge capacity and capacity retention of NaMgMnO samples

Material	DC at the 1st cycle (mAh/g)	CE at the 1st cycle (%)	CR at the 20th cycle (%)	CR at the 30th cycle (%)	CR at the 50th cycle (%)	CR at the 100th cycle (%)
NaMgMnO-a	116	66	81	76	67	50
NaMgMnO-ma	125	57	82	82	78	71
Ref [8]	220	~ 96	~ 80	~ 68	n/a	n/a

Key: DC = Discharge capacity; CE = Coulombic efficiency; CR = Capacity retention; n/a = Not available

As shown in Table 7.4, the first discharge capacities obtained are lower than those in Ref [8]. Kobama and co-workers [8] work is similar to the one reported here except that they used a solid state synthesis method instead of the combustion method used in this work. However, it is evident from Table 7.4 that this present work showed better capacity retention compared to literature [8]. The discrepancies may be attributed to the differences in the chemical compositions and synthesis methods employed. This is because the synthesis methods and experimental conditions influence the stoichiometry, crystal structure, morphology, and electrochemistry of the electrode materials. The results obtained in this work show that combustion method as opposed to solid state method is able to reduce the capacity fade in the NaMgMnO materials by reducing the structural transition P2-O2 upon cycling which is observable by a voltage plateau in the charge cycle when charging above 4.0 V. The voltage plateau above 4.0 V is due to the evolution of the O2-phase which is accompanied by unavoidable volume expansion which then causes capacity fade upon cycling. In the present work, the voltage plateau above 4.0 V is observed in the 1st and 2nd cycles whereas in Ref [8] the voltage plateau is observable even at the 5th cycle. The existence of the voltage plateau is also the reason for the large capacity obtained in Ref [8], because when charging NaMgMnO materials above 4.0 V oxygen redox reactions occurs which result in additional capacity [8].

7.2.5.4 Rate Capability

Figure 7.9 displays the rate capability studies of the materials conducted at different current rates viz. 1, 2, 5, 10 and 30 C with 5 charge-discharge cycles for each step in the voltage range from 1.5 to 4.4 V. The discharge capacity decreased as the current density increased since at higher currents the Na-ions are removed rapidly during charging and there is no enough time for all of them to return to the cathode during discharging. NaMgMnO-a and NaMgMnO-ma have similar rate capability due to similar particle sizes.

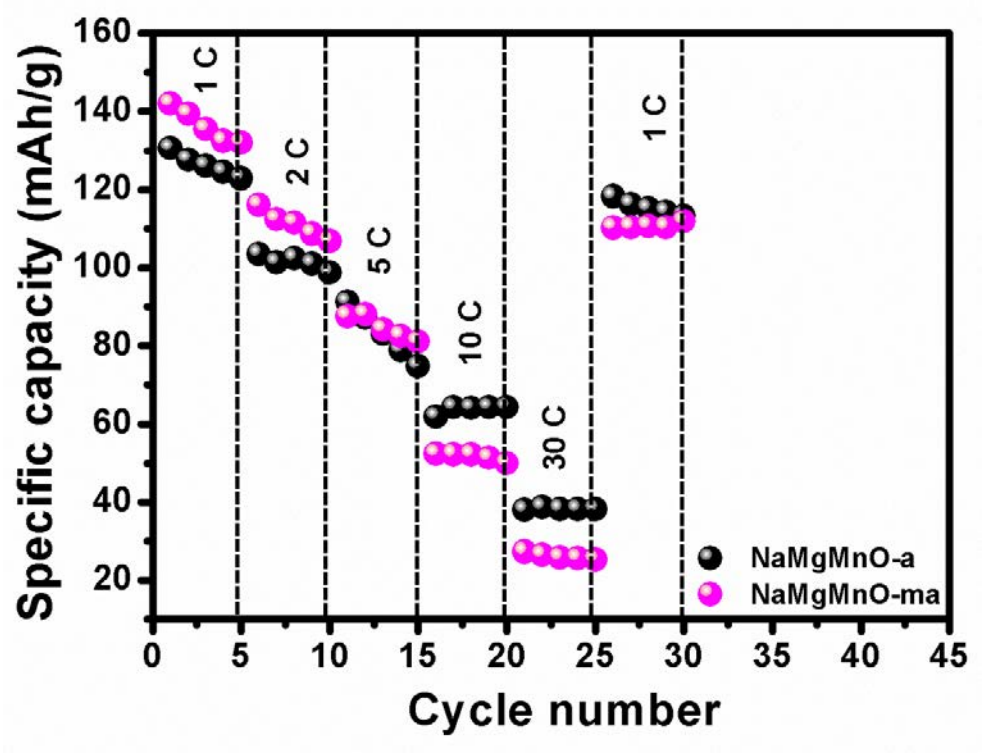


Figure 7.9: Rate performance at different current densities of the NaMgMnO samples.

7.2.5.5 Electrochemical Impedance Spectroscopy (EIS)

Electrochemical impedance spectroscopy (EIS) was conducted to establish the effects of microwave irradiation on the impedance and kinetics of NaMnMgO materials. The coin cells were analyzed before and after 100 cycles at the open circuit voltage, where OCV ~3.0 V vs. Na/Na^+. The Nyquist plots shown in Figure 7.10 were fitted with the electrical equivalent and fitting parameters as described in Chapter 4.

The values obtained from the fitted EIS data are summarized in Table 7.5. NaMgMnO-ma shows a lower impedance compared to NaMgMnO-a, suggesting that the microwave irradiation

decreases the impedance of the materials, hence its enhanced conductivity and kinetics of the Na^+ ions during the repetitive cycling. The fresh cell of NaMgMnO-ma has smaller R_s, R_f and R_{ct} values compared to NaMgMnO-a. There is also a much larger increase in the impedance values after 100 cycles for NaMgMnO-a compared to NaMgMnO-ma. This is consistent with the poor capacity retention observed for NaMgMnO-a sample. From the total series resistance ($R_s + R_f + R_{ct}$), the percentage increase of resistance after the 100^{th} cycle shows NaMgMnO-ma (92 %) < NaMgMnO-a (247 %), clearly showing that the best-conducting material is the NaMgMnO-ma.

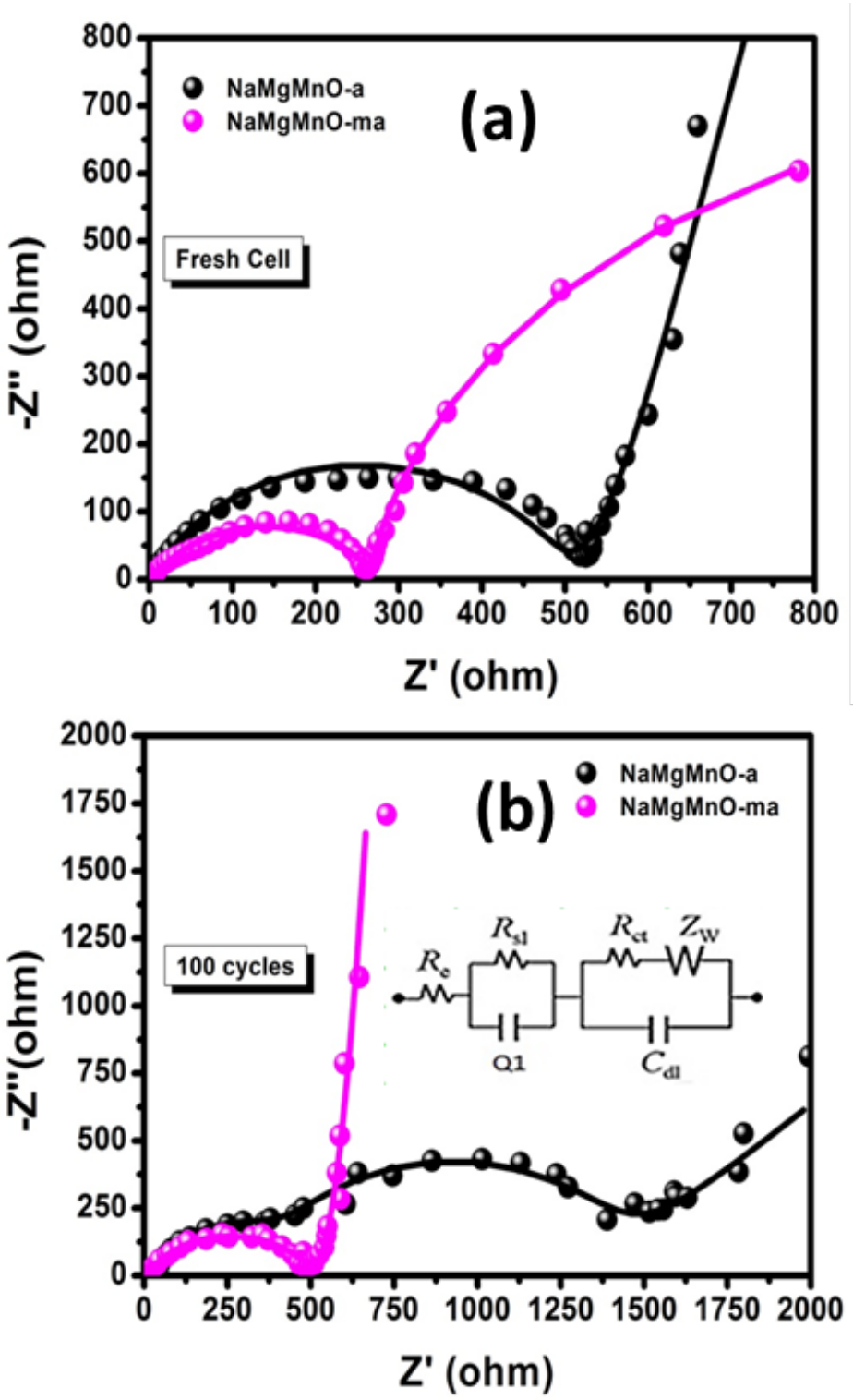


Figure 7.10: Nyquist plots (Z″ vs. Z') measured (a) before (OCV) and (b) after cycling (100 cycles). The dots and the straight line represent the experimental and fitted data, respectively.

Table 7.5: Impedimetric data of NaMgMnO-a and NaMgMnO-ma.

Material	Aging cells	R_s (±5Ω)	R_f (±5Ω)	R_{ct}(±5Ω)	Z_w(±10Ω)
NaMgMnO-a	Fresh cells	3.50	21.79	516.40	39.50
	100^{th} cycle	36.30	3.09	1840.00	182.40
NaMgMnO-ma	Fresh cells	3.50	2.18	261.90	1.30
	100^{th} cycle	6.20	13.14	494.80	23.40

7.2.5.6 Diffusion coefficient

Figure 7.11 shows plots of Z′ vs. $\omega^{-1/2}$ of NaMgMnO-a and NaMgMnO-ma samples used in determining the diffusion coefficients and Table 7.6 displays the obtained values. The Na-ion diffusion coefficients were obtained for fresh cells and aged cells (100 cycles) using EIS data. The Na-ion diffusion coefficients were found to be 9.3 x 10^{-14} and 2.6 x 10^{-12} after 100 cycles for NaMgMnO-a and NaMgMnO-ma, respectively. The microwaved sample (NaMgMnO-ma) gave the highest value compared to the pristine sample (NaMgMnO-a) and this is due to the morphological differences of the samples. The clean and smooth surface facets due to microwave irradiation observed in NaMgMnO-ma improves the contact of the sample with the electrolyte and the transport of Na-ions and electrons during charge and discharge.

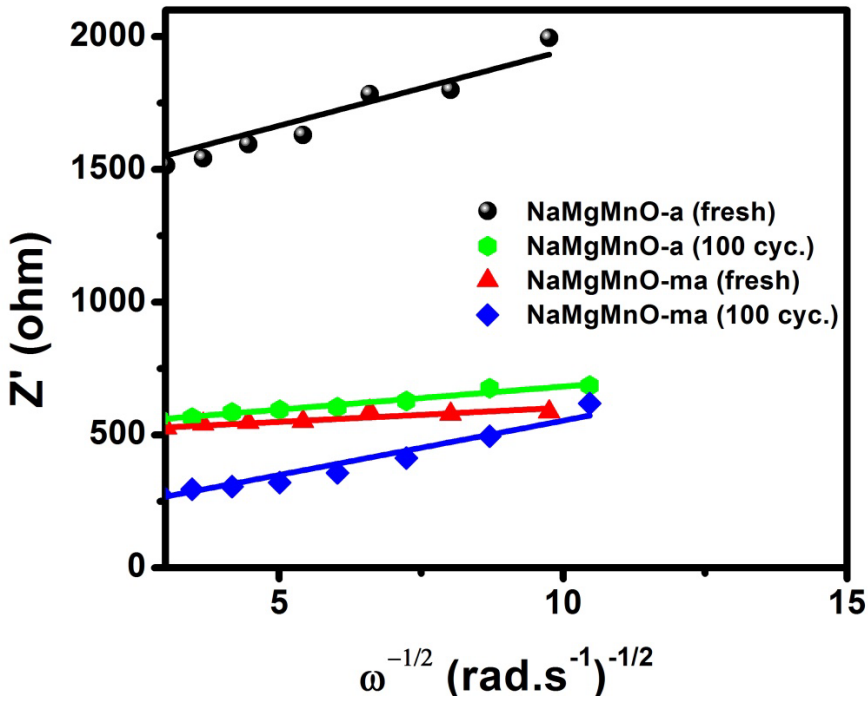


Figure 7.11: Plots of Z′ vs. $\omega^{-1/2}$ of NaMgMnO-a and NaMgMnO-ma.

Table 7.6: The calculated diffusion coefficients.

Material	Aging cells	D_{Na^+} (cm^2s^{-1})
NaMgMnO-a	Fresh cell	9.8×10^{-13}
	100^{th} cycle	9.3×10^{-14}
NaMgMnO-ma	Fresh cell	1.8×10^{-13}
	100^{th} cycle	2.6×10^{-12}

7.3 Conclusion

The urea-based combustion method has been utilized to synthesize P2-type $Na_{0.67}Mg_{0.28}Mn_{0.72}O_2$ cathode material for sodium-ion batteries. The prepared cathode materials are pure with well-defined Mg-Mn cation ordering. Microwave irradiation in the NaMgMnO-ma sample enhanced the morphology and crystallinity which, in turn, improved the capacity and capacity retention of the sample. The key finding clearly shows the impact of microwave irradiation in suppressing the P2-O2 phase transformation process and the Mn^{3+} induced Jahn-Teller distortion effect.

7.4 References

[1] S. Chitra, P. Kalyani, T. Mohan, R. Gangadharan, B. Yebka, S. Castro-Garcia, M. Massot, C. Julien, M. Eddrief, Journal of Electroceramics, 3 (1999) 433-441.

[2] W. Yang, G. Zhang, J. Xie, L. Yang, Q. Liu, Journal of Power Sources, 81 (1999) 412-415.

[3] K. Lee, H. Choi, J. Lee, Journal of Materials Science Letters, 20 (2001) 1309-1311.

[4] M.V. Reddy, B.L. Wei Wen, K.P. Loh, B.V.R. Chowdari, ACS Applied Materials & Interfaces, 5 (2013) 7777-7785.

[5] C.J. Jafta, K. Raju, M.K. Mathe, N. Manyala, K.I. Ozoemena, Journal of the Electrochemical Society, 162 (2015) A768-A773.

[6] F.P. Nkosi, C.J. Jafta, M. Kebede, L. le Roux, M.K. Mathe, K.I. Ozoemena, RSC Advances, 5 (2015) 32256-32262.

[7] K. Raju, F.P. Nkosi, E. Viswanathan, M.K. Mathe, K. Damodaran, K.I. Ozoemena, Physical Chemistry Chemical Physics, 18 (2016) 13074-13083.

[8] N. Yabuuchi, R. Hara, K. Kubota, J. Paulsen, S. Kumakura, S. Komaba, Journal of Materials Chemistry A, 2 (2014) 16851-16855.

[9] J. Paulsen, R. Donaberger, J. Dahn, Chemistry of Materials, 12 (2000) 2257-2267.

[10] H. Hou, B. Gan, Y. Gong, N. Chen, C. Sun, Inorganic Chemistry, 55 (2016) 9033-9037.

[11] J. Li, H. Lü, X. Zhang, Y. Xing, G. Wang, H. Guan, X. Wu, Chemical Engineering Journal, 316 (2017) 499-505.

[12] S. Bao, Y. Liang, W. Zhou, B. He, H. Li, Journal of Power Sources, 154 (2006) 239-245.

[13] B. Hafner, Characterization Facility, University of Minnesota-Twin Cities, (2007).

[14] J. Zheng, P. Yan, W.H. Kan, C. Wang, A. Manthiram, Journal of the Electrochemical Society, 163 (2016) A584-A591.

[15] N. Yabuuchi, M. Kajiyama, J. Iwatate, H. Nishikawa, S. Hitomi, R. Okuyama, R. Usui, Y. Yamada, S. Komaba, Nature Materials, 11 (2012) 512-517.

[16] C.J. Jafta, K.I. Ozoemena, M.K. Mathe, W.D. Roos, Electrochimica Acta, 85 (2012) 411-422.

CHAPTER 8

Fluorination of P2-type $Na_{0.67}Mg_{0.28}Mn_{0.72}O_2$ cathode materials for sodium-ion batteries

8.1 Introduction

Finding alternative solutions to reduce capacity fade in P2-type NaMgMnO materials is very important as this cathode material for sodium-ion batteries has the potential for commercialization. This is because it is well-known as a high-volumetric capacity/energy cathode material for sodium-ion batteries [1] and the huge natural abundance of its precursor materials makes it low cost. Thus this cathode material is favourable for grid-scale storage where high energy density and low costs are very critical.

One of the causes of the capacity fade in the electrode material is the solid electrolyte interface film (SEI) formation or interfacial reaction of the electrode reaction with the electrolyte. Anion doping is one of the strategies used to improve the cycle stability of cathode materials. However surface anion doping is beneficial for improving the capacity fade caused by interfacial reaction of the electrode material with the electrolyte. Among the anions such F^-, Br^-, S^{2-} and PO_4^{3-}, fluorine doping has been reported to enhance the electrochemical performance of the cathode materials with various structures including spinels, olivines and layered cathode materials [2-6].

Fluorination has been found to improve the stability of electrode materials [7-9]. Fluorine surface doping of cathode material is expected to improve electrochemical performance by: (a) increasing surface electric conductivity, (b) stabilizing the surface structure during charge and discharge, and (c) reducing electrolyte oxidation [10-15].

Therefore this chapter introduces surface fluorine-doping of P2-type NaMgMnO which has not been reported in literature before and studies the effect of both microwave irradiation and fluorine-doping on the electrochemistry of the material.

The fluorinated sample (NaMgMnO-af) and microwave irradiated and fluorine-doped sample (NaMgMnO-maf) were prepared using a combustion synthesis method as outlined in the experimental section Chapter 3. A low-temperature (450 ℃) method using NH_4F is used to modify the surface structure of NaMgMnO with F-ions, and this method is advantageous for doping compared to high temperature annealing methods [16] which promote fluorination towards the core of the materials [10].

The fluorinated samples were doped with a minute content of fluorine atoms making the stoichiometry of the samples to be $Na_{0.67}Mg_{0.28}Mn_{0.72}O_{1.98}F_{0.02}$. Studies by Khalil Amine and co-workers clearly demonstrate that doping with 0.02 F can effectively improve the capacity retention and reduce the impedance of the cathode materials [11].

Therefore this work interrogates and clearly confirms the synergistic effect of the redox property-enhancing features of microwave irradiation and fluorination towards the electrochemical performance of P2-type NaMgMnO material.

8.2 Results and Discussion

8.2.1 Powder X-ray Diffraction Characterization

Figure 8.1 reports the PXRD results of the prepared NaMgMnO-af and NaMgMnO-maf samples. The XRD diffractograms were indexed to a P2-type hexagonal structure with the space group *P6$_3$/mmc* [1]. The pattern also shows a (1/3, 1/3, 0) diffraction peak at ca. 21° due to the presence of stacking faults in the superlattice layers due to the in-plane ordering between (Mg^{2+} and Mn^{3+}) and Mn^{4+} [1]. As shown in Figure 8.1, the NaMgMnO-af and NaMgMnO-maf samples are pure as there are no new peaks or impurity peaks such as LiF. Therefore this confirms the successful preparation of the samples and shows that fluorine doping and microwave irradiation does not distort or change the layered NaMgMnO structure. The lattice parameters (*a* and *c*), crystal density and cell volume were calculated using Rietveld refinement.

Table 8.1 summarises the crystallographic data of the NaMgMnO-af and NaMgMnO-maf samples and compares the results with that of pristine NaMgMnO-a sample. Fluorination in NaMgMnO-af and NaMgMnO-maf slightly decreased the *a* lattice parameter. This confirms that the fluorine has been successfully doped in the oxygen site, due to the smaller atomic radius of the fluorine (0.71 nm atomic radius) than oxygen (0.73 nm atomic radius). Importantly, it is clear that the crystal density of the fluorinated materials are higher than those of the pristine materials, decreasing in density as follows: NaMgMnO-maf (~84 g cm^{-3}) > NaMgMnO-af (~78

g cm^{-3}) > NaMgMnO-a (~68 g cm^{-3}). The crystal density values suggest that the combination of microwave irradiation with fluorination leads to high molecular packing arrangement of the materials. Also, the increased crystal density upon fluorination may be related to fluorine atoms being heavier than oxygen atoms.

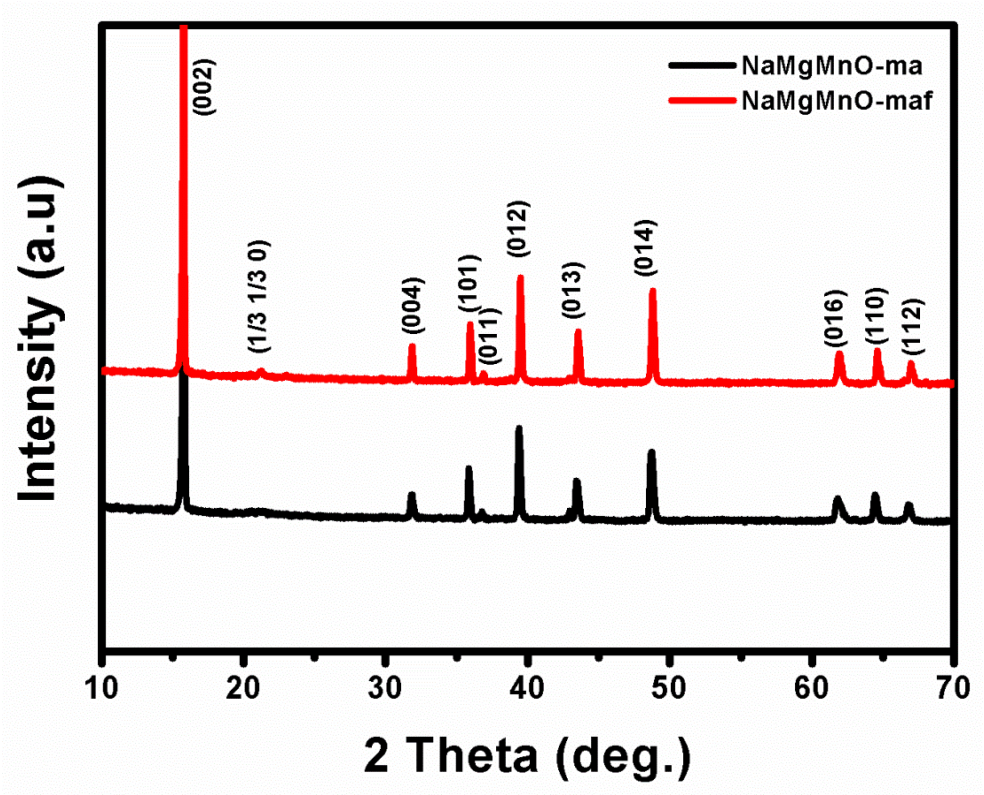


Figure 8.1: PXRD pattern of the prepared (a) NaMgMnO-af and (b) NaMgMnO-maf samples.

Table 8.1: Summary of crystallographic data of NaMgMnO-af and NaMgMnO-maf compared to NaMgMnO-a sample.

Materials	Lattice parameter ±0.002 (Å)	d-spacing (002) ±0.002 (nm)	Cell volume ±0.002 ($Å^3$)	Crystal density ±0.002 (g cm^{-3})	R_p (%)	R_{wp} (%)	R_{bragg} (%)
NaMgMnO-a	***a***-2.895 ***c***-11.265	5.632	245.259	67.894	2.86	3.82	1.761
NaMgMnO-af	***a***-2.888 ***c***-11.275	5.637	244.382	77.606	2.09	3.28	1.969
NaMgMnO-maf	***a***-2.883 ***c***-11.236	5.628	242.628	83.882	1.85	2.66	1.960

8.2.2 X-ray Photoelectron Spectroscopy Characterization (XPS)

Figure 8.2 represents the deconvoluted XPS spectra of the Mn $2p_{3/2}$ peak for NaMgMnO-af and NaMgMnO-maf samples. The spectra for both samples were deconvoluted into two peaks attributed to Mn^{3+} and Mn^{4+} ions as expected.

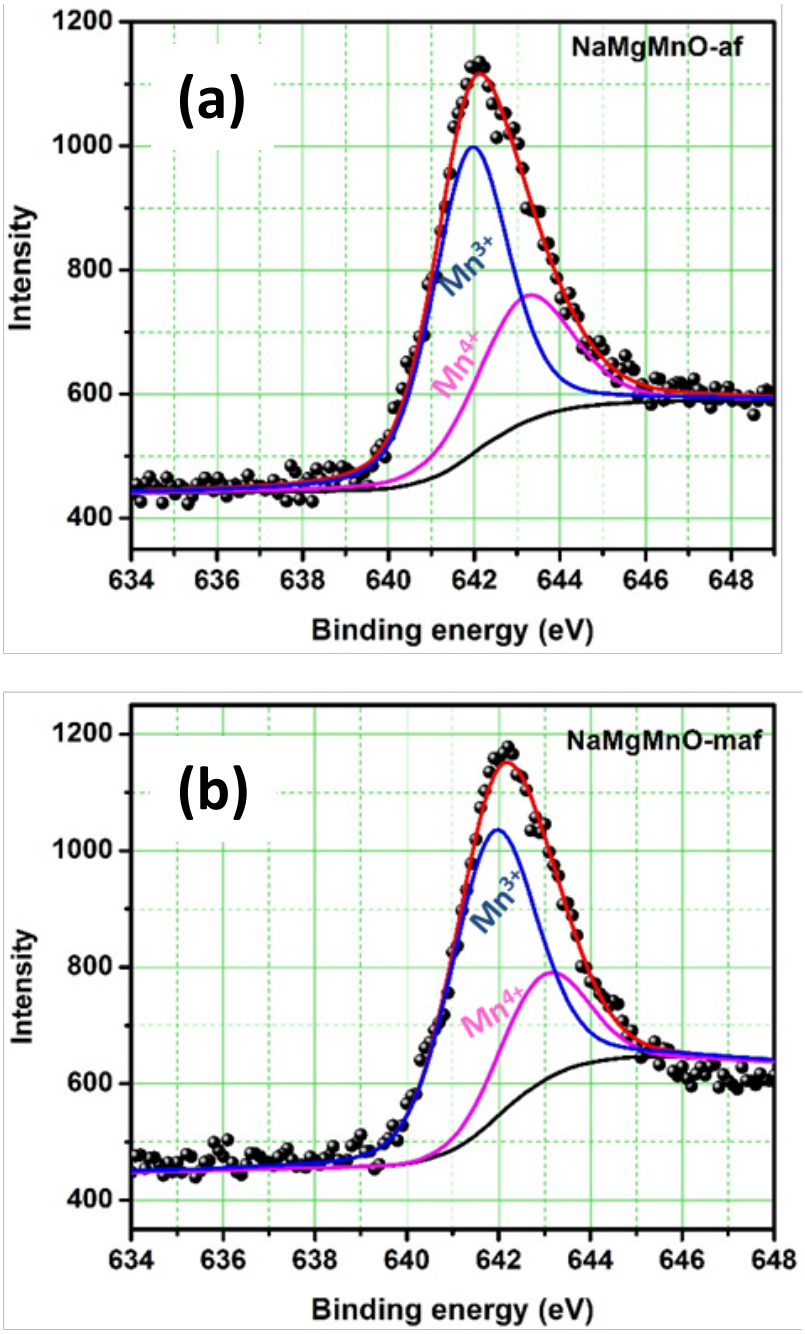


Figure 8.2: XPS spectra for the (a) NaMgMnO-af and (b) NaMgMnO-maf samples.

The binding energies and the distribution of the manganese ions in the samples are summarised in Table 8.2. The binding energies of Mn^{3+} and Mn^{4+} ions for the NaMgMnO-af and NaMgMnO-maf samples are comparable to the values reported in literature and the values found in the previous section of this study. From Table 8.2, it is interesting to observe some unique changes in the ratio of the percentage concentrations for Mn^{3+}/Mn^{4+}: upon fluorination the ratio decreases (compare the ratio of 2.24 for NaMgMnO-a with the ratio of 2.00 of NaMgMnO-af) but dramatically increases if microwave irradiation is followed by fluorination

(compare the ratio of 2.24 for NaMgMnO-a with the ratio of 3.03 for the NaMgMnO-maf. In summary, this result suggests that microwave irradiation and fluorination (NaMgMnO-maf) can increase the amount of the redox-active Mn^{3+}, but without affecting the average valence state of the manganese significantly.

Table 8.2: XPS (Mn $2p_{3/2}$ spectra) data of the NaMgMnO-af and NaMgMnO-maf samples compared to the pristine NaMgMnO-a sample.

Sample	Binding energy position (eV)		Cation distribution			Mn valence (average redox state)
	Mn^{4+}	Mn^{3+}	Mn^{4+} (%)	Mn^{3+} (%)	Mn^{3+}/Mn^{4+}	
NaMgMnO-a	640.1	638.5	30.9	69.1	2.24	3.31
NaMgMnO-af	643.2	641.9	33.3	66.7	2.00	3.33
NaMgMnO-maf	643.0	641.9	24.8	75.2	3.03	3.25

8.2.3 Scanning Electron Microscopy Characterization (SEM)

The morphology of the samples is shown in the SEM images in Figure 8.3 (a-c) for NaMgMnO-af and Figure 8.3 (d-f) for NaMgMnO-maf. The SEM images Figure 8.3 (a,d) show that both samples exhibit hexagonal plate-like shaped micron-sized particles (1–3 μm diameters). There is surface roughness which appears to indicate coating with fluorine atoms. Coating of the particles with fluorine leads to surface roughness indicating that the fluorine-doping is surface-confined. Surface-doping is expected to improve the electrochemical properties because the transport of Na-ions and electrons during charge and discharge occurs on the surface of the electrodes [17].

However, agglomeration and growth in particle size was observed in the fluorinated samples and this is consistence with reports for fluorine doped cathode materials [14,18]. NH_4F is known as a crystal growth flux and sintering agent [19,20]. This is because a small of amount of ammonium fluoride acts as a mineralizing agent thus increases the grain growth rate during annealing [16,21]. These results demonstrate that the surface fluorine doping has an impact on the growth kinetics, surface properties and morphology of NaMgMnO. Fluorination of microwave irradiated sample (NaMgMnO-maf) promotes blanket-like covering of the surface of the particles with the fluorine atoms (see Figure 8.3 (f)), while in the fluorinated sample

without microwave irradiation (NaMgMnO-af) the fluorine atoms are disperse on the particle surface.

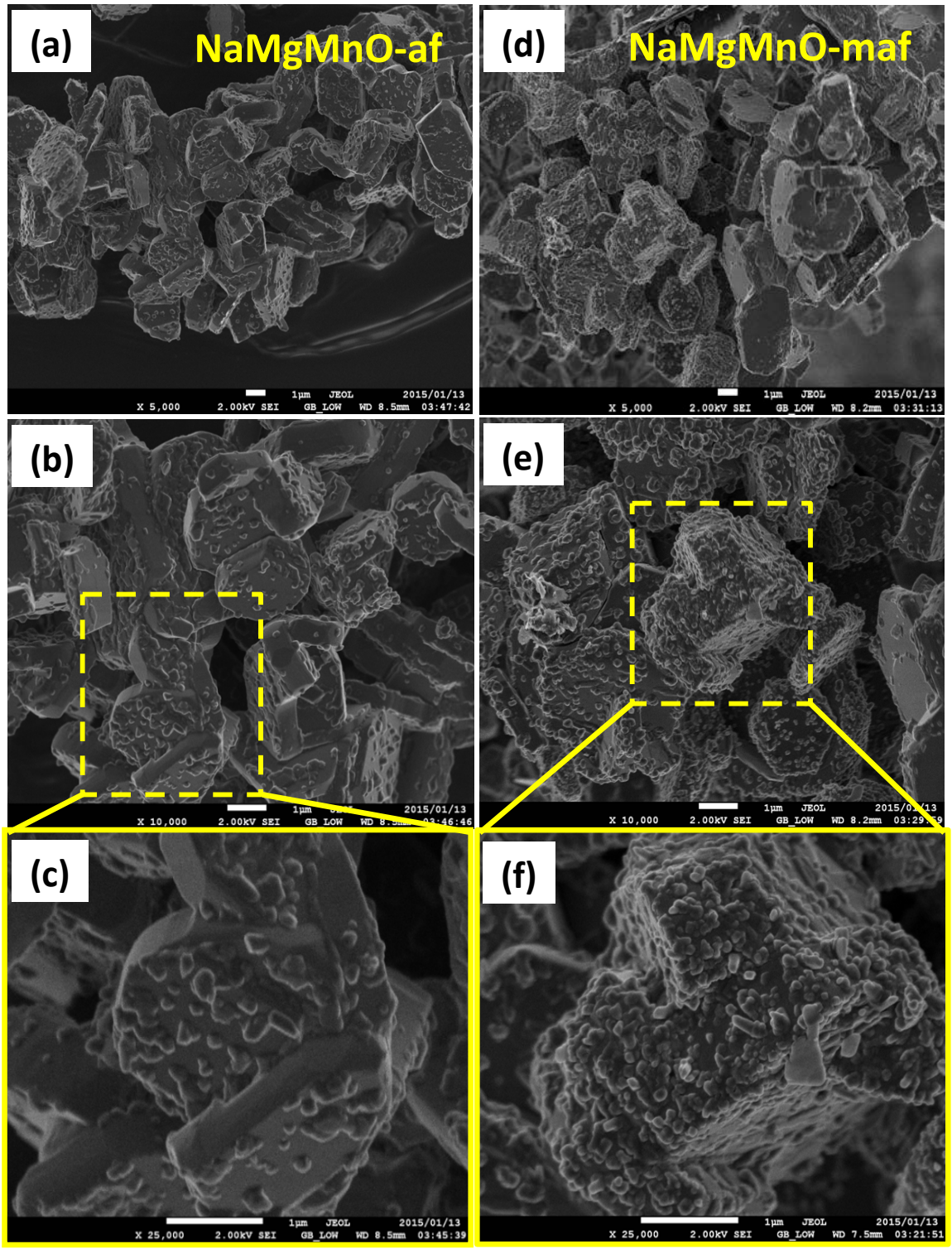


Figure 8.3: SEM analysis NaMgMnO-af (a,b,c) and NaMgMnO-maf (d, e, f) samples.

8.2.4 Electron Dispersive X-ray spectroscopy

Figure 8.4 and Figure 8.5 show EDX elemental mapping and composition of NaMgMnO-af and NaMgMnO-maf, respectively. These images show the elements present in the NaMgMnO-af and NaMgMnO-maf samples and confirm the presence of fluorine in the sample. The fluorine and the main elements (Na, Mg, Mn) are uniformly distributed.

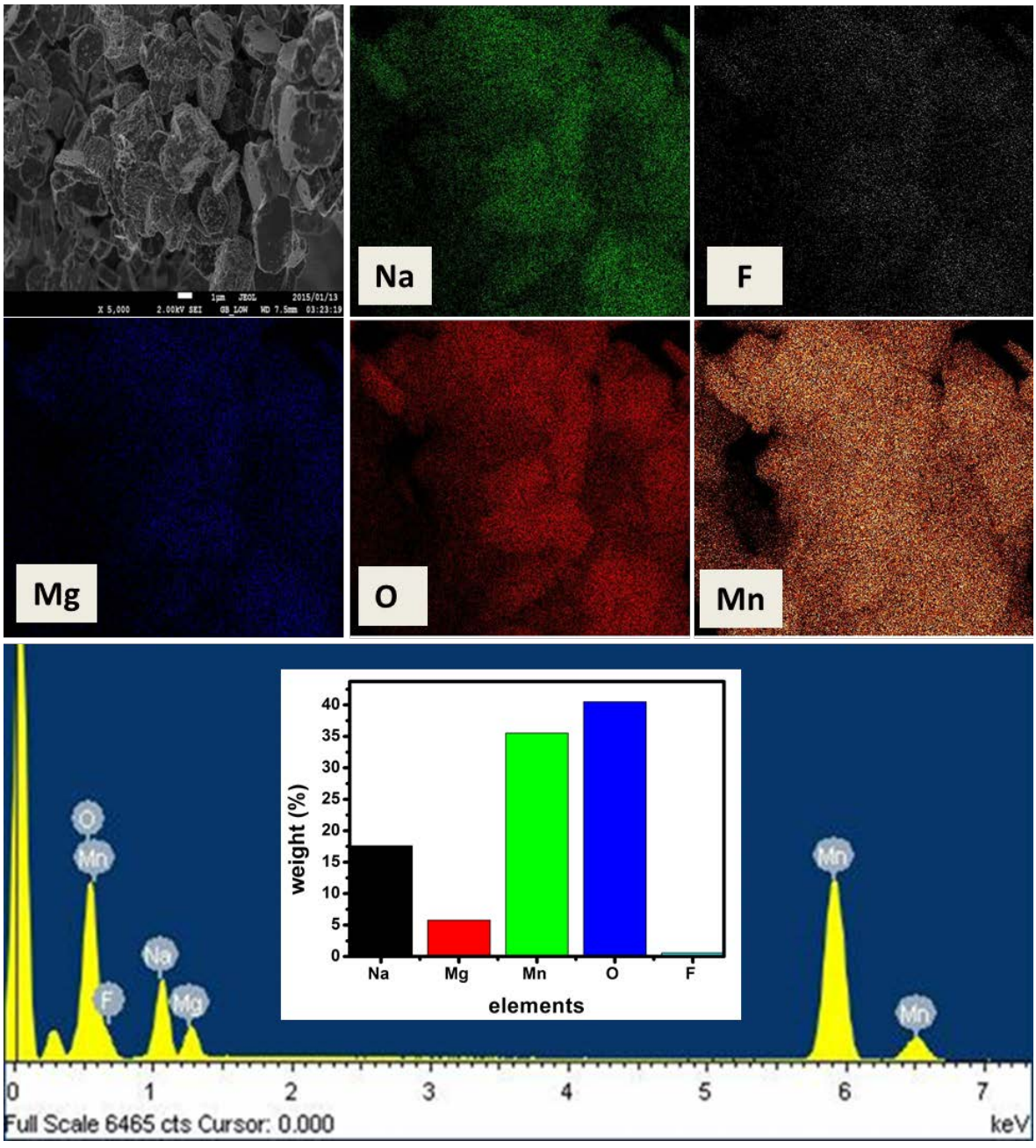


Figure 8.4: EDX mapping of the NaMgMnO-af samples.

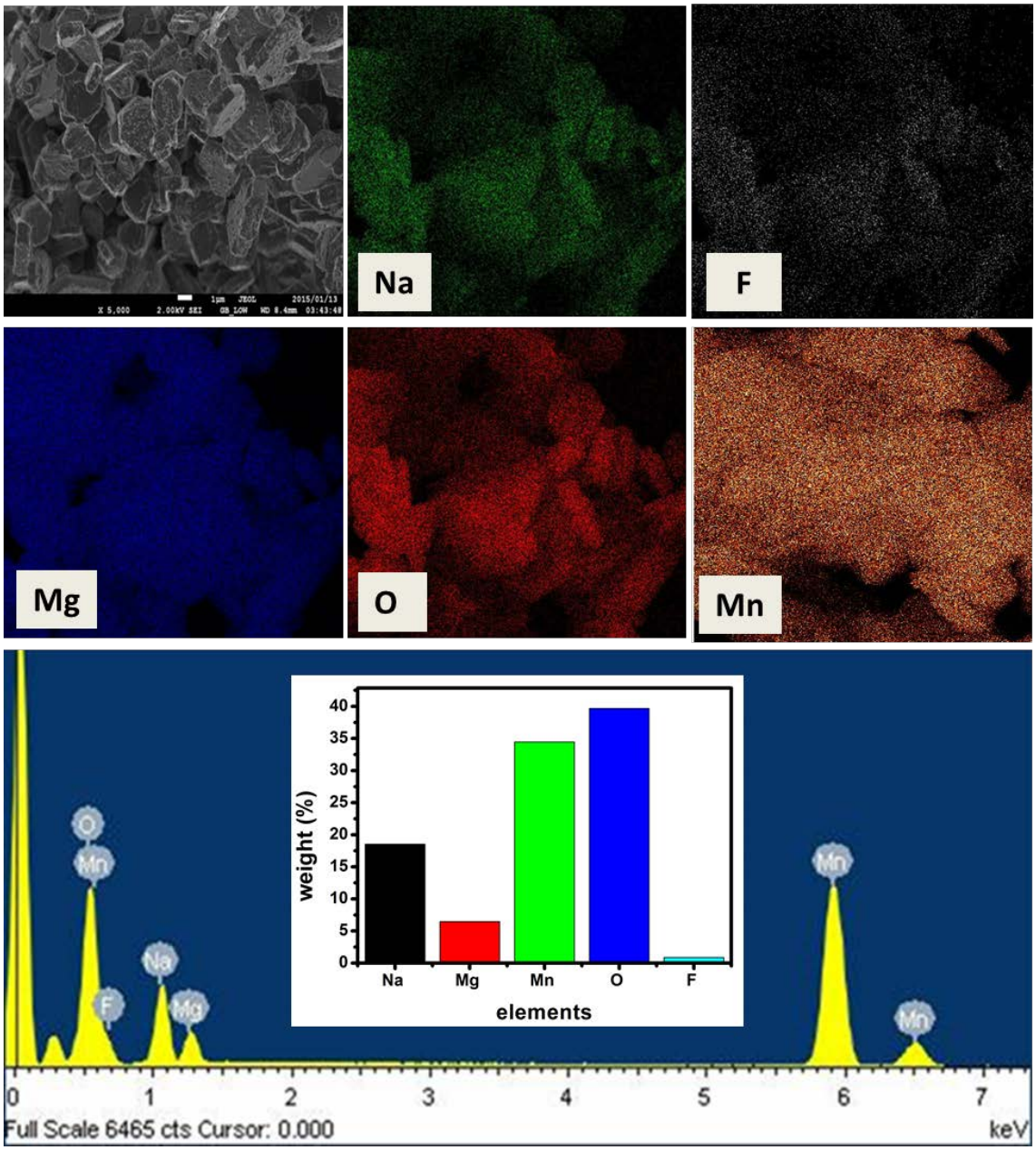


Figure 8.5: EDX mapping of the NaMgMnO-maf samples.

8.2.5 Transmission Electron Microscopy Characterization (TEM)

Figure 8.6 shows the typical TEM analysis of the fluorine-doped NaMgMnO sample. TEM images confirm that the particle shape is not changed by fluorination (Figure 8.6 (a)). The high resolution TEM proves that the powders are crystalline (Figure 8.6 (c)), showing a lattice fringe with an in interlayer distance of 0.4367 nm corresponding the (010) plane in the lattice structure. This was confirmed by the corresponding Fast Fourier Transformation (FFT) pattern (Figure 8.6 (d)), which is also consistent with the XRD results.

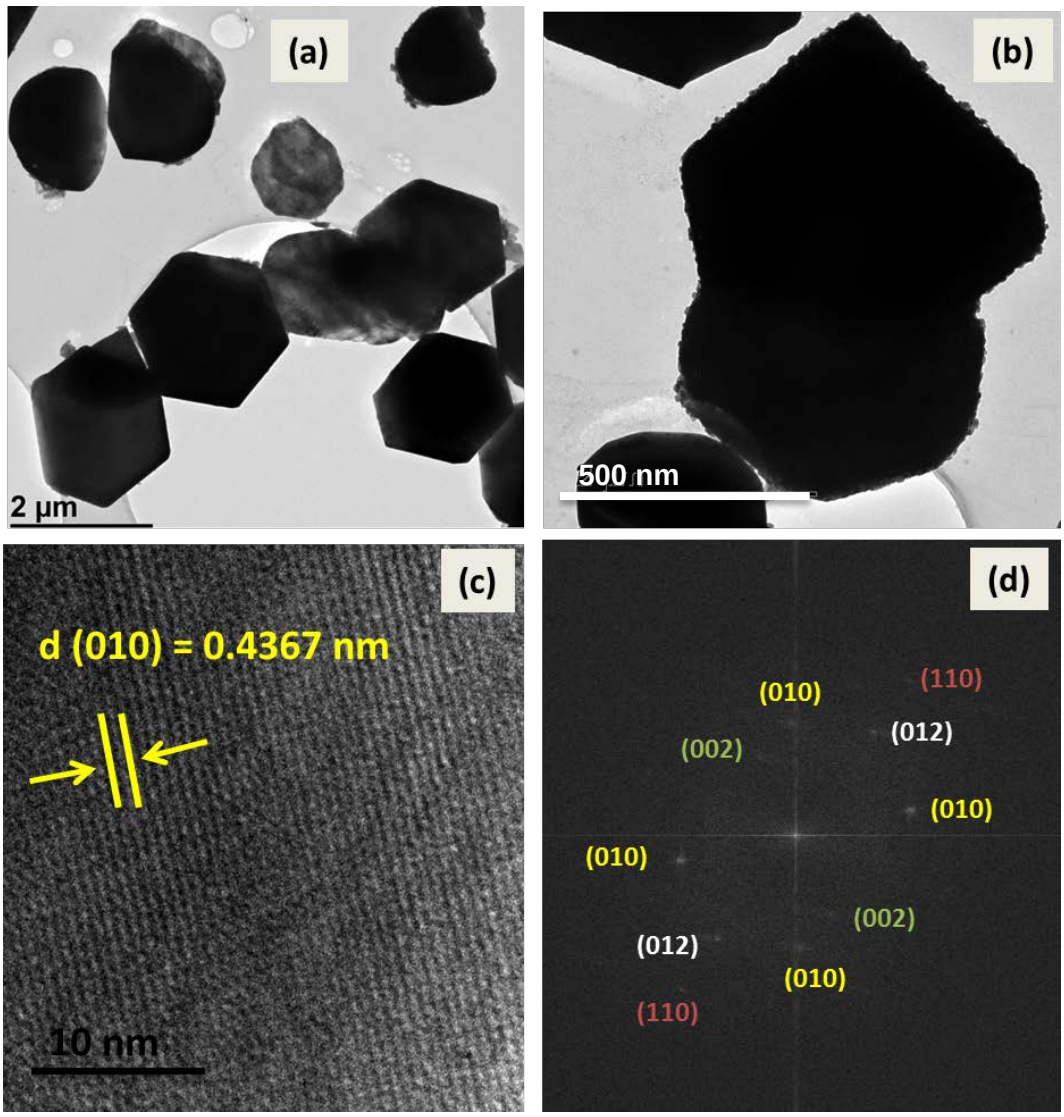


Figure 8.6: Typical TEM analysis of the fluorine-doped NaMgMnO (a,b) TEM images, (c) HR-TEM image and FFT image mapping of the NaMgMnO-af sample.

8.2.6 Electrochemical Characterization

8.2.6.1 Cyclic voltammetry

Figure 8.7 shows the cyclic voltammetric evolutions of the fluorine doped samples for the fresh cell and after the 100th cycle and compares the results with that of pristine NaMgMnO-a sample Figure 8.7 (a) (inset). The CV behaviour of the fluorinated samples is similar to that of the pristine sample, but NaMgMnO-af and NaMgMnO-maf exhibit sharp peaks with higher peak currents than the pristine material. This indicates good reversibility between charge and discharge processes and improved electrochemical performance for NaMgMnO-af and NaMgMnO-maf compared to NaMgMnO-a. The NaMgMnO-af and NaMgMnO-maf samples having similar cyclic voltammograms indicate that the dual microwave irradiation and fluorination treatment has the same effect on the redox reactions as the fluorination alone.

After 100 cycles, the area under the curve of the pristine samples is much smaller than that of NaMgMnO-af and NaMgMnO-maf. The decrease is as follows: NaMgMnO-maf > NaMgMnO-af > NaMgMnO-a. This indicates larger capacity fade for the pristine sample compared to fluorinated samples, which is consistent with the cycling performance.

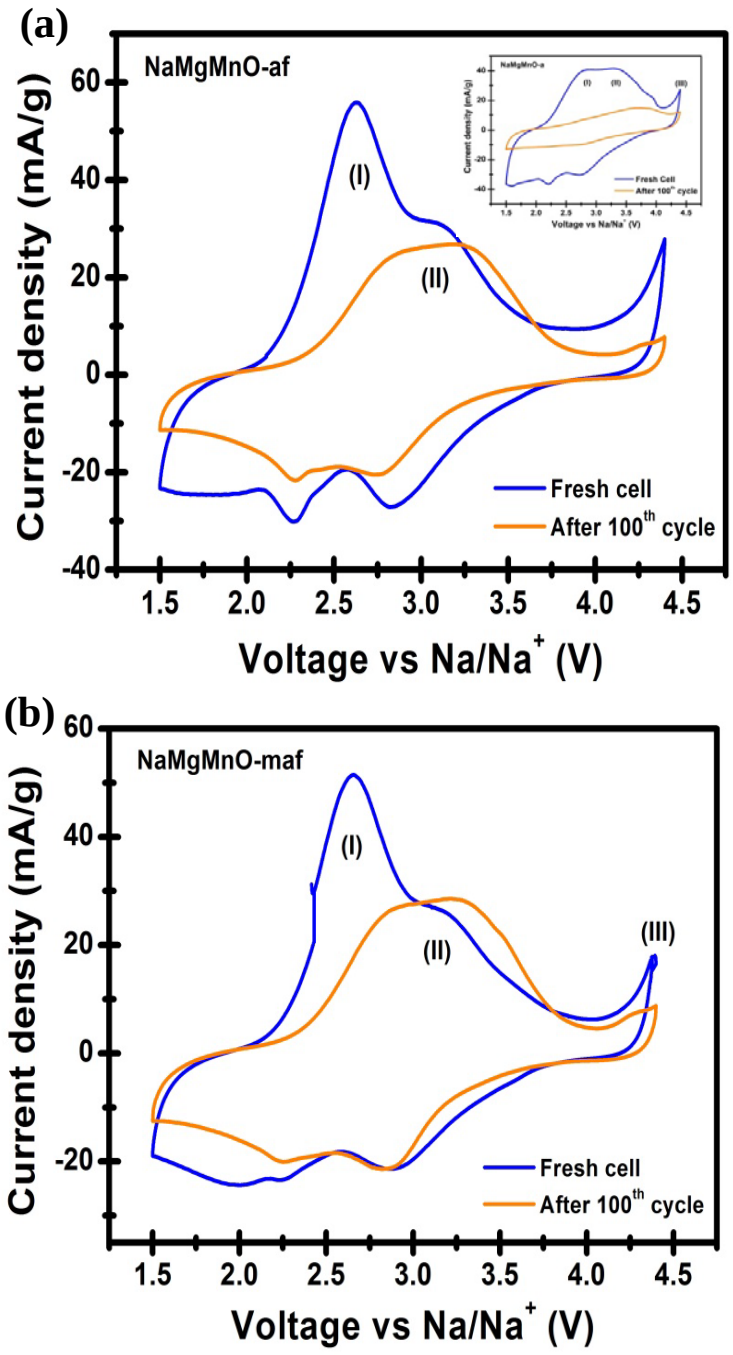


Figure 8.7: Cyclic voltammograms (current density vs. voltage) of (a) NaMgMnO-af, NaMgMnO-a (inset) and (b) NaMgMnO-maf. Scan rate: 0.1 mV s^{-1}. Voltage range: 1.5 – 4.4 V vs. Na/Na^{+}.

8.2.6.2 Galvanostatic charge-discharge

Figure 8.8 shows the charge-discharge performances of the materials cycled between 1.5 and 4.4 V at 0.1 C. The galvanostatic charge-discharge behavior is also similar to that of the pristine sample. However; microwave irradiation and fluorination are observed to increase the capacity of the NaMgMnO material. The discharge capacity for the first cycle is ca. 130 and 140 mAh/g for NaMgMnO-af and NaMgMnO-maf, respectively. This is higher than 116 mAh/g for pristine NaMgMnO-a. The microwave irradiation increased the capacity for the NaMgMnO-maf due to the improved the morphology and crystallinity, as observed in the SEM and XRD analyses. Fluorination increased the capacity for NaMgMnO-af because the fluoride ions are doped on the surface of the NaMgMnO materials and thus result in increased surface electric conductivity and protect the cathode materials from HF attack. The fluorinated samples also show reduced voltage fade during cycling compared to pristine sample.

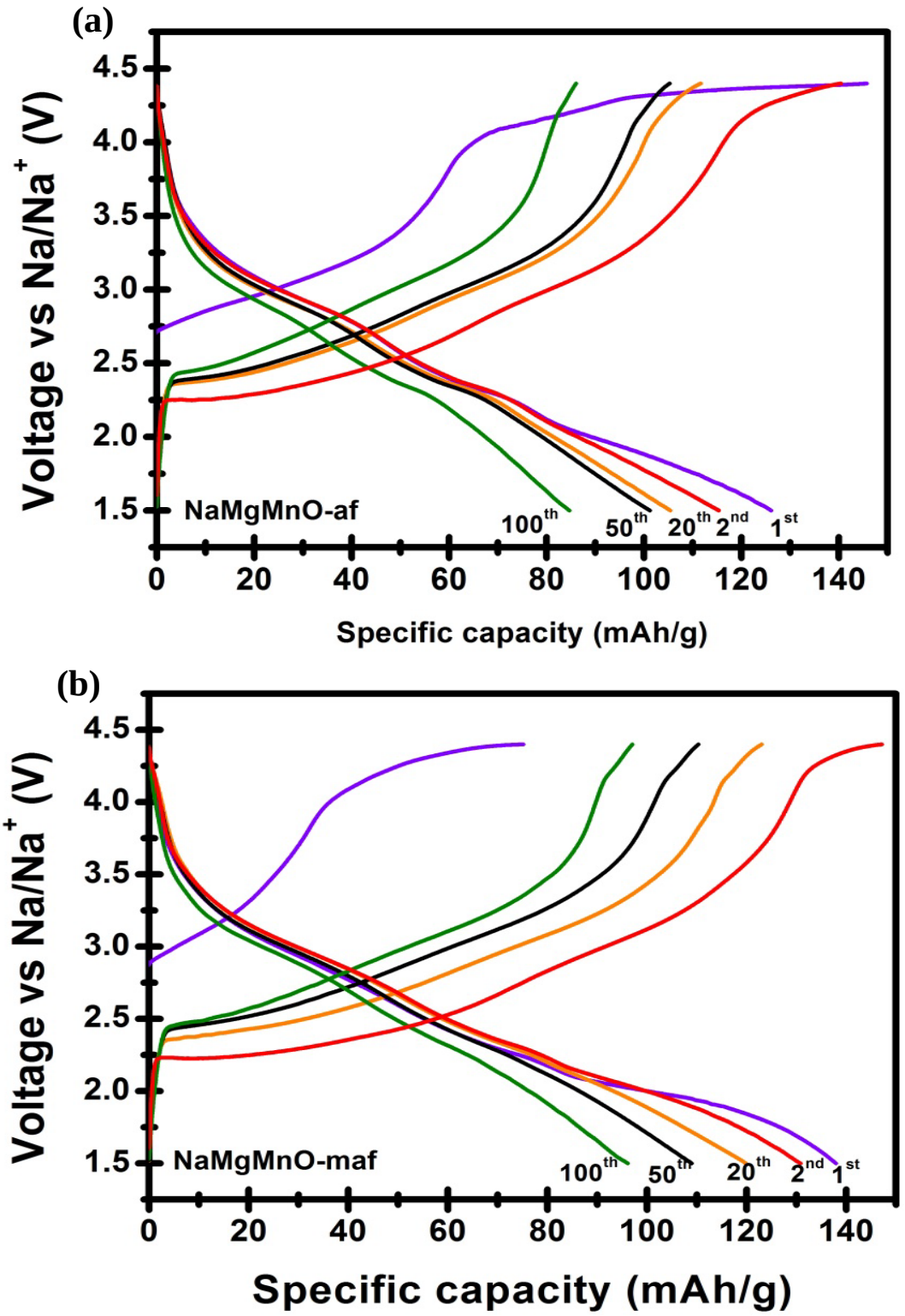


Figure 8.8: Galvanostatic charge-discharge graphs (voltage vs. specific capacity) of (a) NaMgMnO-af and (b) NaMgMnO-maf.

8.2.6.3 Cycle performance and Coulombic efficiency (CE)

Figure 8.9 shows the cycling performance as well as the coulombic efficiency profiles of the NaMgMnO-af and NaMgMnO-maf samples compared to the NaMgMnO-a. The capacity retention and coulombic efficiency data are summarised in Table 8.3. NaMgMnO-af and NaMgMnO-maf samples exhibit better cycling performance than the pristine sample. Stable coulombic efficiency of higher than 95 % after 5 cycles is also observed for NaMgMnO-af and NaMgMnO-maf. Fluorination stabilizes electrode/electrolyte interface and thus improves the electrochemical performance. These results further confirm that the improved cycling performance is mainly attributed to the stabilized electrode surface. The capacity retention after 100 cycles for NaMgMnO-maf and NaMgMnO-af was 70 % and 62 %, respectively. The results clearly show that microwave irradiation and fluorination are able to stabilize the structure of the materials upon continuous cycling.

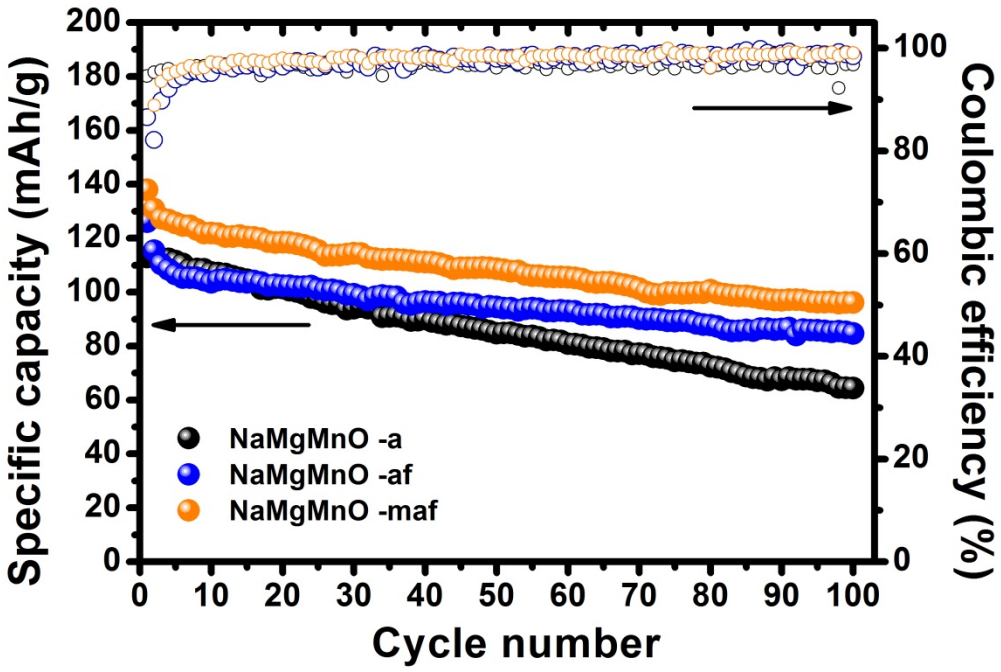


Figure 8.9: Discharge capacity vs. cycle number and coulombic efficiency graphs of NaMgMnO-af and NaMgMnO-maf compared to the pristine NaMgMnO-a sample.

Table 8.3: Summary of discharge capacity and capacity retention of fluorine doped NaMgMnO samples compared to the pristine NaMgMnO-a sample.

Material	DC at the 1st cycle (mAh/g)	CE at the 1st cycle (%)	CR at the 20th cycle (%)	CR at the 30th cycle (%)	CR at the 50th cycle (%)	CR at the 100th cycle (%)
NaMgMnO-a	116	95	81	76	67	50
NaMgMnO-af	125	86	81	79	75	62
NaMgMnO-maf	140	83	86	83	79	70

Key: DC = Discharge capacity; CE = Coulombic efficiency; CR = Capacity retention; n/a = Not available

8.2.6.4 Rate capability

Figure 8.10 shows the rate capability studies of the materials at different current densities in the voltage range from 1.5 to 4.4 V. All the samples show decrease in capacity at high current densities. However the fluorinated samples decrease slowly, suggesting improved rate capability. Although, the discharge capacity of NaMgMnO-a is high at 26 mA/g, the rate capability is poor at high current densities, the discharge capacity dropped to below 40 mAh/g at 780 mA/g.

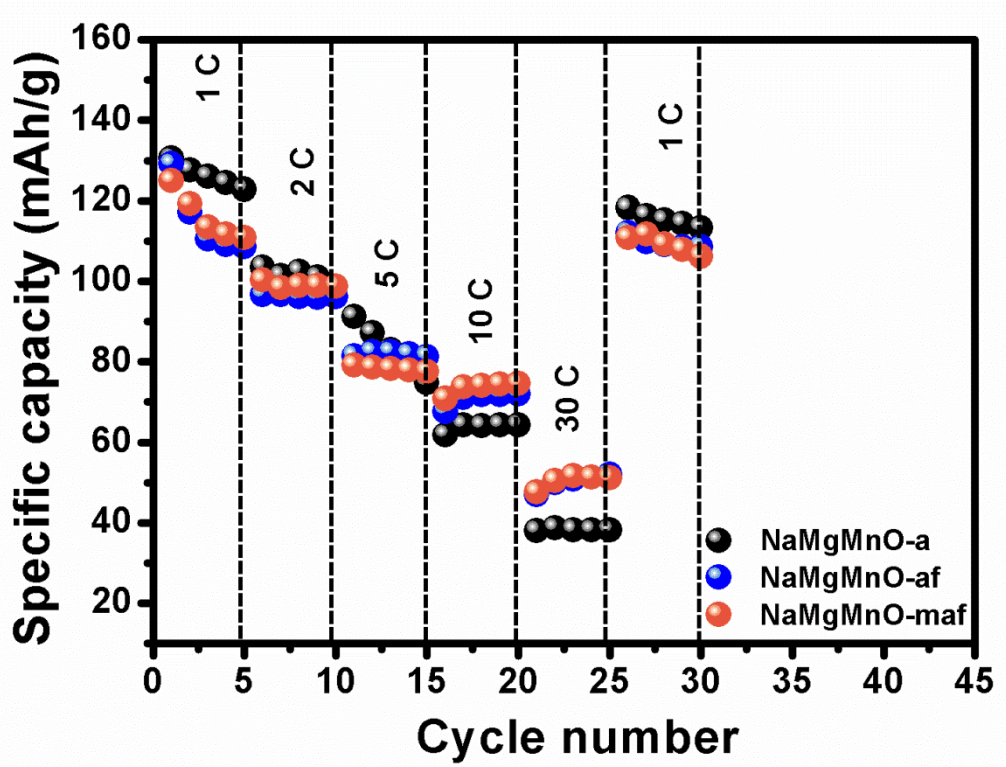


Figure 8.10: Rate capability curves of NaMgMnO-af and NaMgMnO-maf compared to the pristine NaMgMnO-a sample.

8.2.6.5 Electrochemical impedance spectroscopy (EIS)

Figure 8.11 shows the Nyquist plots of pristine NaMgMnO-a, NaMgMnO-af and NaMgMnO-maf for fresh cells (Figure 8.11 (a)) and aged cells (100 cycles) (Figure 8.11 (b)). The Nyquist plots were fitted with the electrical equivalent circuit as described before.

Figure 8.11 reveals that the fluorination decreases the impedance in the NaMgMnO materials and fluorination coupled with microwave irradiation results in even lower impedance both before and after cycling. The values obtained from the fitted EIS data are summarized in Table 8.4. The R_{ct} values are high for pristine NaMgMnO-a and drastically increases after 100 cycles, which is consistent with the poor cycle performance, while increases for the fluorinated sample consistent with the improved cycle performance. The total impedance (R_s +R_f + R_{ct}) after 100 cycles is 1879, 321 and 317 Ω for NaMgMnO-a, NaMgMnO-af and NaMgMnO-maf, respectively.

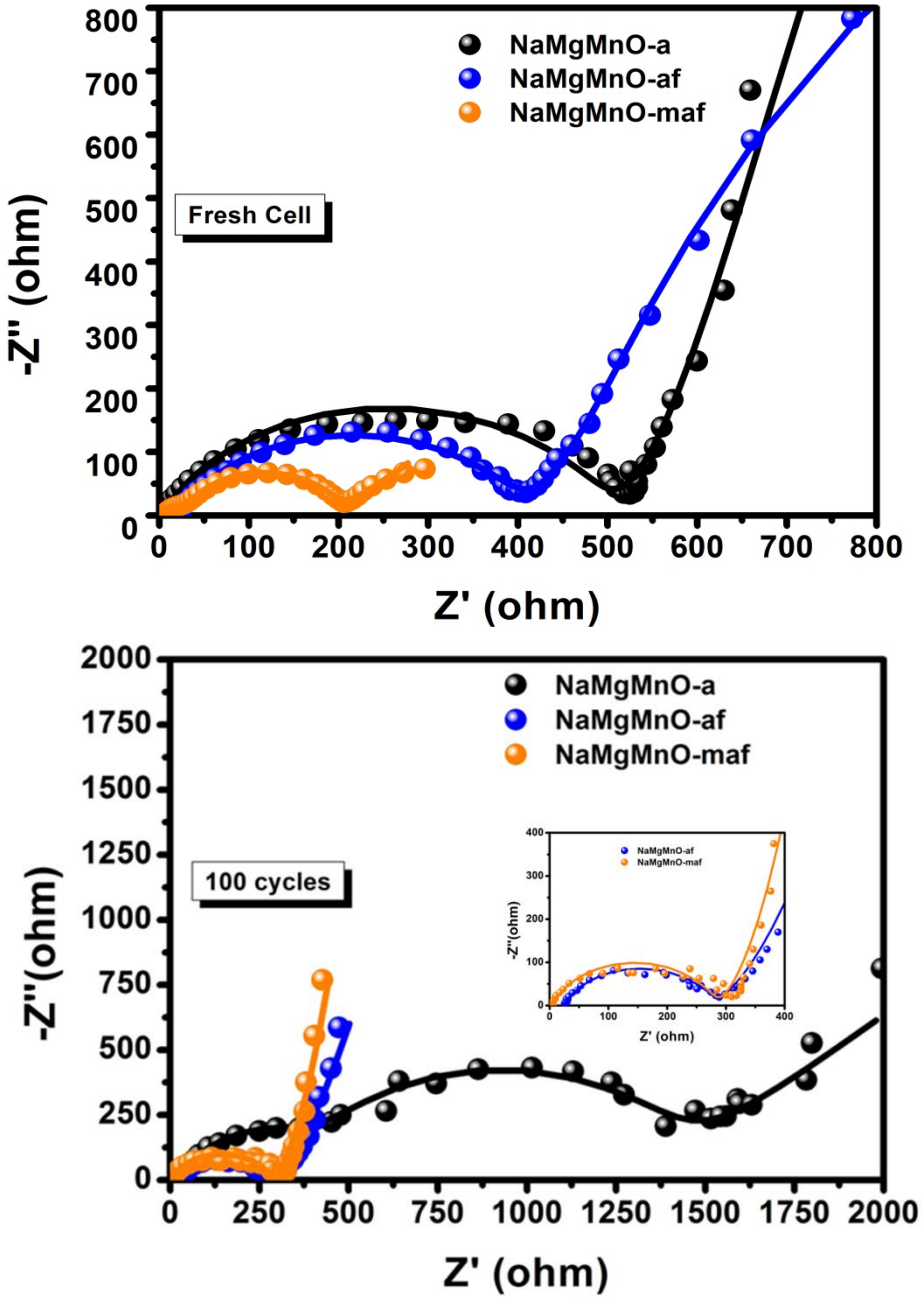


Figure 8.11: Nyquist plots (-Z″ vs. Z′) of NaMgMnO-af and NaMgMnO-maf compared to the pristine NaMgMnO-a sample measured before (at OCV) and after cycling (100 cycles). The dots and the straight lines represent the experimental and fitted data, respectively.

Table 8.4: Impedimetric data of NaMgMnO-af and NaMgMnO-maf compared to the pristine NaMgMnO-a sample.

Material	Aging cells	R_s (±5Ω)	R_f (±5Ω)	$R_{(ct)}$(±5Ω)	Z_w (±10Ω)
NaMgMnO-a	Fresh cells	3.50	21.79	516.40	39.50
	100^{th} cycle	36.30	3.09	1840.00	182.40
NaMgMnO-af	Fresh cells	19.40	3.83	386.30	37.20
	100_{th} cycle	23.80	41.18	256.80	45.20
NaMgMnO-maf	Fresh cells	6.20	25.00	166.70	65.70
	100^{th} cycle	4.10	31.62	281.60	27.70

8.2.6.6 Diffusion coefficient

The diffusion coefficient of lithium ions was calculated using the Warburg factor obtained from the EIS results. The Warburg factor (σ) of the samples was obtained from the slope of a plot of real impedance (Z') vs. reciprocal square root of frequency ($\omega^{-1/2}$) in the low frequency region curves shown in Figure 8.12.

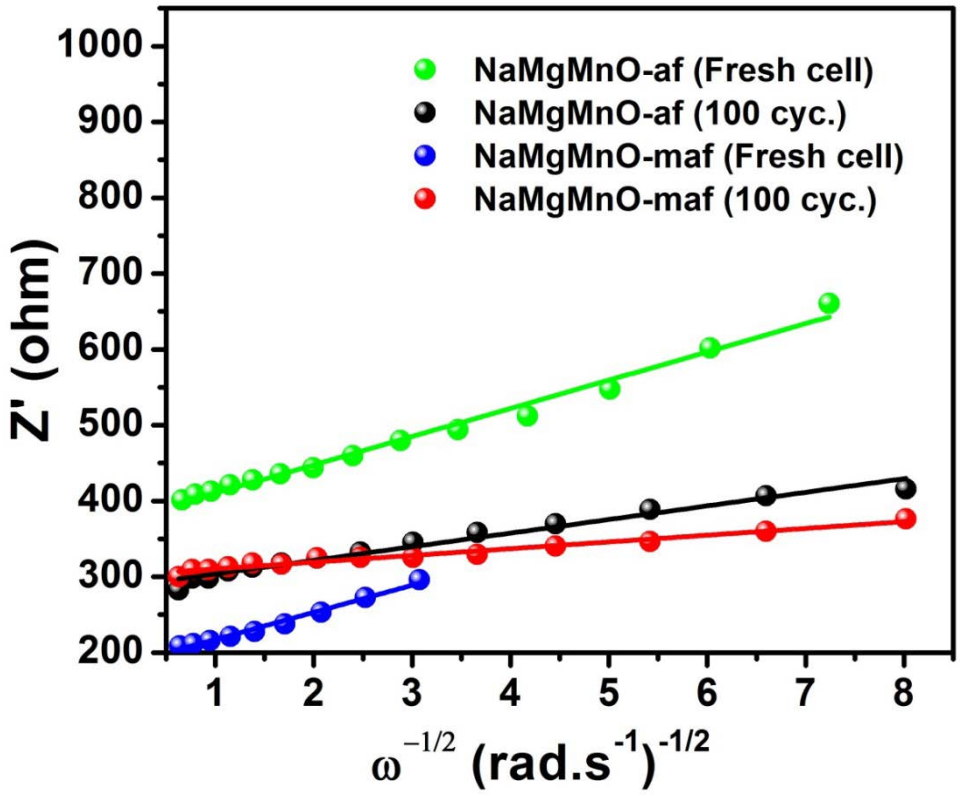


Figure 8.12: Z' vs. $\omega^{-1/2}$ curves for NaMgMnO-af and NaMgMnO-maf for fresh and aged cells.

Table 8.5 displays the calculated Na-ion diffusion coefficients in the NaMgMnO-af and NaMgMnO-maf. The Na-ion diffusion coefficients after 100 cycles were found to be 1.2 x 10^{-12} and 4.3 x 10^{-12} cm^2s^{-1} for NaMgMnO-af and NaMgMnO-maf, respectively. These are higher than the pristine sample with Na-ion diffusion coefficient of 9.3 x 10^{-14} cm^2s^{-1}. The values decrease in this order: NaMgMnO-maf > NaMgMnO-af > NaMgMnO-a. The microwave irradiated and fluorinated sample (NaMgMnO-maf) has the highest diffusion coefficient. It is also greater than the microwave irradiated sample that was not fluorinated. This is consistent with the galvanostatic charge-discharge results for the most enhance electrochemical performance. The fluorinated samples gave the high Na-ion diffusion coefficient values compared to the pristine sample and this due to the morphological differences of the samples. The surface doping with F-ions in NaMgMnO-af and NaMgMnO-maf stabilizes the structure and reduces the manganese dissolution reaction and the electrolyte oxidation.

Table 8.5: The calculated Na-ion diffusion coefficients

Material	Aging cells	D_{Na^+} (cm^2s^{-1})
NaMgMnO-af	Fresh cell	9.2 x 10^{-13}
	100^{th} cycle	1.2 x 10^{-12}
NaMgMnO-maf	Fresh cell	2.1 x 10^{-13}
	100^{th} cycle	4.3 x 10^{-12}

8.3 Conclusions

Fluorine doped NaMgMnO (NaMgMnO-af) and fluorine-doped and microwave irradiated (NaMgMnO-maf) have been prepared by combustion method using NH_4F as fluorine source. EDX analysis shows the presence of fluorine in the samples and XRD analysis shows that the fluorine ions successfully substitute for oxygen sites. The F-doped materials show improved capacity, rate capability, impedance and cycling performance in comparison with the pristine materials. In particular, NaMgMnO-maf shows capacity retention of 79 % after 50 cycles which is higher than 67 % for pristine material. Microwave irradiation for the un-fluorinated sample enhanced the morphology and crystallinity which, in turn, improved the capacity and capacity retention of the sample. NaMnMgO-ma and NaMnMgO-maf have similar capacity retention at 100 cycles but the NaMnMgO-maf sample gives high capacity compared to NaMnMgO-ma. Therefore, microwave irradiation combined with fluorination resulted in even better electrochemical performance, proving the synergy of these dual treatment methods to curb the negative P2-O2 phase transformation process and the Mn^{3+}-induced Jahn-Teller effect.

8.4 References

[1] N. Yabuuchi, R. Hara, K. Kubota, J. Paulsen, S. Kumakura, S. Komaba, Journal of Materials Chemistry A, 2 (2014) 16851-16855.

[2] K. Kubo, M. Fujiwara, S. Yamada, S. Arai, M. Kanda, Journal of Power Sources, 68 (1997) 553-557.

[3] X. Li, F. Kang, W. Shen, X. Bai, Electrochimica Acta, 53 (2007) 1761-1765.

[4] Y. Qi, Y. Huang, D. Jia, S. Bao, Z. Guo, Electrochimica Acta, 54 (2009) 4772-4776.

[5] Y. Sun, Y. Jeon, H.J. Leeb, Electrochemical and Solid-State Letters, 3 (2000) 7-9.

[6] H. Zhang, Q. Qiao, G. Li, X. Gao, Journal of Materials Chemistry A, 2 (2014) 7454-7460.

[7] S. Kang, K. Amine, Journal of Power Sources, 146 (2005) 654-657.

[8] P. Barpanda, J. Chotard, N. Recham, C. Delacourt, M. Ati, L. Dupont, M. Armand, J. Tarascon, Inorganic Chemistry, 49 (2010) 7401-7413.

[9] P. Yue, Z. Wang, H. Guo, X. Xiong, X. Li, Electrochimica Acta, 92 (2013) 1-8.

[10] G.G. Amatucci, N. Pereira, Journal of Fluorine Chemistry, 128 (2007) 243-262.

[11] K. Amine, Z. Chen, S. Kang, Journal of Fluorine Chemistry, 128 (2007) 263-268.

[12] G. Du, Y. NuLi, J. Yang, J. Wang, Materials Research Bulletin, 43 (2008) 3607-3613.

[13] Y. Liu, X. Zhou, Y. Guo, Electrochimica Acta, 54 (2009) 3184-3190.

[14] S. Oh, S. Park, J. Kim, Y.C. Bae, Y. Sun, Journal of Power Sources, 157 (2006) 464-470.

[15] T. Nakajima, H. Groult, Fluorinated Materials for Energy Conversion, Elsevier 2005.

[16] X. Li, Z. Xie, W. Liu, W. Ge, H. Wang, M. Qu, Electrochimica Acta, 174 (2015) 1122-1130.

[17] G.G. Amatucci, N. Pereira, Journal of Fluorine Chemistry, 128 (2007) 243-262.

[18] Y. He, L. Pei, X. Liao, Z. Ma, Journal of Fluorine Chemistry, 128 (2007) 139-143.

[19] B. Bogdanov, I. Chomakov, Y. Iliev, P. Tanev, Journal of the American Ceramic Society, 69 (1986).

[20] J. Zheng, X. Wu, Y. Yang, Electrochimica Acta, 105 (2013) 200-208.

[21] S. Woo, B. Park, C. Yoon, S. Myung, J. Prakash, Y. Sun, Journal of the Electrochemical Society, 154 (2007) A649-A655.

CHAPTER 9

General conclusions and Future work

9.1 Introduction

This chapter presents the conclusions pertaining to all the results obtained in this thesis and the recommendations for future work.

9.2 Conclusion

9.2.1 Preparation of LMNCA cathode materials using urea and ethylene glycol combustion synthesis.

- The effect of the fuel for the combustion synthesis of LMNCA cathode materials was investigated. Both fuels resulted in pure and crystalline LMNCA powders.
- The different types of fuel resulted in different morphology and particle sizes. This then resulted in different electrochemical behaivors.

9.2.2 The effect of microwave irradiation on LMNCA cathode materials prepared using urea and ethylene glycol combustion synthesis.

- This study investigated the effect of microwave irradiation on the electrochemistry of LMNCA cathode materials. LMNCA powders were successfully synthesised using a microwave assisted combustion method.
- The strategic application of microwave irradiation resulted in reduced particle size, enhanced the structural stability by strengthening the Mn–O bonds, and increased crystallinity.
- Microwave irradiated samples (LMNCA-urea mic and LMNCA-EG mic) showed improved cycle performance, capacity retention, coulombic efficiency and rate capability. The reaction kinetics and lithium ion diffusivity were also improved for the LMNCA-urea mic and LMNCA-EG mic materials.

9.2.3 Preparation of LMNCA cathode materials from α-MnO_2 nanowires

- α-MnO_2 nanowires were successfully prepared using the molten salts method. They proved themselves to be effective manganese precursor for the preparation of LMNCA cathode materials.
- The prepared LMNCA cathode materials using the α-MnO_2 nanowires precursors were successfully prepared without impurities or change in the structure. The thickness of the plates was between 38-167 nm and the particle size was 135-322 nm.
- Interestingly, α-MnO_2 nanowires resulted in a LMNCA materials with hexagonal plate-like morphology, uncommon for the LMNCA cathode materials.
- The prepared LMNCA materials exhibited very good cycle performance because of the exposed electrochemically active {010} planes.

9.2.4 The effect of microwave irradiation on the preparation of P2-type $Na_{0.67}Mg_{0.28}Mn_{0.72}O_2$ cathode materials for sodium-ion batteries

- P2-type $Na_{0.67}Mg_{0.28}Mn_{0.72}O_2$ (NaMgMnO) cathode materials were prepared for the first time using the urea combustion synthesis. The prepared materials are pure and highly crystalline.
- The effect of microwave irradiation was also investigated in the preparation of NaMgMnO materials. The microwave irradiation was applied in the pre-annealing step of the synthesis.
- Microwave irradiation in NaMgMnO materials resulted in enhanced the morphology and crystallinity.
- The prepared NaMgMnO materials exhibited improved the capacity and capacity retention of the sample.

9.2.5 Fluorination on the electrochemistry of P2-type $Na_{0.67}Mg_{0.28}Mn_{0.72}O_2$ cathode materials for sodium-ion batteries

- Surface fluorination of NaMgMnO performed using a low temperature annealing procedure employing NH_4F was successful in doping surface oxygen atoms with fluoride atoms. The fluorination of microwave irradiated sample was also studied.
- Surface fluorination impacted the morphology and crystal density of the NaMgMnO cathode materials.
- Surface fluorination improved capacity, rate capability, impedance and cycling performance of NaMgMnO materials. This is due to that fluorine doping enhances the

stability of electrode surface, improves surface conductivity and maintains a stable charge transfer resistance

- However, microwave irradiation combined with fluorination resulted in even better electrochemical performance, proving the synergy of these dual treatment methods to curb the negative P2-O2 phase transformation process and the Mn^{3+}-induced Jahn-Teller effect.

9.3 Future work

- This study comprises of work carried out at room temperature. It is, therefore, recommended that the electrochemical studies should be performed at lower temperatures (-10 °C), medium temperatures (40 °C) and high temperatures (>50℃). This will study the performance of LMNCA and NaMgMnO materials as these temperatures important for electric vehicle application and stationary storage applications, respectively.
- The effect of microwave irradiation can be also investigated for LMNC and NaMgMnO cathode materials doped with different cations such Ru, Fe, Cr, Ti and Zn.
- The effect of microwave irradiation can be also investigated for NaMgMnO cathode materials synthesized using other different synthesis methods such as sol-gel, co-precipitation, Pechini, etc.
- The effect of microwave irradiation may be studied for the synthesis of manganese oxide based anode materials for lithium-ion and sodium-ion batteries.
- The electrochemical studies of the cathode materials studied in this thesis were perfomed using half-cells, where the anode was the lithium or sodium metal. Therefore future work will involve investigating the performance of these cathode materials in full cells where the anode can be graphite or lithium titanate. This study will validate the materials for commercialization.